

# **Theoretical Astroparticle Physics**



# Contents

|  |            |
|--|------------|
| <b>1. Topics</b>   | <b>553</b> |
| <b>2. Participants</b>   | <b>555</b> |
| 2.1. ICRANet participants . . . . .  | 555        |
| 2.2. Past collaborators . . . . .  | 555        |
| 2.3. Ongoing collaborations . . . . .  | 556        |
| 2.4. Students . . . . .  | 557        |
| <b>3. Brief description</b>  | <b>559</b> |
| 3.1. Electron-positron plasma . . . . .  | 559        |
| 3.1.1. Relativistic degeneracy in the pair plasma . . . . .  | 560        |
| 3.1.2. Dynamics and emission of mildly relativistic plasma . . . . .   | 561        |
| 3.1.3. Evolution of the pair plasma generated by a strong electric field . . . . .                                       | 561        |
| 3.1.4. Electron-positron plasma in GRBs and in cosmology . . . . .   | 562        |
| 3.2. Transparency of relativistically expanding plasma and GRBs . . . . .  | 563        |
| 3.2.1. Photospheric emission from ultrarelativistic outflows . . . . .   | 566        |
| 3.2.2. Monte Carlo simulations of the photospheric emission in GRBs . . . . .  | 567        |
| 3.2.3. Comptonization of photons near the photosphere of relativistic outflows . . . . .                                 | 567        |
| 3.3. Neutrinos in cosmology . . . . .  | 567        |
| 3.3.1. Massive neutrino and structure formation . . . . .  | 569        |
| 3.3.2. Cellular structure of the Universe . . . . .  | 569        |
| 3.3.3. Lepton asymmetry of the Universe . . . . .  | 570        |
| 3.4. Semidegenerate self-gravitating system of fermions as a model for dark matter halos and universality laws . . . . . | 570        |
| 3.5. Constraining cosmological models with observations . . . . .  | 572        |
| 3.5.1. Features in the primordial spectrum: improving constraints by the most recent CMB and SDSS data. . . . .          | 573        |
| 3.6. Variation of the fundamental constants . . . . .  | 574        |
| <b>4. Publications</b>   | <b>577</b> |
| 4.1. Publications before 2005 . . . . .  | 577        |
| 4.2. Publications (2005 – 2011) . . . . .  | 580        |
| 4.3. Publications (2012) . . . . .   | 594        |

|   |            |
|---|------------|
| 4.4. Invited talks at international conferences . . . . .                   | 598        |
| 4.5. Lecture courses . . . . .  | 604        |
| <b>5. APPENDICES</b>  | <b>607</b> |
| <b>A. Relativistic degeneracy in the pair plasma</b>                        | <b>609</b> |
| A.1. Introduction . . . . .   | 609        |
| A.2. Modeling of the pair plasma . . . . .                                  | 610        |
| A.3. Kinetic and thermal equilibrium . . . . .                              | 612        |
| A.3.1. Two-particle interactions and kinetic equilibrium . . . . .          | 612        |
| A.3.2. Three-particle interactions and thermal equilibrium . . . . .        | 614        |
| A.4. Boltzmann equation with QED collision integrals . . . . .              | 615        |
| A.5. Two-particle collision integrals . . . . .                             | 615        |
| A.6. Three-particle collision integrals . . . . .                           | 618        |
| A.7. The numerical scheme . . . . .   | 621        |
| A.7.1. Detailed description of scheme . . . . .                             | 623        |
| A.8. Characteristic time scales of plasma relaxation . . . . .              | 629        |
| A.9. Conclusions . . . . .  | 630        |
| <b>B. Dynamics and emission of mildly relativistic plasma</b>               | <b>633</b> |
| B.1. Introduction . . . . .   | 633        |
| B.2. Formulation of the problem . . . . .                                   | 634        |
| B.3. Computational method . . . . .   | 635        |
| B.4. Results . . . . .  | 636        |
| B.5. Conclusions and future perspectives . . . . .                          | 640        |
| <b>C. Evolution of the pair plasma generated by a strong electric field</b> | <b>641</b> |
| C.1. Framework . . . . .  | 643        |
| C.2. Computational scheme . . . . .   | 645        |
| C.2.1. Acceleration and electric field evolution . . . . .                  | 646        |
| C.2.2. Emission and absorption coefficients . . . . .                       | 647        |
| C.2.3. Two particle kinematics . . . . .                                    | 652        |
| C.3. Results . . . . .  | 654        |
| C.3.1. Collisionless systems . . . . .                                      | 655        |
| C.3.2. Interacting systems . . . . .  | 658        |
| C.4. Conclusions . . . . .  | 662        |
| <b>D. Electron-positron plasma in GRBs and in cosmology</b>                 | <b>665</b> |
| D.1. Introduction . . . . .   | 665        |
| D.2. General equations . . . . .  | 665        |
| D.2.1. Early Universe . . . . .   | 667        |
| D.2.2. GRBs . . . . .   | 668        |
| D.3. Heavy elements . . . . .   | 671        |
| D.4. Recombination . . . . .  | 672        |

|   |            |
|---|------------|
| D.5. Conclusions . . . . .  | 675        |
| <b>E. Photospheric emission from relativistic outflows</b>  | <b>677</b> |
| E.1. Introduction . . . . .   | 677        |
| E.2. Optically thick relativistic outflows: wind vs. explosion . . . . .  | 678        |
| E.3. Optical depth and photospheric radius . . . . .  | 680        |
| E.3.1. Comparison with previous works . . . . .   | 686        |
| E.4. Photon diffusion . . . . .   | 689        |
| E.5. Photospheric emission from photon thick outflows . . . . .   | 690        |
| E.5.1. Geometry and dynamics of the photosphere . . . . .   | 690        |
| E.5.2. Observed flux and spectrum . . . . .   | 692        |
| E.5.3. Comparison with previous works . . . . .   | 698        |
| E.6. Photospheric emission from photon thin outflows . . . . .  | 700        |
| E.6.1. Radiative diffusion in relativistic outflow . . . . .  | 700        |
| E.6.2. Flux and spectrum of photospheric emission . . . . .   | 703        |
| E.7. Discussion . . . . .   | 704        |
| E.8. Conclusions . . . . .  | 706        |
| <b>F. Monte Carlo simulations of the photospheric emission in GRBs</b>  | <b>709</b> |
| F.1. Introduction . . . . .   | 709        |
| F.2. The model . . . . .  | 709        |
| F.3. Monte Carlo simulation . . . . .   | 710        |
| F.4. Results . . . . .  | 712        |
| F.4.1. Probability density function of position of last scattering  | 712        |
| F.4.2. Spectra and light-curves from photon thick outflow . . .   | 714        |
| F.4.3. Spectra and light curves from photon thin outflow . . .  | 717        |
| F.5. Conclusions . . . . .  | 719        |
| <b>G. Comptonization of photons near the photosphere of relativistic outflows</b>                                   | <b>721</b> |
| G.1. Introduction . . . . .   | 721        |
| G.2. The radiative transfer equation . . . . .  | 722        |
| G.3. Results . . . . .  | 725        |
| G.4. Conclusions . . . . .  | 728        |
| <b>H. Semidegenerate self-gravitating system of fermions as a model for dark matter halos and universality laws</b> | <b>729</b> |
| H.1. Introduction . . . . .   | 729        |
| H.2. Model . . . . .  | 730        |
| H.2.1. Properties of the equilibrium configurations . . . . .   | 733        |
| H.3. Comparison with other DM profiles . . . . .  | 734        |
| H.4. Scaling Laws . . . . .   | 735        |
| H.4.1. Solving the scaling laws system of equations . . . . .   | 738        |
| H.4.2. Application to spiral, elliptical and group of galaxies . .  | 738        |

|   |            |
|---|------------|
| <b>I. Featuring the primordial power spectrum: new constraints on interrupted slow-roll from CMB and LRG data</b> | <b>743</b> |
| I.1. Introduction . . . . .   | 743        |
| I.2. Inflationary perturbations in models with interrupted slow roll  | 745        |
| I.2.1. Inflationary perturbations . . . . .   | 745        |
| I.2.2. Models with interrupted slow roll . . . . .  | 746        |
| I.3. Analysis Method . . . . .  | 746        |
| I.4. Results and Discussion . . . . .   | 752        |
| I.5. Concluding Remarks . . . . .   | 757        |
| <b>J. The Fine Structure Constant and the CMB Damping Scale</b>   | <b>759</b> |
| J.1. Introduction . . . . .   | 759        |
| J.2. Analysis Method . . . . .  | 761        |
| J.3. Results . . . . .  | 762        |
| <b>K. Future constraints on the fine structure constant from combined CMB and weak lensing measurements</b>       | <b>765</b> |
| K.1. Future data . . . . .  | 766        |
| K.1.1. CMB data . . . . .   | 767        |
| K.1.2. Galaxy weak lensing data . . . . .   | 768        |
| K.1.3. Analysis method . . . . .  | 769        |
| K.2. Results . . . . .  | 769        |
| K.3. Conclusions . . . . .  | 772        |
| <b>Bibliography</b>   | <b>775</b> |

# 1. Topics

- Electron-positron plasma
  - Relativistic degeneracy in the pair plasma
  - Dynamics and emission of mildly relativistic plasma
  - Evolution of the pair plasma generated by a strong electric field
  - Electron-positron plasma in GRBs and in cosmology
- Transparency of relativistically expanding plasma and GRBs
  - Photospheric emission from relativistic outflows
  - Monte Carlo simulations of the photospheric emission in GRBs
  - Comptonization of photons near the photosphere of relativistic outflows
- Neutrinos in cosmology
- Semidegenerate self-gravitating system of fermions as a model for dark matter halos and universality laws
- Constraining cosmological models with observations



## 2. Participants

### 2.1. ICRANet participants

- Carlo Luciano Bianco
- Remo Ruffini
- Gregory Vereshchagin
- She-Sheng Xue

### 2.2. Past collaborators

- Marco Valerio Arbolino (DUNE s.r.l., Italy)
- Andrea Bianconi (INFN Pavia, Italy)
- Neta A. Bahcall (Princeton University, USA)
- Daniella Calzetti (University of Massachusetts, USA)
- Valeri Chechetkin (Keldysh Institute, Russia)
- Gustavo de Barros (former IRAP PhD, Brazil)
- Jaan Einasto (Tartu Observatory, Estonia)
- Roberto Fabbri (University of Firenze, Italy)
- Long-Long Feng (University of Science and Technology of China, China)
- Jiang Gong Gao (Xinjiang Institute of Technology, China)
- Mauro Giavalisco (University of Massachusetts, USA)
- Gabriele Ingrosso (INFN, University of Lecce, Italy)
- Yi-peng Jing (Shanghai Astronomical Observatory, China)
- Wien Biao Han (Shanghai Astronomical Observatory, Chinese Academy of Science, China)

- Massimiliano Lattanzi (University of Ferrara, Italy)
- Hyung-Won Lee (Inje University, South Korea)
- Alessandro Melchiorri (Univ. "Sapienza" di Roma, Italy)
- Marco Merafina (University of Rome "Sapienza", Italy)
- Houjun Mo (University of Massachusetts, USA)
- Enn Saar (Tartu Observatory, Estonia)
- Jay D. Salmonson (Livermore Lab, USA)
- Luis Alberto Sanchez (National University Medellin, Colombia)
- Costantino Sigismondi (ICRA and University of Rome "La Sapienza", Italy)
- Doo Jong Song (Korea Astronomy Observatory, South Korea)
- Luigi Stella (Astronomical Observatory of Rome, Italy)
- William Stoeger (Vatican Observatory, University of Arizona USA)
- Sergio Taraglio (ENEA, Italy)
- Gerda Wiedenmann (MPE Garching, Germany)
- Jim Wilson (Livermore Lab, USA)
- Urbano França (Instituto de Física Corpuscular, Valencia, Spain)
- Julien Lesgourgues (CERN, Theory Division, Geneva, Switzerland)
- Lidia Pieri (Institute d'Astrophysique, Paris, France)
- Sergio Pastor (Instituto de Física Corpuscolar, Valencia, Spain)
- Joseph Silk (Oxford University, UK)
- Roustam Zalaletdinov (Tashkent University, Uzbekistan)

### 2.3. Ongoing collaborations

- Alexey Aksenov (ICAD, RAS, Russia)

## 2.4. Students

- Damien Begue (Erasmus Mundus IRAP PhD, France)
- Alberto Benedetti (Erasmus Mundus IRAP PhD, Italy)
- Micol Benetti (IRAP PhD, Italy)
- Eloisa Menegoni (IRAP PhD, Italy)
- Ivan Siutsou (IRAP PhD, Belarus)



## 3. Brief description

Astroparticle physics is a new field of research emerging at the intersection of particle physics, astrophysics and cosmology. Theoretical development in these fields is mainly triggered by the growing amount of experimental data of unprecedented accuracy, coming both from the ground based laboratories and from the dedicated space missions.

### 3.1. Electron-positron plasma

Electron-positron plasma is of interest in many fields of physics and astrophysics, e.g. in the early universe, active galactic nuclei, the center of our Galaxy, compact astrophysical objects such as hypothetical quark stars, neutron stars and gamma-ray bursts sources. It is also relevant for the physics of ultraintense lasers and thermonuclear reactions. We study physical properties of dense and hot electron-positron plasmas. In particular, we are interested in the issues of its creation and relaxation, its kinetic properties and hydrodynamic description, baryon loading and radiation from such plasmas.

Two different states exist for electron-positron plasma: optically thin and optically thick. Optically thin pair plasma may exist in active galactic nuclei and in X-ray binaries. The theory of relativistic optically thin nonmagnetic plasma and especially its equilibrium configurations was established in the 80s by Svensson, Lightman, Gould and others. It was shown that relaxation of the plasma to some equilibrium state is determined by a dominant reaction, e.g. Compton scattering or bremsstrahlung.

Developments in the theory of gamma ray bursts from one side, and observational data from the other side, unambiguously point out on existence of optically thick pair dominated non-steady phase in the beginning of formation of GRBs. The spectrum of radiation from optically thick plasma is usually assumed to be thermal.

This year we have been focusing on two topics: electron-positron plasma and transparency of relativistically expanding plasma and GRBs. In the first topic we considered creation of plasma from strong electric field, effects of relativistic degeneracy, dynamics and emission from relativistic plasma as well as analogies and differences between pair plasma in cosmology and in GRB sources. For doing this we have generalized the numerical schemes for solution of Boltzmann equations for pairs and photons, used in previous works. As the outcome, we have developed a computer code which we are planning

to apply for study of transparency of relativistically expanding plasma, the second topic. In the mean time some preparatory work has been carried out, in particular based on equation of radiative transfer we have considered photospheric emission from relativistic outflows. Theoretical results obtained in this work have been confirmed with Monte Carlo simulations of photon scattering in relativistically expanding outflows.

In what follows all this work is discussed in details, while in Appendix all relevant papers can be found.

#### 3.1.1. Relativistic degeneracy in the pair plasma

It is well known that at relativistic temperatures plasma becomes degenerate Landau and Lifshitz (1980). In order to study relativistic degeneracy we have introduced the Bose enhancement and Pauli blocking factors in the Boltzmann equation that allows us to follow the relaxation of the pair plasma to Planck spectrum of photons and Fermi-Dirac distribution of electrons and positrons. This improvement allows us to study higher energy densities with respect to those treated before in Aksenov et al. (2007, 2009). However, for such high energy densities the assumption adopted in these works, namely that three-particle interactions operate on longer timescale with respect to two-particle ones, does not hold any longer. For this reason we had to introduce the collisional integrals for three-particle interactions based on the exact QED matrix elements, in full analogy with previously treated two-particle interactions.

Thus in this work we consider relaxation of nonequilibrium optically thick pair plasma to complete thermal equilibrium by integrating numerically relativistic Boltzmann equations with collisional integrals computed from the first principles, namely from the QED matrix elements both for two-particle and three-particle interactions.

We point out that unlike classical Boltzmann equation for binary interactions such as scattering, more general interactions are typically described by four collisional integrals for each particle that appears both among incoming and outgoing particles.

Our numerical results indicate that the rates of three-particle interactions become comparable to those of two-particle ones for temperatures exceeding the electron rest-mass energy. Thus three particle interactions such as relativistic bremsstrahlung, double Compton scattering and radiative pair creation become essential not only for establishment of thermal equilibrium, but also for correct evaluation of interaction rates, energy losses etc. Our results on this topic are reported in Appendix A.

### 3.1.2. Dynamics and emission of mildly relativistic plasma

Interactions and emission in a spherical region with optically thick relativistic plasma is studied using kinetic Boltzmann equations, see Appendix B. Being limited by the computational requirements, we selected initial optical depth of the order of  $\tau = 10^7$ , and initial temperature of the order of electron rest mass energy. Such initial conditions allow as first of all to study optically thick pair plasma. Secondly, we may follow the process of self acceleration and formation of the shell which reaches mildly relativistic bulk velocity of expansion before it becomes transparent for radiation, similarly to electron-positron plasma in GRB sources. Such initial value of the optical depth is too small for GRBs, and consequently large Lorentz factors are not attained, but important relativistic effect may be studied. At the same time such initial optical depth is too large for existing laboratory experiments. However we believe that this simulation, exploring intermediate region between laboratory and astrophysical conditions, allows to obtain some important physical insights into kinetic evolution of electron-positron plasma. We follow dynamical evolution of particle number density, optical depth, hydrodynamic velocity, luminosity and spectra. Most important we find unexpectedly that the spectrum of emission near its peak is different from pure thermal one.

### 3.1.3. Evolution of the pair plasma generated by a strong electric field

We investigate the behavior of the electron-positron pairs created by a strong electric field, see Appendix C. This problem has been studied analytically in our previous work (Benedetti et al., 2011) using simple formalism based on continuity and energy-momentum conservation equations. Now we extend that work using the more general kinetic approach Aksenov et al. (2009).

We consider a system which is uniform and homogeneous in the physical space and axially symmetric in the momentum space. The axis of symmetry is given by the direction of the initial external electric field. With these hypotheses, the relativistic Boltzmann equation is solved numerically for different starting values of the field. In this framework we can describe the Distribution Function (DF) for each kind of particle in a two dimensional momentum space. Our numerical code allows us to take into account the interactions between particles as well. We study the non-interacting and the interacting cases separately, then we compare the two runs and the role of the interactions can be analyzed; in particular we are interested in the dynamical approach to the thermal equilibrium configuration.

There are many analogies between the results we obtain using the two methods, in particular the time dependence during the first half oscillation of all the quantities involved. However, after this short period, the two methods give substantially different results.

We analyzed in details the case when interactions are not taken into account. For all the considered parameter sets we find that after several oscillations the magnitude of the electric field becomes much less than the starting value; as a consequence, acceleration and pair production are strongly suppressed. The bulk momentum parallel to the external field becomes very small, while the number density of the pairs saturates to a small fraction of the maximum achievable one, well below five percent for all cases considered. This result comes out only when kinetic treatment is adopted, and consequently distribution of particles in momentum space is accounted for. We find that production of pairs and their acceleration in the same electric field simultaneously produce a peculiar DF of particles which quickly settles down in a sort of equilibrium. This equilibrium is well described using a relativistic two-temperature DF, with the temperature along the electric field being much larger than the one in orthogonal direction. Therefore we find that substantial part of total energy, initially stored in the electric field is converted after few oscillations into internal energy. This effect could not be obtained within the simple treatment we used before, since all particles were assumed to have the same momentum (Benedetti et al., 2011) (delta-function distribution in momentum space).

When particle interactions are taken into account photon interactions are expected to bring this two-temperature system into thermal equilibrium. In fact we found that the photons DF appears to be perfectly symmetric with respect to the plane with null parallel momentum while the electrons and positrons DFs are nearly symmetric. In fact the interactions scatter particles all over the momentum space even if the external electric field is accelerating electrons and positrons toward opposite directions. It was not so for the non-interacting system where electrons and positrons were initially distributed over disjoint regions in the momentum space as soon as they were produced.

#### 3.1.4. Electron-positron plasma in GRBs and in cosmology

We study the analogy and difference between electron-positron plasma in the early Universe and in sources of GRBs. We focus on dynamical differences, namely thermal acceleration of the outflow in GRB sources vs. cosmological deceleration. Starting from the Einstein equations and energy-momentum conservation equations as their consequence, we derive the basic conservation equations which are valid for electron-positron plasma both in GRBs and in the early Universe.

We also consider nuclear composition differences as synthesis of light elements in the early Universe and possible destruction of heavy elements in GRB plasma. We show that the range of number densities and temperatures for both cases are similar, and consequently nuclear reprocessing should take place in GRB sources, similarly to the cosmological nucleosynthesis. Some

important differences are also outlined.

Finally we study different physical conditions during last scattering of photons by electrons in both cases leading to nearly perfect black body spectrum of the microwave background radiation vs. non thermal spectrum of the photospheric emission in GRBs. In particular we obtain the lower limit on the temperature in GRB plasma before it reaches the transparency condition. This lower limit turns out to be extremely insensitive to the basic parameters and initial conditions, being always higher than the ionization potential of hydrogen. It implies that hydrogen recombination does not occur in GRB plasma, unlike the early Universe. Therefore, unlike cosmological case, where the last scattering of photons is due to recombination, in GRB plasma the last scattering involves Compton scattering process. For more results on this topic see Appendix D.

### **3.2. Transparency of relativistically expanding plasma and GRBs**

Emission from optically thick stationary plasma is an important topic in astrophysics. Such plasma confined by the gravitational field constitutes stars, accretion disks and other objects. The light from these systems is coming from the so called photosphere defined as a region where the optical depth computed from the interior of the optically thick plasma outwards reaches unity.

There are also dynamical sources where bulk velocities of plasma reach ultrarelativistic values such as microquasars, active galactic nuclei and gamma-ray bursts (GRBs). While in the former two objects there is clear evidence for jets which contain optically thin plasma, in the latter objects the issue of jets is controversial, and the source is required to be optically thick. This observational fact poses a new problem: the emission from (spherically) expanding plasma which initially is optically thick. Such plasma eventually becomes optically thin during its expansion, and initially trapped photons should be released.

Such problem in application to GRBs has been considered already by Goodman and Paczynski in 1986, albeit in completely different frameworks. These papers laid the basis for two main models of GRBs: coined as shell and wind, respectively. Goodman Goodman (1986) considered instantaneous creation of plasma in a given volume, while Paczynski Paczynski (1986) proposed a steady generation of energy at a given boundary. In both models created plasma expands driven by the radiative pressure. The dynamics of plasma expansion, being subject to relativistic hydrodynamics, becomes similar as soon as ultrarelativistic bulk velocities are reached. The key difference in these frameworks is however, that in the shell model of Goodman

expanding plasma occupies only finite region of space, and hence the model is intrinsically dynamic, while in the wind model of Paczynski expanding plasma occupies all the space, and the problem is intrinsically steady.

This difference resulted in the different treatment of the transition between optically thick and optically thin regimes in plasma expansion. While in the wind model of Paczynski such transition occurs at some position which does not depend on time, this position was referred to as the "photosphere", in analogy with stellar photospheres. Actually, it was realized later by Abramowitz et al. Abramowicz et al. (1991) that the shape of this surface, as it appears to a distant observer for which the source of plasma is at rest, has nothing to do with the sphere: because of relativistic effects it has a concave shape. Now the entire literature on "photospheric emission" from GRBs refers to this wind model.

In contrast, in the shell model of Goodman the "photosphere" is a dynamic surface. Its dynamics is, in principle, different from the dynamics of the expanding shell itself. For this reason the term "transparency" introduced by Ruffini et al. Ruffini et al. (1999), which denotes transition from optically thick to optically thin regime in plasma expansion appears more suitable and less confusing.

Goodman computed the spectrum of photons assuming the photon distribution is thermal at the "photosphere". He realized that the relativistic radiative transfer problem is much more difficult than the approach he adopted. We are pursuing this general approach focusing on several physical aspects of the problem. We adopt a hydrodynamic model of the outflow as a spherical shell with the particle density distributed inside the shell according to the  $1/r^2$  law, similar to the distribution in the steady wind. Within this model in ultrarelativistic case we recover both Goodman's shell and Paczynski's wind as asymptotic cases.

In order to find the observed spectrum from expanding plasma reaching transparency we proceed in several different directions: a) approximations to the radiative transfer equations Ruffini et al. (2011); b) Monte Carlo simulations of photon scattering at the dynamical "photosphere" Begue et al. (2012); c) Kompaneets equation with anisotropic photon field Aksenov et al. (2012) and d) relativistic Boltzmann equations Benedetti and Vereshchagin (2012). The result of these works is summarized in Fig. 3.1. All these results indicate that the photospheric spectrum is wider than the Planck one. Results of Monte Carlo simulations agree well with approximate solutions of the radiative transfer equation for the isotropic scattering model. The role of the stimulated emission of photons which is not taken into account in both these treatments, is to increase the low energy slope of the spectrum, resulting in the photon index  $\alpha = -0.7$ , in contrast with the Planck photon index  $\alpha = 1$ .

The first direction turns out to be useful as it represents a second step after the simplest approach adopted by Goodman. In fact, for estimations of observed spectrum Goodman used superpositions of thermal spectra cor-

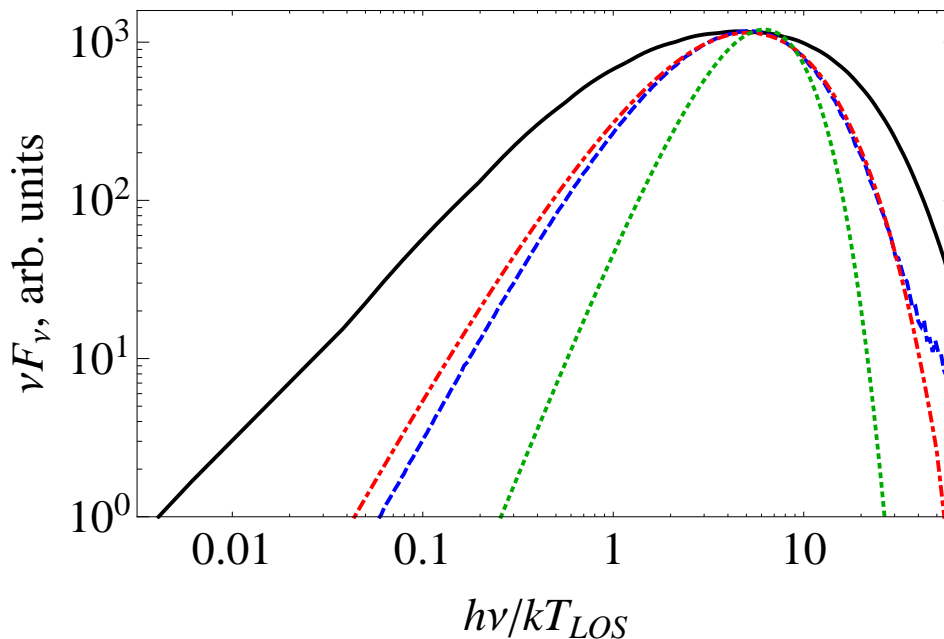


**Figure 3.1.:** The spectrum of photospheric emission from photon thick outflow obtained with different approximations. Dotted curve shows the Planck spectrum. Dashed-dotted curve shows the result from Ruffini et al. (2011) obtained using the fuzzy photosphere approximation. Dotted curve shows the result from Begue et al. (2012) obtained from Monte Carlo simulations. Solid curve shows the result from Aksenov et al. (2012) obtained by the solution of the radiative transfer equation with the Fokker-Planck approximation to the collision integral.

responding to different emitting regions with temperatures obtained from hydrodynamic equations. In approximate solutions of the radiative transfer equations using our “fuzzy photosphere” and “sharp photosphere” approximations the spectrum coming from a given region is no longer thermal, although the source function in the comoving frame is still assumed to be isotropic and thermal. Even if the approximations adopted in this approach look plausible and consistent, they must be verified by different methods.

The second direction is completely independent. Here each photon is followed in the frame where the plasma is initially at rest while it experience numerous collisions with the cross sections of Compton and isotropic scattering models, until it ceases scattering. Photons are injected in the expanding plasma well before it becomes transparent. Resulting photons constitute the final spectrum. The drawbacks of this approach are: a prescribed distribution of electron component and impossibility to account for stimulated emission of photons. The first limitation originates from the fact that Monte Carlo simulations need a prescribed background of electrons, and any back-

reaction of photons on electron distribution can be only accounted for by iterative scheme. The second limitation constrains the spectrum of photons in optically thick region to have a Wien shape, instead of the Planck one, if the model of Compton scattering is used. In addition, good statistics required to resolve both low and high energy parts of photon spectrum implies the need for large number of photons which in turn demands long computational times.

The third direction where Fokker-Planck approximation to the Boltzmann equation is adopted, allows to take into account stimulated emission of photons. It however does not allow to account of variations in electron component. In this approach which solves partial differential equations a rather good resolution in spectrum can be achieved.

Finally, the fourth direction where the system of Boltzmann equations for electrons and photons has to be solved, is the most promising one. Here Compton scattering of photons is followed from high optical depth regions to low optical depth ones, and complete evolution of both photon and electron distributions can be obtained self consistently. As finite difference methods are involved, the only limitation in this approach is the size of the grid in the phase space.

#### 3.2.1. Photospheric emission from ultrarelativistic outflows

Two popular models of optically thick relativistic outflows exist: the wind and the shell. In this work we propose a unified treatment of photospheric emission within these models, see Appendix E. We show that quite counterintuitive situations may appear when e.g. geometrically thin shell may behave as thick wind. For this reason we introduce notions of photon thick and photon thin outflows. They appear more general and better physically motivated than winds and shells when photospheric emission is considered.

We obtain light curves and observed spectra for both photon thick and photon thin outflows. In the photon thick case we generalize the results obtained for steady wind by introducing the fuzzy photosphere approximation. It is our main finding that the photospheric emission from the photon thin outflow is dominated by diffusion and produces non thermal time integrated spectra, which may be described by the Band function well known in the GRB literature.

We find that energetic GRBs should produce photon thin outflows and therefore when only time integrated spectra for such GRBs are available we naturally expect them to have a Band shape. In the literature Band spectra for the photospheric emission of GRBs are obtained only involving additional dissipative mechanisms which are not required in this approach.

### 3.2.2. Monte Carlo simulations of the photospheric emission in GRBs

We study the decoupling of photons from ultra-relativistic spherically symmetric outflows expanding with constant velocity by means of Monte-Carlo (MC) simulations. For outflows with finite width we confirm the existence of two regimes: photon thick and photon thin, found by Ruffini et al. (2011). We compute the probability density function of photon last scattering.

We show that it is very different in these two cases, as expected. We also obtain spectra as well as light curves. In photon thick case, the time integrated spectrum is much broader than the Planck function and its shape is well described by the fuzzy photosphere approximation of Ruffini et al. (2011).

In the photon thin case we confirm the crucial role of photon diffusion in formation of photon spectrum from the photosphere. Hence the probability density of decoupling has a maximum near the diffusion radius, well below the photosphere. The time integrated spectrum of the photon thin outflow has a Band shape (Band et al., 1993). It is produced when the outflow is optically thick and its peak is formed at diffusion radius. The instantaneous spectrum is close to Planck one. For details see Appendix F.

### 3.2.3. Comptonization of photons near the photosphere of relativistic outflows

The formation of photon spectrum at the photosphere of ultrarelativistically expanding outflow can be explained as a combination of several effects. Firstly, there is contribution from different angles with respect to the line of sight of photons, arriving to the observer at the same time from the Equi-Temporal Surface (EQTS). This effect is purely geometrical. Secondly, photons have different comoving temperatures at each point of EQTS and the observed spectrum is a superposition of that comoving spectra, blueshifted to the observer's reference frame (a multicolor blackbody). Thirdly, local spectral distortions arise due decoupling of photons from the plasma near the photosphere. In this work we are concentrated with the latter effect. We use the Fokker-Planck approximation to the Boltzmann equation, and obtain the generalized Kompaneets equation which takes into account anisotropic distribution of photons developed near the photosphere. This equation is solved numerically and the results are discussed and compared to those obtained by alternative methods. For details see Appendix G.

## 3.3. Neutrinos in cosmology

Many observational facts make it clear that luminous matter alone cannot account for the whole matter content of the Universe. Among them there

is the cosmic background radiation anisotropy spectrum, that is well fitted by a cosmological model in which just a small fraction of the total density is supported by baryons.

In particular, the best fit to the observed spectrum is given by a flat  $\Lambda$ CDM model, namely a model in which the main contribution to the energy density of the Universe comes from vacuum energy and cold dark matter. This result is confirmed by other observational data, like the power spectrum of large scale structures.

Another strong evidence for the presence of dark matter is given by the rotation curves of galaxies. In fact, if we assume a spherical or ellipsoidal mass distribution inside the galaxy, the orbital velocity at a radius  $r$  is given by Newton's equation of motion. The peculiar velocity of stars beyond the visible edge of the galaxy should then decrease as  $1/r$ . What is instead observed is that the velocity stays nearly constant with  $r$ . This requires a halo of invisible, dark, matter to be present outside the edge. Galactic size should then be extended beyond the visible edge. From observations it follows that the halo radius is at least 10 times larger than the radius of visible part of the galaxy. Then it follows that a halo is at least 10 times more massive than all stars in a galaxy.

Neutrinos were considered as the best candidate for dark matter about twenty years ago. Indeed, it was shown that if these particles have a small mass  $m_\nu \sim 30$  eV, they provide a large energy density contribution up to critical density. Tremaine and Gunn (1979) have claimed, however, that massive neutrinos cannot be considered as dark matter. Their paper was very influential and turned most of cosmologists away from neutrinos as cosmologically important particles.

Tremaine and Gunn paper was based on estimation of lower and upper bounds for neutrino mass; when contradiction with these bounds was found, the conclusion was made that neutrinos cannot supply dark matter. The upper bound was given by cosmological considerations, but compared with the energy density of clustered matter. It is possible, however, that a fraction of neutrinos lays outside galaxies.

Moreover, their lower bound was found on the basis of considerations of galactic halos and derived on the ground of the classical Maxwell-Boltzmann statistics. Gao and Ruffini (1980) established a lower limit on the neutrino mass by the assumption that galactic halos are composed by degenerate neutrinos. Subsequent development of their approach Arbolino and Ruffini (1988) has shown that contradiction with two limits can be avoided.

At the same time, in 1977 the paper by Lee and Weinberg (1977) appeared, in which authors turned their attention to massive neutrinos with  $m_\nu \gg 2$  GeV. Such particles could also provide a large contribution into the energy density of the Universe, in spite of much smaller value of number density.

Recent experimental results from laboratory (see Dolgov (2002) for a review) rule out massive neutrinos with  $m_\nu > 2$  GeV. However, the paper by



One of the interesting possibilities, from a conceptual point of view, is the change from the description of the physical properties by a continuous function, to a new picture by introducing a self-similar fractal structure. This approach has been relevant, since the concept of homogeneity and isotropy formerly apply to any geometrical point in space and leads to the concept of a Universe observer-homogeneous (Ruffini (1989)). Calzetti et al. (1987), Giavalisco (1992), Calzetti et al. (1988) have defined the correlation length of a fractal

$$r_0 = \left(1 - \frac{\gamma}{3}\right)^{1/\gamma} R_S, \quad (3.3.1)$$

where  $R_S$  is the sample size,  $\gamma = 3 - D$ , and  $D$  is the Hausdorff dimension of the fractal. Most challenging was the merging of the concepts of fractal, Jeans mass of dark matter and the cellular structure in the Universe, advanced by Ruffini et al. (1988). The cellular structure emerging from this study is represented in Figure 3.2. There the upper cutoff in the fractal structure  $R_{\text{cutoff}} \approx 100$  Mpc, was associated to the Jeans mass of the "ino"

$$M_{\text{cell}} = \left(\frac{m_{pl}}{m_{ino}}\right)^2 m_{pl}.$$

### 3.3.3. Lepton asymmetry of the Universe

Lattanzi et al. (2005), Lattanzi et al. (2006) studied how the cosmological constraints on neutrino mass are affected by the presence of a lepton asymmetry. The main conclusion is that while constraints on neutrino mass do not change by the inclusion into the cosmological model the dimensional chemical potential of neutrino, as an additional parameter, the value of lepton asymmetry allowed by the present cosmological data is surprisingly large, being

$$L = \sum_{\nu} \frac{n_{\nu} - n_{\bar{\nu}}}{n_{\gamma}} \lesssim 0.9. \quad (3.3.2)$$

Therefore, large lepton asymmetry is not ruled out by the current cosmological data.

## 3.4. Semidegenerate self-gravitating system of fermions as a model for dark matter halos and universality laws

The problem of dark matter distribution in galactic halos has traditionally been treated in the realm of newtonian physics in view of the low velocities of the stars in the galaxies, like the simulations from Navarro et al. (1997). In the meantime, phenomenological profiles of dark matter have been advanced by Einasto (1965); Burkert (1995), and universal properties of the

dark matter distribution have been inferred from dwarf galaxies and probably globular clusters all the way to very massive galaxies (Gentile et al., 2009; Donato et al., 2009; Walker et al., 2010; Boyarsky et al., 2009). However, a problem arises: while simulations like those from NFW point to a cusped halo, observations from various types of galaxies seem to show cored halos Salucci et al. (2011). This discrepancy between theory and observations is not yet fully understood, but could show a problem with the simulations done so far.

In a completely unrelated field (as of yet), the physics of Active Galactic Nuclei (AGN) has been recognized for more than 50 years as dominated by relativistic gravitational effects of a black hole. The formation of these black holes is not yet fully understood, although black holes formed all the way to  $z \approx 8$  have been observed in AGNs with mass ranging all the way to  $10^8 M_{\odot}$  Peterson (2010). Due to the lack of understanding on the energetics of AGNs and on the formation of the black holes, the possibility of an extended object in the core of galaxies has been advanced by Viollier et al. (1993).

The aim of this work is to present a unified approach to the dark matter distribution in the galactic halos and also in the galactic center. In order to do that, some assumptions have been made:

1. The treatment must be a fully relativistic one from the beginning, in order to explain both the galactic nuclei and galactic haloes.
2. The matter particles are semi-degenerated fermions and so obey the Fermi-Dirac statistics, together with the relativistic thermodynamical equilibrium conditions.

We show how the distribution of Dark Matter (DM) in galaxies can be explained within a model based on a semidegenerate self-gravitating system of fermions in General Relativity. We reproduce the observed properties of galaxies as the core, the halo, as well as the flattening of the rotation curves. In order to account for the evaporation phenomena (the escape velocity) we introduced a cut-off in the fermion momentum space. The model provides physical interpretation of phenomenological pseudo-isothermal sphere and Burkert DM profiles. It is consistent with a mass of the DM particle of the order of 14 KeV, compatible with a possible sterile neutrino interpretation. We have also extended the application of the model to general spiral, elliptical and group of galaxies, by explaining the phenomenological features of DM halos, i.e. the Universality laws found by Gentile et al. (2009); Donato et al. (2009) and Walker et al. (2010) in two different scopes, describing universality of galactic surface densities within a Dark Matter scale length, and by Boyarsky et al. (2009), providing an analogous Universality law but extended in the DM halo mass range. For details see Appendix H.

### 3.5. **Constraining cosmological models with observations**

The measurements of Cosmic Microwave Background anisotropies provided by balloon-borne experiments as BOOMERanG (de Bernardis et al., 2000) and by satellite experiments as WMAP (Komatsu et al., 2011; Larson et al., 2011) have fully confirmed the predictions of the standard cosmological model usually known as  $\Lambda$ CDM model. When combined with observations of galaxy clustering from the Sloan Digital Sky Survey (SDSS) (Tegmark et al., 2006) or with luminosity distances of type Ia supernovae (Frieman et al., 2008), the WMAP data provides extremely precise constraints on several parameters of the  $\Lambda$ CDM model.

However, several aspects of the model are still unclear, mysterious and of difficult theoretical interpretation. For example, the presence of a dark energy component, responsible for the current accelerating expansion of the universe, is puzzling and its nature remains an unsolved mystery. Dark energy could be made of a cosmological constant but also scalar fields models have been studied and proposed that could provide a similar dynamical behaviour. Moreover, the accelerating universe could be hinting for a failure of general relativity at large scales, leading to a dramatic revolution in our understanding of the universe.

In the next couple of years, new and current on-going experiments will deliver datasets that will simply dwarf WMAP in terms of size, with even higher quality and information content. In particular, the Planck CMB satellite experiment (Planck Collaboration, 2006) will release new high resolution and multi-frequency temperature CMB maps by early 2013. The Planck data will not only improve the current constraints on standard cosmological parameters by a factor five but it will also offer the opportunity to test novel, hitherto out of reach aspects of particle physics. For example, Planck will constrain with great accuracy the neutrino mass and number density and provide new limits on possible time and space variations of fundamental constants. New constraints on the gravity wave background will be presented by early 2013 and especially one year later when the Planck polarization data will be released. It is conceivable that the impact on science of the next-to-be-released Planck measurements will be as relevant as the one achieved by WMAP, and possibly even more.

The data currently available can be used to constraint fundamental physics. Our research during the past year has focused on two such topics: constraining the variation of fundamental constants (Martinelli et al., 2012; Menegoni et al., 2012) and investigating alternative models of inflation (Benetti et al., 2012).

### 3.5.1. Features in the primordial spectrum: improving constraints by the most recent CMB and SDSS data.

In the past year, we have worked on updating the constraints on possible features in the primordial inflationary density perturbation spectrum using the latest data from Cosmic Microwave Background (CMB) experiments, namely the 7-year Wilkinson Microwave Anisotropy Probe data (WMAP7), and the Atacama Cosmology Telescope (ACT) and South Pole Telescope (SPT) data. To these, we have also added the Luminous Red Galaxies (LRG) data from the Sloan Digital Sky Survey (SDSS).

It is a well known fact that current cosmological observations can be explained in terms of the so-called concordance  $\Lambda$ CDM model in which the primordial fluctuations are created during an early period of inflationary expansion of the Universe. In particular, the spectrum of anisotropies of the cosmic microwave background (CMB) is in excellent agreement with the inflationary prediction of adiabatic primordial perturbations with a nearly scale-invariant power spectrum (Komatsu et al., 2011; Larson et al., 2011; Das et al., 2011; Dunkley et al., 2011; Hlozek et al., 2011). In its simplest implementation, inflation is driven by the potential energy of a single scalar field, the inflaton, slowly rolling down towards a minimum of its potential and in more general inflationary models, there is the possibility that slow roll is briefly violated. A violation of slow-roll will possibly lead to detectable effects on the cosmological observables, or at least to the opportunity to constraint these models by the absence of such effects. In particular, step-like features in the primordial power spectrum have been shown (Adams et al., 2001; Hunt and Sarkar, 2004) to lead to characteristic localized oscillations in the power spectrum of the primordial curvature perturbation. Such oscillations have been considered as a possible explanation to the “glitches” observed by the Wilkinson Microwave Anisotropy Probe (WMAP) in the temperature anisotropy spectrum of the CMB.

In Benetti et al. (2012), we have considered inflation models with a small-amplitude step-like feature in the inflaton potential as introduced by Adams *et al.* where the chaotic inflation potential is  $V(\phi) = m_{\text{eff}}^2(\phi)\phi^2/2$  and its correspondent potential is  $V(\phi) = \frac{1}{2}m^2\phi^2 \left[1 + c \tanh\left(\frac{\phi-b}{d}\right)\right]$ . It depends on the inflaton mass  $m$  and the three step parameters:  $b$  is of the order of the critical value of the inflaton field for which the phase transition occurs,  $c$  is the height of the step (related to the change in the inflaton mass) and  $d$  is its width (related to the duration of the phase transition). Features of these kind can be due for example to phase transitions occurring during the slow roll in multi-field inflationary models. In these models the primordial perturbation spectrum has the form of a power-law (as in the standard featureless case) with superimposed oscillations, localized in a finite range of scales that basically depends on the position of the step in the potential. We have thus

compared the theoretical predictions of a specific model, i.e., chaotic inflation, and of a more general phenomenological model to the CMB data like WMAP7, ACT and SPT data, in order to find constraints on the parameter describing the model (Benetti et al., 2012). We have found that models with features can improve the fit to the WMAP7 data when the step in the potential is placed in way to produce oscillations in the region  $20 \lesssim \ell \lesssim 60$ , where the WMAP7 data shows some glitches. Increasing the dataset with SDSS data, we found confirmation but not further evidence for small scales glitches. From our analysis we have also found that models with too high step are excluded by the data. We can conclude that models with a step provide a significantly better fit than standard featureless power-law spectra, even if there isn't clear statistical evidence in the data for extensions to the simplest inflationary model. This work is described in more detail in Appendix I.

## 3.6. Variation of the fundamental constants

There is ample experimental evidence showing that fundamental couplings run with energy, and many particle physics and cosmology models suggest that they should also roll with time. This explains why the European Space Agency (ESA) and the European Southern Observatory (ESO) now list varying fundamental constants among their key science drivers for the next generation of facilities.

A time varying fine structure constant can leave an imprint on CMB anisotropies by changing the time of recombination and the size of the acoustic horizon at photon-electron decoupling. The CMB datasets have been extensively used to constrain  $\alpha$  by parametrizing a variation in the fine structure constant as  $\Delta\alpha = (\alpha - \alpha_0)/\alpha_0$ , where  $\alpha_0 = 1/137.03599907$  is the standard, local, value and  $\alpha$  is the value during the recombination process.

An interesting discrepancy with the expectations of the standard model has recently been uncovered in the small CMB scale measurements of the ACT Das et al. (2011); Dunkley et al. (2011) and SPT Keisler et al. (2011) experiments. Namely, the effective number of relativistic degrees of freedom  $N_{\text{eff}}$  has been reported as higher (at more than two standard deviations) than the expected than the value expected in the case of 3 relativistic neutrinos species. This result has been confirmed by several recent analyses of the ACT and SPT datasets. However it is important to stress that the current bounds on  $N_{\text{eff}}$  rely on the assumption of a theoretical model. In Menegoni et al. (2012) we have revisited the issue in the case of a non-standard recombination process like that induced by a different value of the fine structure constant in the early Universe. This work is described in more detail in Appendix J.

More recently, we have also started to forecast the ability of future weak lensing surveys, as those expected from the Euclid satellite experiment

(Laureijs et al., 2011), to constrain variation in fundamental constants. In (Martinelli et al., 2012) we have produced mock datasets as those expected from the Euclid satellite and analysed them with cosmological parameters extraction methods based on Monte Carlo Markov Chains. This procedure, which is certainly more time consuming than a simple Fisher Matrix analysis, has however the advantage of better describing a possible non gaussian shape of the posterior functions. The code has been approved by the Euclid consortium. This work is described in more detail in Appendix K.



# 4. Publications

## 4.1. Publications before 2005

1. R. Ruffini, D. J. Song, and L. Stella, "On the statistical distribution of massive fermions and bosons in a Friedmann universe" *Astronomy and Astrophysics*, Vol. 125, (1983) pp. 265-270.

The distribution function of massive Fermi and Bose particles in an expanding universe is considered as well as some associated thermodynamic quantities, pressure and energy density. These considerations are then applied to cosmological neutrinos. A new limit is derived for the degeneracy of a cosmological gas of massive neutrinos.

2. R. Ruffini and D. J. Song, "On the Jeans mass of weakly interacting neutral massive leptons", in *Gamow cosmology*, eds. F. Melchiorri and R. Ruffini, (1986) pp. 370–385.

The cosmological limits on the abundances and masses of weakly interacting neutral particles are strongly affected by the nonzero chemical potentials of these leptons. For heavy leptons ( $m_x > \text{GeV}$ ), the value of the chemical potential must be much smaller than unity in order not to give very high values of the cosmological density parameter and the mass of heavy leptons, or they will be unstable. The Jeans' mass of weakly interacting neutral particles could give the scale of cosmological structure and the masses of astrophysical objects. For a mass of the order 10 eV, the Jeans' mass could give the scenario of galaxy formation, the supercluster forming first and then the smaller scales, such as clusters and galaxies, could form inside the large supercluster.

3. D. Calzetti, M. Giavalisco, R. Ruffini, J. Einasto, and E. Saar, "The correlation function of galaxies in the direction of the Coma cluster", *Astrophysics and Space Science*, Vol. 137 (1987) pp. 101-106.

Data obtained by Einasto et al. (1986) on the amplitude of the correlation function of galaxies in the direction of the Coma cluster are compared with theoretical predictions of a model derived for a self-similar observer-homogeneous structure. The observational samples can be approximated by cones of angular width  $\alpha$  of about 77 deg. Eliminating sources of large observational error, and by making a specified correction, the observational data are found to agree very well with the theoretical predictions of Calzetti et al. (1987).

4. R. Ruffini, D. J. Song, and S. Taraglio, "The 'ino' mass and the cellular large-scale structure of the universe", *Astronomy and Astrophysics*, Vol. 190, (1988) pp. 1-9.

Within the theoretical framework of a Gamow cosmology with massive "inos", the authors show how the observed correlation functions between galaxies and between clusters of galaxies naturally lead to a "cellular" structure for the Universe. From the size of the "elementary cells" they derive constraints on the value of the masses and chemical potentials of the cosmological "inos". They outline a procedure to estimate the "effective" average mass density of the Universe. They also predict the angular size of the inhomogeneities to be expected in the cosmological black body radiation as remnants of this cellular structure. A possible relationship between the model and a fractal structure is indicated.

5. D. Calzetti, M. Giavalisco, and R. Ruffini, "The normalization of the correlation functions for extragalactic structures", *Astronomy and Astrophysics*, Vol. 198 (1988), pp. 1-15.

It is shown that the spatial two-point correlation functions for galaxies, clusters and superclusters depend explicitly on the spatial volume of the statistical sample considered. Rules for the normalization of the correlation functions are given and the traditional classification of galaxies into field galaxies, clusters and superclusters is replaced by the introduction of a single fractal structure, with a lower cut-off at galactic scales. The roles played by random and stochastic fractal components in the galaxy distribution are discussed in detail.

6. M. V. Arbolino and R. Ruffini, "The ratio between the mass of the halo and visible matter in spiral galaxies and limits on the neutrino mass", *Astronomy and Astrophysics*, Vol. 192, (1988) pp. 107-116.

Observed rotation curves for galaxies with values of the visible mass ranging over three orders of magnitude together with considerations involving equilibrium configurations of massive neutrinos, impose constraints on the ratio between the masses of visible and dark halo components in spiral galaxies. Upper and lower limits are derived for the mass of the particles making up the dark matter.

7. A. Bianconi, H. W. Lee, and R. Ruffini, "Limits from cosmological nucleosynthesis on the leptonic numbers of the universe", *Astronomy and Astrophysics*, Vol. 241 (1991) pp. 343-357.

Constraints on chemical potentials and masses of 'inos' are calculated using cosmological standard nucleosynthesis processes. It is shown that the electron neutrino chemical potential (ENCP) should not be greater than a value of the order of 1, and that the possible effective chemical potential of the other neutrino species should be about 10 times the ENCP in order not to conflict

with observational data. The allowed region (consistent with the He-4 abundance observations) is insensitive to the baryon to proton ratio  $\eta$ , while those imposed by other light elements strongly depend on  $\eta$ .

8. R. Ruffini, J. D. Salmonson, J. R. Wilson, and S.-S. Xue, "On the pair electromagnetic pulse of a black hole with electromagnetic structure", *Astronomy and Astrophysics*, Vol. 350 (1999) pp. 334-343.

We study the relativistically expanding electron-positron pair plasma formed by the process of vacuum polarization around an electromagnetic black hole (EMBH). Such processes can occur for EMBH's with mass all the way up to  $6 \cdot 10^5 M_{\odot}$ . Beginning with a idealized model of a Reissner-Nordstrom EMBH with charge to mass ratio  $\zeta = 0.1$ , numerical hydrodynamic calculations are made to model the expansion of the pair-electromagnetic pulse (PEM pulse) to the point that the system is transparent to photons. Three idealized special relativistic models have been compared and contrasted with the results of the numerically integrated general relativistic hydrodynamic equations. One of the three models has been validated: a PEM pulse of constant thickness in the laboratory frame is shown to be in excellent agreement with results of the general relativistic hydrodynamic code. It is remarkable that this precise model, starting from the fundamental parameters of the EMBH, leads uniquely to the explicit evaluation of the parameters of the PEM pulse, including the energy spectrum and the astrophysically unprecedented large Lorentz factors (up to  $6 \cdot 10^3$  for a  $10^3 M_{\odot}$  EMBH). The observed photon energy at the peak of the photon spectrum at the moment of photon decoupling is shown to range from 0.1 MeV to 4 MeV as a function of the EMBH mass. Correspondingly the total energy in photons is in the range of  $10^{52}$  to  $10^{54}$  ergs, consistent with observed gamma-ray bursts. In these computations we neglect the presence of baryonic matter which will be the subject of forthcoming publications.

9. R. Ruffini, J. D. Salmonson, J. R. Wilson, and S.-S. Xue, "On the pair-electromagnetic pulse from an electromagnetic black hole surrounded by a baryonic remnant", *Astronomy and Astrophysics*, Vol. 359 (2000) pp. 855-864.

The interaction of an expanding Pair-Electromagnetic pulse (PEM pulse) with a shell of baryonic matter surrounding a Black Hole with electromagnetic structure (EMBH) is analyzed for selected values of the baryonic mass at selected distances well outside the dyadosphere of an EMBH. The dyadosphere, the region in which a super critical field exists for the creation of  $e^+e^-$  pairs, is here considered in the special case of a Reissner-Nordstrom geometry. The interaction of the PEM pulse with the baryonic matter is described using a simplified model of a slab of constant thickness in the laboratory frame (constant-thickness approximation) as well as performing the integration of the general relativistic hydrodynamical equations. The validation of the constant-thickness approximation, already presented in a previous paper Ruffini et al. (1999) for a

PEM pulse in vacuum, is here generalized to the presence of baryonic matter. It is found that for a baryonic shell of mass-energy less than 1% of the total energy of the dyadosphere, the constant-thickness approximation is in excellent agreement with full general relativistic computations. The approximation breaks down for larger values of the baryonic shell mass, however such cases are of less interest for observed Gamma Ray Bursts (GRBs). On the basis of numerical computations of the slab model for PEM pulses, we describe (i) the properties of relativistic evolution of a PEM pulse colliding with a baryonic shell; (ii) the details of the expected emission energy and observed temperature of the associated GRBs for a given value of the EMBH mass;  $10^3 M_\odot$ , and for baryonic mass-energies in the range  $10^{-8}$  to  $10^{-2}$  the total energy of the dyadosphere.

10. M. Lattanzi, R. Ruffini, and G. Vereshchagin, "On the possible role of massive neutrinos in cosmological structure formation", in *Cosmology and Gravitation*, eds. M. Novello and S. E. Perez Bergliaffa, Vol. 668 of AIP Conference Series, (2003) pp. 263–287.

In addition to the problem of galaxy formation, one of the greatest open questions of cosmology is represented by the existence of an asymmetry between matter and antimatter in the baryonic component of the Universe. We believe that a net lepton number for the three neutrino species can be used to understand this asymmetry. This also implies an asymmetry in the matter-antimatter component of the leptons. The existence of a nonnull lepton number for the neutrinos can easily explain a cosmological abundance of neutrinos consistent with the one needed to explain both the rotation curves of galaxies and the flatness of the Universe. Some propedeutic results are presented in order to attack this problem.

## 4.2. Publications (2005 – 2011)

1. A. Benedetti, W.-B. Han, R. Ruffini and G.V. Vereshchagin, "On the frequency of oscillations in the pair plasma generated by a strong electric field", *Physics Letters B*, Vol. 698 (2011) 75-79.

We study the frequency of the plasma oscillations of electron-positron pairs created by the vacuum polarization in a uniform electric field with strength  $E$  in the range  $0.2E_c < E < 10E_c$ . Following the approach adopted in Ruffini et al. (2007) we work out one second order ordinary differential equation for a variable related to the velocity from which we can recover the classical plasma oscillation equation when  $E \rightarrow 0$ . Thereby, we focus our attention on its evolution in time studying how this oscillation frequency approaches the plasma frequency. The time-scale needed to approach to the plasma frequency and the power spectrum of these oscillations are computed. The characteristic frequency of the power spectrum is determined uniquely from the initial value

of the electric field strength. The effects of plasma degeneracy and pair annihilation are discussed.

2. B. Patricelli, M.G. Bernardini, C.L. Bianco, L. Caito, L. Izzo, R. Ruffini and G.V. Vereshchagin, "A New Spectral Energy Distribution of Photons in the Fireshell Model of GRBs", *International Journal of Modern Physics D*, Vol. 20 (2011) 1983-1987.

The analysis of various Gamma-Ray Bursts (GRBs) having a low energetics within the fireshell model has shown how the  $N(E)$  spectrum of their prompt emission can be reproduced in a satisfactory way by a convolution of thermal spectra. Nevertheless, from the study of very energetic bursts such as, for example, GRB 080319B, some discrepancies between the numerical simulations and the observational data have been observed. We investigate a different spectrum of photons in the comoving frame of the fireshell in order to better reproduce the spectral properties of GRB prompt emission within the fireshell model. We introduce a phenomenologically modified thermal spectrum: a thermal spectrum characterized by a different asymptotic power-law index in the low energy region. Such an index depends on a free parameter  $\alpha$ , so that the pure thermal spectrum corresponds to the case  $\alpha = 0$ . We test this spectrum by comparing the numerical simulations with the observed prompt emission spectra of various GRBs. From this analysis it has emerged that the observational data can be correctly reproduced by assuming a modified thermal spectrum with  $\alpha = -1.8$ .

3. Elena Giusarma, Martina Corsi, Maria Archidiacono, Roland de Putter, Alessandro Melchiorri, Olga Mena, Stefania Pandolfi. "Constraints on massive sterile neutrino species from current and future cosmological data", *Phys.Rev. D*83, 115023 (2011)

Sterile massive neutrinos are a natural extension of the standard model of elementary particles. The energy density of the extra sterile massive states affects cosmological measurements in an analogous way to that of active neutrino species. We perform here an analysis of current cosmological data and derive bounds on the masses of the active and the sterile neutrino states, as well as on the number of sterile states. The so-called (3+2) models, with three sub-eV active massive neutrinos plus two sub-eV massive sterile species, is well within the 95% CL allowed regions when considering cosmological data only. If the two extra sterile states have thermal abundances at decoupling, big bang nucleosynthesis bounds compromise the viability of (3+2) models. Forecasts from future cosmological data on the active and sterile neutrino parameters are also presented. Independent measurements of the neutrino mass from tritium beta-decay experiments and of the Hubble constant could shed light on sub-eV massive sterile neutrino scenarios.

4. M. Archidiacono, A. Melchiorri, S. Pandolfi, "The impact of Reioniza-

tion modelling on CMB Neutrino Mass Bounds”, Nuclear Physics B, Proceedings Supplements, Volume 217, Issue 1, p. 65-67. (2011)

We investigate the bounds on the neutrino mass in a general reionization scenario based on a principal component approach. We found the constraint on the sum of the neutrino masses from CMB data can be relaxed by a  $\sim 40\%$  in a generalized reionization scenario.

5. Erminia Calabrese, Eloisa Menegoni, C. J. A. P. Martins, Alessandro Melchiorri, and Graca Rocha, “Constraining variations in the fine structure constant in the presence of early dark energy”, Phys.Rev. D84 (2011) 023518.

We discuss present and future cosmological constraints on variations of the fine structure constant  $\alpha$  induced by an early dark energy component having the simplest allowed (linear) coupling to electromagnetism. We find that current cosmological data show no variation of the fine structure constant at recombination respect to the present-day value, with  $\alpha/\alpha_0 = 0.975 \pm 0.020$  at 95% c.l., constraining the energy density in early dark energy to  $\Omega_e < 0.060$  at 95% c.l. Moreover, we consider constraints on the parameter quantifying the strength of the coupling by the scalar field. We find that current cosmological constraints on the coupling are about 20 times weaker than those obtainable locally (which come from Equivalence Principle tests). However forthcoming or future missions, such as Planck Surveyor and CMBPol, can match and possibly even surpass the sensitivity of current local tests.

6. Micol Benetti, Massimiliano Lattanzi, Erminia Calabrese, Alessandro Melchiorri, “Features in the primordial spectrum: new constraints from WMAP7+ACT data and prospects for Planck”, Phys. Rev. D 84, 063509 (2011)

We update the constraints on possible features in the primordial inflationary density perturbation spectrum by using the latest data from the WMAP7 and ACT Cosmic Microwave Background experiments. The inclusion of new data significantly improves the constraints with respect to older work, especially to smaller angular scales. While we found no clear statistical evidence in the data for extensions to the simplest, featureless, inflationary model, models with a step provide a significantly better fit than standard featureless power-law spectra. We show that the possibility of a step in the inflationary potential like the one preferred by current data will soon be tested by the forthcoming temperature and polarization data from the Planck satellite mission.

7. Stefania Pandolfi, Elena Giusarma, Edward W. Kolb, Massimiliano Lattanzi, Alessandro Melchiorri, Olga Mena, Manuel Pena, Asantha Cooray, Paolo Serra, “Impact of general reionization scenarios on extraction of inflationary parameters”, Phys.Rev. D82, 123527, (2010).

Determination of whether the Harrison–Zel’dovich spectrum for primordial scalar perturbations is consistent with observations is sensitive to assumptions about the reionization scenario. In light of this result, we revisit constraints on inflationary models using more general reionization scenarios. While the bounds on the tensor-to-scalar ratio are largely unmodified, when different reionization schemes are addressed, hybrid models are back into the inflationary game. In the general reionization picture, we reconstruct both the shape and amplitude of the inflaton potential. We find a broader spectrum of potential shapes when relaxing the simple reionization restriction. An upper limit of  $10^{16}$  GeV to the amplitude of the potential is found, regardless of the assumptions on the reionization history.

8. A.G. Aksenov, R. Ruffini and G.V. Vereshchagin, “Pair plasma relaxation time scales”, *Physical Review E*, Vol. 81 (2010) 046401.

By numerically solving the relativistic Boltzmann equations, we compute the time scale for relaxation to thermal equilibrium for an optically thick electron-positron plasma with baryon loading. We focus on the time scales of electromagnetic interactions. The collisional integrals are obtained directly from the corresponding QED matrix elements. Thermalization time scales are computed for a wide range of values of both the total energy density (over 10 orders of magnitude) and of the baryonic loading parameter (over 6 orders of magnitude). This also allows us to study such interesting limiting cases as the almost purely electron-positron plasma or electron-proton plasma as well as intermediate cases. These results appear to be important both for laboratory experiments aimed at generating optically thick pair plasmas as well as for astrophysical models in which electron-positron pair plasmas play a relevant role.

9. R. Ruffini, G.V. Vereshchagin and S.-S. Xue, “Electron-positron pairs in physics and astrophysics: from heavy nuclei to black holes” *Physics Reports*, Vol. 487 (2010) No 1-4, pp. 1-140.

From the interaction of physics and astrophysics we are witnessing in these years a splendid synthesis of theoretical, experimental and observational results originating from three fundamental physical processes. They were originally proposed by Dirac, by Breit and Wheeler and by Sauter, Heisenberg, Euler and Schwinger. For almost seventy years they have all three been followed by a continued effort of experimental verification on Earth-based experiments. The Dirac process,  $e^+e^- \rightarrow 2\gamma$ , has been by far the most successful. It has obtained extremely accurate experimental verification and has led as well to an enormous number of new physics in possibly one of the most fruitful experimental avenue by introduction of storage rings in Frascati and followed by the largest accelerators worldwide: DESY, SLAC etc. The Breit-Wheeler process,  $2\gamma \rightarrow e^+e^-$ , although conceptually simple, being the inverse process of the

Dirac one, has been by far one of the most difficult to be verified experimentally. Only recently, through the technology based on free electron X-ray laser and its numerous applications in Earth-based experiments, some first indications of its possible verification have been reached. The vacuum polarization process in strong electromagnetic field, pioneered by Sauter, Heisenberg, Euler and Schwinger, introduced the concept of critical electric field  $E_c = m_e^2 c^3 / e\hbar$ . It has been searched without success for more than forty years by heavy-ion collisions in many of the leading particle accelerators worldwide. The novel situation today is that these same processes can be studied on a much more grandiose scale during the gravitational collapse leading to the formation of a black hole being observed in Gamma Ray Bursts (GRBs). This report is dedicated to the scientific race in act. The theoretical and experimental work developed in Earth-based laboratories is confronted with the theoretical interpretation of space-based observations of phenomena originating on cosmological scales. What has become clear in the last ten years is that all the three above mentioned processes, duly extended in the general relativistic framework, are necessary for the understanding of the physics of the gravitational collapse to a black hole. Vice versa, the natural arena where these processes can be observed in mutual interaction and on an unprecedented scale, is indeed the realm of relativistic astrophysics. We systematically analyze the conceptual developments which have followed the basic work of Dirac and Breit-Wheeler. We also recall how the seminal work of Born and Infeld inspired the work by Sauter, Heisenberg and Euler on effective Lagrangian leading to the estimate of the rate for the process of electron-positron production in a constant electric field. In addition of reviewing the intuitive semi-classical treatment of quantum mechanical tunneling for describing the process of electron-positron production, we recall the calculations in *Quantum Electro-Dynamics* of the Schwinger rate and effective Lagrangian for constant electromagnetic fields. We also review the electron-positron production in both time-alternating electromagnetic fields, studied by Brezin, Itzykson, Popov, Nikishov and Narozhny, and the corresponding processes relevant for pair production at the focus of coherent laser beams as well as electron beam-laser collision. We finally report some current developments based on the general JWKB approach which allows to compute the Schwinger rate in spatially varying and time varying electromagnetic fields. We also recall the pioneering work of Landau and Lifshitz, and Racah on the collision of charged particles as well as experimental success of AdA and ADONE in the production of electron-positron pairs. We then turn to the possible experimental verification of these phenomena. We review: A) the experimental verification of the  $e^+e^- \rightarrow 2\gamma$  process studied by Dirac. We also briefly recall the very successful experiments of  $e^+e^-$  annihilation to hadronic channels, in addition to the Dirac electromagnetic channel; B) ongoing Earth based experiments to detect electron-positron production in strong fields by focusing coherent laser beams and by electron beam-laser collisions; and C) the multiyear attempts to detect electron-positron production in Coulomb fields

for a large atomic number  $Z > 137$  in heavy ion collisions. These attempts follow the classical theoretical work of Popov and Zeldovich, and Greiner and their schools. We then turn to astrophysics. We first review the basic work on the energetics and electro-dynamical properties of an electromagnetic black hole and the application of the Schwinger formula around Kerr-Newman black holes as pioneered by Damour and Ruffini. We only focus on black hole masses larger than the critical mass of neutron stars, for convenience assumed to coincide with the Rhoades and Ruffini upper limit of  $3.2M_{\odot}$ . In this case the electron Compton wavelength is much smaller than the spacetime curvature and all previous results invariantly expressed can be applied following well established rules of the equivalence principle. We derive the corresponding rate of electron-positron pair production and the introduction of the concept of Dyadosphere. We review recent progress in describing the evolution of optically thick electron-positron plasma in presence of supercritical electric field, which is relevant both in astrophysics as well as ongoing laser beam experiments. In particular we review recent progress based on the Vlasov-Boltzmann-Maxwell equations to study the feedback of the created electron-positron pairs on the original constant electric field. We evidence the existence of plasma oscillations and its interaction with photons leading to energy and number equipartition of photons, electrons and positrons. We finally review the recent progress obtained by using the Boltzmann equations to study the evolution of an electron-positron-photon plasma towards thermal equilibrium and determination of its characteristic timescales. The crucial difference introduced by the correct evaluation of the role of two and three body collisions, direct and inverse, is especially evidenced. We then present some general conclusions. The results reviewed in this report are going to be submitted to decisive tests in the forthcoming years both in physics and astrophysics. To mention only a few of the fundamental steps in testing in physics we recall the starting of experimental facilities at the National Ignition Facility at the Lawrence Livermore National Laboratory as well as corresponding French Laser the Mega Joule project. In astrophysics these results will be tested in galactic and extragalactic black holes observed in binary X-ray sources, active galactic nuclei, microquasars and in the process of gravitational collapse to a neutron star and also of two neutron stars to a black hole giving origin to GRBs. The astrophysical description of the stellar precursors and the initial physical conditions leading to a gravitational collapse process will be the subject of a forthcoming report. As of today no theoretical description has yet been found to explain either the emission of the remnant for supernova or the formation of a charged black hole for GRBs. Important current progress toward the understanding of such phenomena as well as of the electro-dynamical structure of neutron stars, the supernova explosion and the theories of GRBs will be discussed in the above mentioned forthcoming report. What is important to recall at this stage is only that both the supernovae and GRBs processes are among the most energetic and transient phenomena ever observed in the Universe: a supernova can reach energy

of  $\sim 10^{54}$  ergs on a time scale of a few months and GRBs can have emission of up to  $\sim 10^{54}$  ergs in a time scale as short as of a few seconds. The central role of neutron stars in the description of supernovae, as well as of black holes and the electron-positron plasma, in the description of GRBs, pioneered by one of us (RR) in 1975, are widely recognized. Only the theoretical basis to address these topics are discussed in the present report.

10. A. G. Aksenov, R. Ruffini, and G. V. Vereshchagin, "Kinetics of the Mildly Relativistic Plasma and GRBs" in the Proceedings of "The Sun, the stars, the Universe and General Relativity" meeting in honor of 95th Anniversary of Ya. B. Zeldovich in Minsk, AIP Conference Proceedings 1205 (2010) 11-16.

We consider optically thick photon-pair-proton plasma in the framework of Boltzmann equations. For the sake of simplicity we consider the uniform and isotropic plasma. It has been shown that arbitrary initial distribution functions evolve to the thermal equilibrium state through so called kinetic equilibrium state with common temperature of all particles and nonzero chemical potentials. For the plasma temperature 0.1 – 10 MeV relevant for GRB (Gamma-Ray Burst) sources we evaluate the thermalization time scale as function of total energy density and baryonic loading parameter.

11. E. Menegoni, S. Pandolfi, S. Galli, M. Lattanzi, A. Melchiorri "Constraints on the dark energy equation of state in presence of a varying fine structure constant" in Int. J. Mod. Phys D19, 507 (2010).

We discuss the cosmological constraints on the dark energy equation of state in the presence of primordial variations in the fine structure constant. We find that the constraints from CMB data alone on  $w$  and the Hubble constant are much weaker when variations in the fine structure constant are permitted. Vice versa, constraints on the fine structure constant are relaxed by more than 50% when dark energy models different from a cosmological constant are considered.

12. C.J.A.P. Martins, E. Menegoni, S. Galli and A. Melchiorri, "Varying couplings in the early universe: correlated variations of  $\alpha$  and  $G$ , Physical Review D 82 023532 (2010)

The cosmic microwave background anisotropies provide a unique opportunity to constrain simultaneous variations of the fine-structure constant  $\alpha$  and Newton's gravitational constant  $G$ . Those correlated variations are possible in a wide class of theoretical models. In this brief paper we show that the current data, assuming that particle masses are constant, give no clear indication for such variations, but already prefer that any relative variations in  $\alpha$  should be of the same sign of those of  $G$  for variations of 1%. We also show that a cosmic complementarity is present with big bang nucleosynthesis and that a combination of current CMB and big bang nucleosynthesis data strongly

constraints simultaneous variations in  $\alpha$  and  $G$ . We finally discuss the future bounds achievable by the Planck satellite mission.

13. E. Menegoni, “New Constraints on Variations of Fine Structure Constant from Cosmic Microwave Background Anisotropies”, GRAVITATIONAL PHYSICS: TESTING GRAVITY FROM SUBMILLIMETER TO COSMIC: Proceedings of the VIII Mexican School on Gravitation and Mathematical Physics. AIP Conference Proceedings, Volume 1256, pp. 288-292 (2010).

The recent measurements of Cosmic Microwave Background temperature and polarization anisotropy made by the ACBAR, QUAD and BICEP experiments substantially improve the cosmological constraints on possible variations of the fine structure constant in the early universe. In this work I analyze this recent data obtaining the constraint  $\alpha/\alpha_0 = 0.987 \pm 0.012$  at 68% c.l.. The inclusion of the new HST constraints on the Hubble constant further increases the bound to  $\alpha/\alpha_0 = 1.001 \pm 0.007$  at 68% c.l., bringing possible deviations from the current value below the 1% level.

14. A. Melchiorri, F. De Bernardis, E. Menegoni, “Limits on the neutrino mass from cosmology”. GRAVITATIONAL PHYSICS: TESTING GRAVITY FROM SUBMILLIMETER TO COSMIC: Proceedings of the VIII Mexican School on Gravitation and Mathematical Physics. AIP Conference Proceedings, Volume 1256, pp. 96-106 (2010).

We use measurements of luminosity-dependent galaxy bias at several different redshifts, SDSS at  $z = 0.05$ , DEEP2 at  $z = 1$  and LBGs at  $z = 3.8$ , combined with WMAP five-year cosmic microwave background anisotropy data and SDSS Red Luminous Galaxy survey three-dimensional clustering power spectrum to put constraints on cosmological parameters.

15. A.G. Aksenov, R. Ruffini and G.V. Vereshchagin, “Thermalization of the mildly relativistic plasma”, Physical Review D, Vol. 79 (2009) 043008.

In the recent Letter Aksenov et al. (2007) we considered the approach of nonequilibrium pair plasma towards thermal equilibrium state adopting a kinetic treatment and solving numerically the relativistic Boltzmann equations. It was shown that plasma in the energy range 0.1-10 MeV first reaches kinetic equilibrium, on a timescale  $t_k \lesssim 10^{-14}$  sec, with detailed balance between binary interactions such as Compton, Bhabha and Møller scattering, and pair production and annihilation. Later the electron-positron-photon plasma approaches thermal equilibrium on a timescale  $t_{th} \lesssim 10^{-12}$  sec, with detailed balance for all direct and inverse reactions. In the present paper we systematically present details of the computational scheme used in Aksenov et al. (2007), as well as generalize our treatment, considering proton loading of the pair plasma. When proton loading is large, protons thermalize first by proton-proton scattering, and then with the electron-positron-photon plasma

by proton-electron scattering. In the opposite case of small proton loading proton-electron scattering dominates over proton-proton one. Thus in all cases the plasma, even with proton admixture, reaches thermal equilibrium configuration on a timescale  $t_{\text{th}} \lesssim 10^{-11}$  sec. We show that it is crucial to account for not only binary but also triple direct and inverse interactions between electrons, positrons, photons and protons. Several explicit examples are given and the corresponding timescales for reaching kinetic and thermal equilibria are determined.

16. A. G. Aksenov, R. Ruffini, and G. V. Vereshchagin, "Thermalization of pair plasma with proton loading" in the Proceedings of "PROBING STELLAR POPULATIONS OUT TO THE DISTANT UNIVERSE" meeting, AIP Conference Proceedings 1111 (2009) 344-350.

We study kinetic evolution of nonequilibrium optically thick electron-positron plasma towards thermal equilibrium solving numerically relativistic Boltzmann equations with energy per particle ranging from 0.1 to 10 MeV. We generalize our results presented in Aksenov et al. (2007), considering proton loading of the pair plasma. Proton loading introduces new characteristic timescales essentially due to proton-proton and proton-electron Coulomb collisions. Taking into account not only binary but also triple direct and inverse interactions between electrons, positrons, photons and protons we show that thermal equilibrium is reached on a timescale  $t_{\text{th}} \simeq 10^{-11}$  sec.

17. A.G. Aksenov, R. Ruffini and G.V. Vereshchagin, "Thermalization of nonequilibrium electron-positron-photon plasmas", Physical Review Letters, Vol. 99 (2007) No 12, 125003.

Starting from a nonequilibrium configuration we analyze the role of the direct and the inverse binary and triple interactions in reaching thermal equilibrium in a homogeneous isotropic pair plasma. We focus on energies in the range 0.1 – 10 MeV. We numerically integrate the relativistic Boltzmann equation with the exact QED collisional integrals taking into account all binary and triple interactions. We show that first, when a detailed balance is reached for all binary interactions on a time scale  $t_k < 10^{-14}$  sec, photons and electron-positron pairs establish kinetic equilibrium. Subsequently, when triple interactions satisfy the detailed balance on a time scale  $t_{eq} < 10^{-12}$  sec, the plasma reaches thermal equilibrium. It is shown that neglecting the inverse triple interactions prevents reaching thermal equilibrium. Our results obtained in the theoretical physics domain also find application in astrophysics and cosmology.

18. C.L. Bianco, R. Ruffini, G.V. Vereshchagin and S.-S. Xue, "Equations of Motion and Initial and Boundary Conditions for Gamma-ray Burst", Journal of the Korean Physical Society, Vol. 49 (2006) No. 2, pp. 722-731.

We compare and contrast the different approaches to the optically thick adiabatic phase of GRB all the way to the transparency. Special attention is given to the role of the rate equation to be self consistently solved with the relativistic hydrodynamic equations. The works of Shemi and Piran (1990), Piran, Shemi and Narayan (1993), Meszaros, Laguna and Rees (1993) and Ruffini, Salmonson, Wilson and Xue (1999,2000) are compared and contrasted. The role of the baryonic loading in these three treatments is pointed out. Constraints on initial conditions for the fireball produced by electro-magnetic black hole are obtained.

19. P. Singh, K. Vandersloot and G.V. Vereshchagin, “Nonsingular bouncing universes in loop quantum cosmology”, *Physical Review D*, Vol. 74 (2006) 043510.

Nonperturbative quantum geometric effects in loop quantum cosmology (LQC) predict a  $\rho^2$  modification to the Friedmann equation at high energies. The quadratic term is negative definite and can lead to generic bounces when the matter energy density becomes equal to a critical value of the order of the Planck density. The nonsingular bounce is achieved for arbitrary matter without violation of positive energy conditions. By performing a qualitative analysis we explore the nature of the bounce for inflationary and cyclic model potentials. For the former we show that inflationary trajectories are attractors of the dynamics after the bounce implying that inflation can be harmoniously embedded in LQC. For the latter difficulties associated with singularities in cyclic models can be overcome. We show that nonsingular cyclic models can be constructed with a small variation in the original cyclic model potential by making it slightly positive in the regime where scalar field is negative.

20. M. Lattanzi, R. Ruffini and G.V. Vereshchagin, “Joint constraints on the lepton asymmetry of the Universe and neutrino mass from the Wilkinson Microwave Anisotropy Probe”, *Physical Review D*, Vol. 72 (2005) 063003.

We use the Wilkinson Microwave Anisotropy Probe (WMAP) data on the spectrum of cosmic microwave background anisotropies to put constraints on the present amount of lepton asymmetry  $L$ , parametrized by the dimensionless chemical potential (also called degeneracy parameter)  $\xi$  and on the effective number of relativistic particle species. We assume a flat cosmological model with three thermally distributed neutrino species having all the same mass and chemical potential, plus an additional amount of effectively massless exotic particle species. The extra energy density associated to these species is parametrized through an effective number of additional species  $\Delta N_{others}^{eff}$ . We find that  $0 < |\xi| < 1.1$  and correspondingly  $0 < |L| < 0.9$  at  $2\sigma$ , so that WMAP data alone cannot firmly rule out scenarios with a large lepton number; moreover, a small preference for this kind of scenarios is actually found. We also discuss the effect of the asymmetry on the estimation of other parameters

and, in particular, of the neutrino mass. In the case of perfect lepton symmetry, we obtain the standard results. When the amount of asymmetry is left free, we find at 2sigma. Finally we study how the determination of  $|L|$  is affected by the assumptions on  $\Delta N_{others}^{eff}$ . We find that lower values of the extra energy density allow for larger values of the lepton asymmetry, effectively ruling out, at 2sigma level, lepton symmetric models with  $\Delta N_{others}^{eff} \simeq 0$ .

21. G.V. Vereshchagin, "Gauge Theories of Gravity with the Scalar Field in Cosmology", in "Frontiers in Field Theory", edited by O. Kovras, Nova Science Publishers, New York, (2005), pp. 213-255 (ISBN: 1-59454-127-2).

Brief introduction into gauge theories of gravity is presented. The most general gravitational lagrangian including quadratic on curvature, torsion and non-metricity invariants for metric-affine gravity is given. Cosmological implications of gauge gravity are considered. The problem of cosmological singularity is discussed within the framework of general relativity as well as gauge theories of gravity. We consider the role of scalar field in connection to this problem. Initial conditions for nonsingular homogeneous isotropic Universe filled by single scalar field are discussed within the framework of gauge theories of gravity. Homogeneous isotropic cosmological models including ultrarelativistic matter and scalar field with gravitational coupling are investigated. We consider different symmetry states of effective potential of the scalar field, in particular restored symmetry at high temperatures and broken symmetry. Obtained bouncing solutions can be divided in two groups, namely nonsingular inflationary and

oscillating solutions. It is shown that inflationary solutions exist for quite general initial conditions like in the case of general relativity. However, the phase space of the dynamical system, corresponding to the cosmological equations is bounded. Violation of the uniqueness of solutions on the boundaries of the phase space takes place. As a result, it is impossible to define either the past or the future for a given solution. However, definitely there are singular solutions and therefore the problem of cosmological singularity cannot be solved in models with the scalar field within gauge theories of gravity.

22. R. Ruffini, M. G. Bernardini, C. L. Bianco, L. Caito, P. Chardonnet, M. G. Dainotti, F. Fraschetti, R. Guida, M. Rotonondo, G. Vereshchagin, L. Vitagliano, S.-S. Xue,

"The Blackholic energy and the canonical Gamma-Ray Burst" in Cosmology and Gravitation: XIIth Brazilian School of Cosmology and Gravitation, edited by M. Novello and S.E. Perez Bergliaffa, AIP Conference Proceedings, Vol. 910, Melville, New York, 2007, pp. 55-217.

Gamma-Ray Bursts (GRBs) represent very likely "the" most extensive computational, theoretical and observational effort ever carried out successfully

in physics and astrophysics. The extensive campaign of observation from space based X-ray and  $\gamma$ -ray observatory, such as the Vela, CGRO, BeppoSAX, HETE-II, INTEGRAL, Swift, R-XTE, Chandra, XMM satellites, have been matched by complementary observations in the radio wavelength (e.g. by the VLA) and in the optical band (e.g. by VLT, Keck, ROSAT). The net result is unprecedented accuracy in the received data allowing the determination of the energetics, the time variability and the spectral properties of these GRB sources. The very fortunate situation occurs that these data can be confronted with a mature theoretical development. Theoretical interpretation of the above data allows progress in three different frontiers of knowledge: a) the ultrarelativistic regimes of a macroscopic source moving at Lorentz gamma factors up to  $\sim 400$ ; b) the occurrence of vacuum polarization process verifying some of the yet untested regimes of ultrarelativistic quantum field theories; and c) the first evidence for extracting, during the process of gravitational collapse leading to the formation of a black hole, amounts of energies up to  $10^{55}$  ergs of blackholic energy — a new form of energy in physics and astrophysics. We outline how this progress leads to the confirmation of three interpretation paradigms for GRBs proposed in July 2001. Thanks mainly to the observations by Swift and the optical observations by VLT, the outcome of this analysis points to the existence of a “canonical” GRB, originating from a variety of different initial astrophysical scenarios. The communality of these GRBs appears to be that they all are emitted in the process of formation of a black hole with a negligible value of its angular momentum. The following sequence of events appears to be canonical: the vacuum polarization process in the dyadosphere with the creation of the optically thick self accelerating electron-positron plasma; the engulfment of baryonic mass during the plasma expansion; adiabatic expansion of the optically thick “fireshell” of electron-positron-baryon plasma up to the transparency; the interaction of the accelerated baryonic matter with the interstellar medium (ISM). This leads to the canonical GRB composed of a proper GRB (P-GRB), emitted at the moment of transparency, followed by an extended afterglow. The sole parameters in this scenario are the total energy of the dyadosphere  $E_{dya}$ , the fireshell baryon loading  $M_B$  defined by the dimensionless parameter  $B = M_B c^2 / E_{dya}$ , and the ISM filamentary distribution around the source. In the limit  $B \rightarrow 0$  the total energy is radiated in the P-GRB with a vanishing contribution in the afterglow. In this limit, the canonical GRBs explain as well the short GRBs. In these lecture notes we systematically outline the main results of our model comparing and contrasting them with the ones in the current literature. In both cases, we have limited ourselves to review already published results in refereed publications. We emphasize as well the role of GRBs in testing yet unexplored grounds in the foundations of general relativity and relativistic field theories.

23. M. Lattanzi, R. Ruffini and G.V. Vereshchagin, “Do WMAP data constraint the lepton asymmetry of the Universe to be zero?” in Albert Ein-

stein Century International Conference, edited by J.-M. Alimi, and A. Füzfa, AIP Conference Proceedings, Vol. 861, Melville, New York, 2006, pp.912-919.

It is shown that extended flat  $\Lambda$ CDM models with massive neutrinos, a sizeable lepton asymmetry and an additional contribution to the radiation content of the Universe, are not excluded by the Wilkinson Microwave Anisotropy Probe (WMAP) first year data. We assume a flat cosmological model with three thermally distributed neutrino species having all the same mass and chemical potential, plus an additional amount of effectively massless exotic particle species X. After maximizing over seven other cosmological parameters, we derive from WMAP first year data the following constraints for the lepton asymmetry  $L$  of the Universe (95% CL):  $0 < |L| < 0.9$ , so that WMAP data alone cannot firmly rule out scenarios with a large lepton number; moreover, a small preference for this kind of scenarios is actually found. We also find for the neutrino mass  $m_\nu < 1.2eV$  and for the effective number of relativistic particle species  $-0.45 < \Delta N^{eff} < 2.10$ , both at 95% CL. The limit on  $\Delta N^{eff}$  is more restrictive than others found in the literature, but we argue that this is due to our choice of priors.

24. R. Ruffini, C.L. Bianco, G.V. Vereshchagin, S.-S. Xue "Baryonic loading and  $e^+e^-$  rate equation in GRB sources" to appear in the proceedings of "Relativistic Astrophysics and Cosmology - Einstein's Legacy" Meeting, November 7-11, 2005, Munich, Germany.

The expansion of the electron-positron plasma in the GRB phenomenon is compared and contrasted in the treatments of Meszaros, Laguna and Rees, of Shemi, Piran and Narayan, and of Ruffini et al. The role of the correct numerical integration of the hydrodynamical equations, as well as of the rate equation for the electron-positron plasma loaded with a baryonic mass, are outlined and confronted for crucial differences.

25. G.V. Vereshchagin, M. Lattanzi, H.W. Lee, R. Ruffini, "Cosmological massive neutrinos with nonzero chemical potential: I. Perturbations in cosmological models with neutrino in ideal fluid approximation", in proceedings of the Xth Marcel Grossmann Meeting on Recent Developments in Theoretical and Experimental General Relativity, World Scientific: Singapore, 2005, vol. 2, pp. 1246-1248.

Recent constraints on neutrino mass and chemical potential are discussed with application to large scale structure formation. Power spectra in cosmological model with hot and cold dark matter, baryons and cosmological term are calculated in newtonian approximation using linear perturbation theory. All components are considered to be ideal fluids. Dissipative processes are taken into account by initial spectrum of perturbations so the problem is reduced to a simple system of equations. Our results are in good agreement with those obtained before using more complicated treatments.

26. M. Lattanzi, H.W. Lee, R. Ruffini, G.V. Vereshchagin, "Cosmological massive neutrinos with nonzero chemical potential: II. Effect on the estimation of cosmological parameters", in proceedings of the Xth Marcel Grossmann Meeting on Recent Developments in Theoretical and Experimental General Relativity, World Scientific: Singapore, 2005, vol. 2, pp. 1255-1257.

The recent analysis of the cosmic microwave background data carried out by the WMAP team seems to show that the sum of the neutrino mass is  $\lesssim 0.7$  eV. However, this result is not model-independent, depending on precise assumptions on the cosmological model. We study how this result is modified when the assumption of perfect lepton symmetry is dropped out.

27. R. Ruffini, M. Lattanzi and G. Vereshchagin, "On the possible role of massive neutrinos in cosmological structure formation" in *Cosmology and Gravitation: Xth Brazilian School of Cosmology and Gravitation*, edited by M. Novello and S.E. Perez Bergliaffa, AIP Conference Proceedings, Vol. 668, Melville, New York, 2003, pp.263-287.

In addition to the problem of galaxy formation, one of the greatest open questions of cosmology is represented by the existence of an asymmetry between matter and antimatter in the baryonic component of the Universe. We believe that a net lepton number for the three neutrino species can be used to understand this asymmetry. This also implies an asymmetry in the matter-antimatter component of the leptons. The existence of a nonnull lepton number for the neutrinos can easily explain a cosmological abundance of neutrinos consistent with the one needed to explain both the rotation curves of galaxies and the flatness of the Universe. Some propedeutic results are presented in order to attack this problem.

28. A.G. Aksenov, C.L. Bianco, R. Ruffini and G.V. Vereshchagin, "GRBs and the thermalization process of electron-positron plasmas" in the Proceedings of the "Gamma Ray Bursts 2007" meeting, AIP Conf.Proc. 1000 (2008) 309-312.

We discuss temporal evolution of the pair plasma, created in Gamma-Ray Bursts sources. A particular attention is paid to the relaxation of plasma into thermal equilibrium. We also discuss the connection between the dynamics of expansion and spatial geometry of plasma. The role of the baryonic loading parameter is emphasized.

29. A. G. Aksenov, R. Ruffini, and G. V. Vereshchagin, "Thermalization of Electron-Positron-Photon Plasmas with an Application to GRB" in *RELATIVISTIC ASTROPHYSICS: 4th Italian-Sino Workshop*, AIP Conference Proceedings, Vol. 966, Melville, New York, 2008, pp. 191-196.

The pair plasma with photon energies in the range  $0.1 - 10$  MeV is believed to play crucial role in cosmic Gamma-Ray Bursts. Starting from a nonequilibrium

rium configuration we analyze the role of the direct and the inverse binary and triple interactions in reaching thermal equilibrium in a homogeneous isotropic pair plasma. We numerically integrate the relativistic Boltzmann equation with the exact QED collisional integrals taking into account all binary and triple interactions. We show that first, when a detailed balance is reached for all binary interactions on a time scale  $t_k = 10^{-14}$  sec, photons and electron-positron pairs establish kinetic equilibrium. Subsequently, when triple interactions satisfy the detailed balance on a time scale  $t_{eq} = 10^{-12}$  sec, the plasma reaches thermal equilibrium. It is shown that neglecting the inverse triple interactions prevents reaching thermal equilibrium. Our results obtained in the theoretical physics domain also find application in astrophysics and cosmology.

30. R. Ruffini, G. V. Vereshchagin and S.-S. Xue, "Vacuum Polarization and Electron-Positron Plasma Oscillations" in RELATIVISTIC ASTROPHYSICS: 4th Italian-Sino Workshop, AIP Conference Proceedings, Vol. 966, Melville, New York, 2008, pp. 207-212.

We study plasma oscillations of electrons-positron pairs created by the vacuum polarization in an uniform electric field. Our treatment, encompassing the case of  $E > E_c$ , shows also in the case  $E < E_c$  the existence of a maximum Lorentz factor acquired by electrons and positrons and allows determination of the a maximal length of oscillation. We quantitatively estimate how plasma oscillations reduce the rate of pair creation and increase the time scale of the pair production.

### 4.3. Publications (2012)

1. A. Benedetti, R. Ruffini and G.V. Vereshchagin, "Evolution of the pair plasma generated by a strong electric field", accepted by Physics Letters A (2012).

We study the process of energy conversion from overcritical electric field into electron-positron-photon plasma. We solve numerically Vlasov-Boltzmann equations for pairs and photons assuming the system to be homogeneous and anisotropic. All the 2-particle QED interactions between pairs and photons are described by collision terms. We evidence several epochs of this energy conversion, each of them associated to a specific physical process. Firstly pair creation occurs, secondly back reaction results in plasma oscillations. Thirdly photons are produced by electron-positron annihilation. Finally particle interactions lead to completely equilibrated thermal electron-positron-photon plasma.

2. R. Ruffini and G.V. Vereshchagin, "Electron-positron plasma in GRBs and in cosmology", submitted to Il Nuovo Cimento C (2012).

3. R. Ruffni, I. A. Siutsou and G. V. Vereshchagin, "Theory of photospheric emission from relativistic outflows" , submitted to the *Astrophysical Journal* (2011).
4. D. Begue, I. A. Siutsou and G. V. Vereshchagin, "Monte Carlo simulations of the photospheric emission in GRBs", submitted to the *Astrophysical Journal* (2012).
5. A.G. Aksenov, R. Ruffni and G. V. Vereshchagin, "Comptonization of photons near the photosphere of relativistic outflows", in preparation (2012).
6. A.G. Aksenov, R. Ruffni, I. A. Siutsou and G. V. Vereshchagin, "Relativistic degeneracy in the pair plasma", in preparation (2012).
7. B. Patricelli, M.G. Bernardini, C.L. Bianco, L. Caito, G. de Barros, L. Izzo, R. Ruffini and G.V. Vereshchagin, "Analysis of GRB 080319B and GRB 050904 within the Fireshell Model: Evidence for a Broader Spectral Energy Distribution", *The Astrophysical Journal*, Volume 756, Issue 1, article id. 16 (2012).

The observation of GRB 080319B, with an isotropic energy  $E_{iso} = 1.32 \cdot 10^{54}$  erg, and GRB 050904, with  $E_{iso} = 1.04 \cdot 10^{54}$  erg, offers the possibility of studying the spectral properties of the prompt radiation of two of the most energetic gamma-ray bursts (GRBs). This allows us to probe the validity of the fireshell model for GRBs beyond  $10^{54}$  erg, well outside the energy range where it has been successfully tested up to now ( $10^{49}$ - $10^{53}$  erg). We find that in the low-energy region, the prompt emission spectra observed by Swift Burst Alert Telescope (BAT) reveals more power than theoretically predicted. The opportunities offered by these observations to improve the fireshell model are outlined in this paper. One of the distinguishing features of the fireshell model is that it relates the observed GRB spectra to the spectrum in the comoving frame of the fireshell. Originally, a fully radiative condition and a comoving thermal spectrum were adopted. An additional power law in the comoving thermal spectrum is required due to the discrepancy of the theoretical and observed light curves and spectra in the fireshell model for GRBs 080319B and 050904. A new phenomenological parameter  $\alpha$  is correspondingly introduced in the model. We perform numerical simulations of the prompt emission in the Swift BAT bandpass by assuming different values of within the fireshell model. We compare them with the GRB 080319B and GRB 050904 observed time-resolved spectra, as well as with their time-integrated spectra and light curves. Although GRB 080319B and GRB 050904 are at very different redshifts ( $z = 0.937$  and  $z = 6.29$ , respectively), a value of  $\alpha = -1.8$  for both of them leads to a good agreement between the numerical simulations and the observed BAT light curves, time-resolved and time-integrated spectra. Such a

modified spectrum is also consistent with the observations of previously analyzed less energetic GRBs and reasons for this additional agreement are given. Perspectives for future low-energy missions are outlined.

8. A.G. Aksenov, R. Ruffni, I. A. Siutsou and G. V. Vereshchagin, "Dynamics and emission of mildly relativistic plasma", *International Journal of Modern Physics: Conference Series*, Vol. 12, Issue 01, (2012) pp. 1-9.

Initially optically thick (with  $\tau = 3 \cdot 10^7$ ) spherically symmetric outflow consisting of electron-positron pairs and photons is considered. We do not assume thermal equilibrium, and include the two-body processes that occur in such plasma: Moller and Bhaba scattering of pairs, Compton scattering, two-photon pair annihilation, two-photon pair production, together with their radiative three-body variants: bremsstrahlung, double Compton scattering, and three-photon pair annihilation, with their inverse processes. We solve numerically the relativistic Boltzmann equations in spherically symmetric case for distribution functions of pairs and photons. Three epochs are considered in details: a) the thermalization, which brings initially nonequilibrium plasma to thermal equilibrium; b) the self-accelerated expansion, which we find in agreement with previous hydrodynamic studies and c) decoupling of photons from the expanding electron-positron plasma. Photon spectra are computed, and appear to be non thermal near the peak of the luminosity. In particular, the low energy part of the spectrum contain more power with respect to the black body one.

9. Stefania Pandolfi, Andrea Ferrara, T. Roy Choudhury, Alessandro Melchiorri, Sourav Mitra, "Data-constrained reionization and its effect on cosmological parameters", *Physical Review D*, vol. 84 (2012) Issue 12, id. 123522

We perform an analysis of the recent WMAP7 data considering physically motivated and viable reionization scenarios with the aim of assessing their effects on cosmological parameter determinations. The main novelties are: (i) the combination of CMB data with astrophysical results from quasar absorption line experiments; (ii) the joint variation of both the cosmological and astrophysical [governing the evolution of the free electron fraction  $x_e(z)$ ] parameters. Including a realistic, data-constrained reionization history in the analysis induces appreciable changes in the cosmological parameter values deduced through a standard WMAP7 analysis. Particularly noteworthy are the variations in  $\Omega_b h^2 = 0.02258 + 0.00057 - 0.00056$  (WMAP7) vs.  $\Omega_b h^2 = 0.02183 \pm 0.00054$  (WMAP7 + ASTRO), and the new constraints for the scalar spectral index, for which WMAP7 + ASTRO excludes the Harrison-Zel'dovich value  $n_s = 1$  at more than  $3\sigma$ . Finally, the e.s. optical depth value is considerably decreased with respect to the standard WMAP7, i.e.  $\tau_e = 0.080 \pm 0.012$ . We conclude that the inclusion of astrophysical datasets, allowing to robustly constrain the reionization history, in the extraction procedure of cosmological

parameters leads to relatively important differences in the final determination of their values.

10. Micol Benetti, S. Pandolfi, M. Lattanzi, M. Martinelli, A. Melchiorri. "Featuring the primordial power spectrum: new constraints on interrupted slow-roll from CMB and LRG data "arXiv:1210.3562, submitted to Phys. Rev. D.

Using the most recent data from the WMAP, ACT and SPT experiments, we update the constraints on models with oscillatory features in the primordial power spectrum of scalar perturbations. This kind of features can appear in models of inflation where slow-roll is interrupted, like multifield models. We also derive constraints for the case in which, in addition to cosmic microwave observations, we also consider the data on the spectrum of luminous red galaxies from the 7th SDSS catalog, and the SNIa Union Compilation 2 data. We have found that: (i) considering a model with features in the primordial power spectrum increases the agreement with data with the respect of the featureless "vanilla"  $\Lambda$ CDM model by  $\Delta\chi^2 \simeq 7$ ; (ii) the uncertainty on the determination of the standard parameters is not degraded when features are included; (iii) the best fit for the features model locates the step in the primordial spectrum at a scale  $k \simeq 0.005 \text{ Mpc}^{-1}$ , corresponding to the scale where the outliers in the WMAP7 data at  $\ell = 22$  and  $\ell = 40$  are located.; (iv) a distinct, albeit less statistically significant peak is present in the likelihood at smaller scales, with a  $\Delta\chi^2 \simeq 3.5$ , whose presence might be related to the WMAP7 preference for a negative value of the running of the scalar spectral index parameter; (v) the inclusion of the LRG-7 data do not change significantly the best fit model, but allows to better constrain the amplitude of the oscillations.

11. Matteo Martinelli, Eloisa Menegoni, Alessandro Melchiorri. "Future constraints on variations of the fine structure constant from combined CMB and weak lensing measurements ", Phys. Rev. D 85 123526 (2012).

We forecast the ability of future CMB and galaxy lensing surveys to constrain variation in the fine structure constant in the early universe. We found that lensing data, as those expected from satellite experiments as Euclid could improve the constraint from the Planck CMB experiment by a factor  $\sim 3$ , leading to a  $\Delta\alpha/\alpha \sim 10^{-4}$  accuracy competitive with current bounds from quasar absorption line systems.

12. Eloisa Menegoni, Maria Archidiacono, Erminia Calabrese, Silvia Galli, C. J. A. P. Martins, Alessandro Melchiorri. "The Fine Structure Constant and the CMB Damping Scale", Phys. Rev. D 85, 107301 (2012). "

The recent measurements of the Cosmic Microwave Background anisotropies at arcminute angular scales performed by the ACT and SPT experiments are probing the damping regime of CMB fluctuations. The analysis of these datasets unexpectedly suggests that the effective number of relativistic degrees

of freedom is larger than the standard value of  $N_{\text{eff}} = 3.04$ , and inconsistent with it at more than two standard deviations. In this paper we study the role of a mechanism that could affect the shape of the CMB angular fluctuations at those scales, namely a change in the recombination process through variations in the fine structure constant. We show that the new CMB data significantly improve the previous constraints on variations of  $\alpha$ , with  $\alpha/\alpha_0 = 0.984 \pm 0.005$ , i.e. hinting also to a more than two standard deviation from the current, local, value  $\alpha_0$ . A significant degeneracy is present between  $\alpha$  and  $N_{\text{eff}}$ , and when variations in the latter are allowed the constraints on  $\alpha$  are relaxed and again consistent with the standard value. Deviations of either parameter from their standard values would imply the presence of new, currently unknown physics.

13. "New limits on the fundamental constants from the CMB data" **Eloisa Menegoni**, Alessandro Melchiorri, Erminia Calabrese, Silvia Galli, to be published as a proceedings for "3rdGalileo-Xu Guangqi meeting" held in Beijing, China.
14. "New Limits on the Neutrino Mass from Cosmology" Melchiorri, A.; de Bernardis F.; **Menegoni, E.** International Journal of Modern Physics: Conference Series, vol. 12, issue 01, p. 36; 368 (2012). DOI: 10.1142/S2010194512006575 [2012IJMPS..12..368M].
15. "Testing the Variation of Fundamental Constants with the CMB" Galli, Silvia; Martins, C. J. A. P.; Melchiorri, Alessandro **Eloisa Menegoni**. From Varying Couplings to Fundamental Physics, Astrophysics and Space Science Proceedings, ISBN 978-3-642-19396-5. Springer-Verlag Berlin Heidelberg, 2011, p. 59 SPRINGER.

#### 4.4. Invited talks at international conferences

1. "Physics of non-dissipative ultrarelativistic photospheres"

(G.V. Vereshchagin)

On recent developments in theoretical and experimental general relativity, gravitation and relativistic field theories: XIII Marcel Grossmann Meeting, Stockholm, 1-7 July 2012.

2. "Photon thick and photon thin relativistic outflows and GRBs"

(I.A. Siutsou, R. Ruffini and G.V. Vereshchagin)

On recent developments in theoretical and experimental general relativity, gravitation and relativistic field theories: XIII Marcel Grossmann Meeting, Stockholm, 1-7 July 2012.

3. "Monte Carlo simulations of the photospheric emission in GRBs"  
(D. Begue, I.A. Siutsou and G.V. Vereshchagin)  
On recent developments in theoretical and experimental general relativity, gravitation and relativistic field theories: XIII Marcel Grossmann Meeting, Stockholm, 1-7 July 2012.
4. "Phase space evolution of pairs created in strong electric fields" (A. Benedetti, R. Ruffini and G.V. Vereshchagin) On recent developments in theoretical and experimental general relativity, gravitation and relativistic field theories: XIII Marcel Grossmann Meeting, Stockholm, 1-7 July 2012.
5. "Applications of the Boltzmann equation: from an interacting plasma toward the photospheric emission of a GRB" (A. Benedetti, R. Ruffini and G.V. Vereshchagin) Erasmus Mundus School, Nice, France, 3rd 19th September, 2012.
6. "Photospheric emission from thermally accelerated relativistic outflows"  
GRBs, their progenitors and the role of thermal emission, Les Houches, France, 2-7 October, 2011  
(G.V. Vereshchagin, R. Ruffini and I.A. Siutsou)
7. "Thermalization of the pair plasma"  
(G.V. Vereshchagin, A.G. Aksenov and R. Ruffini)  
From Nuclei to White Dwarfs and Neutron Stars, Les Houches, France, 3-8 April, 2011
8. "Photospheric emission from relativistic outflows: 1DHD"  
(G.V. Vereshchagin, R. Ruffini and I.A. Siutsou)  
Recent News from the MeV, GeV and TeV Gamma-Ray Domains, Pescara, Italy, 21-26 March, 2011
9. "Thermalization of degenerate electron-positron plasma"  
I.A. Siutsou, A.G. Aksenov, R. Ruffini and G.V. Vereshchagin  
IRAP Ph.D. Erasmus Mundus School—May 27, 2011, Nice, France
10. "Semidegenerate self-gravitating systems of fermions as central objects and dark matter halos in galaxies"  
(I. A. Siutsou, A. Geralico and R. Ruffini)  
Recent News from the MeV, GeV and TeV Gamma-Ray Domains, March 24, 2011, Pescara, Italy

11. "Thermalization of degenerate electron-positron plasma"  
(I.A. Siutsou, A.G. Aksenov, G.V. Vereshchagin and R. Ruffini)  
3rd Galileo-Xu Guangqi Meeting—October 12, 2011, Beijing, China
12. "Photospheric emission of relativistically expanding outflows"  
(I.A. Siutsou, G.V. Vereshchagin and R. Ruffini)  
12th Italian-Korean Symposium on Relativistic Astrophysics—July 5, 2011, Pescara, Italy
13. On the frequency of oscillations in the pair plasma generated by a strong electric field.  
(Alberto Benedetti, W.-B. Han, R. Ruffini, G.V. Vereshchagin)  
IRAP Ph.D. Erasmus Mundus Workshop, April 5, 2011, Pescara (Italy)
14. Oscillations in the pair plasma generated by a strong electric field  
(Alberto Benedetti, W.-B. Han, R. Ruffini, G.V. Vereshchagin)  
Italian-Korean Meeting, July 4-9, 2011, Pescara (Italy)
15. Electron-Positron plasma oscillations: hydro-electrodynamic and kinetic approaches  
(Alberto Benedetti, R. Ruffini, G.V. Vereshchagin)  
IRAP Ph.D. Erasmus Mundus School, September 7, 2011, Nice (France)
16. Boltzmann equation: from an interacting plasma toward the photospheric emission of a GRB  
(Alberto Benedetti, A. Aksenov, R. Ruffini, I. Siotsou, G.V. Vereshchagin)  
IRAP Ph.D. Erasmus Mundus Workshop, October 6, 2011, Les Houches (France)
17. Electron-Positron plasma oscillations: hydro-electrodynamic and kinetic approaches.  
(Alberto Benedetti, A. Aksenov, R. Ruffini, I. Siutsou, G.V. Vereshchagin)  
Galileo-Xu Guanqui Meeting, October 12, 2011, Beijing (China)
18. "Inflation in a general reionization scenario "  
(S. Pandolfi)  
Essential Cosmology for the Next Generation, Puerto Vallarta , Mexico, January 10-14, 2011

19. "Constraints on Inflation in extended cosmological scenarios "  
(S. Pandolfi)  
28 January 2011, Dark Cosmology Center, Copenhagen, Denmark.
20. "Theoretical Development toward the Planck mission "  
(S. Pandolfi)  
IRAP PhD and Erasmus Mundus Workshop: Workshop on Recent News from the GeV and TeV Gamma-Ray Domains: Results and Interpretations, 21-26 March 2011, ICRANet (Pescara), Italy.
21. "Joint Astrophysical and Cosmological constraints on reionization "  
(S. Pandolfi)  
DAVID WORKSHOP VI, Scuola Normale Superiore, Pisa, October 18-20 2011
22. "New constraints on features in the primordial spectrum "  
(M. Benetti)  
3rd Galileo- Xu Guangqi meeting, Beijing (China), October 11-15, 2011.
23. "Thermalization of the pair plasma"  
(G.V. Vereshchagin with A.G. Aksenov and R. Ruffini)  
Korean Physical Society 2010 Fall Meeting, Pyeong-chang, Korea, 20-22 October, 2010.
24. "The spatial structure of expanding optically thick relativistic plasma and the onset of GRBs"  
(G.V. Vereshchagin with A.G. Aksenov, G. de Barros and R. Ruffini)  
GRB 2010 / Dall'eV al TeV tutti i colori dei GRB, Secondo Congresso Italiano sui Gamma-ray Burst, Cefalu' 15-18 June 2010.
25. "From thermalization mechanisms to emission processes in GRBs"  
(G.V. Vereshchagin)  
XII Marcel Grossmann Meeting, Paris, 12-18 July 2009.
26. "Kinetics of the mildly relativistic plasma and GRBs"  
(A.G. Aksenov R. Ruffini, and G.V. Vereshchagin)  
"The Sun, the Stars, the Universe, and General Relativity" - International conference in honor of Ya. B. Zeldovich 95th Anniversary, Minsk, Belarus, April 19-23, 2009.

27. "Pair plasma around compact astrophysical sources: kinetics, electro-dynamics and hydrodynamics"  
(G.V. Vereshchagin and R. Ruffini)  
Invited seminar at RMKI, Budapest, February 24, 2009.
28. "Thermalization of the pair plasma with proton loading"  
(G.V. Vereshchagin, R. Ruffini, and A.G. Aksenov)  
Probing Stellar Populations out to the Distant Universe, Cefalu', Italy, September 7-19, 2008.
29. "Thermalization of the pair plasma with proton loading"  
(G.V. Vereshchagin, R. Ruffini, and A.G. Aksenov)  
3rd Stueckelberg Workshop, Pescara, Italy, 8-18 July, 2008.
30. "Thermalization of the pair plasma"  
(G.V. Vereshchagin, R. Ruffini, and A.G. Aksenov)
31. "Non-singular solutions in Loop Quantum Cosmology"  
(G.V. Vereshchagin)  
2nd Stueckelberg Workshop, Pescara, Italy, 3-7 September, 2007.
32. "(From) massive neutrinos and inos and the upper cutoff to the fractal structure of the Universe (to recent progress in theoretical cosmology)"  
(G.V. Vereshchagin, M. Lattanzi and R. Ruffini)  
A Century of Cosmology, San Servolo, Venice, Italy, 27-31 August, 2007.
33. "Pair creation and plasma oscillations"  
(G.V. Vereshchagin, R. Ruffini, and S.-S. Xue)  
4th Italian-Sino Workshop on Relativistic Astrophysics, Pescara, Italy, 20-29 July, 2007.
34. "Thermalization of electron-positron plasma in GRB sources"  
(G.V. Vereshchagin, R. Ruffini, and A.G. Aksenov)  
Xth Italian-Korean Symposium on Relativistic Astrophysics, Pescara, Italy, 25-30 June, 2007.
35. "Kinetics and hydrodynamics of the pair plasma"  
(G.V. Vereshchagin, R. Ruffini, C.L. Bianco, A.G. Aksenov)
36. "Pair creation and plasma oscillations"  
(G.V. Vereshchagin, R. Ruffini and S.-S. Xue)  
Cesare Lattes Meeting on GRBs, Black Holes and Supernovae, Mangaratiba-Portobello, Brazil, 26 February - 3 March 2007.

37. "Cavallo-Rees classification revisited"  
(G.V. Vereshchagin, R. Ruffini and S.-S. Xue)  
On recent developments in theoretical and experimental general relativity, gravitation and relativistic field theories: XIth Marcel Grossmann Meeting, Berlin, Germany, 23-29 July, 2006.
38. "Kinetic and thermal equilibria in the pair plasma"  
(G.V. Vereshchagin)  
The 1st Bego scientific rencontre, Nice, 5-16 February 2006.
39. "From semi-classical LQC to Friedmann Universe"  
(G.V. Vereshchagin)  
Loops '05, Potsdam, Golm, Max-Planck Institut für Gravitationsphysik (Albert-Einstein-Institut), 10-14 October 2005.
40. "Equations of motion, initial and boundary conditions for GRBs"  
(G.V. Vereshchagin, R. Ruffini and S.-S. Xue)  
IXth Italian-Korean Symposium on Relativistic Astrophysics, Seoul, Mt. Kungang, Korea, 19-24 July 2005.
41. "On the Cavallo-Rees classification and GRBs"  
(G.V. Vereshchagin, R. Ruffini and S.-S. Xue)  
II Italian-Sino Workshop on Relativistic Astrophysics, Pescara, Italy, 10-20 June, 2005.
42. "New constraints on features in the primordial spectrum "  
(M. Benetti)  
Essential Cosmology for the Next Generation Ph.D School, January 16-21 2012, Cancun, Mexico
43. "New constraints on features in the primordial spectrum "  
(M. Benetti)  
XIth School of Cosmology, Gravitational Lenses: their impact in the study of galaxies and Cosmology, Ph.D School, September 17-22 2012, Cargese, France
44. "New constraints on variations of the fine structure constant from CMB anisotropies "  
(E. Menegoni)  
XIth Cosmology School, held at IESC, in Cargese, France, from 17th to 21th of September, 2012.

45. "The Fine Structure Constant and the CMB Damping Scale "  
(E. Menegoni)  
13th Marcel Grossmann Meeting -MG13, Stockholms Universitet, in Stockholm, Sweden, from 1<sup>th</sup> – 7<sup>th</sup> of July, 2012.
46. "New constraints on variations of the fine structure constant from CMB anisotropies "  
(E. Menegoni)  
Cosmology on the Beach: Essential Cosmology for the Next Generation, conference organized by Berkeley Center for Cosmological Physics (USA) and Instituto Avanzado de Cosmologia (Mexico) Cancun, Mexico, January 16-20, 2012.

## 4.5. Lecture courses

1. "First light from Gamma Ray Bursts", 3 lectures  
(G.V. Vereshchagin)  
IRAP Ph.D. Erasmus Mundus September school, Nice, 3 – 21 September, 2012.
2. "Relativistic kinetic theory and its applications in astrophysics and cosmology", 5 lectures  
(G.V. Vereshchagin)  
XV Brazilian School of Cosmology and Gravitation, Mangaratiba - Rio de Janeiro – Brazil, August 19 - September 1, 2012.
3. "Pair plasma in GRBs and cosmology"  
(G.V. Vereshchagin)  
2 lectures, IRAP Ph.D. Erasmus Mundus September school, 12 – 23 September, 2011, University of Nice Sophia Antipolis, Nice, France.
4. "Relativistic kinetic theory and its applications in astrophysics and cosmology"  
(G.V. Vereshchagin)  
Lecture course for International Relativistic Astrophysics PhD, Erasmus Mundus Joint Doctorate Program from the  
European Commission, September 6-24, 2010, University of Nice Sophia Antipolis, Nice, France.

5. “Relativistic kinetic theory and its applications”, IRAP Ph.D. lectures  
(G.V. Vereshchagin)  
February 1-19, 2010, Observatoire de la Cote d’Azur, Nice, France.
6. Inflationary Constraints and reionization  
(S. Pandolfi)  
IRAP Ph.D. Lectures in Nice, Observatoire de la Cote d’Azur, 12-16  
February 2010



## 5. APPENDICES



# A. Relativistic degeneracy in the pair plasma

## A.1. Introduction

The description of processes involving electron-positron pairs is required in many phenomena in physics and astrophysics (Ruffini et al., 2010). The standard cosmological model includes lepton era with electron-positron plasma at high temperature and initially in thermal equilibrium (see e.g. Weinberg (2008)). Strong electromagnetic fields are generated in laser experiments aiming at production of electron-positron pairs (Gerstner, 2010; Chen et al., 2009). When electromagnetic field invariants  $\mathbf{E}^2 - \mathbf{H}^2$  and  $\mathbf{E} \cdot \mathbf{H}$  approach critical value vacuum breakdown leads to copious pair production ultimately leading to formation of electron-positron plasma (Mustafa and Kämpfer, 2009). Strong electromagnetic fields are thought to occur in astrophysical conditions, near such compact objects as black holes (Damour and Ruffini, 1975), hypothetical strange stars (Alcock et al., 1986; Usov, 1998) and possibly neutron stars (Rotondo et al., 2011).

Pair production by vacuum breakdown or by laser beam interactions is in principle the out of equilibrium process. Relaxation of electron-positron plasma to thermal equilibrium has been considered in Aksenov et al. (2007, 2009). There relativistic Boltzmann equations with exact QED collision integrals taking into account all relevant two-particle (scatterings and pair creation/annihilation, etc.) and three-particle (e.g. relativistic bremsstrahlung, double Compton scattering etc.) interactions were solved numerically. It was confirmed that a metastable state called "*kinetic equilibrium*" (Pilla and Shaham, 1997) exists in such plasma, which is characterized by the same temperature of all particles, but nonnull chemical potentials. Such state occurs when the detailed balance of all two-particle reactions is established. It was pointed out that direct and inverse  $3p$  interactions are essential in bringing electron-positron plasma to thermal equilibrium. In Aksenov et al. (2010) relaxation timescales for optically thick electron-positron plasma in a wide range of temperatures and proton loadings were computed numerically using the kinetic code developed in Aksenov et al. (2007, 2009). These timescales were previously estimated in the literature by order of magnitude arguments using the reaction rates of the dominant processes (Gould, 1981; Stepney, 1983). It was shown that these numerically ob-

tained timescales differ from previous estimations by several orders of magnitude. In the description of plasma Boltzmann statistics of particles was used in these works.

## A.2. Modeling of the pair plasma

The qualitative character of processes in the plasma is defined by a number of parameters, which we describe here.

First parameter is the average energy per particle  $\langle \varepsilon \rangle$ . Following Aksenov et al. (2007, 2009, 2010), we consider mildly relativistic plasma with

$$0.01 \lesssim \frac{\langle \varepsilon \rangle}{m_e c^2} \lesssim 10, \quad (\text{A.2.1})$$

where  $k$  is the Boltzmann constant,  $m_e$  is the mass of electron, and  $c$  is the speed of light. The range was selected to avoid production of neutrinos and muons (upper limit) and to have sufficient density of pairs (lower limit) Ruffini et al. (2010).

Second parameter is the average occupation number for particle quantum states in the plasma:  $\langle c_{\pm} \rangle$  for electrons/positrons and  $\langle c_{\gamma} \rangle$  for photons. These numbers characterize relative importance of Bose enhancement and Pauli blocking in particle interactions in the plasma. As initial state of plasma can be out of equilibrium, these numbers can be of order unity (or even higher in the case of photons), that implies importance of quantum corrections to interaction rates.

The simple approach used in the literature, (Groot et al., 1980, p. 352), to estimate the importance of quantum corrections is to compare number density of states inside volume of momentum space with energies  $\varepsilon \sim pc \lesssim kT$  and actual particle density  $n$ . For nondegenerate plasma with  $\langle c \rangle \ll 1$  number of states should be much higher than number of particles, that leads to the following condition

$$\left( \frac{kT}{c\hbar} \right)^3 \gg n \quad \Leftrightarrow \quad D = \frac{1}{n\lambda_{th}^3} \gg 1, \quad (\text{A.2.2})$$

where  $D$  is the so-called degeneracy parameter and  $\lambda_{th} = \frac{c\hbar}{kT}$  is the thermal wave-length. In the case of relativistic plasma temperature is connected to energy density  $\rho$  as  $kT \simeq \rho/(3n)$  and after substitution of parameter values to Eq. (A.2.2) we arrive to the condition for plasma to be nondegenerate

$$\log_{10} \frac{\rho}{\text{erg} \cdot \text{cm}^{-3}} > \frac{4}{3} \log_{10} \frac{n}{\text{cm}^{-3}} - 16.0. \quad (\text{A.2.3})$$

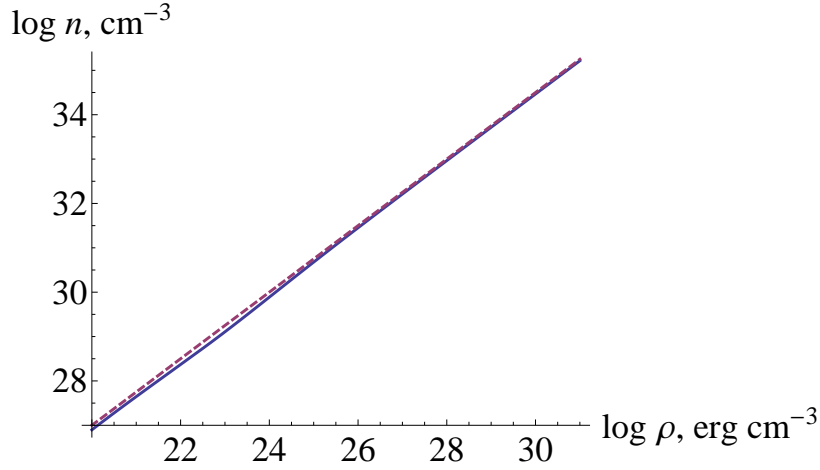


**Figure A.1.:** Concentration-energy density diagram of relativistic electron-positron-photon plasma. Solid curve shows thermal particle density  $n_{th}(\rho)$ , dashed line corresponds to transition from nondegenerate to degenerate plasma by  $D = 1$  (A.2.2).

On the concentration-energy density diagram, see Fig. A.1, the line  $D = 1$  is close to the curve of plasma density in thermal equilibrium  $n_{th}(\rho)$  and it means that thermal plasma cannot be treated as nondegenerate. Indeed, if stimulated emission of photons is not taken into account, then thermal equilibrium spectrum has incorrect low-energy dependence, i.e. Wien law  $dn/d\epsilon \propto \epsilon^2$ , instead of correct Rayleigh-Jeans law  $dn/d\epsilon \propto \epsilon$ . Thus we conclude that *Bose enhancement and Pauli blocking of reaction rates play an important role in the process of thermalization of pair plasma.*

Third parameter is the plasma parameter  $g$  defining the applicability of kinetic approach with one-particle distribution functions to the plasma, analogous to ideality parameter in gas kinetics, see e.g. (Landau and Lifshitz, 1981, § 27). To ensure that two-particle correlations are negligible the plasma should contain many particles inside the Debye sphere, i.e. average effect of Debye screening of electrical charge in the plasma should dominate over chaotic fluctuations of the screening due to variations of number of charged particles inside the Debye sphere. The plasma parameter  $g$  is proportional to inverse number of charged particles inside the Debye sphere

$$g = \frac{1}{n_{\pm} \lambda_D^3}, \quad (\text{A.2.4})$$

where the Debye length

$$\lambda_D = \begin{cases} \sqrt{\frac{kT}{4\pi e^2 n}} & \text{in nondegenerate plasma, } \mu_{\pm} < kT, \\ \sqrt{\frac{E_F}{4\pi e^2 n}} & \text{in degenerate plasma, } \mu_{\pm} > kT. \end{cases} \quad (\text{A.2.5})$$

and  $E_F$  is the Fermi energy (Groot et al., 1980, p. 351). Kinetic approach with one-particle distribution functions is sufficient for plasma with  $g \ll 1$ .

As it is shown in (Groot et al., 1980, p. 352), in the average energy range considered here (A.2.1) plasma parameter is always small and Boltzmann equation approach is totally justified.

In this chapter we present the extension of the previous results on thermalization of pair plasma, including exact QED treatment of three-particle interaction and quantum corrections to collision integrals by the corresponding Pauli blocking and Bose enhancement factors. In section A.3 the principle of detailed equilibrium is discussed and kinetic and thermal equilibrium states are recalled. In section A.4 relativistic Boltzmann equation with quantum corrections is introduced for both two- and three-particle interactions. In section A.7 the details of adopted numerical scheme are given. In section A.8 we report our results. Discussion and conclusions follow.

## A.3. Kinetic and thermal equilibrium

### A.3.1. Two-particle interactions and kinetic equilibrium

Firstly we consider two-particle interactions. The final state of electron-positron-photon plasma in this case is completely characterized by two parameters: number density of particles  $n$  and energy density  $\rho$ . This is the state of kinetic equilibrium, characterized by vanishing rates of two-particle reactions, see e.g. Pilla and Shaham (1997) and (Ehlers, 1973, sec. 3.8).

Detailed equilibrium conditions imply the equal rates for direct and inverse reaction involving the same quantum states of initial and final particles. For example, in electron-positron pair creation/annihilation process

$$e_1^+ + e_2^- \longleftrightarrow \gamma_3 + \gamma_4 \quad (\text{A.3.1})$$

the equality of rates means that for occupation numbers the following relation is held in equilibrium, e.g. (Ehlers, 1973, p. 81)

$$c_1 c_2 (1 + c_3) (1 + c_4) = c_3 c_4 (1 - c_1) (1 - c_2), \quad (\text{A.3.2})$$

because the transition probability for direct and inverse reaction is the same

due to PT-invariance of quantum electrodynamics, e.g. Brenig and Haag (1959), (Ehlers, 1973, p. 76). This functional equation implies, in turn, that occupation numbers  $c_i$  should follow: for electrons and positrons—Fermi-Dirac distribution, and for photons—Bose-Einstein distribution, for the proof see e.g. Chernikov (1964). Then for reaction (A.3.1) we have equation

$$\begin{aligned} & \frac{1}{\exp \frac{\epsilon_1 - \mu_+}{kT_+} + 1} \frac{1}{\exp \frac{\epsilon_2 - \mu_-}{kT_-} + 1} \left( 1 + \frac{1}{\exp \frac{\epsilon_3 - \mu_\gamma}{kT_\gamma} - 1} \right) \left( 1 + \frac{1}{\exp \frac{\epsilon_4 - \mu_\gamma}{kT_\gamma} - 1} \right) = \\ & = \frac{1}{\exp \frac{\epsilon_3 - \mu_\gamma}{kT_\gamma} - 1} \frac{1}{\exp \frac{\epsilon_4 - \mu_\gamma}{kT_\gamma} - 1} \left( 1 - \frac{1}{\exp \frac{\epsilon_1 - \mu_+}{kT_+} + 1} \right) \left( 1 - \frac{1}{\exp \frac{\epsilon_2 - \mu_-}{kT_-} + 1} \right), \end{aligned} \quad (\text{A.3.3})$$

to be solved simultaneously with equations from another possible reactions and taking into account conservation of energy  $\epsilon_1 + \epsilon_2 = \epsilon_3 + \epsilon_4$ .

Consequently, parameters of the equilibrium, resulting from different two-particle interactions that are listed in Table A.1, are connected by the following relations Aksenov et al. (2009)

$$T_+ = T_- = T_\gamma = T, \quad 2\mu_\gamma = \mu_+ + \mu_-, \quad (\text{A.3.4})$$

and in the case of electrically neutral plasma ( $n_+ = n_-$ ) additionally

$$\mu_\gamma = \mu_+ = \mu_- = \mu. \quad (\text{A.3.5})$$

Here we are concerned with this case only.

Instead of  $\rho$  and  $n$  one can characterize kinetic equilibrium by temperature  $T$  and chemical potential  $\mu$ . We will use instead dimensionless temperature  $\theta = \frac{kT}{m_e c^2}$  and chemical potential  $\zeta = \frac{\mu}{kT}$ . We have two equations determining these parameters from given  $n$  and  $\rho$ :

$$\begin{cases} n = \frac{8\pi m_e^3 c^3}{h^3} \left( 2 \int_1^\infty \frac{\epsilon \sqrt{\epsilon^2 - 1}}{e^{\epsilon/\theta - \zeta} + 1} d\epsilon + \int_0^\infty \frac{\epsilon^2}{e^{\epsilon/\theta - \zeta} - 1} d\epsilon \right), \\ \rho = \frac{8\pi m_e^4 c^5}{h^3} \left( 2 \int_1^\infty \frac{\epsilon^2 \sqrt{\epsilon^2 - 1}}{e^{\epsilon/\theta - \zeta} + 1} d\epsilon + \int_0^\infty \frac{\epsilon^3}{e^{\epsilon/\theta - \zeta} - 1} d\epsilon \right), \end{cases} \quad (\text{A.3.6})$$

where  $\epsilon = \frac{\varepsilon}{m_e c^2}$  is dimensionless energy.

There is a phase transition in the equilibrium at  $\zeta = 0$  (Van Vliet, 2008, sec. 8.2). As for bosons chemical potential cannot increase over 0, for concentrations higher than concentration in full thermal equilibrium  $n_{th}(\rho)$ , if only

**Table A.1.:** Two-particle interactions in electron-positron-photon plasma and their implications in detailed equilibrium

| Binary interactions   | Results  |
|---|--|
| Møller and Bhabha scattering                                |  |
| $e_1^\pm e_2^\pm \longleftrightarrow e_1^{\pm'} e_2^{\pm'}$ | $n_\pm = \frac{1}{\exp \frac{\epsilon_\pm - \mu_\pm}{kT_\pm} + 1}$                                   |
| $e^\pm e^\mp \longleftrightarrow e^{\pm'} e^{\mp'}$         | $T_+ = T_-$  |
| Compton scattering  |  |
| $e^\pm \gamma \longleftrightarrow e^\pm \gamma'$            | $n_\gamma = \frac{1}{\exp \frac{\epsilon_\gamma - \mu_\gamma}{kT_\gamma} - 1}$<br>$T_\pm = T_\gamma$ |
| Pair production and annihilation                            |  |
| $\gamma \gamma' \longleftrightarrow e^\pm e^\mp$            | $2\mu_\gamma = \mu_+ + \mu_-$  |

two-particle interactions are considered, Bose condensation of photons can occur only by Compton scattering Khatri et al. (2012). Critical concentration can be found as

$$n_{th}(\rho) = \frac{8\pi m_e^3 c^3}{h^3} \left( 2 \int_1^\infty \frac{\epsilon \sqrt{\epsilon^2 - 1}}{e^{\epsilon/\theta_{th}(\rho)} + 1} d\epsilon + \int_0^\infty \frac{\epsilon^2}{e^{\epsilon/\theta_{th}(\rho)} - 1} d\epsilon \right), \quad (\text{A.3.7})$$

where  $\theta_{th}(\rho)$  is determined by an equation

$$\rho = \frac{8\pi m_e^4 c^5}{h^3} \left( 2 \int_1^\infty \frac{\epsilon^2 \sqrt{\epsilon^2 - 1}}{e^{\epsilon/\theta_{th}(\rho)} + 1} d\epsilon + \int_0^\infty \frac{\epsilon^3}{e^{\epsilon/\theta_{th}(\rho)} - 1} d\epsilon \right). \quad (\text{A.3.8})$$

Such a transition has an interesting effect: as part of the particles completely loose their energy, average energy of particles with non-zero energy increases. Namely, concentration of the particles of non-zero energy is equal to  $n_{th}(\rho)$ , so average energy per particle increases  $n/n_{th}(\rho)$  times. As a result temperature of the plasma in kinetic equilibrium cannot be lower than  $\theta_{th}(\rho)$ .

### A.3.2. Three-particle interactions and thermal equilibrium

Three-particle interactions do not conserve particle numbers, for example, double Compton scattering can split a photon into two photons or, in inverse reaction, can merge two photons into one

$$e_1^\pm + \gamma_2 \longleftrightarrow e_3^\pm + \gamma_4 + \gamma_5. \quad (\text{A.3.9})$$

The equation analogous to (A.3.3) can be written for this reaction, and its solution leads Aksenov et al. (2009) to additional constraint on the state of detailed equilibrium

$$\mu_\gamma = 0, \quad (\text{A.3.10})$$

and for electrically neutral plasma ( $n_- = n_+$ ) we have

$$\mu_\gamma = \mu_+ = \mu_- = \mu = 0. \quad (\text{A.3.11})$$

This state is the state of complete thermal equilibrium, and it is characterized by temperature  $\theta$  only, which for a given total energy density  $\rho$  can be found via equation

$$\rho = \frac{8\pi m_e^4 c^5}{h^3} \left( 2 \int_1^\infty \frac{\epsilon^2 \sqrt{\epsilon^2 - 1}}{e^{\epsilon/\theta(\rho)} + 1} d\epsilon + \int_0^\infty \frac{\epsilon^3}{e^{\epsilon/\theta(\rho)} - 1} d\epsilon \right). \quad (\text{A.3.12})$$

## A.4. Boltzmann equation with QED collision integrals

In uniform isotropic pair plasma relativistic Boltzmann equation for distribution function  $f_\alpha$  of the particle specie  $\alpha$ , where  $\alpha$  stands for electron, positron, and photon, has the following form (Aksenov et al., 2007):

$$\frac{1}{c} \frac{d}{dt} f_\alpha(\mathbf{p}, t) = \sum_q (\eta_\alpha^q - \chi_\alpha^q f_\alpha(\mathbf{p}, t)), \quad (\text{A.4.1})$$

where the sum is taken over all two- and three-particle reactions  $q$ ,  $\eta_\alpha^q$  and  $\chi_\alpha^q$  are, respectively, the emission and absorption coefficients, and  $f_\alpha$  is normalized as

$$n_\alpha(t) = \int f_\alpha(\mathbf{p}, t) d^3 \mathbf{p}, \quad (\text{A.4.2})$$

where  $n_\alpha$  is the number density of particles  $\alpha$ .

Collision integrals describe various interactions occurring in relativistic electron-positron-photon plasma, as listed in Table A.2. Such interactions are generally divided in two groups: two-particle interactions and three-particle interactions.

## A.5. Two-particle collision integrals

Consider interaction of two incoming particles of species  $\alpha$  and  $\beta$  in quantum states  $a$  and  $b$ , having momenta in the phase space volumes  $d^3 \mathbf{p}_a$  around  $\mathbf{p}_a$  and  $d^3 \mathbf{p}_b$  around  $\mathbf{p}_b$ , respectively, resulting in two outgoing particles of

| Two-particle interactions   | Three-particle interactions  |
|---|--|
| Compton scattering<br>$e^\pm \gamma \longrightarrow e^{\pm'} \gamma'$   | Double Compton<br>$e^\pm \gamma \longleftrightarrow e^{\pm'} \gamma' \gamma''$   |
| Coulomb, Møller and Bhabha scattering<br>$e_1^\pm e_2^\pm \longrightarrow e_1^{\pm'} e_2^{\pm'}$<br>$e^+ e^- \longrightarrow e^{+'} e^{-'}$ | Bremmstrahlung<br>$e_1^\pm e_2^\pm \longleftrightarrow e_1^{\pm'} e_2^{\pm'} \gamma$<br>$e^+ e^- \longleftrightarrow e^{+'} e^{-'} \gamma$   |
| Creation/annihilation<br>$e^+ e^- \longleftrightarrow \gamma_1 \gamma_2$  | Three-photon annihilation<br>$e^+ e^- \longleftrightarrow \gamma_1 \gamma_2 \gamma_3$  |
|   | Pair creation/annihilation<br>$\gamma_1 \gamma_2 \longleftrightarrow e^+ e^- \gamma'$<br>$e^\pm \gamma \longleftrightarrow e^{\pm'} e^+ e^-$ |

**Table A.2.:** Particle interactions in the pair plasma.

species  $\kappa$  and  $\lambda$  in quantum states  $k$  and  $l$ , having momenta in the phase space volumes  $d^3 \mathbf{p}_k$  around  $\mathbf{p}_k$  and  $d^3 \mathbf{p}_l$  around  $\mathbf{p}_l$ , respectively:

$$\alpha_a + \beta_b \longrightarrow \kappa_k + \lambda_l \quad (\text{A.5.1})$$

For simplification of notation the indices of particle species will be omitted where possible. Energy and momentum conservations read

$$\epsilon_a + \epsilon_b = \epsilon_k + \epsilon_l, \quad \mathbf{p}_a + \mathbf{p}_b = \mathbf{p}_k + \mathbf{p}_l. \quad (\text{A.5.2})$$

The differential emission and absorption coefficients for this reaction are respectively Uehling and Uhlenbeck (1933); Uehling (1934)

$$\begin{aligned} \chi_\alpha f_\alpha(\mathbf{p}_a, t) d^3 \mathbf{p}_a &= \chi_\beta f_\beta(\mathbf{p}_b, t) d^3 \mathbf{p}_b = \eta_\kappa(\mathbf{p}_k, t) d^3 \mathbf{p}_k = \eta_\lambda(\mathbf{p}_l, t) d^3 \mathbf{p}_l = \\ &= d^3 \mathbf{p}_k d^3 \mathbf{p}_l d^3 \mathbf{p}_a d^3 \mathbf{p}_b \times \\ &\times W_{(\alpha_a, \beta_b | \kappa_k, \lambda_l)} \times f_\alpha(\mathbf{p}_a, t) f_\beta(\mathbf{p}_b, t) \left( 1 \pm \frac{f_\kappa(\mathbf{p}_k, t)}{g_\kappa h^{-3}} \right) \left( 1 \pm \frac{f_\lambda(\mathbf{p}_l, t)}{g_\lambda h^{-3}} \right), \end{aligned} \quad (\text{A.5.3})$$

where  $W$  is the transition function and  $(1 \pm f(\mathbf{p}, t)/(gh^{-3}))$  are respectively Bose enhancement (sign "+") and Pauli blocking (sign "-") factors,  $g = 2s + 1$  being spin weight for a particle with spin  $s$ .

To take into account all the possible processes we should span all over possible initial and final quantum states, i.e. over all the momentum spaces of incoming and outgoing particles. There are several complications, however, connected to the direct and inverse reactions and to the quantum nature of the particles involved.

First, if the process is a scattering, it does not have an inverse process in strict sense. Indeed, if  $\alpha = \kappa$  and  $\beta = \lambda$  and we span over all states  $a, b, k, l$ ,

then inverse reaction to reaction with fixed states  $a, b, k, l$  (A.5.1)

$$\alpha_a + \beta_b \longrightarrow \alpha_k + \beta_l, \quad (\text{A.5.4})$$

i.e. reaction

$$\alpha_k + \beta_l \longrightarrow \alpha_a + \beta_b, \quad (\text{A.5.5})$$

was already taken into account in our span when reaction with initial states  $k, l$  for particles  $\alpha$  and  $\beta$ , respectively, and final states  $a, b$  for particles  $\alpha$  and  $\beta$ , respectively, was considered.

In this specific case the emission coefficient of the particle  $\alpha$  in some chosen state  $i$  is an integral over all possible reactions with different sets of states  $(a, b, k, l)$  with  $k = i$

$$\begin{aligned} \eta_\alpha(\mathbf{p}_i, t) = & \int d^3\mathbf{p}_l d^3\mathbf{p}_a d^3\mathbf{p}_b \times W_{(\alpha_a, \beta_b | \alpha_i, \beta_l)} \times \\ & \times f_\alpha(\mathbf{p}_a, t) f_\beta(\mathbf{p}_b, t) \left(1 \pm \frac{f_\alpha(\mathbf{p}_i, t)}{g_\alpha h^{-3}}\right) \left(1 \pm \frac{f_\beta(\mathbf{p}_l, t)}{g_\beta h^{-3}}\right). \end{aligned} \quad (\text{A.5.6})$$

The absorption coefficient of the particle  $\alpha$  in the same state  $i$  is an integral over all possible reactions with different sets of states  $(a, b, k, l)$  with  $a = i$ , that after change of indices  $k \rightarrow a$  and  $l \leftrightarrow b$  takes the form analogous to (A.5.6)

$$\begin{aligned} \chi_\alpha f_\alpha(\mathbf{p}_i, t) = & \int d^3\mathbf{p}_l d^3\mathbf{p}_a d^3\mathbf{p}_b \times W_{(\alpha_i, \beta_l | \alpha_a, \beta_b)} \times \\ & \times f_\alpha(\mathbf{p}_i, t) f_\beta(\mathbf{p}_l, t) \left(1 \pm \frac{f_\alpha(\mathbf{p}_a, t)}{g_\alpha h^{-3}}\right) \left(1 \pm \frac{f_\beta(\mathbf{p}_b, t)}{g_\beta h^{-3}}\right). \end{aligned} \quad (\text{A.5.7})$$

Then Boltzmann equation for particle  $\alpha$  in state  $i$  reads

$$\begin{aligned} \frac{1}{c} \frac{d}{dt} f_\alpha(\mathbf{p}_i, t) = & \int d^3\mathbf{p}_l d^3\mathbf{p}_a d^3\mathbf{p}_b \times \\ & \times \left[ W_{(\alpha_a, \beta_b | \alpha_i, \beta_l)} \times f_\alpha(\mathbf{p}_a, t) f_\beta(\mathbf{p}_b, t) \left(1 \pm \frac{f_\alpha(\mathbf{p}_i, t)}{g_\alpha h^{-3}}\right) \left(1 \pm \frac{f_\beta(\mathbf{p}_l, t)}{g_\beta h^{-3}}\right) - \right. \\ & \left. - W_{(\alpha_i, \beta_l | \alpha_a, \beta_b)} \times f_\alpha(\mathbf{p}_i, t) f_\beta(\mathbf{p}_l, t) \left(1 \pm \frac{f_\alpha(\mathbf{p}_a, t)}{g_\alpha h^{-3}}\right) \left(1 \pm \frac{f_\beta(\mathbf{p}_b, t)}{g_\beta h^{-3}}\right) \right]. \end{aligned} \quad (\text{A.5.8})$$

Taking into account PT-invariance of QED, e.g. Brenig and Haag (1959), (Ehlers, 1973, p. 76),

$$W_{(\alpha_a, \beta_b | \alpha_k, \beta_l)} = W_{(\alpha_k, \beta_l | \alpha_a, \beta_b)}, \quad (\text{A.5.9})$$

that is equal to the so-called detailed balance condition Groot et al. (1980),

classical form of Boltzmann equation is recovered

$$\begin{aligned} \frac{1}{c} \frac{d}{dt} f_\alpha(\mathbf{p}_i, t) &= \int d^3 \mathbf{p}_l d^3 \mathbf{p}_a d^3 \mathbf{p}_b \times W_{(\alpha_a, \beta_b | \alpha_i, \beta_l)} \times \\ &\times \left[ f_\alpha(\mathbf{p}_a, t) f_\beta(\mathbf{p}_b, t) \left( 1 \pm \frac{f_\alpha(\mathbf{p}_i, t)}{g_\alpha h^{-3}} \right) \left( 1 \pm \frac{f_\beta(\mathbf{p}_l, t)}{g_\beta h^{-3}} \right) - \right. \\ &\left. - f_\alpha(\mathbf{p}_i, t) f_\beta(\mathbf{p}_l, t) \left( 1 \pm \frac{f_\alpha(\mathbf{p}_a, t)}{g_\alpha h^{-3}} \right) \left( 1 \pm \frac{f_\beta(\mathbf{p}_b, t)}{g_\beta h^{-3}} \right) \right]. \end{aligned} \quad (\text{A.5.10})$$

The Boltzmann equation for particle  $\beta$  is obtained in full analogy.

Second, when the process is not a scattering, the Boltzmann equation is close to (A.5.10) in form, namely

$$\begin{aligned} \frac{1}{c} \frac{d}{dt} f_\alpha(\mathbf{p}_a, t) &= \int d^3 \mathbf{p}_k d^3 \mathbf{p}_l d^3 \mathbf{p}_b \\ &\times \left[ W_{(\kappa_k, \lambda_l | \alpha_a, \beta_b)} \times f_\kappa(\mathbf{p}_k, t) f_\lambda(\mathbf{p}_l, t) \times \left( 1 \pm \frac{f_\alpha(\mathbf{p}_a, t)}{g_\alpha h^{-3}} \right) \left( 1 \pm \frac{f_\beta(\mathbf{p}_b, t)}{g_\beta h^{-3}} \right) - \right. \\ &\left. - W_{(\alpha_a, \beta_b | \kappa_k, \lambda_l)} \times f_\alpha(\mathbf{p}_a, t) f_\beta(\mathbf{p}_b, t) \times \left( 1 \pm \frac{f_\kappa(\mathbf{p}_k, t)}{g_\kappa h^{-3}} \right) \left( 1 \pm \frac{f_\lambda(\mathbf{p}_l, t)}{g_\lambda h^{-3}} \right) \right]. \end{aligned} \quad (\text{A.5.11})$$

but now the source of the additional term is the inverse process

$$\kappa_k + \lambda_l \longrightarrow \alpha_a + \beta_b, \quad (\text{A.5.12})$$

that is now different from direct one (A.5.1).

Third, when there are two particles of the same kind in the initial or final state, we need to take into account their quantum indistinguishability (Greenberger et al., 2009, p. 311–317). It simply means that, for example, in annihilation process

$$\gamma_1 + \gamma_2 \longrightarrow e_3^+ + e_4^- \quad (\text{A.5.13})$$

the initial state of two photons with momenta  $\mathbf{p}_a$  and  $\mathbf{p}_b$  for the first and second photon, respectively, is the same state as with momenta  $\mathbf{p}_b$  and  $\mathbf{p}_a$  for the first and second photon, respectively. If we still want to span integration in  $\mathbf{p}_a$  and  $\mathbf{p}_b$  over all momentum space, we should add a corresponding symmetrization multiplier, in this case equal to  $\frac{1}{2}$ .

## A.6. Three-particle collision integrals

Consider now three-particle interactions. In direct reaction two incoming particles of species  $\alpha$  and  $\beta$  have momenta in the phase space volumes  $d^3 \mathbf{p}_a$

around  $\mathbf{p}_a$  and  $d^3\mathbf{p}_b$  around  $\mathbf{p}_b$ , respectively. Three outgoing particles of species  $\iota$ ,  $\kappa$ , and  $\lambda$  have momenta in the phase space volumes  $d^3\mathbf{p}_i$  around  $\mathbf{p}_i$ ,  $d^3\mathbf{p}_k$  around  $\mathbf{p}_k$ , and  $d^3\mathbf{p}_l$  around  $\mathbf{p}_l$ , respectively

$$\alpha_a + \beta_b \longrightarrow \iota_i + \kappa_k + \lambda_l. \quad (\text{A.6.1})$$

In this case inverse reaction always exists

$$\iota_i + \kappa_k + \lambda_l \longrightarrow \alpha_a + \beta_b. \quad (\text{A.6.2})$$

The energy and momentum conservation read

$$\epsilon_a + \epsilon_b = \epsilon_i + \epsilon_k + \epsilon_l, \quad \mathbf{p}_a + \mathbf{p}_b = \mathbf{p}_i + \mathbf{p}_k + \mathbf{p}_l. \quad (\text{A.6.3})$$

The differential emission and absorption coefficients for the direct reaction are

$$\begin{aligned} \eta_i(\mathbf{p}_i, t) d^3\mathbf{p}_i &= \eta_\kappa(\mathbf{p}_k, t) d^3\mathbf{p}_k = \eta_\lambda(\mathbf{p}_l, t) d^3\mathbf{p}_l = \\ &= \chi_\alpha f_\alpha(\mathbf{p}_a, t) d^3\mathbf{p}_a = \chi_\beta f_\beta(\mathbf{p}_b, t) d^3\mathbf{p}_b = \\ &= d^3\mathbf{p}_a d^3\mathbf{p}_b d^3\mathbf{p}_i d^3\mathbf{p}_k d^3\mathbf{p}_l \times W_{(\alpha_a, \beta_b | \iota_i, \kappa_k, \lambda_l)} \times f_\alpha(\mathbf{p}_a, t) f_\beta(\mathbf{p}_b, t) \times \\ &\quad \times \left(1 \pm \frac{f_i(\mathbf{p}_i, t)}{g_i h^{-3}}\right) \left(1 \pm \frac{f_\kappa(\mathbf{p}_k, t)}{g_\kappa h^{-3}}\right) \left(1 \pm \frac{f_\lambda(\mathbf{p}_l, t)}{g_\lambda h^{-3}}\right), \end{aligned} \quad (\text{A.6.4})$$

and for the inverse one

$$\begin{aligned} \chi_i f_i(\mathbf{p}_i, t) d^3\mathbf{p}_i &= \chi_\kappa f_\kappa(\mathbf{p}_k, t) d^3\mathbf{p}_k = \chi_\lambda f_\lambda(\mathbf{p}_l, t) d^3\mathbf{p}_l = \\ &= \eta_\alpha(\mathbf{p}_a, t) d^3\mathbf{p}_a = \eta_\beta(\mathbf{p}_b, t) d^3\mathbf{p}_b = \\ &= d^3\mathbf{p}_a d^3\mathbf{p}_b d^3\mathbf{p}_i d^3\mathbf{p}_k d^3\mathbf{p}_l \times W_{(\iota_i, \kappa_k, \lambda_l | \alpha_a, \beta_b)} \times f_i(\mathbf{p}_i, t) f_\kappa(\mathbf{p}_k, t) f_\lambda(\mathbf{p}_l, t) \times \\ &\quad \times \left(1 \pm \frac{f_\alpha(\mathbf{p}_a, t)}{g_\alpha h^{-3}}\right) \left(1 \pm \frac{f_\beta(\mathbf{p}_b, t)}{g_\beta h^{-3}}\right). \end{aligned} \quad (\text{A.6.5})$$

Consequently Boltzmann equation for particle specie  $\alpha$  in the state  $a$  reads

$$\begin{aligned} \frac{1}{c} \frac{d}{dt} f_\alpha(\mathbf{p}_a, t) &= \int d^3\mathbf{p}_i d^3\mathbf{p}_k d^3\mathbf{p}_l d^3\mathbf{p}_b \\ &\times \left[ W_{(\iota_i, \kappa_k, \lambda_l | \alpha_a, \beta_b)} \times f_i(\mathbf{p}_i, t) f_\kappa(\mathbf{p}_k, t) f_\lambda(\mathbf{p}_l, t) \times \left(1 \pm \frac{f_\alpha(\mathbf{p}_a, t)}{g_\alpha h^{-3}}\right) \left(1 \pm \frac{f_\beta(\mathbf{p}_b, t)}{g_\beta h^{-3}}\right) - \right. \\ &\quad \left. - W_{(\alpha_a, \beta_b | \iota_i, \kappa_k, \lambda_l)} \times f_\alpha(\mathbf{p}_a, t) f_\beta(\mathbf{p}_b, t) \right. \\ &\quad \left. \times \left(1 \pm \frac{f_i(\mathbf{p}_i, t)}{g_i h^{-3}}\right) \left(1 \pm \frac{f_\kappa(\mathbf{p}_k, t)}{g_\kappa h^{-3}}\right) \left(1 \pm \frac{f_\lambda(\mathbf{p}_l, t)}{g_\lambda h^{-3}}\right) \right]. \end{aligned} \quad (\text{A.6.6})$$

It may happen that some particle specie is present among both incoming and outgoing particles, for instance  $\alpha$  coincides with  $\iota$ , as in the case of bremsstrahlung  $e^+e^- \rightarrow e^+e^-\gamma$ . There are the following emission and absorption terms for this particle specie: absorption of incoming particle in state  $a$  and emission of outgoing particle in state  $i$ , corresponding to the direct reaction (A.6.1). In addition there are emission of outgoing particle in state  $a$  and absorption of incoming particle in state  $i$ , corresponding to the inverse reaction (A.6.2). Thus the collision integral for that particle consists of four terms instead of two. Two additional terms are obtained by interchanging particle states indices  $a \leftrightarrow i$ . Boltzmann equation in this case reads

$$\begin{aligned}
 \frac{1}{c} \frac{d}{dt} f_\alpha(\mathbf{p}_a, t) = & \int d^3 \mathbf{p}_i d^3 \mathbf{p}_k d^3 \mathbf{p}_l d^3 \mathbf{p}_b \times \\
 & \times \left[ -W_{(\alpha_a, \beta_b | \alpha_i, \kappa_k, \lambda_l)} \times f_\alpha(\mathbf{p}_a, t) f_\beta(\mathbf{p}_b, t) \times \right. \\
 & \quad \times \left( 1 \pm \frac{f_\alpha(\mathbf{p}_i, t)}{g_\alpha h^{-3}} \right) \left( 1 \pm \frac{f_\kappa(\mathbf{p}_k, t)}{g_\kappa h^{-3}} \right) \left( 1 \pm \frac{f_\lambda(\mathbf{p}_l, t)}{g_\lambda h^{-3}} \right) + \\
 & + W_{(\alpha_i, \beta_b | \alpha_a, \kappa_k, \lambda_l)} \times f_\alpha(\mathbf{p}_i, t) f_\beta(\mathbf{p}_b, t) \times \\
 & \quad \times \left( 1 \pm \frac{f_\alpha(\mathbf{p}_a, t)}{g_\alpha h^{-3}} \right) \left( 1 \pm \frac{f_\kappa(\mathbf{p}_k, t)}{g_\kappa h^{-3}} \right) \left( 1 \pm \frac{f_\lambda(\mathbf{p}_l, t)}{g_\lambda h^{-3}} \right) + \\
 & + W_{(\alpha_i, \kappa_k, \lambda_l | \alpha_a, \beta_b)} \times f_\alpha(\mathbf{p}_i, t) f_\kappa(\mathbf{p}_k, t) f_\lambda(\mathbf{p}_l, t) \times \left( 1 \pm \frac{f_\alpha(\mathbf{p}_a, t)}{g_\alpha h^{-3}} \right) \left( 1 \pm \frac{f_\beta(\mathbf{p}_b, t)}{g_\beta h^{-3}} \right) - \\
 & \left. - W_{(\alpha_a, \kappa_k, \lambda_l | \alpha_i, \beta_b)} \times f_\alpha(\mathbf{p}_a, t) f_\kappa(\mathbf{p}_k, t) f_\lambda(\mathbf{p}_l, t) \times \left( 1 \pm \frac{f_\alpha(\mathbf{p}_i, t)}{g_\alpha h^{-3}} \right) \left( 1 \pm \frac{f_\beta(\mathbf{p}_b, t)}{g_\beta h^{-3}} \right) \right].
 \end{aligned} \tag{A.6.7}$$

Generally speaking, *such four terms should be present in collision integral of any reaction for a particle specie which is present both among incoming and outgoing particles, unless the process is a scattering*. This statement is valid for arbitrary number of incoming and outgoing particles. It is not limited to the case of quantum electrodynamics but applies to any quantum field theory in general.

There are no additional terms in Boltzmann equation in the case when in one side of the reaction we have two particles coinciding, i.e.  $\alpha = \iota = \kappa$ , for example, double Compton scattering  $e^\pm \gamma \rightarrow e^\pm \gamma \gamma$ . The only modification is just symmetrization factors due to particle indistinguishability, like in two-particle interactions.

As for QED processes considered here the corresponding collision integrals in all three-particle interactions, but three-photon annihilation  $e^+e^- \leftrightarrow \gamma\gamma\gamma$ , contain four terms instead of two, as analysis of Table A.2 indicates. In par-

ticular, four terms in double Compton scattering with symmetrization factors was considered by Chluba Chluba (2005). It should be noted that the equilibrium conditions may be obtained by only two terms in collision integrals without interchanging the states  $a$  and  $i$ , as it was done in e.g. Lightman (1981); Thorne (1981). However, due to different structure of all four emission and absorption coefficients their presence is essential in Boltzmann equation (A.6.7).

## A.7. The numerical scheme

The main difficulty arising in computation of collision integrals in comparison with the previous works Aksenov et al. (2007, 2009, 2010) is that the rate of particle emission/absorption depends not only on the incoming particles, but also on the outgoing particles. Therefore we adopt a new approach which we refer to as "*reaction-oriented*" instead of "*particle-oriented*" one used before.

Recall that the finite difference conservative scheme used there instead of distribution functions operated with spectral energy densities

$$E_i(\epsilon_i) = \frac{d\rho}{d\epsilon} = \frac{4\pi\epsilon_i^3\beta_i f_i}{c^3}, \quad (\text{A.7.1})$$

where  $\beta_i = \sqrt{1 - (m_i c^2 / \epsilon_i)^2}$  ( $m_i$ , is the mass of  $i$ -th particle specie), in the energy phase space  $\epsilon_i$ . The number density of particle  $i$  is then given by

$$n_i = \int f_i d\mathbf{p}_i = \int \frac{E_i}{\epsilon_i} d\epsilon_i, \quad dn_i = f_i d\mathbf{p}_i, \quad (\text{A.7.2})$$

while the corresponding energy density is

$$\rho_i = \int \epsilon_i f_i d\mathbf{p}_i = \int E_i d\epsilon_i.$$

Here to reduce the computational effort instead of energy densities we use particle densities

$$N_i(\epsilon_i) = \frac{dn}{d\epsilon} = \frac{4\pi\epsilon_i^2\beta_i f_i}{c^3}, \quad (\text{A.7.3})$$

and the corresponding energy density is

$$\rho_i = \int \epsilon_i f_i d\mathbf{p}_i = \int N_i \epsilon_i d\epsilon_i.$$

In these variables the Boltzmann equations (A.4.1) read

$$\frac{1}{c} \frac{dN_i}{dt} = \sum_q (\tilde{\eta}_i^q - \chi_i^q N_i), \quad (\text{A.7.4})$$

where  $\tilde{\eta}_i^q = (4\pi\epsilon_i^2\beta_i/c^3)\eta_i^q$ .

To obtain emission and absorption coefficients the computational grids are introduced in the phase space  $\{\epsilon_i, \kappa_i, \phi_i\}$ , where  $\kappa_i = \cos \vartheta_i$ ,  $\vartheta_i$  and  $\phi_i$  are angles in spherical coordinates of particle momentum space  $\mathbf{p}_i$ . The zone boundaries are  $\epsilon_{i,\omega\mp 1/2}$ ,  $\kappa_{k\mp 1/2}$ ,  $\phi_{l\mp 1/2}$  for  $1 \leq \omega \leq \omega_{\max}$ ,  $1 \leq k \leq k_{\max}$ ,  $1 \leq l \leq l_{\max}$ . The length of the  $i$ -th interval is  $\Delta\epsilon_{i,\omega} \equiv \epsilon_{i,\omega+1/2} - \epsilon_{i,\omega-1/2}$ . On the finite grid the functions (A.7.1) become

$$Y_a = Y_{i,\omega} \equiv \frac{1}{\Delta\epsilon_{i,\omega}} \int_{\Delta\epsilon_{i,\omega}} d\epsilon N_i(\epsilon), \quad (\text{A.7.5})$$

where for simplification of formulae we use collective indices  $a = \{i, \omega\}$ .

The collision integrals in (A.7.4) are replaced by the corresponding sums. When particles fulfill classical statistics we have for time derivative of functions  $Y_a$  the following expression

$$\dot{Y}_a = \sum_{b,c} A_{(b,c|a,d)} Y_b Y_c - \sum_{b,c} B_{(a,b|c,d)} Y_a Y_b, \quad (\text{A.7.6})$$

where first sum on the RHS is for emission in reaction  $b + c \rightarrow a + d$  and second is for absorption in reaction  $a + b \rightarrow c + d$ . There is no third summation (by index  $d$ ) because of delta-function in the initial integrals originating from the energy conservation. This can be effectively rewritten as just one sum

$$\dot{Y}_a = \sum_{b,c} A_{b,c}^a Y_b Y_c, \quad (\text{A.7.7})$$

$$A_{b,c}^a = A_{(b,c|a,d)} - \delta_a^c \sum_e B_{(a,b|e,d)}, \quad (\text{A.7.8})$$

and this sum can be found by direct computation.

When the quantum statistics effects are included we have instead

$$\begin{aligned} \dot{Y}_a = & \sum_{b,c} (1 \pm Y_a/\mathcal{Y}_a)(1 \pm Y_d/\mathcal{Y}_d) A_{(b,c|a,d)} Y_b Y_c - \\ & - \sum_{b,c} (1 \pm Y_d/\mathcal{Y}_d)(1 \pm Y_c/\mathcal{Y}_c) B_{(a,b|c,d)} Y_a Y_b, \end{aligned} \quad (\text{A.7.9})$$

which  $\mathcal{Y}_a$  is the spectral density corresponding to occupation numbers of

quantum states inside the phase space cell  $a$  equal to unity

$$\mathcal{Y}_a = \int_a g_a h^{-3} \epsilon d^3 \mathbf{p}_a. \quad (\text{A.7.10})$$

It turns out that while the sums on the RHS of (A.7.9) can be reduced to one sum only, but due to different structure of Bose enhancement and Pauli blocking factors the numerical scheme based on the resulting expression will not be optimal.

Instead noticing that if we do not fix  $a$  and just span over all possible processes  $a + b \rightarrow c + d$  the phase space blocking/enhancement factors  $(1 \pm Y_c/\mathcal{Y}_c)(1 \pm Y_d/\mathcal{Y}_d)$  are the same for all four particles involved in the process, and the corresponding parts of collision integrals arising in the above-mentioned sums can be computed only once instead of four times, for each particle separately. As a result it is convenient not to fix  $a$  and sum over all possible  $b, c$ , as in (A.7.9), which we refer to as "particle-oriented" approach, but instead sum over all possible reactions, which we refer to as "reaction-oriented" approach. It means that at each step of calculations we fix  $a, b$  and for all possible reaction results the emission rates of outcomes  $c$  and  $d$  and the absorption rates of incomes  $a, b$  are added to array of derivatives  $\dot{Y}_{i,\omega}$ . This approach considerably reduces the computational time and memory consumption.

In our method exact energy and number of particles conservation laws are satisfied, as we adopt interpolation of grid functions  $Y_a$  inside the energy intervals. The number of energy intervals is typically 20, while internal grid of angles has 32 points in  $\mu_i$  and 64 in  $\phi_i$ . Most time-consuming part of the numerical solution is initial integration over particle angles.

### A.7.1. Detailed description of scheme

We proceed with detailed description of the numerical scheme, starting from the coefficients of emission and absorption of two-particle interactions (A.5.3) and of three-particle interactions (A.6.4) and (A.6.5).

In the case of two-particle interactions standard treatment leads to the following relation between matrix elements of the reaction  $M_{fi}$  and transition function  $W$ , see e.g. Aksenov et al. (2009)

$$W_{(\alpha_a, \beta_b | \kappa_k, \lambda_l)} = \frac{\hbar^2 c^6}{(2\pi)^2} \frac{|M_{fi}|^2}{16\epsilon_a \epsilon_b \epsilon_k \epsilon_l} \delta(\epsilon_a + \epsilon_b - \epsilon_k - \epsilon_l) \delta^3(\mathbf{p}_a + \mathbf{p}_b - \mathbf{p}_k - \mathbf{p}_l). \quad (\text{A.7.11})$$

To span all the phase space we have to integrate 12 times over all components

of momenta, i.e. over

$$d^{12}\mathbf{q} = d^3\mathbf{p}_a d^3\mathbf{p}_b d^3\mathbf{p}_k d^3\mathbf{p}_l, \quad (\text{A.7.12})$$

to obtain all possible reaction rates  $\dot{f}$ . Number of integrations can be reduced by use of delta-functions in  $W$  and spherical symmetry.

At first we rewrite our rates in spherical coordinates  $(\epsilon, \mu = \cos \theta, \varphi)$  and get for particle  $k$ <sup>1</sup>

$$\begin{aligned} & c\eta_k^q(\epsilon_k, \mu_k, \varphi_k, t) c^{-3} \epsilon_k \sqrt{\epsilon_k^2 - m_k^2 c^4} d\epsilon_k d\mu_k d\varphi_k = \\ & = d^{12}\mathbf{q} \times W_{(\alpha_a, \beta_b | \kappa_k, \lambda_l)} \times \left[ 1 \pm \frac{f_k(\mathbf{p}_k, t)}{g_k h^{-3}} \right] \left[ 1 \pm \frac{f_l(\mathbf{p}_l, t)}{g_l h^{-3}} \right] \times f_a(\mathbf{p}_a, t) f_b(\mathbf{p}_b, t), \end{aligned} \quad (\text{A.7.13})$$

where now

$$\begin{aligned} d^{12}\mathbf{q} = & c^{-12} \epsilon_a \sqrt{\epsilon_a^2 - m_a^2 c^4} \times d\epsilon_a d\mu_a d\varphi_a \times \epsilon_b \sqrt{\epsilon_b^2 - m_b^2 c^4} \times d\epsilon_b d\mu_b d\varphi_b \times \\ & \times \epsilon_k \sqrt{\epsilon_k^2 - m_k^2 c^4} \times d\epsilon_k d\mu_k d\varphi_k \times \epsilon_l \sqrt{\epsilon_l^2 - m_l^2 c^4} \times d\epsilon_l d\mu_l d\varphi_l. \end{aligned} \quad (\text{A.7.14})$$

To get discrete version of the Boltzmann equation for given discrete cell  $\Omega_{k,\omega}$  in the phase space we have to integrate emission and absorption coefficients over cell volume:

$$c\eta_{k,\omega}^q(\Omega_{k,\omega}, t) = \int_{(\epsilon_k, \mu_k, \varphi_k) \in \Omega_{k,\omega}} c\eta_k^q(\epsilon_k, \mu_k, \varphi_k, t) c^{-3} \epsilon_k \sqrt{\epsilon_k^2 - m_k^2 c^4} d\epsilon_k d\mu_k d\varphi_k. \quad (\text{A.7.15})$$

There are 4 delta-functions in  $W$  (A.7.11) following from conservation of energy and momentum:  $\epsilon_a + \epsilon_b = \epsilon_k + \epsilon_l$ ,  $\mathbf{p}_a + \mathbf{p}_b = \mathbf{p}_k + \mathbf{p}_l$ . So 4 integrations disappear and 8 remains. Rewrite delta-functions to exclude integrations over  $l$ -th particle  $(\epsilon_l, \mu_l, \varphi_l)$  and over  $\epsilon_k$ , so that result of reaction is

---

<sup>1</sup>As in the "reaction-oriented" approach the correct number of collision integrals are obtained automatically, it is possible to omit indexes of particles and work only with indexes of momenta.

defined by particles  $a, b$  and direction of particle  $k$ :

$$\begin{aligned}
& \delta(\epsilon_k + \epsilon_l - \epsilon_a - \epsilon_b) \delta^3(\mathbf{p}_k + \mathbf{p}_l - \mathbf{p}_a - \mathbf{p}_b) = \\
& = c^{-3} \delta(\epsilon_k + \epsilon_l - \epsilon_b - \epsilon_a) \times \\
& \times \delta(\sqrt{\epsilon_k^2 - m_k^2 c^4} \mu_k + \sqrt{\epsilon_l^2 - m_l^2 c^4} \mu_l - \sqrt{\epsilon_a^2 - m_a^2 c^4} \mu_a - \sqrt{\epsilon_b^2 - m_b^2 c^4} \mu_b) \times \\
& \times \delta(\sqrt{\epsilon_k^2 - m_k^2 c^4} \sqrt{1 - \mu_k^2} \cos \varphi_k + \sqrt{\epsilon_l^2 - m_l^2 c^4} \sqrt{1 - \mu_l^2} \cos \varphi_l - \\
& - \sqrt{\epsilon_a^2 - m_a^2 c^4} \sqrt{1 - \mu_a^2} \cos \varphi_a - \sqrt{\epsilon_b^2 - m_b^2 c^4} \sqrt{1 - \mu_b^2} \cos \varphi_b) \times \\
& \times \delta(\sqrt{\epsilon_k^2 - m_k^2 c^4} \sqrt{1 - \mu_k^2} \sin \varphi_k + \sqrt{\epsilon_l^2 - m_l^2 c^4} \sqrt{1 - \mu_l^2} \sin \varphi_l - \\
& - \sqrt{\epsilon_a^2 - m_a^2 c^4} \sqrt{1 - \mu_a^2} \sin \varphi_a - \sqrt{\epsilon_b^2 - m_b^2 c^4} \sqrt{1 - \mu_b^2} \sin \varphi_b) = \\
& c^3 \frac{\delta(\epsilon_k - \epsilon_k^*) \delta(\epsilon_l - \epsilon_l^*) \delta(\varphi_l - \varphi_l^*) \delta(\mu_l - \mu_l^*)}{\epsilon_l^* \sqrt{(\epsilon_l^*)^2 - m_l^2 c^4} [1 - \beta_l^* / \beta_k^* (\boldsymbol{\mu}_k \cdot \boldsymbol{\mu}_l^*)]}, \quad (\text{A.7.16})
\end{aligned}$$

where  $\boldsymbol{\mu} = \mathbf{p}/p$  is the direction of particle momentum and the values of variables with asterisks should be found as functions of remaining energies and angles from the system of equations representing conservation laws.

Then integral (A.7.15) become

$$\begin{aligned}
c\eta_{k,\omega}^q(\Omega_{k,\omega}, t) &= \int d\epsilon_a d\mu_a d\varphi_a \times d\epsilon_b d\mu_b d\varphi_b \times d\mu_k d\varphi_k \times \\
& \times c^{-9} \frac{\sqrt{\epsilon_a^2 - m_a^2 c^4} \times \sqrt{\epsilon_b^2 - m_b^2 c^4} \times \sqrt{(\epsilon_k^*)^2 - m_k^2 c^4}}{\epsilon_l^* [1 - \beta_l^* / \beta_k^* (\boldsymbol{\mu}_k \cdot \boldsymbol{\mu}_l^*)]} \times \frac{\hbar^2 c^6}{(2\pi)^2} \frac{|M_{fi}|^2}{16} \times \\
& \times \left[ 1 \pm \frac{f_k(\mathbf{p}_k, t)}{g_k h^{-3}} \right] \left[ 1 \pm \frac{f_l(\mathbf{p}_l, t)}{g_l h^{-3}} \right] \times f_a(\epsilon_a^*, \mu_a, \varphi_a, t) f_b(\mathbf{p}_b^*, t). \quad (\text{A.7.17})
\end{aligned}$$

Now integral should be discretized as a sum over cells in phase space, but at first we can use spherical symmetry of the system and exclude 3 integrations corresponding to arbitrary final direction of  $a$ -th particle, giving us

$$\int d\mu_a d\varphi_a \cdots = 4\pi \dots, \quad \text{and setting} \quad \mu_a = 1, \varphi_a = 0, \quad (\text{A.7.18})$$

and arbitrary azimuthal angle of  $b$ -th particle

$$\int d\varphi_b \cdots = 2\pi \dots, \quad \text{and setting} \quad \varphi_b = 0. \quad (\text{A.7.19})$$

We arrive to

$$c\eta_{k,\omega}^q(\Omega_{k,\omega}, t) = \frac{\hbar^2}{8} \int d\epsilon_a \times d\epsilon_b d\mu_b \times d\mu_k d\varphi_k \times \frac{p_a p_b p_k^* \times |M_{fi}|^2}{\epsilon_i^* [1 - \beta_l^* / \beta_k^* (\boldsymbol{\mu}_k \cdot \boldsymbol{\mu}_l^*)]} \times \\ \times \left[ 1 \pm \frac{f_k(\epsilon_k, t)}{g_k h^{-3}} \right] \left[ 1 \pm \frac{f_l(\epsilon_l, t)}{g_l h^{-3}} \right] \times f_a(\epsilon_a, t) f_b(\epsilon_b, t), \quad (\text{A.7.20})$$

as  $\sqrt{\epsilon^2 - m^2 c^4} = pc$ .

Following "reaction-oriented" approach, discussed in the previous section, we will work with particle content of each cell in the momentum space

$$Y_{i,\omega} = \int_{\Omega_{i,\omega}} f_i(\mathbf{p}_i, t) d^3 \mathbf{p}_i = 4\pi c^{-3} \epsilon_{i,\omega} \sqrt{\epsilon_{i,\omega}^2 - m_i^2 c^4} \Delta \epsilon_{i,\omega} f_i(\epsilon_{i,\omega}, t). \quad (\text{A.7.21})$$

Then rate of change of  $Y_{i,\omega}$  for particles involved in the reaction is

$$\dot{Y}_{i,\omega}(t) = c\eta_{i,\omega}^q(\Omega_{i,\omega}, t) = \frac{\hbar^2 c^3}{(4\pi)^2} \sum_{a,b,\mu_b,\mu_k,\varphi_k} \frac{\Delta \mu_b}{2} \times \frac{\Delta \mu_k \Delta \varphi_k \sqrt{(\epsilon_k^*)^2 - m_k^2 c^4}}{\epsilon_i^* [1 - \beta_l^* / \beta_k^* (\boldsymbol{\mu}_k \cdot \boldsymbol{\mu}_l^*)]} \times \\ \times \frac{|M_{fi}|^2}{8} \times \left[ 1 \pm \frac{Y_k(t)}{G_k} \right] \left[ 1 \pm \frac{Y_l(t)}{G_l} \right] \times \frac{Y_a(t)}{\epsilon_a} \frac{Y_b(t)}{\epsilon_b}, \quad (\text{A.7.22})$$

where  $G_a$  is the particle content, corresponding to occupation numbers  $n_a \equiv 1$  all across the cell in the momentum space

$$G_{i,\omega} = \int_{\Omega_{i,\omega}} g_i h^{-3} d^3 \mathbf{p}_i = 4\pi g_i h^{-3} c^{-3} \epsilon_{i,\omega} \sqrt{\epsilon_{i,\omega}^2 - m_i^2 c^4} \Delta \epsilon_{i,\omega}. \quad (\text{A.7.23})$$

Thus in this "reaction-oriented" approach for each set of  $\epsilon_{\omega_a}, \epsilon_{\omega_b}$  we go over all possible  $\mu_b, \mu_k, \varphi_k$  and find corresponding  $\epsilon_k^*, \epsilon_l^*$  and reaction rates. Then we subtract initial particles from cells  $\omega_a, \omega_b$ . Final particles are generally not on the grid of  $\epsilon_{\omega_k}, \epsilon_{\omega_l}$  so each resulting particle should be distributed over two adjacent cells with energies of the particles  $\epsilon_{\omega_k}, \epsilon_{\omega_{k+1}}$  ( $\epsilon_{\omega_k} \leq \epsilon_k^* < \epsilon_{\omega_{k+1}}$ ) and  $\epsilon_{\omega_l}, \epsilon_{\omega_{l+1}}$  ( $\epsilon_{\omega_l} \leq \epsilon_l^* < \epsilon_{\omega_{l+1}}$ ) correspondingly for  $k$ -th and  $l$ -th particle. We ensure correct number of particles involved in the reaction and energy conservation implementing the following condition

$$\dot{Y}_{\omega_i} + \dot{Y}_{\omega_{i+1}} = \dot{Y}_i, \quad (\text{A.7.24}) \\ \epsilon_{\omega_i} \dot{Y}_{\omega_i} + \epsilon_{\omega_{i+1}} \dot{Y}_{\omega_{i+1}} = \epsilon_i^* \dot{Y}_i,$$

where index  $i$  states for  $k$  and  $l$ . Introducing coefficients  $c_{\omega_i}, c_{\omega_{i+1}}$  so that

$$\dot{Y}_{\omega_i} = c_{\omega_i} \dot{Y}_i, \quad (\text{A.7.25})$$

we get

$$c_{\omega_i} + c_{\omega_{i+1}} = 1, \quad (\text{A.7.26})$$

$$\epsilon_{\omega_i} c_{\omega_i} + \epsilon_{\omega_{i+1}} c_{\omega_{i+1}} = \epsilon_i^*, \quad (\text{A.7.27})$$

with explicit solution

$$c_{\omega_{i+1}} = \frac{\epsilon_i^* - \epsilon_{\omega_i}}{\epsilon_{\omega_{i+1}} - \epsilon_{\omega_i}}, \quad c_{\omega_i} = \frac{\epsilon_{\omega_{i+1}} - \epsilon_i^*}{\epsilon_{\omega_{i+1}} - \epsilon_{\omega_i}}. \quad (\text{A.7.28})$$

Redistribution of final particles affects also the Bose enhancement/Pauli blocking coefficients. There is a problem, however, arising from attempt to introduce an interpolation of these coefficients, that we illustrate by an example. Let us take a fermion in final state, that should be redistributed into two adjacent cells, when one of these cells is completely full of particles, other being empty. Any interpolation of Pauli blocking between these cells will not suppress completely addition of particles to the full cell, providing there unphysical density and instability in the numerical scheme. Similar problem arise for Bose enhancement, especially in the regions of the phase space with steep gradients of distribution function.

To solve the problem mentioned above we introduce the Bose enhancement/Pauli blocking coefficient in the following way ( $i = k, l$ )

$$\left[ 1 \pm \frac{Y_i(t)}{G_i} \right] = \min \left( 1 \pm \frac{Y_{\omega_i}(t)}{G_{\omega_i}}, 1 \pm \frac{Y_{\omega_{i+1}}(t)}{G_{\omega_{i+1}}} \right), \quad (\text{A.7.29})$$

decreasing resolution of the coefficients, but preventing unphysical densities and numerical problems.

Extension of the scheme to many-particle interactions is straightforward. The only aspect not covered in the papers Aksenov et al. (2007, 2009, 2010) is the exact correspondence between collision integrals and dimensionless matrix element for three-particle interactions, given for double Compton scattering in Mandl and Skyrme (1952) and for bremsstrahlung in Haug and Nakel (2004).

For a three-particle interaction (A.6.1) and (A.6.2) we have an integral for absorption of  $a$ -th particle

$$\begin{aligned} \dot{f}(\mathbf{p}_a, t) d^3 \mathbf{p}_a &= - \int d^{15} \mathbf{q} W_{(\alpha_a, \beta_b | \nu_i, \kappa_k, \lambda_l)} \times \\ &\times f_\alpha(\mathbf{p}_a, t) f_\beta(\mathbf{p}_b, t) \times \left[ 1 \pm \frac{f_i(\mathbf{p}_i, t)}{g_i h^{-3}} \right] \left[ 1 \pm \frac{f_\kappa(\mathbf{p}_k, t)}{g_\kappa h^{-3}} \right] \left[ 1 \pm \frac{f_\lambda(\mathbf{p}_l, t)}{g_\lambda h^{-3}} \right], \end{aligned} \quad (\text{A.7.30})$$

where now

$$d^{15}\mathbf{q} = d^3\mathbf{p}_a d^3\mathbf{p}_b d^3\mathbf{p}_i d^3\mathbf{p}_k d^3\mathbf{p}_l. \quad (\text{A.7.31})$$

Taking into account relation between transition function  $W$  and differential cross-section  $d\sigma$ , see, e.g., Appendix H of Aksenov et al. (2009)

$$W_{(\alpha_a, \beta_b | \iota_i, \kappa_k, \lambda_l)} d^3\mathbf{p}_i d^3\mathbf{p}_k d^3\mathbf{p}_l \equiv c \frac{\sqrt{(\epsilon_a \epsilon_b - \mathbf{p}_a \mathbf{p}_b c^2)^2 - (m_a m_b c^4)^2}}{\epsilon_a \epsilon_b} d\sigma, \quad (\text{A.7.32})$$

which in the rest frame of particle  $a$  or  $b$  reduces to

$$W_{(\alpha_a, \beta_b | \iota_i, \kappa_k, \lambda_l)} d^3\mathbf{p}_i d^3\mathbf{p}_k d^3\mathbf{p}_l = |\mathbf{v}_{rel}| d\sigma, \quad (\text{A.7.33})$$

where  $\mathbf{v}_{rel}$  is the relative velocity of these particles, we obtain from known differential cross-section (4-momentum  $\mathbf{p} = (\epsilon, c\mathbf{p})$  is taken in energetic units)

$$\begin{aligned} W_{(\alpha_a, \beta_b | \iota_i, \kappa_k, \lambda_l)} &= \frac{\sqrt{(\epsilon_a \epsilon_b - \mathbf{p}_a \mathbf{p}_b c^2)^2 - (m_a m_b c^4)^2}}{\epsilon_a \epsilon_b} \frac{\alpha r_e^2}{(4\pi)^2} \times \\ &\quad \times \frac{c^8 X}{|\epsilon_a \epsilon_b / c^2 - \mathbf{p}_a \mathbf{p}_b | \epsilon_i \epsilon_k \epsilon_l} \delta^4(\mathbf{p}_{initial} - \mathbf{p}_{final}) = \\ &= \frac{\alpha r_e^2}{(4\pi)^2} \times \frac{c^7 X}{\epsilon_a \epsilon_b \epsilon_i \epsilon_k \epsilon_l} \delta(\epsilon_{initial} - \epsilon_{final}) \delta^3(\mathbf{p}_{initial} - \mathbf{p}_{final}), \end{aligned} \quad (\text{A.7.34})$$

where  $\alpha$  is the fine-structure constant,  $r_e$  is the classical electron radius,  $X$  is the dimensionless matrix element of the process, given for double Compton scattering by Eqs. (3), (9), (10) of Mandl and Skyrme (1952) and for bremsstrahlung by Eqs. in Appendix B of Haug and Nakel (2004), and  $\mathbf{p}$  is 4-momentum. This expression is to be compared with (A.7.11).

Proceeding with the same route as in derivation of (A.7.22) we came to the rate of the direct reaction

$$\begin{aligned} \dot{Y}_{j,\omega}(t) &= \frac{\alpha r_e^2}{(4\pi)^2} \sum_{a,b,\mu_b,i,\mu_i,\varphi_i,\mu_k,\varphi_k} \frac{\Delta\mu_b}{2} \sqrt{\epsilon_i^2 - m_i^2 c^4} \Delta\epsilon_i \Delta\mu_i \Delta\varphi_i \times cX \times \\ &\times \frac{\Delta\mu_k \Delta\varphi_k \sqrt{(\epsilon_k^*)^2 - m_k^2 c^4}}{\epsilon_l^* [1 - \beta_l^* / \beta_k^* (\boldsymbol{\mu}_k \cdot \boldsymbol{\mu}_l^*)]} \times \frac{Y_a(t)}{\epsilon_a} \frac{Y_b(t)}{\epsilon_b} \times \left[ 1 \pm \frac{Y_i(t)}{G_i} \right] \left[ 1 \pm \frac{Y_k(t)}{G_k} \right] \left[ 1 \pm \frac{Y_l(t)}{G_l} \right]. \end{aligned} \quad (\text{A.7.35})$$

Applying principle of detailed equilibrium to the reaction (A.6.1) and its inverse (A.6.2), we get for inverse reaction transition function

$$W_{(\iota_i, \kappa_k, \lambda_l | \alpha_a, \beta_b)} = W_{(\alpha_a, \beta_b | \iota_i, \kappa_k, \lambda_l)} \frac{g_a g_b h^3}{g_i g_k g_l}, \quad (\text{A.7.36})$$

and, as all  $g$  are equal to 2 in our case, exchanging  $a \leftrightarrow i$ ,  $b \leftrightarrow k$  and using (A.7.21), we have

$$\begin{aligned} \dot{Y}_{j,\omega}(t) = & \frac{\alpha r_e^2 h^3 c^3}{(4\pi)^2 2} \sum_{i,k,\mu_k,l,\mu_l,\varphi_l,\mu_a,\varphi_a} \frac{\Delta\mu_k}{2} \frac{\Delta\mu_l}{2} \frac{\Delta\varphi_l}{2\pi} \times cX \times \\ & \times \frac{\Delta\mu_a \Delta\varphi_a \sqrt{(\epsilon_a^*)^2 - m_a^2 c^4}}{\epsilon_b^* [1 - \beta_b^* / \beta_a^* (\boldsymbol{\mu}_a \cdot \boldsymbol{\mu}_b^*)]} \times \frac{Y_i(t)}{\epsilon_i} \frac{Y_k(t)}{\epsilon_k} \frac{Y_l(t)}{\epsilon_l} \times \left[ 1 \pm \frac{Y_a(t)}{G_a} \right] \left[ 1 \pm \frac{Y_b(t)}{G_b} \right]. \end{aligned} \quad (\text{A.7.37})$$

## A.8. Characteristic time scales of plasma relaxation

We solved numerically Boltzmann equation (A.4.1) in two cases. Initially only photons are present with constant spectral energy density and total energy density  $\rho = 10^{23}$  erg/cm<sup>3</sup> and  $\rho = 10^{29}$  erg/cm<sup>3</sup>. Such energy densities corresponds to the temperature  $\theta$  in thermal equilibrium of 0.3 and 8, respectively.

In Figs. A.2 and A.3 we present number density, energy density, temperature and chemical potential of photons and pairs in both cases. We also show the difference between quantum and Boltzmann statistics by including and omitting the Pauli blocking and Bose enhancement factors in evolution equations (A.7.9). Time is expressed in units of Compton time

$$\tau_C = \frac{1}{\sigma_T n_{\pm} c}, \quad (\text{A.8.1})$$

where  $n_{\pm}$  is number density of pairs in thermal equilibrium,  $\sigma_T$  is Thomson cross section.

Timescales of relaxation to thermal equilibrium for quantum (classical) statistics nearly coincide:  $15\tau_C$  ( $18\tau_C$ ) for  $\rho = 10^{23}$  erg/cm<sup>3</sup>, and  $27\tau_C$  ( $23\tau_C$ ) for  $\rho = 10^{29}$  erg/cm<sup>3</sup>. Inspection of Figs. A.2 and A.3 indicates that both temperatures and chemical potentials of leptonic and photon components become nearly equal when the total number density of particles shown by blue curves is almost constant. This fact indicates that three-particle interactions become relevant when almost detailed balance (kinetic equilibrium) is established by two-particle interactions Aksenov et al. (2007). Notice, however, that due to energy dependence of reaction rates the characteristic timescale on which kinetic equilibrium is established is larger than Compton time (A.8.1). For the same reason the characteristic timescale on which thermal equilibrium is established is smaller than the simple estimate  $\alpha^{-1}\tau_C$ . Thus the ratio of the timescales of kinetic and thermal equilibrium is no longer  $\alpha$  but higher. This fact shows why the exact treatment of three-particle interactions, espe-

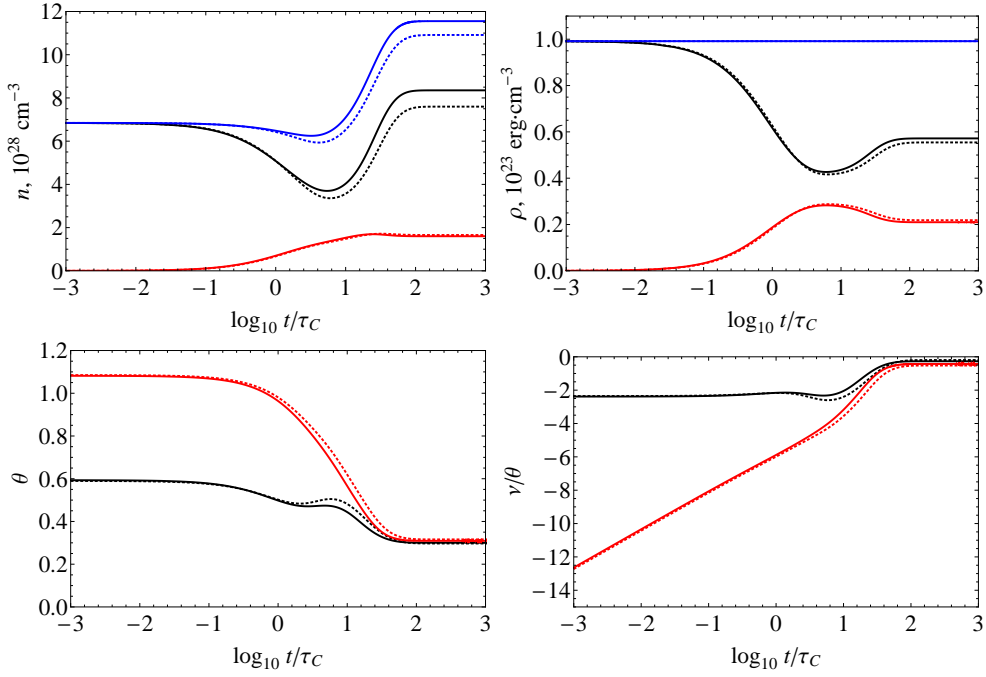


**Figure A.2.:** Comparison of evolution of number  $n$  and energy  $\rho$  densities, dimensionless temperature  $\theta$ , chemical potential  $\xi$ , for quantum (solid curves) and classical (dotted curves) statistics with total energy density  $\rho = 10^{23}$  erg/cm<sup>3</sup>. Black and red curves correspond to photons and pairs, respectively, blue curve gives the sum of densities.

cially for high energy densities, becomes important.

In Figs. A.4 and A.5 we show spectral evolution for both our initial conditions. The final spectra shown for  $t = 10^3 \tau_C$  are in good agreement with Planck/Fermi-Dirac distribution functions, correspondingly, obtained for the given energy density, typically within 5 % accuracy. Notice that at the Compton time both electron/positron and photon spectra are far from equilibrium shape, with the only exception of leptonic spectrum for  $\rho = 10^{23}$  erg/cm<sup>3</sup>. This quick relaxation of leptonic component is due to large Coulomb logarithm for non-relativistic temperatures.

## A.9. Conclusions

In this work we consider relaxation of nonequilibrium optically thick pair plasma to complete thermal equilibrium by integrating numerically relativistic Boltzmann equations with exact QED two-particle and three-particle collision integrals. Quantum nature of particle statistics is accounted for in collision integrals by the corresponding Bose enhancement and Pauli blocking

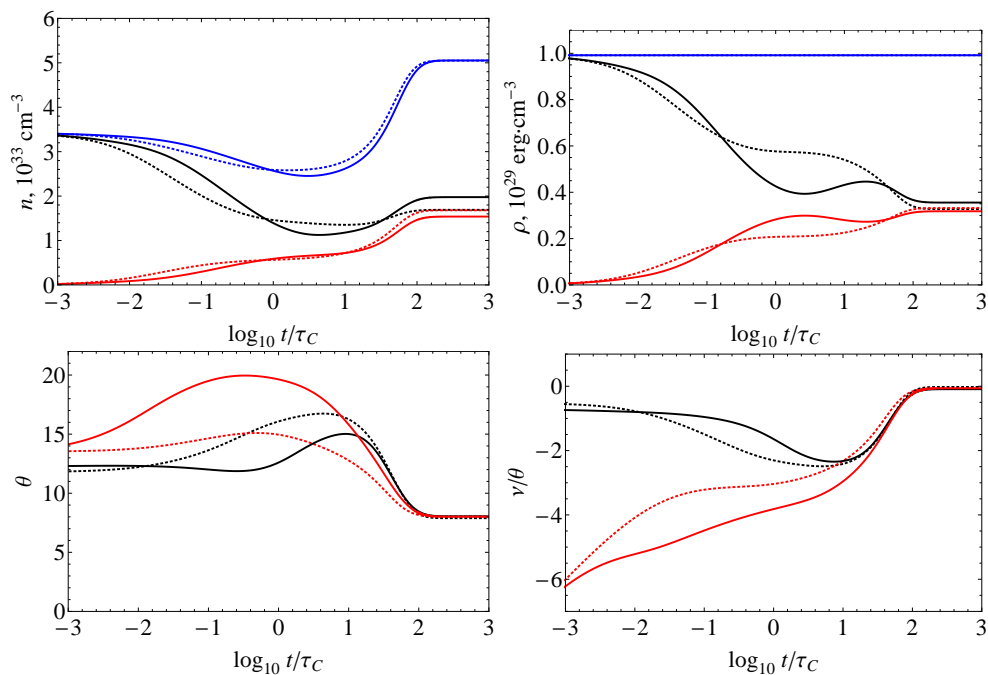


**Figure A.3.:** The same as in Fig. A.2, but for total energy density  $\rho = 10^{29}$  erg/cm<sup>3</sup>.

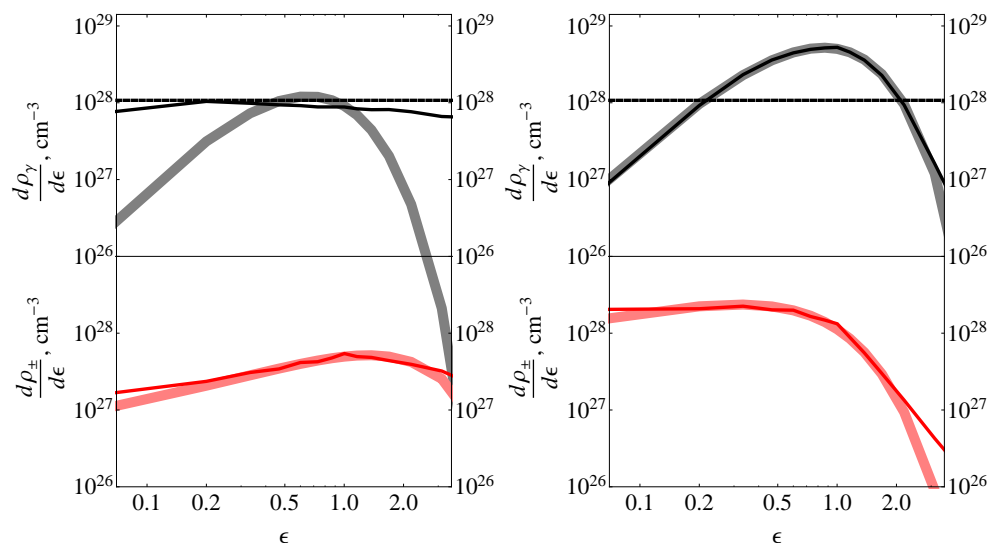


**Figure A.4.:** Numerical spectral energy densities of photons (black line) and pairs (red line) at  $t = \tau_C$  (left) and at  $t = 10^3 \tau_C$  (right) for  $\rho = 10^{23}$  erg/cm<sup>3</sup>. Thick curves show the corresponding Bose-Einstein and Fermi-Dirac distributions with the same number and energy densities, respectively. Dashed thin line shows initial photon spectrum.

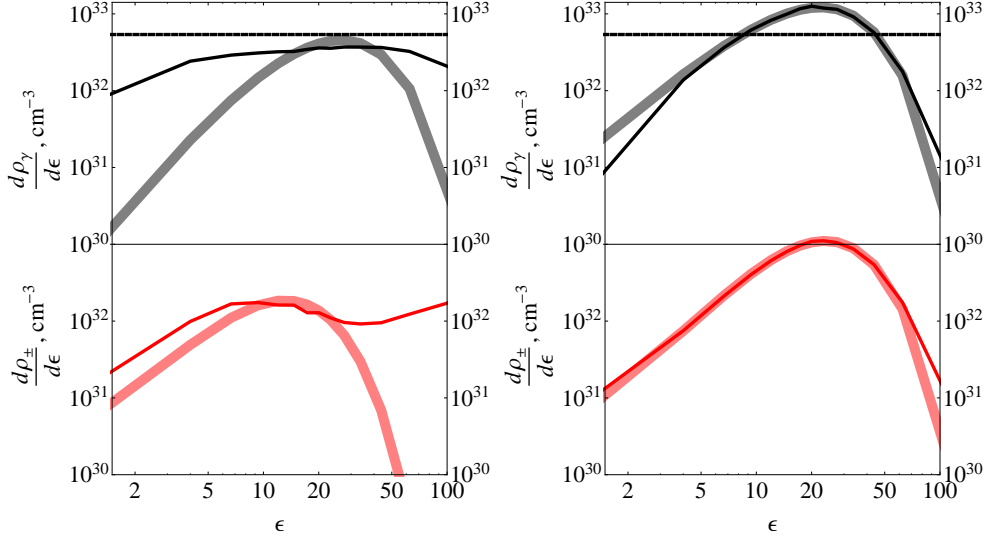


**Figure A.5.:** The same as in Fig. A.4 for  $\rho = 10^{29}$  erg/cm<sup>3</sup>.

factors.

We point out that unlike classical Boltzmann equation for binary interactions such as scattering, more general interactions are typically described by four collision integrals for each particle that appears both among incoming and outgoing particles.

Our numerical results indicate that the rates of three-particle interactions become comparable to those of two-particle ones for temperatures exceeding the electron rest-mass energy. Thus three particle interactions such as relativistic bremsstrahlung, double Compton scattering and radiative pair creation become essential not only for establishment of thermal equilibrium, but also for correct estimation of interaction rates, energy losses etc.

# B. Dynamics and emission of mildly relativistic plasma

## B.1. Introduction

Electron-positron plasma are expected to be present in compact astrophysical objects (Damour and Ruffini, 1975), (Alcock et al., 1986), (Usov, 1998) and plays crucial role in the Gamma-Ray Burst (GRB) phenomenon (Ruffini et al., 2009b), (Ruffini et al., 2010). Electron-positron pairs are detected in the center of our Galaxy (Churazov et al., 2005), leaving their characteristic imprint in the observed radiation spectra. The observed annihilation line 511 keV near the Earth indicates that pair plasma can be created in the upper atmosphere at the thunderstorm (Briggs et al., 2011). Also interest in electron-positron plasmas is due to the exciting possibility of generating such plasmas in laboratory facilities using ultraintense focused short laser pulses, (Ruffini et al., 2010; Blaschke et al., 2006; Myatt et al., 2009; Thoma, 2009; Chen et al., 2009; Wilks et al., 1992).

Electrons-positron plasmas in the laboratory experiment or in thunderstorms have low density and are consequently optically thin (Mustafa and Kämpfer, 2009; Katz, 2000). In contrast, in GRB source pair plasma is dense and optically thick (Ruffini et al., 2009b; Goodman, 1986; Piran, 1999). Such optically thick plasma is expected to expand, cool down and eventually become transparent for radiation, producing the characteristic flash of quasi-thermal radiation, the so called photospheric emission. Many recent works are devoted to study of this phenomenon, see e.g. (Beloborodov, 2011), (Pe'er and Ryde, 2011), (Toma et al., 2011).

For the simulation of the photospheric emission of expanding plasma one can use suitable Monte Carlo techniques based on well known reaction rates (Bisnovatyi-Kogan et al., 1971; Lightman, 1982; Svensson, 1982; Guilbert and Stepney, 1985). While in the optically thick case usually hydrodynamic approach is postulated (Piran, 1999). Such approximation is justified for large optical depth, or in the beginning of expansion. Due to complexity of the calculations only very few works adopt the kinetic approach for the description of the plasma and try to calculate the spectra when the optical depth is not very far from one (Beloborodov, 2010).

In this paper we report on our study of mildly relativistic plasma, which is initially optically thick. The description of plasma is based on relativistic

Boltzmann equations. By means of this instrument we verify the application of hydrodynamic description of the plasma. We focus on the difference between the hydrodynamic description and more detailed kinetic one. In particular, we consider the optical depth, the number density and average particle energy evolution with time. We also report photon spectra from this expanding electron-positron plasma, which allows us to describe the photospheric emission in great details.

## B.2. Formulation of the problem

**Table B.1.:** Physical Processes Included in Simulations.

| Binary interactions  | Radiative and pair producing variants   |
|--|---|
| Møller and Bhabha scattering<br>$e_1^\pm e_2^\pm \longrightarrow e_1^{\pm'} e_2^{\pm'}$<br>$e^\pm e^\mp \longrightarrow e^{\pm'} e^{\mp'}$ | Bremsstrahlung<br>$e_1^\pm e_2^\pm \longleftrightarrow e_1^{\pm'} e_2^{\pm'} \gamma$<br>$e^\pm e^\mp \longleftrightarrow e^{\pm'} e^{\mp'} \gamma$                                |
| Single Compton scattering<br>$e^\pm \gamma \longrightarrow e^\pm \gamma'$  | Double Compton scattering<br>$e^\pm \gamma \longleftrightarrow e^{\pm'} \gamma' \gamma''$   |
| Pair production and annihilation<br>$\gamma \gamma' \longleftrightarrow e^\pm e^\mp$   | Radiative pair production and three photon annihilation<br>$\gamma \gamma' \longleftrightarrow e^\pm e^\mp \gamma''$<br>$e^\pm e^\mp \longleftrightarrow \gamma \gamma' \gamma''$ |
|  | $e^\pm \gamma \longleftrightarrow e^{\pm'} e^{\mp'} e^{\pm''}$  |

We use the relativistic Boltzmann equations for the  $e^\pm$  pairs and photons. The distribution function for the particles of type  $i$ ,  $f_i(|\mathbf{p}|, \mu, r, t)$  ( $i = e^\pm, \gamma$ ), satisfies (Mihalas and Mihalas, 1984)

$$\frac{1}{c} \frac{\partial f_i}{\partial t} + \beta_i \left( \mu \frac{\partial f_i}{\partial r} + \frac{1 - \mu^2}{r} \frac{\partial f_i}{\partial \mu} \right) = \sum_q (\tilde{\eta}_i^q - \chi_i^q f_i), \quad (\text{B.2.1})$$

where  $\mu = (\mathbf{r}\mathbf{p})/(|\mathbf{r}||\mathbf{p}|)$ ,  $\beta_i = v_i/c = \sqrt{1 - (m_i c^2/\epsilon_i)^2}$ ,  $\epsilon_i = c\sqrt{p^2 + (m_i c^2)^2}$ .  $\tilde{\eta}_i^q$  is the emission coefficient for the production of a particle of type  $i$  via the physical process by  $q$ , and  $\chi_i^q$  is the corresponding absorption coefficient. The summation runs over all considered physical processes that involve a particle of type  $i$ . We take into account all two-body interactions, see e.g. Berestetskii et al. (1982), Greiner and Reinhardt (2003), and corresponding triple interactions (Svensson, 1984) written in Table B.1.

The particle concentrations and energy densities are

$$n_i(r, t) = \int f_i(\mathbf{p}, r, t) d\mathbf{p}, \quad \rho_i(r, t) = \int f_i(\mathbf{p}, r, t) \epsilon d\mathbf{p}. \quad (\text{B.2.2})$$

For the GRB source plasma, for example, the corresponding temperatures in thermal equilibrium are (Aksenov et al., 2007)

$$0.1 \leq T_{th} \leq 10 \text{ MeV}. \quad (\text{B.2.3})$$

At such conditions the number of particles in Debye sphere is large. We can use one-particle distributions functions. Another important property is that such pair plasma can not generate additional particles like neutrinos.

### B.3. Computational method

To make the scheme conservative we use, instead of  $f_i$ , the spectral energy densities

$$E_i(\epsilon_i, \mu, r, t) = \frac{2\pi\epsilon_i^3 \beta_i f_i}{c^3}, \quad (\text{B.3.1})$$

because the energy density in our phase space  $(\epsilon, \mu, r, t)$  is

$$\epsilon_i f_i d\mathbf{r} d\mathbf{p} = \frac{2\pi\epsilon^3 \beta_i f_i}{c^3} \mathbf{r} d\epsilon_i d\mu = E_i \mathbf{r} d\epsilon_i d\mu. \quad (\text{B.3.2})$$

For  $E_i$  the Boltzmann equation has the conservative form

$$\frac{1}{c} \frac{\partial E_i}{\partial t} + \frac{\mu}{r^2} \frac{\partial}{\partial r} (r^2 \beta_i E_i) + \frac{1}{r} \frac{\partial}{\partial \mu} [(1 - \mu^2) \beta_i E_i] = \sum_q (\eta_i^q - \chi_i^q f_i). \quad (\text{B.3.3})$$

We use the lines method to solve above task (Aksenov et al., 2004). We introduced grid in phase space  $\epsilon_{\omega+1/2}$ ,  $\mu_{k+1/2}$ ,  $r_{j+1/2}$ . After the replacing of all derivatives except the derivative over time in Eq. (B.3.3) by finite differences (Aksenov et al., 2004) and collisional integrals by sums (Aksenov et al., 2009) we have the set of ordinary differential equations for grid values

$$E_{i,\omega,k,j} \equiv \frac{\int_{\Delta\epsilon_\omega \Delta\mu_k \Delta(r_j^3/3)} d\epsilon d\mu d(r^3/3) E_i(\epsilon, \mu, r)}{\Delta\epsilon_\omega \Delta\mu_k \Delta(r_j^3/3)}. \quad (\text{B.3.4})$$

To carry out numerical evolution in the optically thick regions we use implicit Gear's method to solve the stiff system of ordinary differential equations (Hall and Watt, 1976).

We evaluate numerically exact expressions for collisional integrals with matrix elements from QED (Aksenov et al., 2009). Our investigations shows the timescale of triple interaction is  $\alpha^{-1} \simeq 137$  times larger, compared to the timescale of binary interactions. Consequently plasma reaches so called kinetic equilibrium with the common temperature but nonnull chemical potentials before triple interactions become important. This fact allows us to

simplify calculations of triple interactions in the nondegenerate cases as described in Aksenov et al. (2009).

For very large optical depths reactions rates cannot be resolved with a rough angle grid. For this reason we adopt the following method for computing reaction rates in a such region  $\tau \gg 1$ . First we compute hydrodynamic velocity  $\beta$  from the known distribution functions, and transform our quantities in the comoving frame by using the following Lorentz transformations, see e.g. Mihalas and Mihalas (1984), p. 414

$$(\epsilon, \mu, \phi, r, t) = \left( \Gamma \left( \epsilon' + \frac{V}{c} c p' \mu' \right), \frac{p' \mu' + \frac{V}{c} \frac{\epsilon'}{c}}{\sqrt{\left( \frac{\epsilon'}{c} + \frac{V}{c} p' \mu' \right)^2 - \frac{m^2 c^2}{\Gamma^2}}}, \phi', r', t' \right).$$

Then we calculate average values  $n'_i$  in the comoving frame, which do not depend on angles. Then in comoving frame we evaluate average absorption coefficients  $\chi' = \text{const}$ . The emission coefficients  $\eta'$  in the comoving frame are taken to be proportional to equilibrium intensities. Finally we transform the emission and absorption coefficients back into the laboratory frame by

$$I(\epsilon, \mu) = \frac{\epsilon^2 p}{\epsilon'^2 p'} I'(\epsilon', \mu'), \quad E(\epsilon, \mu, r, t) \equiv \frac{2\pi \epsilon^3 \beta f}{c^3} \propto I,$$

$$\eta(\epsilon, \mu) = \frac{\epsilon p}{\epsilon' p'} \eta'(\epsilon', \mu'), \quad \chi(\epsilon, \mu) = \frac{\epsilon'}{\epsilon} \chi'(\epsilon', \mu'),$$

also preserving exact energy and momentum conservation on the finite grid.

## B.4. Results

We consider kinetic evolution of nonequilibrium optically thick plasma consisting at the moment  $t = 0$  of electron-positron pairs with number density  $n = 10^{30} \text{ cm}^{-3}$  in the small region with radius  $R_0 = 200 \text{ cm}$ . Although such parameters are far from both laboratory conditions and the real GRB sources, we consider this choice of parameters important since it provides some new insights with respect to the traditional hydrodynamic description (Goodman, 1986), (Piran et al., 1993), (Mészáros et al., 1993), (Mustafa and Kämpfer, 2009), (Yaresko et al., 2010). Figs. B.1–B.5 show the plasma evolution with time, and Fig. B.6 shows spectra of photons near the maximum of emission at  $t = 7 \cdot 10^{-7} \text{ sec}$ , crossing the sphere with radius  $2.2 \cdot 10^4 \text{ cm}$ .

Initially nonequilibrium plasma relaxes to the thermal state on the timescale  $5 \cdot 10^{-11} \text{ sec}$ , and it starts to expand, on the dynamical timecale  $R_0/c \simeq 6 \cdot 10^{-9} \text{ sec}$ , see Fig. B.3. The concentrations (Fig. B.2) and the optical

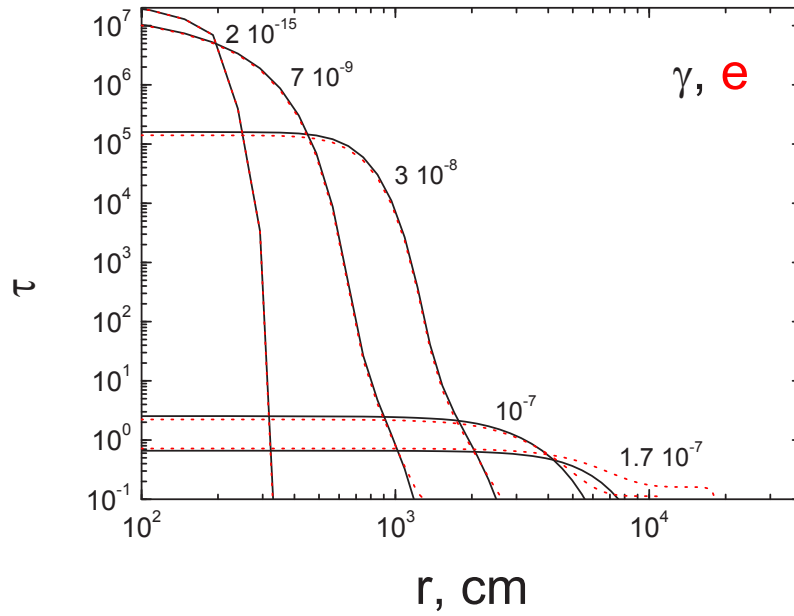


**Figure B.1.:** Mean optical depth for photons (solid) and pairs (dashed) as a function of the radius at different time moments, as marked on the curves.

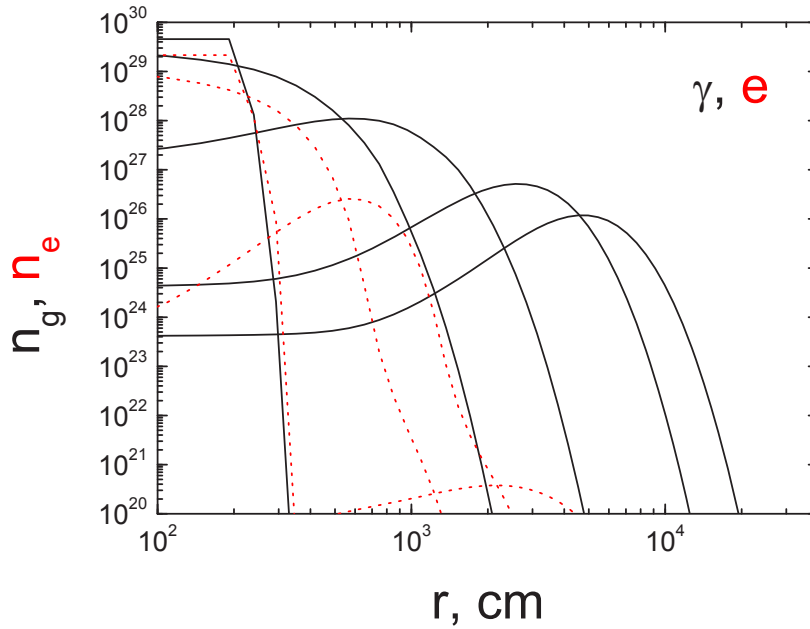


**Figure B.2.:** Photon number density (solid) and pair number density (dashed) as a function of the radius at different time moments, as in Fig. B.1.

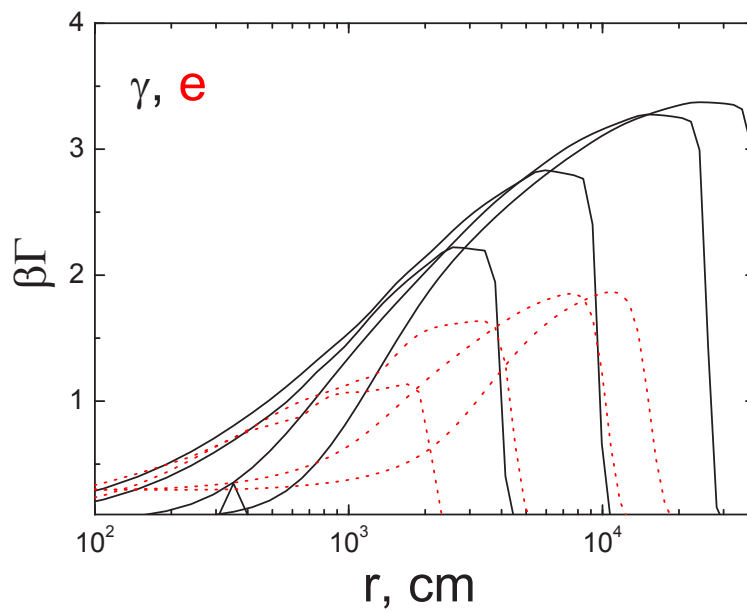


**Figure B.3.:** Photon (solid) and pair (dashed) radial velocity as a function of the radius at different time moments, as in Fig. B.1.

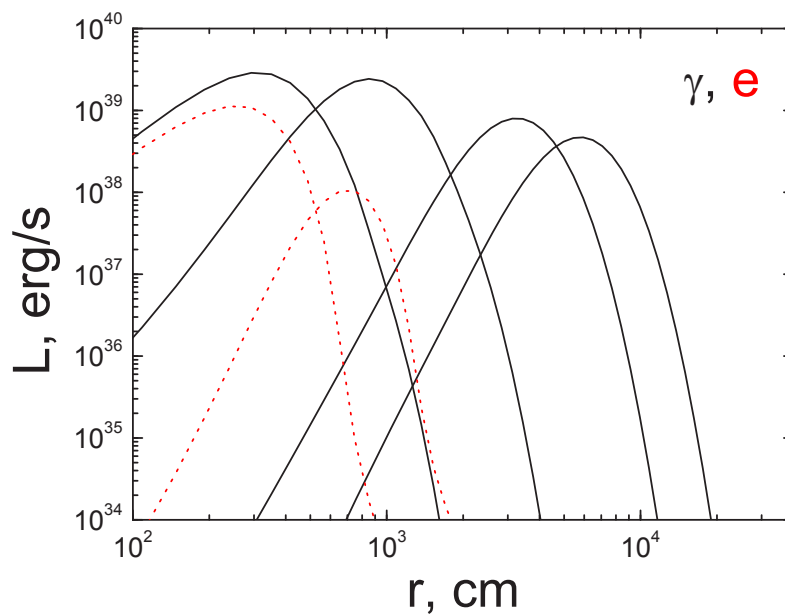


**Figure B.4.:** Rates of energy flow in photons (solid), in pairs (dashed) through the surface at radius  $r$  as a function of the radius at different time moments, as in Fig. B.1.

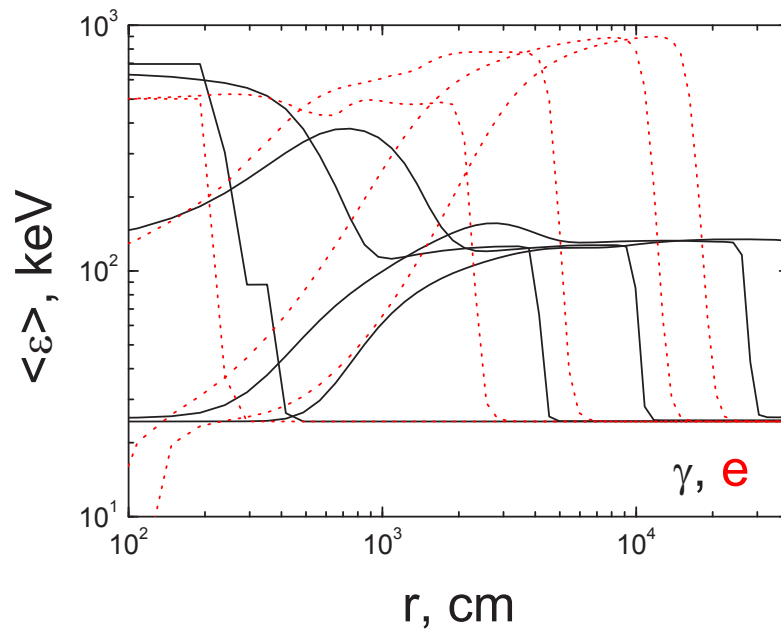


**Figure B.5.:** Average energy of photons (solid) and of pairs (dashed) as a function of the radius at different time moments, as in Fig. B.1.

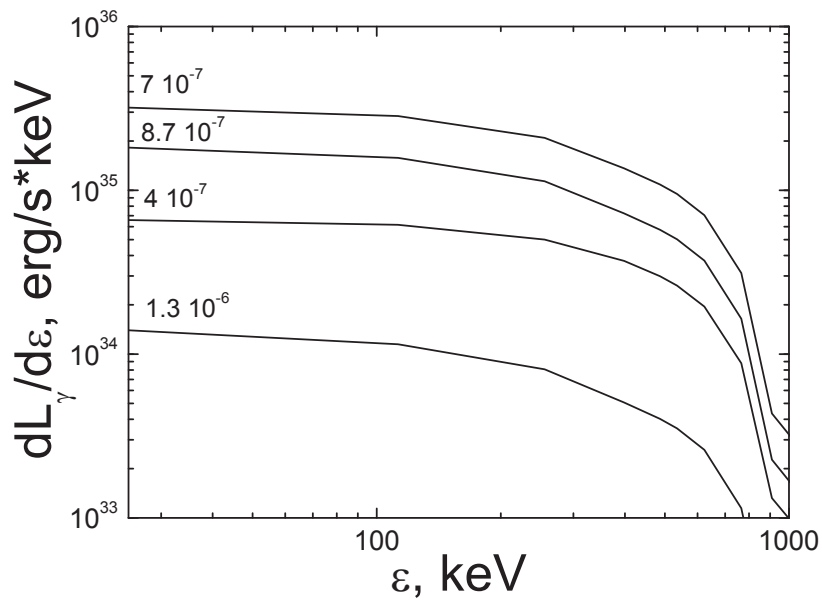


**Figure B.6.:** Energy spectrum of emerging photons in the laboratory reference frame, at the radius  $2.2 \cdot 10^4$  cm at selected time moments near the maximum luminosity.

depths of both electrons/positrons and photons (Fig. B.1) decrease with time. As the temperature becomes smaller than  $m_e c^2$  the energy density in pairs starts to decrease exponentially, since they remain in thermal equilibrium. When the optical depth of photons is large, we find hydrodynamic description accurate enough to calculate the photons spectra. At  $t = 1.5 \cdot 10^{-7}$  sec the optical depth for photons decreases below unity, see Fig. B.1. After this moment the radial distribution of photons in the expanding shell becomes fixed, see Fig. B.4. The average energy shown in Fig. B.5 indicates that the peak of the photon spectrum is in the range 10 – 1000 keV. Photon spectra around the maximal luminosity are nonthermal, see Fig. B.6. They possess an exponential cut-off at high energy, and the spectral energy density is almost flat in its low energy part. This result may be an explanation of additional power in low energy spectra observed in GRBs (Patricelli et al., 2011).

## **B.5. Conclusions and future perspectives**

In this work we obtained for the first time the detailed kinetic information including photon spectra from initially optically thick outflow, composed of electron-positron pairs and photons. Initial conditions are selected in the intermediate region between conditions which are expected to be reached in laboratory experiments, and those thought to occur in astrophysical settings. This allows us to study the radial self-acceleration of electron-positron plasma up to mildly relativistic velocities. We found that photon spectra near the peak of the luminosity are non-thermal, they possess an exponential cut-off at high energy, and are almost flat in the low energy part. This result may shed some light on the issue why GRBs have nonthermal spectra, and in particular why the low energy part of the spectrum contains more power with respect to Planck spectrum. We hope to extend our analysis for ultra-relativistic case which is necessary to be explored for realistic description of Gamma-Ray Bursts phenomenon.

# C. Evolution of the pair plasma generated by a strong electric field

## Introduction

Quantum electrodynamics predicts that vacuum breakdown in a strong electric field  $E$  comparable to the critical value  $E_c = m_e^2 c^3 / e \hbar$  where  $m_e$  is the electron mass,  $e$  is its charge,  $c$  is the speed of light and  $\hbar$  is the Planck constant results in non-perturbative electron-positron pair production Sauter (1931); Heisenberg and Euler (1935); Schwinger (1951). Nonlinear effects in high intensity fields can be observed already in undercritical electric field, see e.g. Bula et al. (1996); Burke et al. (1997). Considerable effort has been made over last two decades in increasing the intensity of high power lasers in order to explore these high field regimes. Yet, the Schwinger field  $E_c$  is far from being reached, see e.g. for recent review Di Piazza et al. (2012). There are indications that such technology is limited to undercritical fields due to occurrence of avalanches Bell and Kirk (2008); Bulanov et al. (2010) which deplete the external field faster than it can potentially grow. Some authors Fedotov et al. (2010) went that far as to claim that “the critical QED field strength can be never attained for a pair creating electromagnetic field”.

While dynamical mechanisms involving increase of initially small electric field toward its critical value appear problematic because of avalanches, existence of overcritical electric field in which pair production is blocked Usov (1998) is widely discussed in astrophysical context in compact stars, e.g. hypothetical quark stars Alcock et al. (1986); Usov (1998), neutron stars Belvedere et al. (2012), see also Ruffini et al. (2010) for review. Pair production in such overcritical field may occur due to several reasons, e.g. heating Usov (2001) or gravitational collapse of the compact object. Assuming existence of such overcritical electric field in this paper we revisit the issue of conversion of energy from initial electric field into electron-positron plasma once the blocking is released.

The most general framework for considering the problem of back reaction of created matter fields on initial strong electric field is QED. Up to now the problem has been treated in QED in 1+1 dimension case for both scalar Kluger et al. (1991) and fermion Kluger et al. (1992) fields. It was shown

there that pair creation is followed by plasma oscillations due to back reaction of pairs on initial electric field. The results were compared with the solutions of the relativistic Vlasov-Boltzmann equations and shown to agree very well. The Vlasov type kinetic equation for description of  $e^+e^-$  plasma creation under the action of a strong electric field was used previously e.g. in the following works Kajantie and Matsui (1985); Smolyansky et al. (1997); Schmidt et al. (1998). The back reaction problem in this framework was considered by Gatoff et al. (1987); Kluger et al. (1998). The kinetic theory to description of the vacuum quark creation under action of a supercritical chromo-electromagnetic field was applied by Bloch et al. (1999); Vinnik et al. (2001). Kinetic equations for electron-positron-photon plasma in strong electric field were obtained in Blaschke et al. (2011) from the Bogoliubov-Born-Green-Kirkwood-Yvon hierarchy.

Much simpler model was developed later, starting from Vlasov-Boltzmann equations Ruffini et al. (2003b) and assuming that all particles are in the same momentum state at a given time, that allowed to consider pair-photon interactions. In this way the system of partial integro-differential equations was reduced to the system of ordinary differential equations which was integrated numerically. This model was studied in details in Ruffini et al. (2007); Benedetti et al. (2011), where existence of plasma oscillations was confirmed and extended to undercritical electric fields. It was also shown that photons are generated and reach equipartition with pairs on a time scale much longer than the oscillation period.

In this work for the first time we study the entire dynamics of energy conversion from initial strong electric field, ending up with thermalized electron-positron-photon plasma which is assumed to be optically thick. With this goal we generalize previous treatments Kluger et al. (1991)-Benedetti et al. (2011). In particular, we relax the delta-function approximation of particle momenta adopted in Ruffini et al. (2003b). In contrast, we obtain the system of partial integro-differential equations which is solved numerically on large timescales, exceeding many orders of magnitude several characteristic timescales of the problem under consideration.

We adopt a kinetic approach in which collisions can be naturally described, assuming invariance under rotations around the direction of the electric field. In this perspective we solve numerically the relativistic Vlasov-Boltzmann equations with collision integrals computed from the exact QED matrix elements for the two particle interactions Aksenov et al. (2009), namely electron-positron annihilation into two photons and its inverse process, Bhabha, Möller and Compton scatterings.

The paper is organized as follows. In the next section we introduce the general framework, then we report our results. Conclusions follow. Details about the computation are presented in the Appendix.

## C.1. Framework

Based on the symmetry of the problem we consider axially symmetric momentum space. Hence, the momentum of the particle is described by two components, one parallel ( $p_{\parallel}$ ) and one orthogonal ( $p_{\perp}$ ) to the direction of the initial electric field. Then the azimuthal angle ( $\phi$ ) describes the rotation of  $p_{\perp}$  around  $p_{\parallel}$ . These momentum space coordinates are defined in the following intervals  $p_{\parallel} \in (-\infty, +\infty)$ ,  $p_{\perp} \in [0, +\infty)$ ,  $\phi \in [0, 2\pi]$ . Within the chosen phase space configuration, the prescription for the integral over the entire momentum space is  $\int d^3\mathbf{p} \rightarrow \int_0^{2\pi} d\phi \int_{-\infty}^{+\infty} dp_{\parallel} \int_0^{+\infty} dp_{\perp} p_{\perp}$  and the relativistic energy is given by the following equation

$$\epsilon = \sqrt{p_{\parallel}^2 + p_{\perp}^2 + m^2}, \quad (\text{C.1.1})$$

where  $m$  is the mass of the considered particle. In the previous equation and hereafter we set  $c = \hbar = 1$ .

In the adopted kinetic scheme the Distribution Function (DF) is the basic object we are dealing with and all the physical quantities can be extracted from it. Denoting with  $\nu$  the kind of particle, the DF  $f_{\nu}$  is commonly used in textbooks such that the corresponding number density is given by its integral over the entire momentum space

$$n_{\nu} = \int d^3\mathbf{p} f_{\nu} = 2\pi \int_{-\infty}^{+\infty} dp_{\parallel} \int_0^{+\infty} dp_{\perp} p_{\perp} f_{\nu}. \quad (\text{C.1.2})$$

Due to the assumed axial symmetry,  $f$  does not depend on  $\phi$  and consequently it is a function of the two components of the momentum only  $f_{\nu} = f_{\nu}(p_{\parallel}, p_{\perp})$ . In this paper we use  $F_{\nu} = 2\pi\epsilon f_{\nu}$  which allows to write down Boltzmann-Vlasov equations in conservative form Aksenov et al. (2004, 2009), essential for numerical computations. The energy density for each type of particle is given by its integral over the parallel and orthogonal component of the momentum

$$\rho_{\nu} = \int_{-\infty}^{+\infty} dp_{\parallel} \int_0^{+\infty} dp_{\perp} F_{\nu}. \quad (\text{C.1.3})$$

In isotropic momentum space this DF is reduced to the spectral energy density  $d\rho_{\nu}/d\epsilon$ .

The time evolution of electron and positron DFs is described by the rela-

tivistic Boltzmann-Vlasov equation

$$\begin{aligned} \frac{\partial F_{\pm}(p_{\parallel}, p_{\perp})}{\partial t} \pm e E \frac{\partial F_{\pm}(p_{\parallel}, p_{\perp})}{\partial p_{\parallel}} = \\ = \sum_q \left( \eta_{\pm}^{*q}(p_{\parallel}, p_{\perp}) - \chi_{\pm}^q(p_{\parallel}, p_{\perp}) F_{\pm}(p_{\parallel}, p_{\perp}) \right) + \\ + S(p_{\parallel}, p_{\perp}, E), \end{aligned} \quad (\text{C.1.4})$$

where  $\eta_{\pm}^{*q}$ ,  $\chi_{\pm}^q$  are the emission and absorption coefficients due to the interaction denoted by  $q$ , and the source term  $S$  is the rate of pair production. The sum over  $q$  covers all the 2-particle QED interactions considered in this work. In particular the electron-positron DFs in Eq. (C.1.4), varies due to the acceleration by the electric field, the creation of pairs due to vacuum breakdown and the interactions, see C.2.1 for details. Indeed, the Vlasov term describes the mean field produced by all particles, plus the external field. In our approach particle collisions, including Coulomb ones, are taken into account by collision terms. Particle motion between collisions is assumed to be subject to external field only, and the mean field is neglected. This is an assumption, but in dense collision dominated plasma such as the one considered in this paper this assumption is justified, see e.g. Groot et al. (1980). The rate of pair production already distributes particles in the momentum space according to Ruffini et al. (2010)

$$\begin{aligned} S(p_{\parallel}, p_{\perp}, E) = -\frac{|e E|}{m_e^3 (2\pi)^2} \epsilon p_{\perp} \times \\ \times \log \left[ 1 - \exp \left( -\frac{\pi(m_e^2 + p_{\perp}^2)}{|e E|} \right) \right] \delta(p_{\parallel}). \end{aligned} \quad (\text{C.1.5})$$

For  $E < E_c$  this rate is exponentially suppressed. Besides, Eq. (C.1.5) already indicates that pairs are produced with orthogonal momentum, up to about  $m_e (E/E_c)$  but at rest along the direction of the electric field.

The Boltzmann equation for photons is

$$\frac{\partial F_{\gamma}(p_{\parallel}, p_{\perp})}{\partial t} = \sum_q \left( \eta_{\gamma}^{*q}(p_{\parallel}, p_{\perp}) - \chi_{\gamma}^q(p_{\parallel}, p_{\perp}) F_{\gamma}(p_{\parallel}, p_{\perp}) \right), \quad (\text{C.1.6})$$

and their DF changes due to the collisions only. In more detail, photons must be produced first by annihilating pairs, then they affect the electron-positron DF through Compton scattering. Besides, also photons annihilation into electron-positron pairs becomes significant at later times. Eqs. (C.1.6) and (C.1.4) are coupled by means of the collision integrals, therefore they are a system of partial integro-differential equations that must be solved numer-

ically. Efficient method for solving such equations in optically thick case was developed in Aksenov et al. (2004) and later generalized in Aksenov et al. (2009), see C.2.2 and C.2.3 for details.

It is well known Ruffini et al. (2003b, 2007) that both acceleration and pair creation terms in Eq. (C.1.4) operate on a much shorter time-scale than interactions with photons described by collision terms in Eqs. (C.1.4) and (C.1.6). For this reasons we run two different classes of simulations, one neglecting collision integrals which is referred to as "*collisionless*" and another one including them called "*interacting*".

## C.2. Computational scheme

The discretization of the phase space is done defining a finite number of elementary volumes which are uniquely identified by triplets of integer numbers  $(i, k, l)$ . Their values run over the ranges  $\{1, 2, \dots, I - 1, I\}$ ,  $\{1, 2, \dots, K - 1, K\}$  and  $\{1, 2, \dots, L - 1, L\}$  respectively. Since we are dealing with an axially symmetric phase space with respect to the direction of the electric field, the parallel momentum is aligned with it while the orthogonal component lays on the plane orthogonal to this preferential axis. Each elementary volume encloses only one momentum vector which can be written explicitly in cylindrical coordinates as  $(p_{\parallel i}, p_{\perp k}, \phi_l)$ . The corresponding boundaries are marked by semi-integer indices  $[p_{\parallel i-1/2}, p_{\parallel i+1/2}]$ ,  $[p_{\perp k-1/2}, p_{\perp k+1/2}]$ ,  $[\phi_{l-1/2}, \phi_{l+1/2}]$ . Due to axial symmetry, the DFs do not depend on the azimuthal angle  $\phi$  and the index  $l$  will be used only to identify angles explicitly. We use also the symbol  $\nu$  which identifies the kind of particle under consideration,  $\{\gamma, -, +\}$  for photons, electrons and positrons respectively. From these definitions, the energy of a particle with mass  $m_\nu$  corresponding to the grid point  $(i, k)$  is

$$\epsilon_{\nu ik} = \sqrt{m_\nu^2 + p_{\parallel i}^2 + p_{\perp k}^2}, \quad (m_\gamma = 0, m_\pm = m_e). \quad (\text{C.2.1})$$

In this finite difference representation the distribution function has a Klimontovich form and can be seen as a sum of Dirac deltas centered on the grid points  $(i, k)$  and multiplied by the energy density of particles on the same grid point  $F_{\nu ik}$

$$F_\nu(p_{\parallel}, p_{\perp}) = \sum_{ik} \delta(p_{\parallel} - p_{\parallel i}) \delta(p_{\perp} - p_{\perp k}) F_{\nu ik}, \quad (\text{C.2.2})$$

where  $\sum_{ik} = \sum_{i=1}^I \sum_{k=1}^K$ . From the definition above and from Eq. (C.1.3) the

energy and number densities of particle  $\nu$  are given by

$$\rho_\nu = \sum_{ik} F_{\nu ik}, \quad (\text{C.2.3})$$

$$n_\nu = \sum_{ik} n_{\nu ik}, \quad (\text{C.2.4})$$

where  $n_{\nu ik} = F_{\nu ik} / \epsilon_{\nu ik}$ . Then the mean parallel momentum, its mean squared value and the mean squared value of the orthogonal momentum are

$$\langle p_{\parallel} \rangle_\nu = \frac{1}{n_\nu} \sum_{ik} n_{\nu ik} p_{\parallel i}, \quad (\text{C.2.5})$$

$$\langle p_{\parallel}^2 \rangle_\nu = \frac{1}{n_\nu} \sum_{ik} n_{\nu ik} (p_{\parallel i} - \langle p_{\parallel} \rangle_\nu)^2, \quad (\text{C.2.6})$$

$$\langle p_{\perp}^2 \rangle_\nu = \frac{1}{n_\nu} \sum_{ik} n_{\nu ik} p_{\perp k}^2. \quad (\text{C.2.7})$$

Due to axial symmetry the mean orthogonal momentum must be null identically  $\langle p_{\perp} \rangle_\nu = 0$ .

### C.2.1. Acceleration and electric field evolution

Once electrons and positrons are produced, they are accelerated by the electric field toward opposite directions. The time derivative of the electron or positron parallel momentum  $dp_{\parallel \pm}$  in the presence of an electric field  $E$  is given by the equation of motion

$$\frac{dp_{\parallel \pm}}{dt} = \pm e E, \quad (\text{C.2.8})$$

where the sign  $+$  ( $-$ ) refer to the positron (electron) and  $-e$  is the electron charge.

Numerically, we move particles from one cell to another one such that the number of particles is conserved and Eq. (C.2.8) is satisfied. Acceleration causes the changing with time of  $F_{\pm ik}$  which can written as follows

$$\frac{\partial F_{\pm ik}}{\partial p_{\parallel}} = \pm \left( \alpha_{i-1k} F_{\pm i-1k} + \alpha_{ik} F_{\pm ik} + \alpha_{i+1k} F_{\pm i+1k} \right), \quad (\text{C.2.9})$$

where the coefficients  $\alpha_{-,0,+}$  are defined below

$$\alpha_{i-1k} = \frac{\epsilon_{\pm ik}}{\epsilon_{\pm i-1k}} \frac{1}{p_{\parallel i} - p_{\parallel i-1}}, \quad (\text{C.2.10})$$

$$\alpha_{ik} = \frac{1}{p_{\parallel i} - p_{\parallel i-1}} - \frac{1}{p_{\parallel i+1} - p_{\parallel i}}, \quad (\text{C.2.11})$$

$$\alpha_{i+1k} = \frac{\epsilon_{\pm ik}}{\epsilon_{\pm i+1k}} \frac{1}{p_{\parallel i+1} - p_{\parallel i}}. \quad (\text{C.2.12})$$

Also the electric field evolves according to the Maxwell equations. Once the currents of the moving pairs are computed, the time derivative of the electric field is known. Consequently a new ordinary differential equation must be added to the system of Eqs. (C.1.4) and (C.1.6). However, due to the uniformity and homogeneity of the physical space, we can describe the electric field simply using the energy conservation law.

### C.2.2. Emission and absorption coefficients

In kinetic theory the time derivative of the DF  $f_\nu$  due to interactions between particles is generally written as Mihalas and Mihalas (1984)

$$\left. \frac{\partial f_\nu(\mathbf{p})}{\partial t} \right|_{coll} = \sum_q \left( \eta_\nu^q(\mathbf{p}) - \chi_\nu^q(\mathbf{p}) f_\nu(\mathbf{p}) \right), \quad (\text{C.2.13})$$

where  $q$  is the label of a specific 2-particle interaction. Eq. (C.2.13) represents a coupled system of partial integro-differential equations and can be rewritten as follows

$$\left. \frac{\partial F_\nu(\mathbf{p})}{\partial t} \right|_{coll} = \sum_q \left( \eta_\nu^{*q}(\mathbf{p}) - \chi_\nu^q(\mathbf{p}) F_\nu(\mathbf{p}) \right), \quad (\text{C.2.14})$$

where  $\eta_\nu^{*q} = 2\pi\epsilon p_\perp \eta_\nu^q$ . The right hand side of the previous equation contains the so called "collision integrals" used in Eqs. (C.1.4) and (C.1.6).

In order to describe how the collision integrals are computed, we write down schematically a general 2-particles interaction as

$$\begin{array}{ccccccc} 1 & 2 & \rightarrow & 3 & 4 & & \\ \mathbf{p}_1 & \mathbf{p}_2 & & \mathbf{p}_3 & \mathbf{p}_4 & & \end{array}$$

which means that particles 1 and 2 having respectively momenta  $\mathbf{p}_1$  and  $\mathbf{p}_2$  are absorbed; while in the same process particles 3 and 4 with momenta  $\mathbf{p}_3$  and  $\mathbf{p}_4$  are produced. The considered interactions are shown in Table (C.1). From the kinetic theory, the absorption and emission coefficients for the spec-

**Table C.1.:** Exemplification of the schematic interaction for each of the considered QED 2-particles interactions.

| Interaction        | 1        | 2        | 3        | 4        |
|--------------------|----------|----------|----------|----------|
| Pair Annihilation  | $e^-$    | $e^+$    | $\gamma$ | $\gamma$ |
| Pair Creation      | $\gamma$ | $\gamma$ | $e^-$    | $e^+$    |
| Compton Scattering | $e^\pm$  | $\gamma$ | $e^\pm$  | $\gamma$ |
| Bhabha Scattering  | $e^\pm$  | $e^\mp$  | $e^\pm$  | $e^\mp$  |
| Möller Scattering  | $e^\pm$  | $e^\pm$  | $e^\pm$  | $e^\pm$  |

ified process are given by

$$\chi_1(\mathbf{p}_1) f_1(\mathbf{p}_1) = \int d^3 \mathbf{p}_2 \int d^3 \mathbf{p}_3 \int d^3 \mathbf{p}_4 \times \\ \times w_{1,2,3,4} f_1(\mathbf{p}_1) f_2(\mathbf{p}_2), \quad (\text{C.2.15})$$

$$\chi_2(\mathbf{p}_2) f_2(\mathbf{p}_2) = \int d^3 \mathbf{p}_1 \int d^3 \mathbf{p}_3 \int d^3 \mathbf{p}_4 \times \\ \times w_{1,2,3,4} f_1(\mathbf{p}_1) f_2(\mathbf{p}_2), \quad (\text{C.2.16})$$

$$\eta_3(\mathbf{p}_3) = \int d^3 \mathbf{p}_1 \int d^3 \mathbf{p}_2 \int d^3 \mathbf{p}_4 \times \\ \times w_{1,2,3,4} f_1(\mathbf{p}_1) f_2(\mathbf{p}_2), \quad (\text{C.2.17})$$

$$\eta_4(\mathbf{p}_4) = \int d^3 \mathbf{p}_1 \int d^3 \mathbf{p}_2 \int d^3 \mathbf{p}_3 \times \\ \times w_{1,2,3,4} f_1(\mathbf{p}_1) f_2(\mathbf{p}_2), \quad (\text{C.2.18})$$

where the integrals must be calculated all over the phase space. The "transition rate"  $w_{1,2,3,4}$  is given by Landau and Lifshitz (1981)

$$w_{1,2,3,4} = \frac{1}{(2\pi)^2} \frac{|M_{fi}|^2}{16\epsilon_1\epsilon_2\epsilon_3\epsilon_4} \times \\ \times \delta(\epsilon_1 + \epsilon_2 - \epsilon_3 - \epsilon_4) \delta^{(3)}(\mathbf{p}_1 + \mathbf{p}_2 - \mathbf{p}_3 - \mathbf{p}_4) \quad (\text{C.2.19})$$

and it contains all the informations about the probability that such a process occurs. The Dirac Delta's are needed to satisfy the energy and momentum conservation laws.

Eqs. (C.2.15)-(C.2.18) can be discretized using the integral prescriptions

given below

$$\chi_{1i_1k_1} F_{1i_1k_1} = \int_{V_{i_1k_1}} d^3 \mathbf{p} \epsilon_{\mathbf{p}} \chi_1(\mathbf{p}) f_1(\mathbf{p}), \quad (\text{C.2.20})$$

$$\chi_{2i_2k_2} F_{2i_2k_2} = \int_{V_{i_2k_2}} d^3 \mathbf{p} \epsilon_{\mathbf{p}} \chi_2(\mathbf{p}) f_2(\mathbf{p}), \quad (\text{C.2.21})$$

$$\eta_{3i_3k_3}^* = \int_{V_{i_3k_3}} d^3 \mathbf{p} \epsilon_{\mathbf{p}} \eta_3(\mathbf{p}), \quad (\text{C.2.22})$$

$$\eta_{4i_4k_4}^* = \int_{V_{i_4k_4}} d^3 \mathbf{p} \epsilon_{\mathbf{p}} \eta_4(\mathbf{p}), \quad (\text{C.2.23})$$

where  $V_{i_nk_n}$  is the volume in the phase space which contains only the grid point with  $p_{\parallel i_n}$  and  $p_{\perp k_n}$ . It is actually a ring with inner radius  $p_{\perp k-1/2}$ , outer radius  $p_{\perp k+1/2}$  and thickness  $p_{\parallel i+1/2} - p_{\parallel i-1/2}$ . An explicit expression for the collision integrals can be obtained inserting Eqs. (C.2.15)-(C.2.18) into the corresponding Eqs. (C.2.20)-(C.2.23). Then we replace all the integrals over the entire momentum space with a sum of integrals over the elementary volumes  $V_{ik}$

$$\int d^3 \mathbf{p} \rightarrow \sum_{ik} \int_{V_{ik}} d^3 \mathbf{p}. \quad (\text{C.2.24})$$

Even if the sums are different, as well as the integrands, we have exactly the same sequence of integrals in all the emission and absorption coefficients. Due to this fact, we can now adopt the same treatment in order to simplify their expressions.

Let us note first that the interaction cross section is invariant by rotations around an arbitrary axis, therefore one angle can be fixed. In this respect we set  $\phi_1 = 0$  and the corresponding integral gives a constant factor  $2\pi$ . Dirac Deltas in the transition rate  $w_{1,2,3,4}$  are used to eliminate three integrals over  $p_{\parallel 4}, p_{\perp 4}, \phi_4$  and one integration over  $\phi_2$ . This procedure is explained in all detail in the following section where the kinematics is studied. However, as a consequence of these choices, the momentum of the particle 4 could differ with respect to those ones selected for the discrete and finite computational grid. For this reason Eq. (C.2.20) is no longer valid and must be modified. This is done "distributing" the particle 4 over three grid points such that number of particles, energy and momentum are conserved Aksenov et al. (2009). Once the correct cells are specified, we label them with letters  $a, b, c$  and consequently the indexes  $i_a, k_a, i_b, k_b, i_c, k_c$  are used to identify the corresponding momentum components on the momentum grid. Hence, Eq. (C.2.23) must be replaced with three equations

$$\eta_{4i_rk_r}^* = \int_{V_{i_rk_r}} d^3 \mathbf{p} \epsilon_{\mathbf{p}} \eta_4(\mathbf{p}), \quad r = \{a, b, c\}. \quad (\text{C.2.25})$$

The emission coefficients in the previous set must be multiplied by the relative weights  $x_a, x_b, x_c$ . In fact the time derivative of the total energy, number of particles and momentum of the system must be null identically

$$\dot{\rho} = \sum_{vik} \dot{F}_{vik} = 0, \quad (\text{C.2.26})$$

$$\dot{n} = \sum_{vik} \frac{\dot{F}_{vik}}{\epsilon_{vik}} = 0, \quad (\text{C.2.27})$$

$$\langle \dot{p}_{\parallel} \rangle = \sum_{vik} \frac{\dot{F}_{vik}}{\epsilon_{vik}} p_{\parallel i} = 0, \quad (\text{C.2.28})$$

where the notation  $\dot{Q}$  means the time derivative  $dQ/dt$  due to interactions only. In the previous set of equations, we used only the parallel momentum since the conservation of the orthogonal one is their direct consequence.

The relative weights can be determined uniquely solving the previous system of algebraic equations. Using Dirac Deltas inside integrals, we can rewrite the absorption and emission coefficients as discrete sums

$$\chi_{1i_1k_1} F_{1i_1k_1} = \epsilon_{1i_1k_1} \sum_{i_2k_2} \sum_{i_3k_3} R_{i_1k_1i_2k_2i_3k_3} F_{2i_2k_2} F_{1i_1k_1}, \quad (\text{C.2.29})$$

$$\chi_{2i_2k_2} F_{2i_2k_2} = \epsilon_{2i_2k_2} \sum_{i_1k_1} \sum_{i_3k_3} R_{i_1k_1i_2k_2i_3k_3} F_{1i_1k_1} F_{2i_2k_2}, \quad (\text{C.2.30})$$

$$\eta_{3i_3k_3}^* = \epsilon_{3i_3k_3} \sum_{i_1k_1} \sum_{i_2k_2} R_{i_1k_1i_2k_2i_3k_3} F_{1i_1k_1} F_{2i_2k_2}, \quad (\text{C.2.31})$$

$$\eta_{4i_rk_r}^* = x_r \epsilon_{4i_rk_r} \sum_{i_1k_1} \sum_{i_2k_2} R_{i_1k_1i_2k_2i_3k_3} F_{1i_1k_1} F_{2i_2k_2}, \quad (\text{C.2.32})$$

where the index  $r$  spans the set  $\{a, b, c\}$  and the following coefficient is used

$$R_{i_1k_1i_2k_2i_3k_3} = \frac{1}{4(2\pi)^3} \frac{p_{\perp k_3}}{\epsilon_{1i_1k_1}^2 \epsilon_{2i_2k_2}^2 \epsilon_{3i_3k_3} \epsilon_4} \times \\ \times \sum_{l_3} J |M_{fi}|^2 (\phi_{l_3+1/2} - \phi_{l_3-1/2}). \quad (\text{C.2.33})$$

The Jacobian, due to the energy to angle change of variable, is given by Eq. (C.2.52) operating the substitution  $\phi_1 = 0$

$$J = \frac{\epsilon_4 / p_{\perp k_2}}{\sin \phi_2 (p_{\perp k_3} \cos \phi_{l_3} - p_{\perp k_1}) - p_{\perp k_3} \cos \phi_2 \sin \phi_{l_3}}. \quad (\text{C.2.34})$$

Let us note that in Eqs. (C.2.33) and (C.2.34) we used  $\epsilon_4$  and  $\phi_2$  because they are obtained from conservation laws and could not be associated with grid values and consequently labeled by indexes. Inserting Eqs. (C.2.29)-(C.2.32)

into Eqs. (C.2.26)-(C.2.28) we get a system of three algebraic equations

$$\sum_r x_r \epsilon_{4i_r k_r} = \epsilon_4, \quad (\text{C.2.35})$$

$$\sum_r x_r = 1, \quad (\text{C.2.36})$$

$$\sum_r x_r p_{\parallel i_r} = p_{\parallel 4}. \quad (\text{C.2.37})$$

Eqs. (C.2.35), (C.2.36) and (C.2.37) state that the global conservation laws are a consequence of the conservation laws for each specific interaction. Now we can solve the system for the 3 unknown  $x_r$  and its solution reads

$$\begin{aligned} x_a &= \left[ p_{\parallel 4}(\epsilon_b - \epsilon_c) + p_{\parallel b}(\epsilon_c - \epsilon_4) + p_{\parallel c}(\epsilon_4 - \epsilon_b) \right] D^{-1}, \\ x_b &= \left[ p_{\parallel 4}(\epsilon_c - \epsilon_a) + p_{\parallel a}(\epsilon_4 - \epsilon_c) + p_{\parallel c}(\epsilon_a - \epsilon_4) \right] D^{-1}, \\ x_c &= \left[ p_{\parallel 4}(\epsilon_a - \epsilon_b) + p_{\parallel a}(\epsilon_b - \epsilon_4) + p_{\parallel b}(\epsilon_4 - \epsilon_a) \right] D^{-1}, \end{aligned}$$

where the common denominator is

$$D = p_{\parallel a}(\epsilon_b - \epsilon_c) + p_{\parallel b}(\epsilon_c - \epsilon_a) + p_{\parallel c}(\epsilon_a - \epsilon_b). \quad (\text{C.2.38})$$

Since  $R_{i_1 k_1 i_2 k_2 i_3 k_3}$  does not depend on the DFs, it can be computed only once before the numerical computation is performed. Looking at Eqs. (C.2.29)-(C.2.32), we easily see that some summations can be also computed as soon as the  $R_{i_1 k_1 i_2 k_2 i_3 k_3}$  are known. Therefore we introduce the following quantities

$$\begin{aligned} A_{1i_1 k_1 i_2 k_2} &= \epsilon_{1i_1 k_1} \sum_{i_3 k_3} R_{i_1 k_1 i_2 k_2 i_3 k_3}, \\ A_{2i_2 k_2 i_1 k_1} &= \epsilon_{2i_2 k_2} \sum_{i_3 k_3} R_{i_1 k_1 i_2 k_2 i_3 k_3}, \\ B_{3i_3 k_3 i_1 k_1 i_2 k_2} &= \epsilon_{3i_3 k_3} R_{i_1 k_1 i_2 k_2 i_3 k_3}, \\ B_{4i_3 k_3 i_1 k_1 i_2 k_2}^r &= x_r \epsilon_{4i_r k_r} R_{i_1 k_1 i_2 k_2 i_3 k_3}, \end{aligned}$$

and the final expression for their time derivatives are

$$\begin{aligned} \chi_{1i_1 k_1} F_{i_1 k_1} &= \sum_{i_2 k_2} A_{1i_1 k_1 i_2 k_2} F_{i_1 k_1} F_{i_2 k_2}, \\ \chi_{2i_2 k_2} F_{i_2 k_2} &= \sum_{i_1 k_1} A_{2i_2 k_2 i_1 k_1} F_{i_1 k_1} F_{i_2 k_2}, \\ \eta_{3i_3 k_3}^* &= \sum_{i_1 k_1} \sum_{i_2 k_2} B_{3i_3 k_3 i_1 k_1 i_2 k_2} F_{i_1 k_1} F_{i_2 k_2}, \\ \eta_{4i_r k_r}^* &= \sum_{i_1 k_1} \sum_{i_2 k_2} B_{4i_3 k_3 i_1 k_1 i_2 k_2}^r F_{i_1 k_1} F_{i_2 k_2}. \end{aligned}$$

The emission coefficients requires  $(I \times K)^2$  operations for each time step which must be multiplied by another factor  $(I \times K)$  due to the computation of the analytical jacobian needed by the adopted method. As a result we have a total of about  $(I \times K)^3$  calculations at each time step which puts strong limits on the maximum number of grid points  $I$  and  $K$ .

In order to describe processes with different timescales we use the Gear's method for stiff ODE's used in Aksenov et al. (2009). In fact, this numerical approach has an adaptive time step which becomes small when the DF time derivative is large, on the contrary it becomes large when the DF time derivative is small.

### **C.2.3. Two particle kinematics**

The interaction between two particles, 1 and 2, that gives the particle 3 and 4 as a product can be represented schematically as follows

$$1 + 2 \rightarrow 3 + 4. \quad (\text{C.2.39})$$

Each particle has 3 phase space coordinates  $(p_{v_{\parallel}}, p_{v_{\perp}}, \phi_v)$ , therefore we have a total of 12 variables for the 2-particles interactions we are dealing with. Since each interaction conserves momentum and energy, they reduce to 8 independent degrees of freedom. That means that 4 quantities can be determined uniquely once the others are specified. For us, the 8 independent variables are  $p_{1_{\parallel}}, p_{1_{\perp}}, \phi_1, p_{2_{\parallel}}, p_{2_{\perp}}, p_{3_{\parallel}}, p_{3_{\perp}}, \phi_3$ ; then  $p_{4_{\parallel}}, p_{4_{\perp}}, \phi_4, \phi_2$  are functions of the previous ones.

The conservation of the parallel momentum gives us the corresponding component of the 4-th particle

$$p_{4_{\parallel}} = p_{1_{\parallel}} + p_{2_{\parallel}} - p_{3_{\parallel}}. \quad (\text{C.2.40})$$

The orthogonal momentum for the same particle can be worked out using the energy conservation law

$$\epsilon_1 + \epsilon_2 = \epsilon_3 + \epsilon_4 \quad (\text{C.2.41})$$

and using the definition of the energy given by Eq. (C.1.1) as follows

$$p_{4_{\perp}} = \sqrt{(\epsilon_1 + \epsilon_2 - \epsilon_3)^2 - p_{4_{\parallel}}^2 - m_4^2}, \quad (\text{C.2.42})$$

where  $p_{4_{\parallel}}$  has been obtained in Eq. (C.2.40). From the conservation of the

orthogonal momentum we have the following relations

$$p_{1\perp} \cos \phi_1 + p_{2\perp} \cos \phi_2 = p_{3\perp} \cos \phi_3 + p_{4\perp} \cos \phi_4 \quad (\text{C.2.43})$$

$$p_{1\perp} \sin \phi_1 + p_{2\perp} \sin \phi_2 = p_{3\perp} \sin \phi_3 + p_{4\perp} \sin \phi_4 \quad (\text{C.2.44})$$

from which we can write down analytical expressions for  $\phi_4$  and  $\phi_2$ . Unfortunately for the previous system of equations we have two valid solutions. For  $\phi_2$  we have the following equation

$$a \cos \phi_2 + b \sin \phi_2 + c = 0, \quad (\text{C.2.45})$$

where the coefficients are given by

$$a = p_{1\perp} \cos \phi_1 - p_{3\perp} \cos \phi_3, \quad (\text{C.2.46})$$

$$b = p_{1\perp} \sin \phi_1 - p_{3\perp} \sin \phi_3, \quad (\text{C.2.47})$$

$$c = \frac{a^2 + b^2 + p_{2\perp}^2 - p_{4\perp}^2}{2 p_{2\perp}}. \quad (\text{C.2.48})$$

The solution of eq. (C.2.45) are given by the following conditions

- if  $b \neq 0$ ,  $a^2 + b^2 \neq 0$ ,  $c = a$   
 $\Rightarrow \phi_2 = -2 \arctan \left( \frac{a}{b} \right),$
- if  $b = 0$ ,  $c = a \Rightarrow \phi_2 = \pi,$
- if  $a \neq c$ ,  $a^2 + b^2 - ac - b\sqrt{a^2 + b^2 - c^2} \neq 0$   
 $\Rightarrow \phi_2 = 2 \arctan \left( \frac{b - \sqrt{a^2 + b^2 - c^2}}{a - c} \right),$
- if  $a \neq c$ ,  $a^2 + b^2 - ac + b\sqrt{a^2 + b^2 - c^2}$   
 $\Rightarrow \phi_2 = 2 \arctan \left( \frac{b + \sqrt{a^2 + b^2 - c^2}}{a - c} \right).$

Once  $\phi_2$  has been chosen,  $\phi_4$  can be easily obtained from the Eqs. (C.2.43) and (C.2.44).

The Jacobian of Eq. (C.2.34) has been computed using the following identity for the Dirac Delta

$$\delta(f(x)) = \sum_i \frac{\delta(x - x_i)}{|(df/dx)_{x_i}|}, \quad (\text{C.2.49})$$

where  $f$  is a function such that  $f(x_i) = 0$ . In our framework the function inside the Dirac delta is given by the energy conservation

$$f(\phi_2) = \epsilon_1 + \epsilon_2 - \epsilon_3 - \epsilon_4(\phi_2), \quad (\text{C.2.50})$$

where  $\phi_2$  is now the independent variable. From the previous equation we compute its derivative with respect to  $\phi_2$  and the value  $\phi_2^*$  such that  $f(\phi_2^*) = 0$ . Rewriting explicitly Eq. (C.2.49) we have that

$$\delta(f(\phi_2)) = \frac{\delta(\phi_2 - \phi_2^*)}{|(df/d\phi_2)_{\phi_2^*}|} = J \delta(\phi_2 - \phi_2^*), \quad (\text{C.2.51})$$

where the explicit equation for  $J$  is

$$J = \frac{\epsilon_4}{p_{2\perp} |\sin(\phi_2 - \phi_4)|}. \quad (\text{C.2.52})$$

### C.3. Results

In this section we describe our results for the collisionless and interacting systems separately. The boundary condition is set when the initial electric field  $E_0$  and the initial DF  $F_{\nu 0}(p_{\parallel}, p_{\perp})$  are specified. For simplicity we performed several runs with different initial electric fields, but always with no particles at the beginning. When in addition to external electric field also particles are present from the beginning, oscillations still occur, but with higher frequency, as given by the plasma frequency Benedetti et al. (2011). So we start computations with DFs null identically in the whole momentum space and our initial conditions can be written as

$$\begin{cases} E_0 = \xi E_c, & \xi = \{1, 3, 10, 30, 100\} \\ F_{\nu 0}(p_{\parallel}, p_{\perp}) = 0, & p_{\perp} \in [0, +\infty), p_{\parallel} \in (-\infty, +\infty). \end{cases}$$

Consequently electrons and positrons are produced exclusively by the Schwinger process.

In order to interpret meaningfully our results, we introduce first some useful quantities. Initially the energy is stored in the electric field and it fixes the energy budget available as given by

$$\rho_0 = \frac{E_0^2}{8\pi}. \quad (\text{C.3.1})$$

We expect therefore the final state of the equilibrated thermal electron-positron-photon plasma to be characterized by the temperature

$$T_{eq} = \sqrt[4]{\frac{\rho_0}{4\sigma}} \simeq 1.7 \sqrt{\frac{E_0}{E_c}} \text{ MeV}, \quad (\text{C.3.2})$$

where  $\sigma$  is the Stefan-Boltzmann constant. The total energy density of pairs  $\rho_{\pm}$  and photons  $\rho_{\gamma}$  are related to the actual and initial electric fields,  $E$  and

$E_0$ , by the energy conservation law

$$\rho_{\pm} = \rho_+ + \rho_- = \frac{E_0^2 - E^2}{8\pi} - \rho_{\gamma}. \quad (\text{C.3.3})$$

Following Benedetti et al. (2011), we define the maximum achievable pairs number density

$$n_{max} = \frac{E_0^2}{8\pi m_e}, \quad (\text{C.3.4})$$

which corresponds to the case of conversion of the whole initial energy density into electron-positron rest energy density

$$\rho_{\pm rest} = (n_- + n_+) m_e, \quad (\text{C.3.5})$$

where  $n_-$  and  $n_+$  are the electrons and positrons number densities respectively. From the electrons and positrons DFs we can extrapolate their bulk parallel momentum  $\langle p_{\parallel} \rangle$  as defined in Eq. (C.2.5) and the symmetry of our problem implies that  $\langle p_{\parallel -} \rangle = -\langle p_{\parallel +} \rangle$ . We make use of this identity to define the kinetic energy density of pairs

$$\rho_{\pm kin} = \rho_{\pm rest} \left( \sqrt{\left( \frac{\langle p_{\parallel \pm} \rangle}{m_e} \right)^2 + 1} - 1 \right). \quad (\text{C.3.6})$$

Therefore  $\rho_{\pm kin}$  is the energy density as if all particles are put together in the momentum state with  $p_{\parallel} = \langle p_{\parallel} \rangle$  and  $p_{\perp} = 0$  while their rest energy density is  $\rho_{\pm rest}$ . The difference between the total energy density and all the others defined above is denoted as internal energy density

$$\rho_{\pm in} = \rho_{\pm} - \rho_{\pm rest} - \rho_{\pm kin}. \quad (\text{C.3.7})$$

The term "internal" refers here to the dispersion of the DF around a given point with coordinates  $(\langle p_{\parallel} \rangle, \langle p_{\perp} \rangle)$  in the momentum space.

### C.3.1. Collisionless systems

Since interactions with photons operate on much larger time scale than the pair creation by vacuum breakdown we first present the results obtained solving the relativistic Boltzmann equation (C.1.4) for electrons and positrons with  $\chi_{\pm}^q = \eta_{\pm}^{*q} = 0$ . With these assumptions we expect the following results to be closely related to those reported in Benedetti et al. (2011).

For all the explored initial conditions, there are important analogies between the approach adopted in Benedetti et al. (2011) and the one presented in this work. For each initial field the first half period of the oscillation  $t_1$

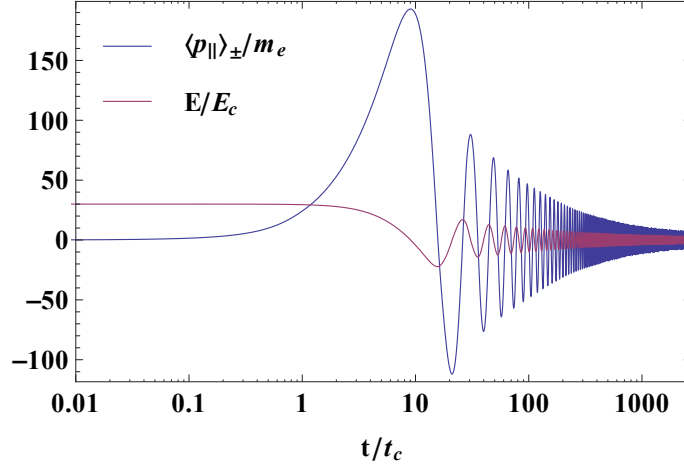


**Figure C.1.:** Evolution of electric field  $E$  and pairs bulk parallel momentum  $\langle p_{\parallel} \rangle_{\pm}$  obtained from the numerical solution of Eq. (C.1.4) setting  $E_0 = 30 E_c$ .

is nearly equal to the corresponding one obtained in Benedetti et al. (2011). Also the evolution with time of  $\langle p_{\parallel} \rangle_{\pm}$  during this time lapse is very similar to the result given by their analytic method. The time evolution of electric field  $E$  and  $\langle p_{\parallel} \rangle_{\pm}$  in Compton units with  $t_c = 1/m_e$  are shown in Fig. C.1 for  $E_0 = 30 E_c$ .

In addition to these similarities some new important features emerge from the current study. The manifestation of these new aspects is represented in Fig. C.2 where we show how the various forms of  $e^{\pm}$  energy defined in the previous paragraph evolve with time. These energy densities are normalized to the total initial energy density  $\rho_0$  defined by Eq. (C.3.1). One of the most important evidences of this figure is that the rest energy density of pairs  $\rho_{\pm kin}$  saturates to a small fraction of the maximum achievable one. This is in contrast with the result presented in Benedetti et al. (2011) where the value given in Eq. (C.3.4) was reached asymptotically.

As a consequence the energy is mainly converted into other forms, namely the kinetic  $\rho_{\pm kin}$  and internal  $\rho_{\pm int}$  ones. Both these quantities oscillate with the same frequency but with shifted phase. Relative maxima and minima of  $\rho_{\pm kin}$  correspond to the peaks of the bulk parallel momentum shown in Fig. C.1 as can be grasped from its definition in Eq. (C.3.6). Looking at Fig. C.2 we see their relative importance changing progressively with time. Even if they oscillate, the internal component dominates over the kinetic one as time advances. This trend points out that all the initial energy will be converted mostly into internal energy, while the contribution of the kinetic one will eventually be small.

In this respect, from the electron and positron DFs we obtain the mean

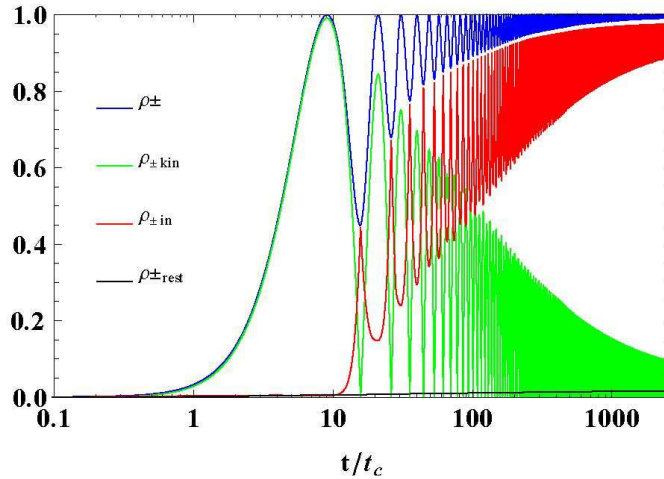


**Figure C.2.:** Evolution with time of the pairs energies as defined by Eqs. (C.3.3), (C.3.5), (C.3.6) and (C.3.7) for the collisionless case  $E_0 = 30 E_c$ . All of them are normalized by the total initial energy  $\rho_0$  given by Eq. (C.3.1).

squared values of the parallel and orthogonal momentum as defined by Eqs. (C.2.6) and (C.2.7). These quantities give us some insight about the spreading of the DF along the parallel and orthogonal components of the momentum. In Tab. C.2 we report their values at the end of runs with different initial fields. It is clear that the larger the initial electric field the larger is  $\langle p_{\perp}^2 \rangle_{\pm}$ . This is a direct consequence of the rate of pair production given by Eq. (C.1.5) that already distributes particle along the orthogonal direction in the momentum space.

The mean squared value of the parallel momentum  $\langle p_{\parallel}^2 \rangle_{\pm}$  reaches a minimum value between 3 and 10 critical electric fields. This minimum was first found in Ruffini et al. (2007), see Fig. 3 in that paper. In Tab. C.2 we report also  $\langle p_{\parallel} \rangle_{\pm 1}$  which is the peak value of the bulk parallel momentum at the moment when electric field vanishes for the first time. We see from the table that also this quantity has a minimum in the same range of initial fields as  $\langle p_{\parallel}^2 \rangle_{\pm}$ . Both these minima are linked to the combined effects of pairs creation and acceleration processes.

However, it is important to compare  $\langle p_{\parallel}^2 \rangle_{\pm}$  and  $\langle p_{\perp}^2 \rangle_{\pm}$  for different initial fields. Indeed, this juxtaposition gives us quantitative informations about the anisotropy of the DFs in the phase space. Looking at the numerical values we observe how this anisotropy decreases with the increase of the initial electric field, which points out how an eventual approach toward isotropy, and therefore thermalization, would be much more difficult for lower initial fields.

In Tab. C.2 we compare also two different number densities  $n_1$  and  $n_s$  nor-

**Table C.2.:** Square root of the mean squared value of orthogonal  $\langle p_{\perp}^2 \rangle_{\pm}$  and parallel  $\langle p_{\parallel}^2 \rangle_{\pm}$  momentum, parallel momentum  $p_{\parallel 1}$ , in units of  $m_e$ , and number density  $n_1$  of pairs at the first zero of the electric field, saturation number density  $n_s$  normalized by the maximum achievable one given by Eq. C.3.4 for different initial electric fields.

| $\frac{E}{E_c}$ | $\sqrt{\langle p_{\perp}^2 \rangle_{\pm}}$ | $\sqrt{\langle p_{\parallel}^2 \rangle_{\pm}}$ | $\langle p_{\parallel} \rangle_1$ | $\frac{n_1}{n_{max}}$ | $\frac{n_s}{n_{max}}$ |
|-----------------|--|--|-----------------------------------|-----------------------|-----------------------|
| 1               | 0.4  | 75   | 160                               | 0.006                 | 0.018                 |
| 3               | 0.8  | 37   | 82                                | 0.018                 | 0.037                 |
| 10              | 1.3  | 35   | 77                                | 0.013                 | 0.041                 |
| 30              | 2.0  | 87   | 192                               | 0.005                 | 0.016                 |
| 100             | 3.5  | 127  | 284                               | 0.003                 | 0.011                 |

malized to the maximum achievable one. The first is the number density of pairs at the first zero of the electric field  $t_1$ . The second is the saturation number density of pairs at the end of the run. We found that the values of  $n_1$  are very close to the same densities computed in Benedetti et al. (2011) with a significant amount of pairs produced already in a very small time lapse. Let us note that there are maxima of both  $n_1$  and  $n_s$  in the range between 1 and 10  $E_c$  in correspondence with minima of  $\langle p_{\parallel}^2 \rangle_{\pm}$  and  $\langle p_{\perp}^2 \rangle_{\pm}$ .

### C.3.2. Interacting systems

Now we turn to the dynamics of our system on much larger time scales. As discussed above, in long run interactions between created pairs become important. We consider 2-particle interactions listed in Tab. C.1 in Appendix and describe them by the collision integrals in Eqs. (C.1.4) and (C.1.6) using the same range of initial fields used for the collisionless systems. More sparse computational grid is used as calculation of collision terms imply performing multidimensional integrals in the phase space, see Appendix C.2.2.

The larger the electric field the higher the rate of pairs production and consequently their number density. Since the interaction rate is proportional to particle number densities, we expect them to be important sooner for higher initial field. In this respect, it is worth mentioning that in Benedetti et al. (2011) the time  $t_{\gamma}$  was estimated at which the optical depth for electron-positron annihilation equals unity  $\tau(t_{\gamma}) = 1$ . There, it was found that  $t_{\gamma}$  decreases when the initial electric field increases. Besides, the order of magnitude of their estimations is in agreement with the time at which the photons number density is around a few percent of the pairs number density.

In the previous subsection dedicated to collisionless systems, we described

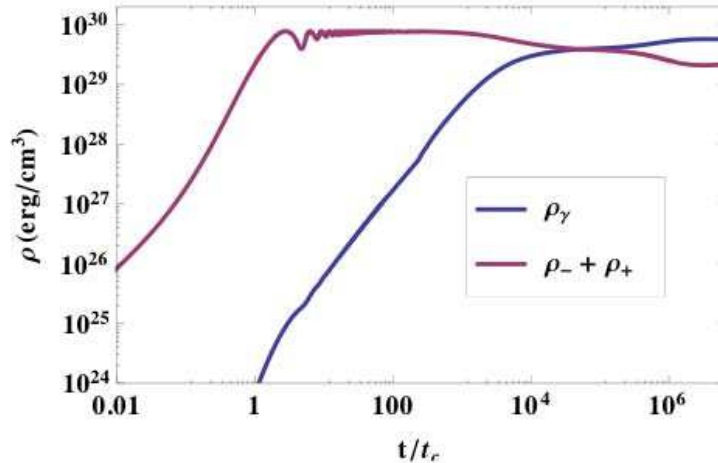


**Figure C.3.:** Energy densities of pairs and photons obtained from the numerical solution of Eqs. (C.1.4) and (C.1.6) with initial field  $E_0 = 100 E_c$ .

the anisotropy of the pairs DF by means of the mean squared value of parallel and orthogonal momentum reported in Tab. C.2. In that case, we knew approximately the range of orthogonal momentum in which the most part of electrons and positron were located and the orthogonal grid was chosen and kept fixed from the beginning. This choice was possible because the dispersion along the orthogonal direction was determined uniquely by the rate  $S$ . The extension of the grid was chosen in such a way that the value of each DF at the grid boundaries was small compared to the maximum value. For the reason that interactions redistribute particles in the phase space and tend to isotropize their distributions, the orthogonal grid must be extended to values comparable to the kinetic equilibrium temperature. To do that, we use initially an orthogonal grid with the same extension as in the collisionless system. We extend it later when particles are scattered toward higher orthogonal momenta and therefore the tails of the DF at the boundaries is not negligible. The extension of the parallel grid remains essentially the same as the collisionless case.

In order to correctly describe the pairs acceleration process, the time step of the computation must be a small fraction of their oscillation period. This constraint prevents us to study the evolution up to the kinetic equilibrium within a reasonable time. After hundreds of oscillations, the energy density carried by the electric field is a small fraction of the pairs and photons energy densities. In other words, most energy has already been converted into electron-positron plasma. Due to this fact, the acceleration of electrons and positrons does not affect their DFs appreciably. This allows us to neglect the presence of the electric field hereafter. To do that we use the distribution

function at this instant as initial condition for a new computation in which the condition  $E = 0$  is imposed. By neglecting oscillations induced by the electric field the constraint on the time step of the numerical calculation is released, and it is now determined by the rate of the interactions.

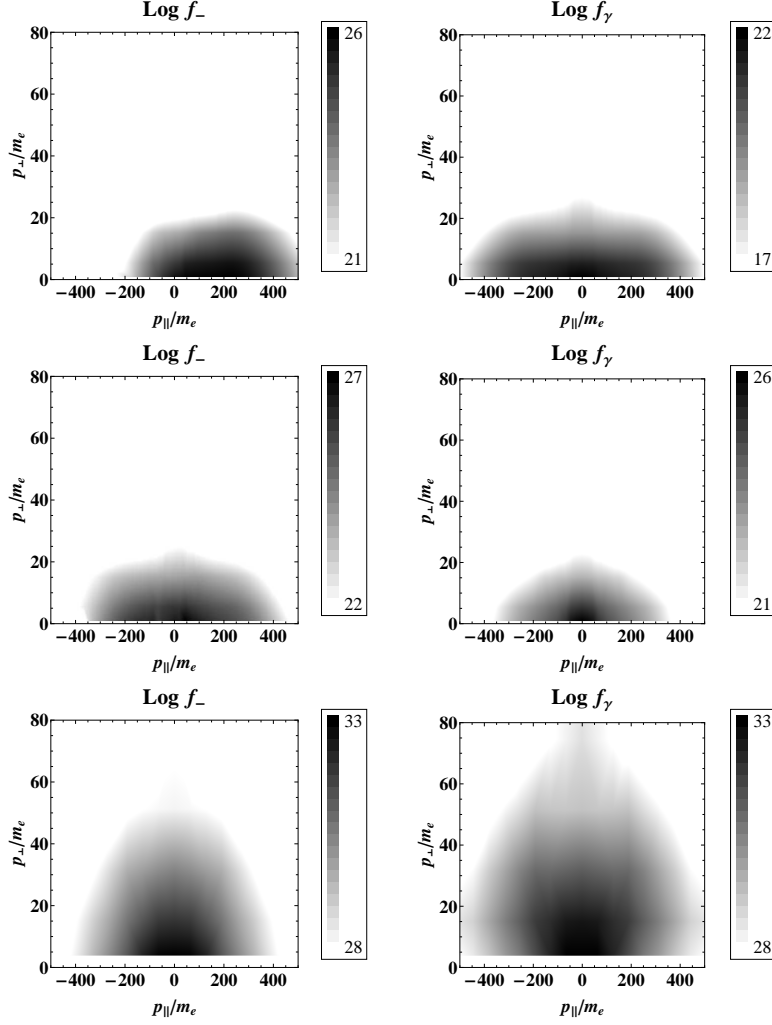


**Figure C.4.:** Phase space distributions of electrons (left column) and photons (right column) for the initial condition  $E_0 = 100 E_c$ . Top:  $2.3 \cdot 10^2 t_c$ , middle:  $2.3 \cdot 10^2 t_c$ , bottom:  $4.6 \cdot 10^6 t_c$ .

In Fig. C.3 we show the time evolution of the pairs and photons energy densities for  $E_0 = 100 E_c$ . From this plot we can understand the hierarchy of time scales associated to the distinct physical phenomena we are dealing with. In presence of an overcritical electric field, electron-positron pairs start to be produced in a shortest time according to Eq. (C.1.5). As soon as they are created, electrons and positrons are accelerated toward opposite directions as the back reaction effect on the external field. The characteristic duration

of this back reaction corresponds approximately to the first half oscillation period. At early times, even after many oscillations, the energy density of photons is negligible compared to that of pairs, meaning that interactions do not play any role. Such a starting period, during which the real system can be considered truly collisionless, exists independently on the initial electric field even if its duration depends on it. From Fig. C.3 it is clear that the photons energy density increases with time as a power law approaching the pairs energy density.

Only when hundreds oscillations have taken place, interactions start to affect the evolution of the system appreciably and can not be neglected any further. The slope of the photons curve in C.3 reduces indicating that pairs annihilation has become less efficient than the photons annihilation process. Now the evolution of the system is mostly governed by interactions. Möller, Bhabha and Compton scatterings give rise to momentum and energy exchange between electron, positron and photon populations. Besides the same collisions have the tendency to distribute particles more isotropically in the momentum space. After some time, the photons energy density becomes equal and then overcomes the pairs energy density. This growth continues until the equilibrium between pairs annihilation and creation processes is established  $e^-e^+ \leftrightarrow \gamma\gamma$ . For this reason both pairs and photons curve are flat on the right of Fig. C.3, see also Aksenov et al. (2007). However, at this point the DF is not yet isotropic in the momentum space indicating that the kinetic equilibrium condition is not yet satisfied. In fact, kinetic equilibrium is achieved only at later times when also Möller, Bhabha and Compton scatterings are in detailed balance. At that time the electron-positron-photon plasma can be identified by a common temperature and nonzero chemical potential. This is also the last evolution stage attainable by our study because only 2-particle interactions are taken into account while thermalization is expected to occur soon after kinetic equilibrium if also 3-particle interactions would be included Aksenov et al. (2009).

As an example, in Fig. C.4 density plots of  $f_-$  and  $f_\gamma$  are shown on the left and right columns respectively, for the initial condition  $E_0 = 100$ . Their time evolution starts from the top line to the bottom one corresponding to three different times. After  $2.3 t_c$  both DFs are highly anisotropic as it is well established by the ratio  $R = \sqrt{\langle p_{\parallel}^2 \rangle_{\pm} / \langle p_{\perp}^2 \rangle_{\pm}} = 0.06$ . At this stage, the electric field is highly overcritical and a very small fraction of initial energy has been converted into rest mass energy of electrons and positrons. For this reason  $e^-e^+$  are easily accelerated up to relativistic velocities explaining why the electron DF is shifted on the right side of the phase space plane characterized by  $p_{\parallel} > 0$ . At this instant electrons are characterized by a relativistic bulk velocity corresponding to a Lorentz gamma factor 170. On the second line the time is  $2.3 \cdot 10^2 t_c$  and the DFs are still anisotropic if we look at the parameter R introduced above. However the situation is different with respect

to the previous stage because the electric field is only slightly overcritical and many more pairs and photons have been generated. As a consequence interaction rates are much larger than before and an efficient momentum exchange between electron and positron populations occurs. Both small electric field and collisions prevent particles to reach ultra-relativistic velocities and for this reason the electron DF is now perfectly symmetric with respect to the plane  $p_{\parallel} = 0$ . Only later on, at  $4.6 \cdot 10^6 t_c$  for the bottom line, collisions dominate the evolution of the system whereas the presence of the electric field can be safely neglected. The pictures show a prominent DFs widening toward higher orthogonal momenta which is confirmed by the value  $R \simeq 0.23$ . This remarkable evidence allows us to predict the forthcoming fate of the system to be an electron-positron-photon plasma in thermal equilibrium. The DFs isotropy in the momentum space not only indicates that the kinetic equilibrium condition is approached but also that the system is going to lose information about the initial preferential direction of the electric field. In the case of isotropic DF, the timescale on which thermal equilibrium is achieved can be estimated as  $\tau_{th} \simeq 1/(n\sigma_T)$  Aksenov et al. (2009). For our anisotropic DF the thermalization timescale is remarkably longer.

## **C.4. Conclusions**

From the conceptual point of view the discovery of plasma oscillations Kluger et al. (1991) as result of back reaction has been an important step. The next step has been the analysis of creation of photons from pairs Ruffini et al. (2003b). In this paper we have studied all these phenomena in great details adopting a kinetic approach with two dimensional phase space. We have found anisotropy in momentum distributions of pairs and photons, which we consider one of the main results of this paper. Another important result is the importance of internal energy which limits heavily the efficiency of energy conversion into electron-positron pairs. Both these effects could be in principle considered as phenomenological evidences of an overcritical electric field, even if they manifest themselves on a very short time scale.

For the first time we studied the entire dynamics of energy conversion from initial overcritical electric field, ending up with thermalized electron-positron-photon plasma. Such conversion occurs in a complicated sequence of processes starting with Schwinger pair production which is followed by oscillations of created pairs due to back-reaction on initial electric field, then production of photons due to annihilation of pairs and finally isotropization of created electron-positron-photon plasma. We solved numerically the relativistic Vlasov-Boltzmann equations for electrons, positrons and photons, with collision integrals for 2-particle interactions computed from exact QED matrix elements.

In order to appreciate the consequences of the kinetic treatment and the rel-

evance of interactions separately, two different computations have been performed for every single initial condition. We called them collisionless and interacting systems in view of the fact that collision terms have been discarded and accounted for, respectively. The collisionless runs allowed us to compare our results with those obtained earlier, and to resolve better the momentum space of pairs. In this way we found that number density of pairs always saturates without exceeding 5 per cent of the maximum achievable number density (C.3.4), in contrast to earlier works. This number is not far from the thermal number density of pairs obtained from the temperature (C.3.2). In particular, for the largest field  $E_0 = 100 E_c$  we obtained almost 30 per cent of the thermal number density of pairs when the interactions are not yet important. It is interesting that the energy stored in initial electric field is mainly converted into internal and kinetic energies of pairs, but the former becomes predominant as time advances. Even if the distribution in momentum space reminds Maxwellian, also at the very beginning it is highly anisotropic, with the dispersion along the direction of electric field exceeding orders of magnitude that in orthogonal direction. We conclude that simultaneous production of pairs and their acceleration in the same electric field is responsible for such peculiar form of DF of particles.

We found that interactions become important at later times with respect to the average oscillation period, in agreement with estimates performed in Benedetti et al. (2011). For higher initial fields interactions become significant earlier and for each initial condition there is a characteristic time scale after which they can not be neglected. We find that photons initially follow the distribution of pairs with nonzero parallel bulk momentum.

The first equilibrium manifests itself when the perfect symmetry between pair annihilation and creation rates is established. Only later on, when scatterings have distributed particles isotropically in the momentum space, the kinetic equilibrium is reached. In such state the electron-positron-photon plasma is generally described by a common temperature and nonzero chemical potentials for all particles and its evolution toward thermal equilibrium is well understood Aksenov et al. (2007).



# D. Electron-positron plasma in GRBs and in cosmology

## D.1. Introduction

Electron-positron plasmas are discussed in connection with astrophysical phenomena such as Galactic Center, microquasars, Gamma-Ray Bursts (GRBs), as well as laboratory experiments with high power lasers, for details see Ruffini et al. (2010). According to the standard cosmological model, such plasma existed also in the early Universe. It is naturally characterized by the energy scale given by the electron rest mass energy, 511 keV. It is interesting that at the epoch when Universe had this temperature, several important phenomena took place almost contemporarily: electron-positron pair annihilation, the Big Bang Nucleosynthesis (BBN) and neutrino decoupling.

Electron-positron plasma also is thought to play an essential role in GRB sources, where simple estimates for the initial temperature give values in MeV region. Such plasma is energy dominated and optically thick due to both Compton scattering and electron-positron pair creation, and relaxes to thermal equilibrium on a time scale less than  $10^{-11}$  sec, see Aksenov et al. (2007). The latter condition results in self-accelerated expansion of the plasma until it becomes either transparent or matter dominated.

In the literature there have been several qualitative arguments mentioning possible similarities between electron-positron plasmas in the early Universe and in GRB sources. However, until now there is no dedicated study which draws analogies and differences between these two cases. This paper aims in confronting dynamics and physical conditions in both cases.

## D.2. General equations

The framework which describes electron-positron plasma both in cosmology and in GRB sources is General Relativity. Both dynamics of expansion of the Universe, and the process of energy release in the source of GRB should be considered within that framework. Hydrodynamic expansion of GRB sources may, however, be studied within much simpler formalism of Special Relativity.

We start with Einstein equations

$$R_{\mu\nu} - \frac{1}{2}g_{\mu\nu}R = \frac{8\pi G}{c^4}T_{\mu\nu}, \quad (\text{D.2.1})$$

where  $R_{\mu\nu}$ ,  $g_{\mu\nu}$  and  $T_{\mu\nu}$  are respectively Ricci, metric and energy-momentum tensors,  $G$  is Newton's constant,  $c$  is the speed of light, and the energy-momentum conservation, following from (D.2.1)

$$(T_{\mu}{}^{\nu})_{;\nu} = \frac{\partial(\sqrt{-g}T_{\mu}{}^{\nu})}{\partial x^{\nu}} + \sqrt{-g}\Gamma_{\nu\lambda}^{\mu}T^{\nu\lambda} = 0, \quad (\text{D.2.2})$$

where  $\Gamma_{\nu\lambda}^{\mu}$  are Cristoffel symbols and  $g$  is determinant of the metric tensor. We assume for the energy-momentum tensor

$$T^{\mu\nu} = p g^{\mu\nu} + \omega U^{\mu}U^{\nu}, \quad (\text{D.2.3})$$

where  $U^{\mu}$ , is four-velocity,  $\omega = \rho + p$  is proper enthalpy,  $p$  is proper pressure and  $\rho$  is proper energy density.

When plasma is optically thick, radiation is trapped in it and entropy conservation applies. It may be obtained multiplying (D.2.2) by four-velocity

$$-U^{\mu}(T_{\mu}{}^{\nu})_{;\nu} = U^{\mu}\rho_{;\mu} + \omega U^{\mu}_{;\mu} = 0. \quad (\text{D.2.4})$$

Using the second law of thermodynamics

$$d\left(\frac{\omega}{n}\right) = Td\left(\frac{\sigma}{n}\right) + \frac{1}{n}dp, \quad (\text{D.2.5})$$

where  $\sigma = \omega/T$  is proper entropy density,  $T$  is temperature, one may rewrite (D.2.4) as

$$(\sigma U^{\mu})_{;\mu} = U^{\mu}\sigma_{;\mu} + \sigma U^{\mu}_{;\mu} = 0. \quad (\text{D.2.6})$$

Baryon number conservation equation has exactly the same form

$$(nU^{\mu})_{;\mu} = U^{\mu}n_{;\mu} + nU^{\mu}_{;\mu} = 0. \quad (\text{D.2.7})$$

Now recalling that  $U^{\mu}\frac{\partial}{\partial x^{\mu}} = \frac{d}{d\tau}$  and  $U^{\mu}_{;\mu} = d \ln V / d\tau$ , where  $V$  is comoving volume,  $\tau$  is the proper time, from (D.2.4) and (D.2.7) we get

$$d\rho + \omega d \ln V = 0, \quad d \ln n + d \ln V = 0, \quad (\text{D.2.8})$$

Finally, introducing the thermal index  $\gamma = 1 + \frac{p}{\rho}$  restricted by the inequality  $1 \leq \gamma \leq 4/3$  we obtain from (D.2.4) the following scaling laws

$$\rho V^{\gamma} = \text{const}, \quad nV = \text{const}. \quad (\text{D.2.9})$$

Both these conservations laws are valid for the early Universe and GRB plasmas.

One can obtain the corresponding scaling laws for comoving temperature by splitting the total energy density into nonrelativistic (with  $\gamma = 1$ ) and ultrarelativistic (with  $\gamma = 4/3$ ) parts  $\rho \rightarrow nmc^2 + \varepsilon$ , where  $m$  is the mass of particles<sup>1</sup>,  $\varepsilon$  is proper internal energy density. The entropy of the ultrarelativistic component is then  $\sigma = \frac{4}{3} \frac{\varepsilon}{T}$ , and (D.2.6) gives

$$\frac{\varepsilon V}{T} = \text{const.} \quad (\text{D.2.10})$$

For  $\varepsilon \gg nmc^2$ , which is the energy dominance condition, internal energy plays dynamical role by influencing the laws of expansion. For  $\varepsilon \ll nmc^2$ , which is the matter dominance condition, internal energy does not play any dynamical role, but determines the scaling law of the temperature. In order to understand the dynamics of thermodynamic quantities in both early Universe and in GRBs, one should write down the corresponding equations of motion.

### D.2.1. Early Universe

For the description of the early Universe we take the Robertson-Walker metric with the interval

$$ds^2 = -c^2 dt^2 + a^2(t) \left[ \frac{dr^2}{1 - kr^2} + r^2 d\theta^2 + r^2 \sin^2 \theta d\varphi^2 \right], \quad (\text{D.2.11})$$

where  $a(t)$  is the scale factor and  $k = 0, \pm 1$  stands for the spatial curvature. In homogeneous and isotropic space described by (D.2.11), Einstein equations (D.2.1) are reduced to Friedmann equations together with the continuity equation

$$\left( \frac{da}{dt} \right)^2 + c^2 k = \frac{8\pi G}{3c^2} \rho a^2, \quad (\text{D.2.12})$$

$$2a \frac{d^2 a}{dt^2} + \left( \frac{da}{dt} \right)^2 + c^2 k = -\frac{8\pi G}{c^2} p a^2, \quad (\text{D.2.13})$$

$$\frac{d\rho}{dt} + \frac{3}{a} \frac{da}{dt} (\rho + p) = 0, \quad (\text{D.2.14})$$

where  $a$  is the scale factor. Notice, that only two equations in the system above are independent. The continuity equation (D.2.14) follows from the

---

<sup>1</sup>Nonrelativistic component is represented by baryons. For simplicity we assume only one sort of baryons, say protons, having mass  $m$ . Ultrarelativistic component is represented by photons and electron-positron pairs.

Einstein equations (D.2.12) and (D.2.13) as the energy conservation. In fact, (D.2.14) may be also obtained from the entropy conservation (D.2.4). The comoving volume in Friedmann's Universe is  $V = a^3$ , so (D.2.14) and the first equality in (D.2.9) are equivalent.

On the radiation dominated stage of Universe expansion one has

$$\rho \propto V^{-4/3} \propto a^{-4}, \quad n \propto V^{-1} \propto a^{-3}, \quad (\text{D.2.15})$$

while on the matter dominated stage

$$\rho \propto n \propto V^{-1} \propto a^{-3}. \quad (\text{D.2.16})$$

Entropy conservation (D.2.10) leads to the unique temperature dependence on the scale factor

$$T \propto V^{-1/3} \propto a^{-1}. \quad (\text{D.2.17})$$

The corresponding time dependence of thermodynamic quantities may be obtained from solutions of Friedmann equation (D.2.12) and continuity equation (D.2.14).

## **D.2.2. GRBs**

Different situation takes place for the sources of GRBs. Assuming spherical symmetry for the case of GRB the interval<sup>2</sup> is

$$ds^2 = -c^2 dt^2 + dr^2 + r^2 d\theta^2 + r^2 \sin^2 \theta d\varphi^2. \quad (\text{D.2.18})$$

Optically thick to Compton scattering and pair production electron-positron plasma in GRB sources is radiation dominated. Its equations of motion follow from the energy-momentum conservation law (D.2.2) and baryon number conservation law (D.2.7). Initially plasma expands with acceleration driven by the radiative pressure.

In spherically symmetric case the number conservation equation (D.2.7) is

$$\frac{\partial (n\Gamma)}{\partial t} + \frac{1}{r^2} \frac{\partial}{\partial r} \left( r^2 n \sqrt{\Gamma^2 - 1} \right) = 0, \quad (\text{D.2.19})$$

Integrating this equation over the volume from certain  $r_i(t)$  to  $r_e(t)$  which we assume to be comoving with the fluid  $\frac{dr_i(t)}{dt} = \beta(r_i, t)$ ,  $\frac{dr_e(t)}{dt} = \beta(r_e, t)$ , and ignoring a factor  $4\pi$  we have

---

<sup>2</sup>General Relativity effects may be included by taking Schwarzschild or Kerr-Newman metric. However, we are interested in optically thick plasma which expands with acceleration and propagates far from its source, where the spatial curvature effects may be neglected. For this reason we simplify the treatment and adopt a spatially flat metric.

$$\begin{aligned}
 & \int_{r_i}^{r_e} \frac{\partial (n\Gamma)}{\partial t} r^2 dr + \int_{r_i}^{r_e} \frac{\partial}{\partial r} \left( r^2 n \sqrt{\Gamma^2 - 1} \right) dr = \quad (D.2.20) \\
 & \frac{\partial}{\partial t} \int_{r_i}^{r_e} (n\Gamma) r^2 dr - \frac{dr_e}{dt} n(r_e, t) \Gamma(r_e, t) r_e^2 + \frac{dr_i}{dt} n(r_i, t) \Gamma(r_i, t) r_i^2 + \\
 & + r_e^2 n(r_e, t) \sqrt{\Gamma^2(r_e, t) - 1} - r_i^2 n(r_i, t) \sqrt{\Gamma^2(r_i, t) - 1} = \\
 & = \frac{d}{dt} \int_{r_i}^{r_e} (n\Gamma) r^2 dr = 0,
 \end{aligned}$$

Since we deal with arbitrary comoving boundaries, this means that the total number of particles integrated over all differential shells is conserved

$$N = 4\pi \int_0^{R(t)} n\Gamma r^2 dr = \text{const}, \quad (D.2.21)$$

where  $R(t)$  is the external radius of the shell.

Following Piran et al. (1993) one can transform (D.2.19) from the variables  $(t, r)$  to the new variables  $(s = t - r, r)$  and then show that

$$\frac{1}{r^2} \frac{\partial}{\partial r} \left( r^2 n \sqrt{\Gamma^2 - 1} \right) = - \frac{\partial}{\partial s} \left( \frac{n}{\Gamma + \sqrt{\Gamma^2 - 1}} \right). \quad (D.2.22)$$

For ultrarelativistic expansion velocity  $\Gamma \gg 1$ , the RHS in (D.2.22) tends to zero, and then the number of particles in each differential shell between the boundaries  $r_i(t)$  and  $r_e(t)$  is also conserved with a good approximation, i.e.

$$dN = 4\pi n\Gamma r^2 dr \approx \text{const}. \quad (D.2.23)$$

Relations (D.2.21) and (D.2.23) then imply

$$\begin{aligned}
 4\pi \int_{r_i}^{r_e} (n\Gamma r^2) dr &= 4\pi \left[ n(r, t) \Gamma(r, t) r^2 \right] \int_{r_i}^{r_e} dr \quad (D.2.24) \\
 &= 4\pi \left( n\Gamma r^2 \right) \Delta \approx \text{const},
 \end{aligned}$$

where the first argument of functions  $n(r, t)$  and  $\Gamma(r, t)$  is restricted to the interval  $r_i < r < r_e$ , and consequently  $\Delta \equiv r_e - r_i \approx \text{const}$ . Taking into account that  $r_i(t)$  and  $r_e(t)$  are arbitrary, this means that ultrarelativistically expand-

ing shell preserves its width measured in the laboratory reference frame. This fact has been used by Ruffini et al. (2000) and referred there as the constant thickness approximation.

The volume element measured in the laboratory reference frame is  $d\mathcal{V} = 4\pi r^2 dr$ , while the volume element measured in the reference frame comoving with the shell is  $dV = 4\pi\Gamma r^2 dr$ . Comoving volume of the expanding ultrarelativistic shell with  $\Gamma \simeq \text{const}$  will be

$$V = 4\pi\Gamma \int_{r-\Delta}^r r^2 dr \simeq 4\pi\Gamma r^2 \Delta. \quad (\text{D.2.25})$$

Then we rewrite the conservation equations (D.2.9) as

$$\rho^{\frac{1}{\gamma}}\Gamma r^2 = \text{const}, \quad n\Gamma r^2 = \text{const}, \quad (\text{D.2.26})$$

Unlike the early Universe, where both energy and entropy conservations reduce to (D.2.14), in the case of GRBs the energy conservation is a separate equation coming from the zeroth component of (D.2.2) as

$$(T_0{}^\nu)_{;\nu} = \omega U_0 U^\nu{}_{;\nu} + U^\nu (\omega U_0)_{;\nu} = 0. \quad (\text{D.2.27})$$

which gives

$$\rho\Gamma^2 r^2 = \text{const}. \quad (\text{D.2.28})$$

From (D.2.26) and (D.2.28) we then find

$$\Gamma \propto r^{\frac{2(\gamma-1)}{2-\gamma}}, \quad n \propto r^{-\frac{2}{2-\gamma}}, \quad \rho \propto r^{-\frac{2\gamma}{2-\gamma}}. \quad (\text{D.2.29})$$

For the ultrarelativistic equation of state with  $\gamma = 4/3$  we immediately obtain

$$\Gamma \propto r, \quad n \propto r^{-3}, \quad \rho \propto r^{-4}. \quad (\text{D.2.30})$$

Taking into account that the relation between the comoving and the physical coordinates in cosmology is given by the scale factor  $a$ , it follows from (D.2.30) that both energy density and baryonic number density behave as in the radiation dominated Universe, see (D.2.15). This analogy between the GRB source and the Friedmann Universe is noticed by Shemi and Piran (1990), Piran et al. (1993).

In the presence of baryons as the pressure decreases, plasma becomes matter dominated and expansion velocity saturates. Hence for the nonrelativistic equation of state with  $\gamma = 1$  different scaling laws come out

$$\Gamma = \text{const}, \quad n \propto r^{-2}, \quad \rho \propto r^{-2}. \quad (\text{D.2.31})$$

Transition between the two regimes (D.2.30) and (D.2.31) occurs at the radius  $R_c = B^{-1}R_0$ , where  $R_0$  is initial size of plasma.

Therefore, one may reach the conclusion that for comoving observer the radiation-dominated plasma looks indistinguishable from a portion of radiation-dominated Universe. However, this is true only in the absence of pressure gradients. Strong gradients are likely present in GRB sources, and they should produce local acceleration in the radiation-dominated electron-positron plasma, making it distinct from the early Universe, where matter inhomogeneities are known to be weak.

It is easy to get from (D.2.26) and (D.2.28) for internal energy density and temperature

$$\varepsilon \propto r^{-4}, \quad T \propto r^{-1}, \quad R_0 < r < R_c, \quad (\text{D.2.32})$$

and

$$\varepsilon \propto r^{-8/3}, \quad T \propto r^{-2/3}, \quad R_c < r < R_{tr}, \quad (\text{D.2.33})$$

where  $R_{tr}$  is the radius at which the outflow becomes transparent. The outflow may become transparent for photons also at the acceleration phase, provided that  $R_{tr} < R_c$ . For instance, a pure electron-positron plasma gets transparent at the acceleration phase.

### D.3. Heavy elements

Cosmological nucleosynthesis is a well established branch of cosmology. Classical computations made in the middle of the XXth century revealed that heavy elements cannot be built in the early Universe. Hydrogen and helium contribute approximately 3/4 and 1/4, leaving some room, much less than 1 per cent for deuterium, tritium and lithium. All the heavier elements must have been produced in stars.

Some of these stars, as indicated by observations, end their life as progenitors of GRBs. For this reason it is likely that initially in the source of GRBs elements heavier than hydrogen are present. In this section we consider chemical evolution of plasma in the sources of GRBs.

Assume that in the source of a GRB the amount of energy  $E_0$  is released in the volume with linear size  $R_0$  during the time  $\Delta t$ , making this region optically thick to Compton scattering and pair production. The amount of baryons which may be present as well is parametrized by

$$B \simeq \begin{cases} \frac{Mc^2}{E_0}, & \Delta t \ll R_0/c, \\ \frac{\dot{M}c^2}{L}, & \Delta t \gg R_0/c, \end{cases} \quad (\text{D.3.1})$$

where  $L = dE/dt$  is the luminosity,  $\dot{M} = dM/dt$  is the mass ejection rate and  $M$  is total baryonic mass. Ultrarelativistic outflow is generated through

thermal acceleration of baryons by the radiative pressure if plasma is initially energy dominated, i.e.

$$B \ll 1. \quad (\text{D.3.2})$$

In the case of instant energy release with  $\Delta t \ll R_0/c$  initial temperature in the source of GRB may be estimated neglecting the baryonic contribution, provided (D.3.2) is satisfied as

$$T_0 \simeq \left( \frac{3E_0}{4\pi a R_0^3} \right)^{1/4} \simeq 6.5 E_{54}^{1/4} R_8^{-3/4} \text{ MeV}, \quad (\text{D.3.3})$$

where  $a = 4\sigma_{SB}/c$ ,  $\sigma_{SB}$  is the Stefan-Boltzmann constant and the last value is obtained by substituting numerical values for  $E_0 = 10^{54} E_{54}$  erg and  $R_0 = 10^8 R_8$  cm.

As it has been shown in Kafexhiu (2010) for temperatures above 1 MeV even low density plasma with density  $n = 10^{18} \text{ cm}^{-3}$  quite quickly destroys all heavier nuclei, and the final state contains just protons and neutrons and some small traces of Deuterium and  $^4\text{He}$ . The timescale of this process ( $\sim 10^{-2}$  sec for  $T_0 = 1$  MeV) strongly depends on temperature, but the rates of almost all reactions increase with temperature, and correspondingly the abundances of nuclei evolve much faster. Therefore, nuclei disintegration is fast enough to occur before plasma starts to expand and cool on the timescale  $R_0/c$ .

During early stages of plasma expansion its temperature decreases in the same way as it happened in the early Universe. Therefore similar synthesis of light elements to BBN occurs also in sources of GRBs. Most important is, however, another similarity with the early Universe: it is well known that practically all free neutrons have been captured into elements heavier than hydrogen. So we do not expect dynamically important free neutrons present in GRB plasma after it started to expand and cool down unless they are engulfed by the expanding plasma later. The role of such free neutrons have been considered in the literature, see e.g. Derishev et al. (2000).

## **D.4. Recombination**

On the radiation dominated phase both in the early Universe and in GRB plasma entropy conservation (D.2.4) results in decrease of temperature (D.2.17). In the early Universe, after the BBN epoch and electron-positron annihilation, cosmological plasma consists of fully ionized hydrogen, helium and small admixture of other light elements. The temperature continues to decrease until it gets sufficiently low to allow formation of neutral atoms: that is the moment in the cosmic history where the formation of the Cosmic Microwave Background Radiation (CMB) happens.

The theory of cosmological recombination of hydrogen, based on three level approximation, has been developed by Zeldovich, Kurt and Sunyaev Zeldovich et al. (1968) and Peebles Peebles (1968) in the late 60s. The only modification that such theory undergone in the later years is the account for dark matter and addition of more levels to the model, currently about 300. There is a basic difference with respect to the equilibrium recombination essentially by the process  $e + p \leftrightarrow H + \gamma$ , described by the Saha equation

$$\frac{n_e n_p}{n_H} = \frac{g_e g_p}{g_H} \frac{(2\pi m_e kT)^{3/2}}{h^3} \exp\left(-\frac{E_i}{kT}\right), \quad (\text{D.4.1})$$

where  $g_i$  are statistical weights,  $h$  is Planck's constant,  $E_i = 13.6$  eV is hydrogen ionization energy. This difference is due to the presence of the  $2p$  quantum level, which produces Ly- $\alpha$  photons. The absorption of such photons is very strong. However, ionization from the  $2p$  level requires only  $E_i/4$ . Therefore the formation of neutral hydrogen proceed through the  $2s - 1s$  transition in the presence of abundant Ly- $\alpha$  photons.

In fact, the early Universe would become transparent for radiation even if formation of hydrogen would have been forbidden, see e.g. Naselsky et al. (2011). The optical depth to Thomson scattering is

$$\tau = \int_t^{t_0} \sigma_T n_b c dt \simeq 4 \times 10^{-2} \frac{\Omega_b}{\Omega_m} h \left\{ \left[ \Omega_\Lambda + \Omega_m (1+z)^3 \right]^{1/2} - 1 \right\}, \quad (\text{D.4.2})$$

where  $\sigma_T$  is the Thomson cross section,  $\Omega_i = \rho_i/\rho_c$ ,  $\rho_c = 3H^2 c^2/8\pi G$ ,  $H = 100h$  km s/Mpc and  $b, m, \Lambda$  stand for, respectively baryons, dark matter and cosmological constant contributions to the total energy density of the Universe. For large  $z$  we have

$$\tau(z_*) = 1, \quad z_* \simeq 8.4 \Omega_b^{-2/3} \Omega_m^{1/3} h^{-2/3}.$$

For typical values  $\Omega_b h^2 \simeq 0.02$ ,  $\Omega_m \simeq 0.3$ , and  $h \simeq 0.7$  we have  $z_* \simeq 60$ . At such redshift the Universe would be expected to become transparent to Thomson scattering. That is exactly what happens in plasma in GRB sources. Below we show that, unlike radiation-dominated cosmological expansion where comoving quantities also fulfill relations (D.2.32), the comoving temperature in GRB outflows remains always high enough to prevent recombination of hydrogen.

From (D.2.32) and (D.2.33) one can see that during both acceleration and coasting phases the comoving temperature decreases. However, when the outflow reaches the radius  $R_s = B^{-2} R_0$ , the comoving temperature saturates. It can be shown, see Ruffini et al. (2011) for details, using the expression for

the photospheric radius

$$R_{tr} = \left( \frac{\sigma E_0 B}{4\pi m_p c^2} \right)^{1/2}, \quad (\text{D.4.3})$$

where  $m_p$  and  $\sigma$  are proton mass and Thompson cross section, respectively. Indeed, using (D.3.3), (D.4.3), (D.2.32) and (D.2.33) we have

$$T_{\min} = BT_0 \left( \frac{R_c}{R_{tr}} \right)^{2/3} = \quad (\text{D.4.4})$$

$$= \left( \frac{3}{4\pi a} \right)^{1/4} \left( \frac{\sigma}{4\pi m_p c^2} \right)^{-1/3} (E_0 R_0)^{-1/12}. \quad (\text{D.4.5})$$

Notice how extremely insensitive this value is with respect to both  $E_0$  and  $R_0$ ! Expressed in units of typical energy and size

$$T_{\min}^{(s)} \simeq 42 (E_{54} R_8)^{-1/12} \text{ eV}. \quad (\text{D.4.6})$$

In the case of gradual energy release with  $\Delta t \gg R_0/c$  and constant luminosity and mass ejection rate the initial temperature is

$$T_0 \simeq \left( \frac{L}{16\pi\sigma_{SB}R_0^2} \right)^{1/4}, \quad (\text{D.4.7})$$

and similar expression to (D.4.4) may be derived

$$T_{\min} = \left( \frac{1}{16\pi\sigma_{SB}} \right)^{1/4} \left( \frac{\sigma}{4\pi m_p c^2} \right)^{-1/3} L^{-1/12} R_0^{1/6} \Delta t^{-1/3}, \quad (\text{D.4.8})$$

which may be rewritten, introducing  $L = 10^{50} L_{50}$  erg/s and  $\Delta t = 1\Delta t_1$  s, as

$$T_{\min}^{(w)} \simeq 17 L_{50}^{-1/12} R_8^{1/6} \Delta t_1^{-1/3} \text{ eV}. \quad (\text{D.4.9})$$

Even if (D.4.9) appears to be less stringent than (D.4.6), they are both quite insensitive to initial parameters. As a result, even if the comoving temperature decreases very much compared to its initial value, typically of the order of MeV, it saturates well above the ionization energy of hydrogen  $E_i = 13.6$  eV, thus preventing formation of neutral hydrogen. In fact, such hydrogen formed would not allow formation of the afterglow of GRBs. Indeed, even having ultrarelativistic velocities of expansion neutral hydrogen would not interact with the interstellar medium!

A simplified way to look at this lower bound on the comoving temperature is to say that if a fraction  $\epsilon$  of solar mass is released in the volume having

radius  $\delta$  solar Schwarzschild radii, then its minimum comoving temperature before transparency is

$$T_{\min}^{(s)} \simeq 66 (\epsilon\delta)^{-1/12} \text{ eV}, \quad (\text{D.4.10})$$

in the case of instant energy release and

$$T_{\min}^{(w)} \simeq 2.8\epsilon^{-1/12}\delta^{1/6}\Delta t_1^{-1/4} \text{ eV}, \quad (\text{D.4.11})$$

in the case of gradual energy release during time  $\Delta t_1$ . Clearly in both cases  $\delta > 1$ , and likely  $\epsilon < 1$ . Notice, that while in the case of instant energy release the lower bound on temperature decreases with increasing  $\delta$ , it instead increases in the case of gradual energy release.

Therefore, we have reached the conclusion that hydrogen recombination which is responsible for transparency of cosmological plasma does not happen in GRB plasma. This difference in physical conditions may result in deviations from black body spectrum, as observed in GRBs. Recently we presented a theory of photospheric emission from relativistic outflows, see Ruffini et al. (2011). Assuming that the spectrum of radiation in the comoving reference frame is the perfect black body one, we have shown that the spectrum seen by a distant observer may be essentially nonthermal due to both geometric and dynamical special relativistic effects. The possibility that the spectrum of photospheric emission is nonthermal also in the comoving frame should be investigated.

## D.5. Conclusions

Regarding the dynamical aspects, there is an apparent similarity between the electron-positron plasma in the early Universe and the one in GRB sources. For an observer comoving with the radiation-dominated plasma in GRB source it may look indistinguishable from a portion of radiation-dominated Universe. However, this is true only in the absence of pressure gradients. Strong gradients are likely present in GRB sources, and they should produce local acceleration in the radiation-dominated electron-positron plasma, making it distinct from the early Universe, where matter inhomogeneities are known to be weak.

There is also an apparent similarity with respect to the nucleosynthesis phenomenon. Given that the temperature reached in GRB sources, see Eq. (D.3.3), may be as high as several MeV, nuclear reactions are expected to operate on timescales of  $10^{-2}$  sec or shorter. That is on the order of magnitude of dynamical timescale of the GRB sources. It means that reprocessing of nuclear abundances may likely take place in GRB sources. Since observations imply that GRBs may originate from compact stellar objects elements heavier

than helium are likely to be present in GRB sources. Such heavy elements are then destroyed, resulting mainly in protons with small admixture of helium. Thus, similarly to the early Universe, we do not expect dynamically important free neutrons present in GRB plasma after it started to expand and cool down unless they are engulfed by the expanding plasma later.

Finally, there is an important difference between the electron-positron plasma in the early Universe and the one in GRB sources. We show in this paper that unlike the primordial plasma which recombines to form neutral hydrogen, and emits the Cosmic Microwave Background Radiation, GRB plasma does not cool down enough to recombine. Therefore GRB plasma becomes transparent due to Compton scattering. The kinetics of this process is different from the cosmic recombination. In particular, cosmic recombination is a photon non-conserving process, which results in an almost perfect black body spectrum of CMB. At the same time, Compton scattering, which is a dominant process at GRB transparency is a photon conserving process. This difference may result in deviations from the perfect thermal spectrum of emission to be observed when GRB plasma becomes transparent.

# E. Photospheric emission from relativistic outflows

## E.1. Introduction

High Lorentz factors of the bulk motion of various outflows are common in relativistic astrophysics. The best known examples are Active Galactic Nuclei (Maraschi, 2003), microquasars and Gamma-Ray Bursts (GRBs) (Piran, 2004). In the latter case outflows indeed reach ultrarelativistic velocities.

Various models are suggested to explain the acceleration of outflows to ultrarelativistic velocities. The electromagnetic model (Lyutikov, 2006) assumes that the energy in the source of GRB is converted into electromagnetic energy which is transported in the form of a Poynting flux. We adopt here another popular idea that the energy release leads to creation of an optically thick source which expands due to thermal acceleration. This idea is the basis of both the fireball (Piran (1999, 2004) and references therein) and the fireshell (Ruffini et al. (2001, 2009a) and references therein) models.

In pioneer works by Goodman (1986) who considered an instant explosion, and by Paczynski (1986) who discussed a gradual energy release, a conclusion was reached that the electron-positron plasma is created in the source of GRB. Assuming further that the plasma reaches thermal equilibrium they focused on hydrodynamic expansion in such models and gave photometric and spectroscopic predictions for GRBs. Later, baryonic loading of fireballs was considered for explosions by Shemi and Piran (1990) and for winds by Paczynski (1990). Abramowicz et al. (1991) considered the appearance of the photosphere of the relativistic wind to a distant observer showing that its shape is concave.

The interest in photospheric emission from relativistic winds has been revived recently in papers by Daigne and Mochkovitch (2002), Pe'er et al. (2007), Beloborodov (2011), Ryde et al. (2011), Pe'er and Ryde (2011), and others. In the fireshell model, which assumes an explosive energy release, the first potentially visible component of any GRB, the Proper GRB (Bianco et al., 2001; Ruffini et al., 2001), comes from the thermal flash of radiation emitted when the outflow becomes transparent for photons.

One of the main scopes of this paper is to show that the association of “instantaneous energy release” with “thin shell” (e.g. Piran et al. (1993) and Mészáros et al. (1993)) and “continuous energy release” with “thick wind”

(e.g. Paczynski (1986, 1990)) generally adopted in the literature is incomplete with respect to the photospheric emission. A unified treatment of ultrarelativistic outflows originating both from instantaneous and from continuous energy release is presented here. We also propose a new classification of such outflows which is complementary to the traditional division on shells and winds. When photospheric emission is considered this new classification provides some additional physical insights. Based on these results we present a semi-analytic treatment for observed flux of photospheric emission assuming isotropic thermal distribution of scattered photons in the comoving frame. We compute both instantaneous and time-integrated spectra. These results are then applied within both the shell and the wind models of GRBs. Remarkably the time-integrated spectrum of energetic GRBs is predicted to have a Band shape (Band et al., 1993).

The structure of the appendix is as follows. In Section 2 we discuss, compare and contrast an impulsive explosion and gradual energy release, giving rise respectively to an ultrarelativistic shell and wind. In Section 3 we present the computation of the optical depth and photospheric radius of the relativistic outflow and discuss applicability of recovered asymptotics to GRBs. In Section 4 we discuss radiation diffusion in an expanding relativistic outflow. Observed light curves and spectra of photon thick and photon thin outflows are computed in Sections 5 and 6, respectively. In Section 7 we discuss main results obtained in this work and their implications for GRBs. Conclusions follow.

## **E.2. Optically thick relativistic outflows: wind vs. explosion**

Relativistic outflows are generally classified as *winds* or *shells* depending on how fast the energy in their sources is released. Consider energy release in a source of linear dimension  $R_0$ . If the time scale of energy release is short  $\Delta t \simeq R_0/c$ , an explosion occurs, which may be characterized by the size  $R_0$ , total energy released  $E_0$  and total baryonic mass  $M$ . Relativistically expanding material forms a shell having width approximately  $R_0$ . When the energy is released gradually, on a time scale  $\Delta t \gg R_0/c$ , but the source luminosity  $L$  exceeds the Eddington limit, a wind is formed, which is characterized by its activity time  $\Delta t$ , luminosity  $L$  and mass ejection rate  $\dot{M}$ .

In both wind and shell models of cosmological GRBs the region of energy release  $R_0$  is clearly macroscopic, being of the order of the size of compact astrophysical objects, about  $R_0 \sim 10^8$  cm. Considering the isotropic energy involved  $E_0 \sim 10^{54}$  erg the temperature of plasma in this region is typically in MeV range. The time scale of thermalization in such plasma is of the order of  $10^{-12}$  sec (Aksenov et al., 2007, 2010), being much shorter than the dy-

namical time scale  $R_0/c$ . Since such dense plasma is optically thick thermal equilibrium is established prior to expansion in both shell and wind models. Opacity in such plasma is dominated by Compton scattering. When the temperature in the source of the relativistic outflow is large enough for electron-positron pair creation,  $e^+e^-$  pairs make an additional contribution to the opacity.

Whether the outflow becomes relativistic or not depends on the entropy in the region where the energy is released. Both the wind and explosion cases can be parameterized (Shemi and Piran, 1990) by a dimensionless entropy parameter  $\eta$ , equal to  $E_0/Mc^2$  for shell model and  $L/\dot{M}c^2$  for wind model. When the baryonic loading  $B = \eta^{-1}$  (Ruffini et al., 2000) is sufficiently small the baryons will be accelerated to a relativistic velocity  $v$  of bulk motion, attaining large Lorentz factors up to  $\Gamma = [1 - (v/c)^2]^{-1/2} \simeq \eta$ , while in the opposite case of large baryonic loading the outflow remains nonrelativistic with  $v \simeq c/\sqrt{2\eta}$ .

In what follows we consider only ultrarelativistic spherically symmetric outflows with  $\Gamma \gg 1$ . In the simplest cases of wind or explosion in vacuum, the dynamics of the outflow is divided into an acceleration phase and a coasting phase (Piran, 1999) with respectively

$$\Gamma \simeq \frac{r}{R_0}, \quad n_c \simeq n_0 \left( \frac{r}{R_0} \right)^{-3}, \quad R_0 < r < \eta R_0, \quad (\text{E.2.1})$$

$$\Gamma \simeq \eta = \text{const}, \quad n_c \simeq \frac{n_0}{\eta} \left( \frac{r}{R_0} \right)^{-2}, \quad r > \eta R_0, \quad (\text{E.2.2})$$

where  $n_c$  is the comoving number density of baryons in the outflow<sup>1</sup>. Notice that in the case of an impulsive explosion for  $r \gg R_0$  the matter and energy appear to a distant observer to be concentrated in a *geometrically thin shell* having width  $l \sim R_0$  due to the relativistic contraction (Piran et al., 1993).

It is important to stress that both *an infinitely long wind* with a time-independent mass ejection rate and luminosity on the one hand, and *an infinitely thin shell* originating from an instantaneous explosion in infinitely thin region represent two limiting cases for the energy release.

During both acceleration and coasting phases the continuity equation for the laboratory number density reduces to  $n \propto r^{-2}$ . We take for the laboratory

---

<sup>1</sup>All quantities with subscript "c" are measured in comoving reference frame, and all quantities without this subscript are measured in laboratory reference frame.

density profile

$$n = \begin{cases} n_0 \left( \frac{R_0}{r} \right)^2, & R(t) < r < R(t) + l, \\ 0, & \text{otherwise,} \end{cases} \quad (\text{E.2.3})$$

where  $R(t)$  is the radial position of the inner boundary of the outflow. Such an outflow may be produced by a gradual energy release with constant luminosity and mass ejection rate on a finite time  $\Delta t$  and we will refer to it as the *portion of wind*.

Below we show that both the shell and the wind defined above may appear for photons emitted inside it as long wind or as thin shell, depending on the initial conditions that specify respectively their width  $l$  and activity duration  $\Delta t$ . This appearance is a consequence of ultrarelativistic expansion of the outflow. It is crucial to keep in mind that photons emitted inside the expanding outflow propagate in a medium whose laboratory number density depends both on radial coordinate and on time  $n(r, t)$ . For photons propagating in the wind the spatial dependence of the number density plays the key role, while for photons propagating in the shell its time dependence is crucial.

### E.3. Optical depth and photospheric radius

The optical depth along the photon world line  $\mathcal{L}$  is defined as

$$\tau = \int_{\mathcal{L}} \sigma j_{\mu} dx^{\mu}, \quad (\text{E.3.1})$$

where  $\sigma$  is Thomson cross section,  $j^{\mu}$  is the 4-current of particles, on which the photon scatters, and  $dx^{\mu}$  is the element of the photon world line.

Consider a spherically symmetric expanding outflow with an ultrarelativistic velocity  $v = \beta c \simeq 1 - 1/2\Gamma^2$ . Assume that the photon is emitted at time  $t$  from the interior boundary  $r = R$  of the outflow and it propagates outwards. This assumption is relaxed in Section E.5.1. The optical depth computed along the photon path from (E.3.1) is (see e.g. Abramowicz et al. (1991))

$$\tau = \int_R^{R+\Delta R} \sigma n (1 - \beta \cos \theta) \frac{dr}{\cos \theta}, \quad (\text{E.3.2})$$

where  $R + \Delta R$  is the radial coordinate at which the photon leaves the outflow, and  $\theta$  is the angle between the velocity vector of the outflow and the direction of propagation of the photon,  $n$  is the laboratory number density of electrons and positrons, which may be present due to pair production. Geometry of the outflow and used variables are illustrated by Fig. E.1.

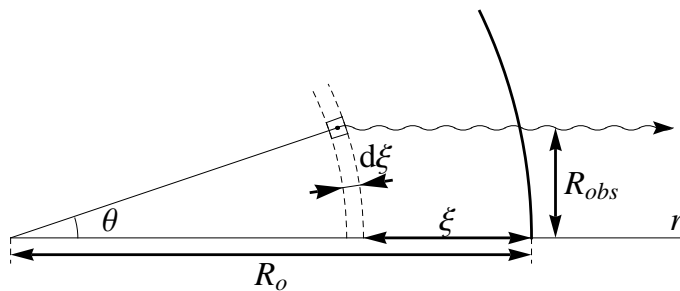


**Figure E.1.:** Geometry of the outflow and variables used. Observer is located to the right at infinity.

A pure electron-positron plasma reaches thermal equilibrium before expansion (Aksenov et al., 2007, 2010) and it remains accelerating until it becomes transparent to radiation. Due to exponential dependence of thermal pair density on the radial coordinate transparency is reached at

$$kT_{\pm} \simeq 0.040m_e c^2 \quad (\text{E.3.3})$$

rather independent of the initial conditions. Note that the optical depth for an expanding electron-positron-photon shell computed by Shemi and Piran (1990) is incorrect since it uses photon thin asymptotics, see 3rd line in (E.3.4) below, which never applies to the pure  $e^+e^-$  outflows. The formula (E.3.3) is in agreement with works of Grimsrud and Wasserman (1998) and Li and Sari (2008).

Electron-positron plasma with baryonic loading also reaches thermal equilibrium before its expansion starts (Aksenov et al., 2009, 2010). With decreasing entropy  $\eta$  opacity due to electrons associated with baryons increases and eventually dominates over pair opacity. Straightforward calculations with the laboratory density profile (E.2.3) gives

$$\tau = \begin{cases} \frac{1}{6}\tau_0 \left(\frac{R_0}{R}\right)^3, & R_0 \ll R \ll \eta R_0, \\ \frac{1}{2\eta^2}\tau_0 \left(\frac{R_0}{R}\right), & \eta R_0 \ll R \ll \eta^2 l, \\ \tau_0 \frac{R_0 l}{R^2}, & R \gg \eta^2 l, \end{cases} \quad (\text{E.3.4})$$

where

$$\tau_0 = \sigma n_0 R_0 = \frac{\sigma E_0}{4\pi m_p c^2 R_0 l \eta} = \frac{\sigma L}{4\pi m_p c^3 R_0 \eta}. \quad (\text{E.3.5})$$

Let us interpret the formula (E.3.4). On the one hand, first two lines in

**Table E.1.:** Dependencies of transparency parameters on initial conditions: energy  $E_0$ , entropy  $\eta$ , and radius  $R_0$  for the shell model.

| Regime of transparency | $R_{ph}$    |               |             | $\Gamma_{ph}$ |               |              | $kT_{ph}$      |              |               | $kT_{obs}$    |              |               |
|------------------------|-------------|---------------|-------------|---------------|---------------|--------------|----------------|--------------|---------------|---------------|--------------|---------------|
| Pair                   | $E_0^{1/4}$ |               | $R_0^{1/4}$ | $E_0^{1/4}$   |               | $R_0^{-3/4}$ | $0.040m_e c^2$ |              |               | $E_0^{1/4}$   |              | $R_0^{-3/4}$  |
| Acceleration           | $E_0^{1/3}$ | $\eta^{-1/3}$ | $R_0^{1/3}$ | $E_0^{1/3}$   | $\eta^{-1/3}$ | $R_0^{-2/3}$ | $E_0^{-1/12}$  | $\eta^{1/3}$ | $R_0^{-1/12}$ | $E_0^{1/4}$   |              | $R_0^{-3/4}$  |
| Coasting photon thick  | $E_0$       | $\eta^{-3}$   | $R_0^{-1}$  |               | $\eta$        |              | $E_0^{-5/12}$  | $\eta^{5/3}$ | $R_0^{7/12}$  | $E_0^{-5/12}$ | $\eta^{8/3}$ | $R_0^{7/12}$  |
| Coasting photon thin   | $E_0^{1/2}$ | $\eta^{-1/2}$ |             |               | $\eta$        |              | $E_0^{-1/12}$  |              | $R_0^{-1/12}$ | $E_0^{-1/12}$ | $\eta$       | $R_0^{-1/12}$ |

(E.3.4) correspond to the case when the photon propagates inside the outflow for a significant time so that the number density on its path substantially decreases before it leaves. In this respect the outflow is “a long wind”, even if the laboratory thickness of the outflow may be small,  $l \ll R$ . We refer to this case as a *photon thick outflow*. On the other hand, the third line in (E.3.4) corresponds to the case when the number density of the outflow does not change substantially on the photon world line before it escapes. In this respect the outflow is “a thin shell” even if the duration of explosion could be long and a wind was launched. We refer to this latter case as a photon thin outflow. For instance, a geometrically thin ultrarelativistically expanding shell may be both thin or thick with respect to the photon propagating inside it.

Similar consideration may be applied to a photon emitted at any distance  $\zeta$  from the outer boundary of the outflow, see Section E.5.1. It is clear then, that even in a photon thick outflow there is always a photon thin layer located near the outer boundary. During acceleration phase such a photon thin part accounts for a fraction not larger than  $\Gamma^{-1}$  of the entire width of the outflow<sup>2</sup>.

In the derivation of (E.3.4) we considered a portion of a relativistic wind, but these results are generic and apply to any density profile of the outflow.

The *photospheric radius*  $R_{ph}$  is defined by equating (E.3.4) to unity. It is worth noting that it is the lower limit in the integral (E.3.2) that is associated with the photospheric radius, but not the upper one. The upper limit in (E.3.2) is the radius at which the photon leaves the outflow, even if it may decouple from the outflow at much smaller radius, as in the photon thick case. The characteristic parameter which determines the type of the outflow at the photospheric radius is the ratio  $\tau_0/(4\Gamma^4)$ . When it is much smaller than one the outflow is photon thick, while in the opposite case the outflow is photon thin.

Consider now the shell model of GRBs with typical parameters expressing their total energy as  $E_0 = 10^{54} E_{54}$  erg, initial size as  $R_0 = l = 10^8 R_8$  cm and entropy parameter as  $\eta = 10^2 \eta_2$ . We find the following asymptotic solutions

<sup>2</sup>Formally photon thin accelerating solution exists, and it is given by the last line in (E.3.4). However, its validity condition is  $l \ll R_0^2/R = R_0/\Gamma$ .

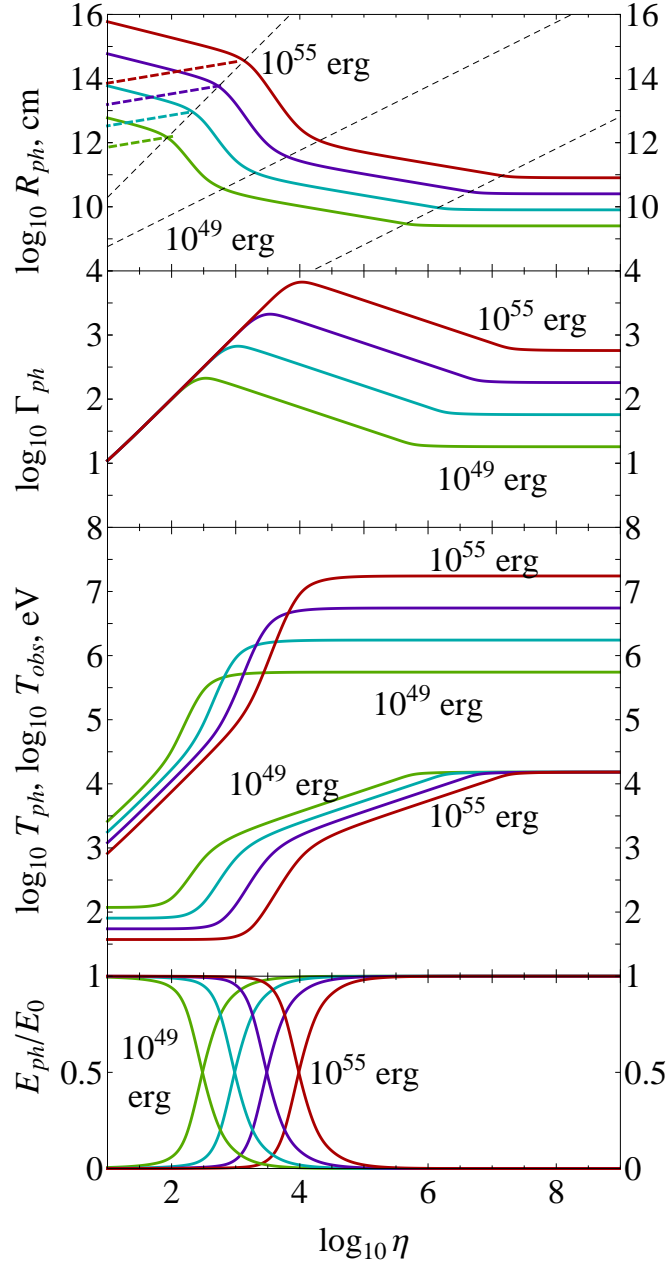
for the photospheric radius together with domains of their applicability

$$R_{ph} = \left\{ \begin{array}{l} 4.4 \times 10^{10} (E_{54} R_8)^{1/4} \text{ cm}, \\ \qquad \qquad \qquad E_{54} \ll 4.8 \times 10^{-20} \eta_2^4 R_8^{-1}, \\ \hline 1.8 \times 10^{12} (E_{54} \eta_2^{-1} R_8)^{1/3} \text{ cm}, \\ 4.8 \times 10^{-20} \eta_2^4 R_8^{-1} \ll E_{54} \ll 3.2 \times 10^{-8} \eta_2^4 R_8^2, \\ \hline 1.8 \times 10^{17} E_{54} \eta_2^{-3} R_8^{-1} \text{ cm}, \\ 3.2 \times 10^{-8} \eta_2^4 R_8^2 \ll E_{54} \ll 1.1 \times 10^{-5} \eta_2^5 R_8^2, \\ \hline 5.9 \times 10^{14} (E_{54} \eta_2^{-1})^{1/2} \text{ cm}, \\ \qquad \qquad \qquad E_{54} \gg 1.1 \times 10^{-5} \eta_2^5 R_8^2. \end{array} \right. \quad (\text{E.3.6})$$

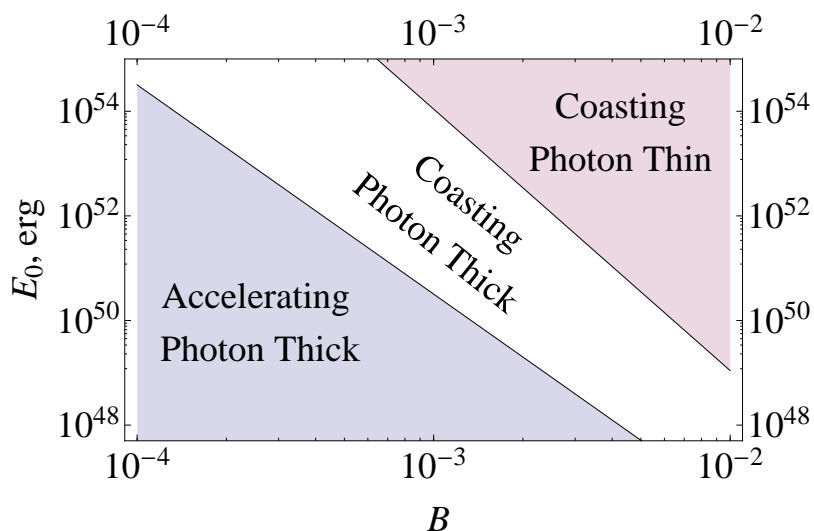
For very small baryonic loading, or in other words for a pure electron-positron plasma, the photospheric radius does not depend on  $\eta$  parameter. For increasing baryonic loading it increases as  $\eta^{-1/3}$  (accelerating photon thick solution). In both these cases the Lorentz factor at the photosphere is not equal to  $\eta$ , but it is much smaller. For larger baryonic loading the photospheric radius steeply increases as  $\eta^{-3}$  (coasting photon thick solution), and finally it increases as  $\eta^{-1/2}$  (coasting photon thin solution), see Fig. E.2. There we also show as function of the entropy parameter the following quantities computed at the photospheric radius: the Lorentz factor, the observed and co-moving temperatures, and fraction of energy emitted from the photosphere to the total energy, for different values of the total energy  $E_0$ . Dependence of parameters of transparency on initial conditions is also illustrated in Tab. E.1. It is clear that the highest Lorentz factors at photospheric radius are attained in photon thick asymptotics. The largest transparency radii are reached instead in photon thin asymptotics.

Fig. E.3 shows the energy-baryonic loading diagram, where the regions of validity of the asymptotics discussed above are indicated explicitly for typical parameters of GRBs. For all the relevant range of GRBs parameters  $10^{48} \text{ erg} < E_0 < 10^{55} \text{ erg}$  and  $10^6 \text{ cm} < R_0 < 10^{12} \text{ cm}$  all four asymptotics are present in the interval  $10 < \eta < 10^{10}$ .

In the case of gradual energy release resulting in relativistic wind an addi-



**Figure E.2.:** From top to bottom: photospheric radius  $R_{ph}$ , Lorentz factor  $\Gamma_{ph}$ , observed  $T_{obs}$  and comoving  $T_{ph}$  temperatures, and ratio of the energy emitted to the total energy  $E_{ph}/E_0$  at photospheric radius as functions of entropy  $\eta$  for shells with different total energy  $E_0$  but the same width  $l = R_0 = 10^8$  cm. All four regimes with different asymptotics are clearly visible and dashed black lines corresponding to their domain of validity from Eq. (E.3.6) are shown. Curves are drawn for  $E_0$  equal to:  $10^{49}$  erg (green),  $10^{51}$  erg (blue),  $10^{53}$  erg (violet), and  $10^{55}$  erg (red). Dashed thick lines denote the diffusion radius for each energy.



**Figure E.3.:** The energy-baryonic loading diagram showing the validity of the various asymptotic solutions for the photospheric radius for typical parameters of GRBs with  $l = R_0 = 10^8$  cm.

tional parameter is present, that is the duration of energy release, which we parameterize as  $\Delta t = 1\Delta t_1$  s. Instead of the total energy  $E_0$  the luminosity  $L = 10^{50}L_{50}$  erg/s is used. The corresponding photospheric radius is

$$R_{ph} = \left\{ \begin{array}{l} 8.1 \times 10^8 L_{50}^{1/4} R_8^{1/2} \text{ cm}, \\ \quad L_{50} \ll 5.3 \times 10^{-15} \eta_2^4 R_8^{-2}, \\ \hline 1.3 \times 10^{10} \left( L_{50} \eta_2^{-1} R_8^2 \right)^{1/3} \text{ cm}, \\ \quad 5.3 \times 10^{-15} \eta_2^4 R_8^{-2} \ll L_{50} \ll 9.8 \times 10^{-2} \eta_2^4 R_8, \\ \hline 5.9 \times 10^{10} L_{50} \eta_2^{-3} \text{ cm}, \\ \quad 9.8 \times 10^{-2} \eta_2^4 R_8 \ll L_{50} \ll 10^5 \eta_2^5 \Delta t_1, \\ \hline 5.9 \times 10^{12} \left( L_{50} \Delta t_1 \eta_2^{-1} \right)^{1/2} \text{ cm}, \\ \quad L_{50} \gg 10^5 \eta_2^5 \Delta t_1. \end{array} \right. \quad (\text{E.3.7})$$

**Table E.2.:** Dependencies of transparency parameters on initial conditions: energy release rate  $L$ , entropy  $\eta$ , duration  $\Delta t$ , and radius  $R_0$  for the wind model.

| Regime of transparency | $R_{ph}$  |               | $\Gamma_{ph}$    |               |              | $kT_{ph}$      |                   |              | $kT_{obs}$  |              |                   |
|------------------------|-----------|---------------|------------------|---------------|--------------|----------------|-------------------|--------------|-------------|--------------|-------------------|
| Pair                   | $L^{1/4}$ | $R_0^{1/2}$   | $L^{1/4}$        | $R_0^{-1/2}$  |              | $0.040m_e c^2$ |                   |              | $L^{1/4}$   |              | $R_0^{-1/2}$      |
| Acceleration           | $L^{1/3}$ | $\eta^{-1/3}$ | $L^{1/3}$        | $\eta^{-1/3}$ | $R_0^{-1/3}$ | $L^{-1/12}$    | $\eta^{1/3}$      | $R_0^{-1/6}$ | $L^{1/4}$   |              | $R_0^{-1/2}$      |
| Coasting photon thick  | $L$       | $\eta^{-3}$   |                  | $\eta$        |              | $L^{-5/12}$    | $\eta^{5/3}$      | $R_0^{1/6}$  | $L^{-5/12}$ | $\eta^{8/3}$ | $R_0^{1/6}$       |
| Coasting photon thin   | $L^{1/2}$ | $\eta^{-1/2}$ | $\Delta t^{1/2}$ | $\eta$        |              | $L^{-1/12}$    | $\Delta t^{-1/3}$ | $R_0^{1/6}$  | $L^{-1/12}$ | $\eta$       | $\Delta t^{-1/3}$ |

In Fig. E.4 we show as function of the entropy parameter the following quantities computed at the photospheric radius: the Lorentz factor, the observed and comoving temperatures, and fraction of energy emitted from the photosphere to the total energy, for different duration of the wind with the total energy  $E_0 = 10^{51}$  erg, and inner boundary radius  $R_0 = 10^8$  cm. Wind duration ranges from 10 ms to 10 s. The corresponding wind luminosity varies from  $10^{53}$  erg/s to  $10^{50}$  erg/s. Fig. E.5 shows the luminosity-baryonic loading diagram where the regions of validity of the asymptotics discussed above are indicated. Dependence of transparency parameters on the initial conditions of the wind is presented in Tab. E.2.

### E.3.1. Comparison with previous works

The expressions for the optical depth of a relativistic wind were obtained e.g. by Mészáros and Rees (2000). Their formulas coincide with our (E.3.4) up to a numerical factor which comes from the integration over the radial coordinate. It should be noted, however, that only the photon thick asymptotic limit is discussed in Mészáros and Rees (2000). The photon thin asymptotic limit may also be valid for relativistic winds in the coasting phase, provided that  $l \ll R/(2\eta^2)$ . This is an independent condition from  $\Delta t \gg R_0/c$  and it is therefore possible to give the following constraints for  $\Delta t$  under which the outflow takes the form of a wind, but it is photon thin at the photospheric radius:

$$\frac{R_0}{c} \ll \Delta t \ll \frac{\tau_0}{4\eta^4} \frac{R_0}{c}. \quad (\text{E.3.8})$$

photospheric radius for photon thick and photon thin asymptotics for a portion of the coasting relativistic wind was obtained by Daigne and Mochkovitch (2002).

Similar considerations apply to an ultrarelativistic shell which is considered e.g. in Shemi and Piran (1990) and Mészáros et al. (1993) and by Ruffini et al. (2000) in the photon thin approximation. The corresponding condition that the shell at the photospheric radius appears to be photon thin is  $\tau_0 \gg 4\eta^4$ . It is possible, however, that initial conditions satisfy the opposite constraint which results in a photon thick shell, see Nakar et al. (2005).

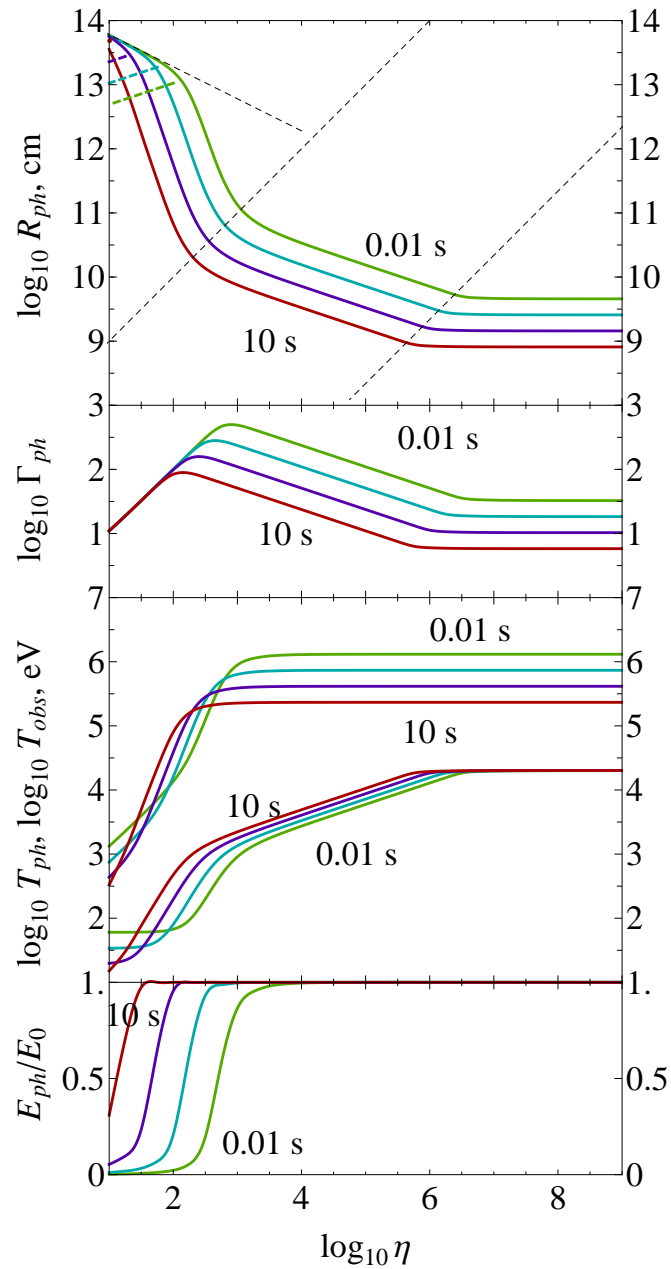


**Figure E.4.:** The same as in Fig. E.2 for winds with different duration, but the same total energy  $E_0 = 10^{51}$  erg and radius of origin  $R_0 = 10^8$  cm. All four regimes with different asymptotics are clearly visible. Curves are drawn for  $\Delta t$  ranging from  $10^{-2}$  s (green) to 10 s (red) in steps of one order of magnitude.

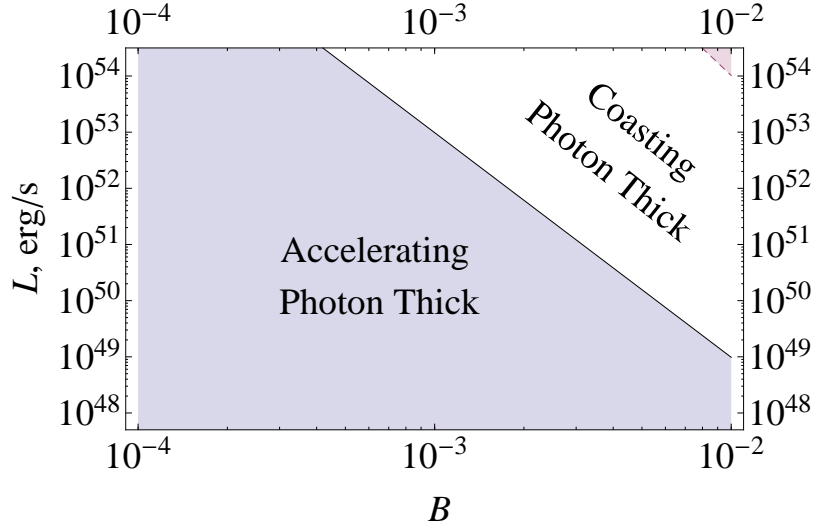


**Figure E.5.:** The luminosity-baryonic loading diagram showing the validity of the various asymptotic solutions for photospheric radius of wind with duration  $\Delta t = 0.1$  s. Notation is the same as on Fig. E.3.

Numerical hydrodynamic simulations produce complex density, temperature and Lorentz factor profiles of the outflow. In particular, Piran et al. (1993) and Mészáros et al. (1993) considered an explosion in a compact region with radius  $R_0$  and studied numerically the hydrodynamic evolution of an optically thick plasma with various initial conditions. They have shown that the plasma forms a relativistically expanding shell with some density and velocity profiles. The characteristic width of the density profile appears to be constant up to large radii, but later it increases linearly with radius due to the fact that the Lorentz factor appears to be monotonically increasing within the main part of the profile

$$l \simeq R_0, \quad R < \eta^2 R_0, \quad (\text{E.3.9})$$

$$l \propto R, \quad R > \eta^2 R_0. \quad (\text{E.3.10})$$

Such a spreading in density profile may result in a substantial increase in the width  $l \gg R_0$  of the shell when it becomes transparent to radiation. Note that condition (E.3.10) coincides with the condition in the third line of (E.3.4), which corresponds to the case of a photon thin outflow. This coincidence may give an impression that photon thin asymptotics does not exist for hydrodynamically spreading outflows. Nevertheless direct integration of (E.3.2) in numerical simulations shows that the photon thin asymptotics is valid even for the shell undergoing such spreading.

All asymptotic solutions for the optical depth have been considered by Mészáros et al. (2002), except the case of pure electron-positron outflow. They derived the photospheric radius considering the expansion in comov-

ing reference frame. Notice, that the photon thin asymptotics is obtained in Mészáros et al. (2002) by assuming hydrodynamic spreading of the outflow found by the same authors in (Mészáros et al., 1993). In absence of such spreading (e.g. portion of wind considered above) such asymptotics cannot be obtained this way. Finally, Toma et al. (2011) discuss all asymptotic solutions, applying them to a relativistic wind.

We conclude that interpretation of the formula (E.3.4) in terms of photon thick and photon thin conditions given above provides additional physical insight to the consideration of optical depth in shell and wind models.

## E.4. Photon diffusion

Up to now we assumed that photons escape the expanding outflow when its optical depth decreases to unity. We have distinguished two possibilities:

- in the photon thick case electron number density decreases along the photon path so rapidly that the medium becomes too rarified to sustain collisions. Most photons however still remain inside the outflow after decoupling;
- in the photon thin case the variation of the electron number density along the photon path can be neglected, but the mean free path of photons increases with expansion and eventually exceeds the radial thickness of the outflow.

In all the previous discussion we explicitly neglected the effect of radiative diffusion out of the outflow by random walks of photons. Diffusion time is given by  $t_{D,c} = l_c^2/D_c$ , where  $l_c = \Gamma l$  is the comoving radial thickness of the outflow, and diffusion coefficient is  $D_c = (c\lambda_c)/3 = c/(3\sigma n_c)$ , where  $\lambda_c$  and  $n_c$  are comoving mean free path of photons and comoving electron number density, respectively.

In order to determine at which radii diffusion becomes important one has to compare this diffusion time with comoving expansion time of the outflow  $t_c = R/(c\Gamma)$ . Taking into account (E.2.3) and (E.3.5) we obtain that it happens when the outflow reaches the radius

$$R_D = \left(\tau_0 \eta^2 R_0 l^2\right)^{1/3} \simeq \begin{cases} 7.2 \times 10^{13} (E_{54} l_8 \eta_2)^{1/3} \text{ cm,} \\ 2.2 \times 10^{13} (L_{50} \Delta t_1^2 \eta_2)^{1/3} \text{ cm.} \end{cases} \quad (\text{E.4.1})$$

This diffusion radius turns out to be always larger than the photospheric radius of photon thick outflows,  $R_D \gg R_{ph}$ , so that diffusion is irrelevant for their description. In the opposite case of photon thin outflows instead the diffusion radius is always smaller than the photospheric radius  $R_D \ll R_{ph}$ .

In this case most radiation leaves the photon thin outflow not at its photospheric radius, but before it reaches the diffusion radius, when the outflow is still opaque. In other words, the decoupling of photons from the outflow occurs not locally, as in the photon thick case, but near its boundaries where photons are transferred to by diffusion. In this sense the characteristic radius of the photospheric emission is not the photospheric radius found from (E.3.4), but the radius of diffusion (E.4.1). Besides, the comoving temperature of escaping radiation is different from that discussed in Section E.3.

In what follows we consider decoupling of photons from photon thick and photon thin outflows separately.

## **E.5. Photospheric emission from photon thick outflows**

### **E.5.1. Geometry and dynamics of the photosphere**

Unlike traditional static sources usually dealt with in astrophysics, relativistic outflows may have strongly time-varying photospheres. For the portion of wind the optical depth can be calculated analytically both at acceleration and coasting phases for photon thin and photon thick outflows. The result is

$$\tau(r, \theta, t) = \tau_0 R_0 \left\{ \frac{1}{r \sin \theta} \left[ \theta - \tan^{-1} \left( \frac{r \sin \theta}{cT + r \cos \theta} \right) \right] - \beta_m \left( \frac{1}{r} - \frac{1}{\sqrt{(cT + r \cos \theta)^2 + (r \sin \theta)^2}} \right) + \frac{R_0^2}{6} \left( \frac{1}{r^3} - \frac{1}{[(cT + r \cos \theta)^2 + (r \sin \theta)^2]^{3/2}} \right) \right\}, \quad (\text{E.5.1})$$

where  $T$  is the time interval during which photon remains inside the outflow, determined by the equations of motion of the photon and of the outflow, and  $\beta_m = 1 - 1/(2\eta^2)$ . For a given laboratory time  $t$  the photosphere geometry  $r = r(\theta)$  is obtained by equating (E.5.1) to unity. Then formula (E.5.1) gives complete information on the dynamics and geometry of the photosphere of portion of ultrarelativistic wind. In order to understand this dynamics it is instructive to consider its limiting cases.

Firstly, the photosphere of the coasting infinitely long relativistic wind with  $\Gamma = \text{const}$  analyzed by Abramowicz et al. (1991) may be recovered from (E.5.1) with  $T \rightarrow \infty$ . In that case the last term in (E.5.1) can be neglected

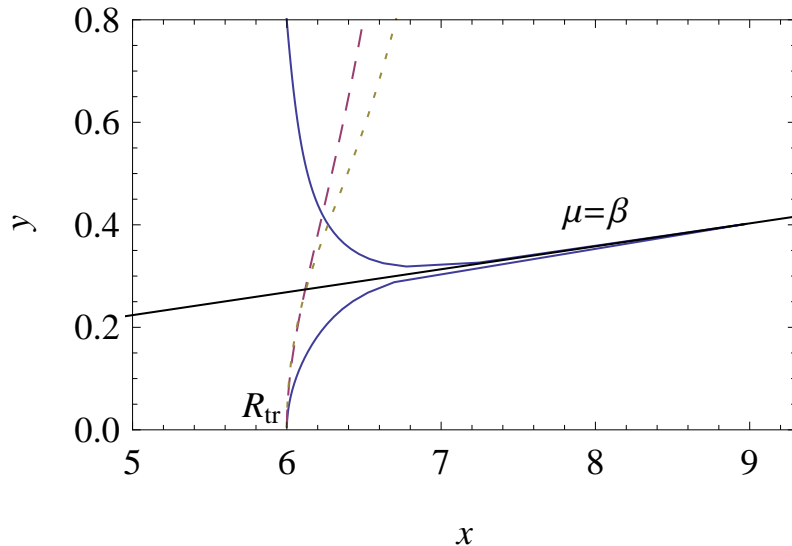


**Figure E.6.:** The shape of photospheres of infinitely long coasting (blue solid curve) and accelerating (black dotted curve) winds for  $\Gamma_{ph} = 100$ . Dashed line shows the relativistic beaming angle.

and we have (see e.g. Pe'er (2008))

$$\frac{r}{R_0} = \tau_0 \left( \frac{\theta}{\sin \theta} - \beta_m \right), \quad (\text{E.5.2})$$

which is a static surface having concave shape, see Fig. E.6.

Secondly, the photosphere of the accelerating infinite wind may be obtained from (E.5.1) for  $T \rightarrow \infty$  and  $\eta \rightarrow \infty$ . It results in a cubic equation describing a static surface with curvature larger than that of the coasting wind, see Fig. E.6. In both cases these photospheres appear for a distant observer as static spots with radius

$$\rho = \pi \tau_0 R_0 \quad (\text{E.5.3})$$

and brightness decreasing from the center to the edge.

Now consider dynamic properties of the photosphere of photon thick outflow described by (E.5.1) as seen by a distant observer. The arrival time of radiation is defined as  $t_a = t - r \cos \theta / c$ . The equitemporal surface (EQTS) of the photospheric emission represents a part of the photosphere visible at a given instant of arrival time  $t_a$ , see e.g. Ruffini et al. (2001). We will refer to that surface as *Photospheric EQTS* (PhE).

PhE of the photon thick outflow has concave shape, see Fig. E.7 and Fig. E.8 for accelerating and coasting cases, respectively. This concave PhE in both cases approaches the photosphere of infinitely long wind. In the coasting case the approach to that surface is only asymptotic, while in the accelerating case

the photosphere actually reaches it at finite arrival time. The external boundary of the PhE for a given  $t_a$  shown in Fig. E.8 is defined by the condition that the optical depth for photons emitted from the outermost layer of the outflow equals unity. Notice that this boundary is wider than the relativistic beaming surface (these are tube and cone for accelerating and coasting outflows, respectively). As soon as the innermost part of the outflow reaches the photospheric radius, i.e. observer sees the switching off of the wind, the inner boundary of the PhE expands with  $t_a$ . The surface of these boundaries is given by (E.5.2) in the case of coasting photon thick outflow.

### E.5.2. Observed flux and spectrum

The basis of spectrum and flux calculation is radiative transfer equation for specific intensity  $I_\nu$  along the ray (see e.g. Rybicki and Lightman (1979), p. 11)

$$\frac{dI_\nu}{ds} = j_\nu - \kappa_\nu I_\nu, \quad (\text{E.5.4})$$

where  $j_\nu$  is monochromatic emission coefficient,  $\kappa_\nu$  is absorption coefficient and  $s$  is distance, measured along the ray.

Spectral intensity of radiation at infinity on a ray coming to observer at some arrival time  $t_a$  is given by formal solution of this equation

$$\begin{aligned} I_\nu(\nu, \rho, t_a) &= \int \mathcal{J}_\nu(\nu, r, \theta, t) \frac{d}{ds} \{ \exp[-\tau(\nu, r, \theta, t)] \} ds \\ &= \int \mathcal{J}_\nu(\nu, r, \theta, t) \exp[-\tau(\nu, r, \theta, t)] d\tau, \end{aligned} \quad (\text{E.5.5})$$

where  $\mathcal{J}_\nu(r, \theta, t)$  is the source function, equal to the ratio of emission and absorption coefficients  $\mathcal{J}_\nu = j_\nu/\kappa_\nu$ , optical depth  $\tau$  is an integral of  $\kappa_\nu$  from the point on the ray under consideration to infinity  $\tau = \int \kappa_\nu ds$ , and variables  $(r, \theta, t)$  are connected by  $t_a = t - r \cos \theta$  and  $r \sin \theta = \rho$ , see Fig. E.1. We use Thomson scattering cross section in comoving frame  $\kappa_c = \text{const}$ .

Total observed flux is an integral over all rays

$$F_\nu(\nu, t_a) = 2\pi\Delta\Omega \int \rho d\rho I_\nu(\nu, \rho, t_a) \quad (\text{E.5.6})$$

where  $\Delta\Omega$  is the solid angle of the observer's detector as seen from the outflow in the laboratory frame and  $2\pi\rho d\rho$  is an element of area in the plane of the sky.

In what follows we assume that emissivity  $j_\nu$  is thermal and isotropic in

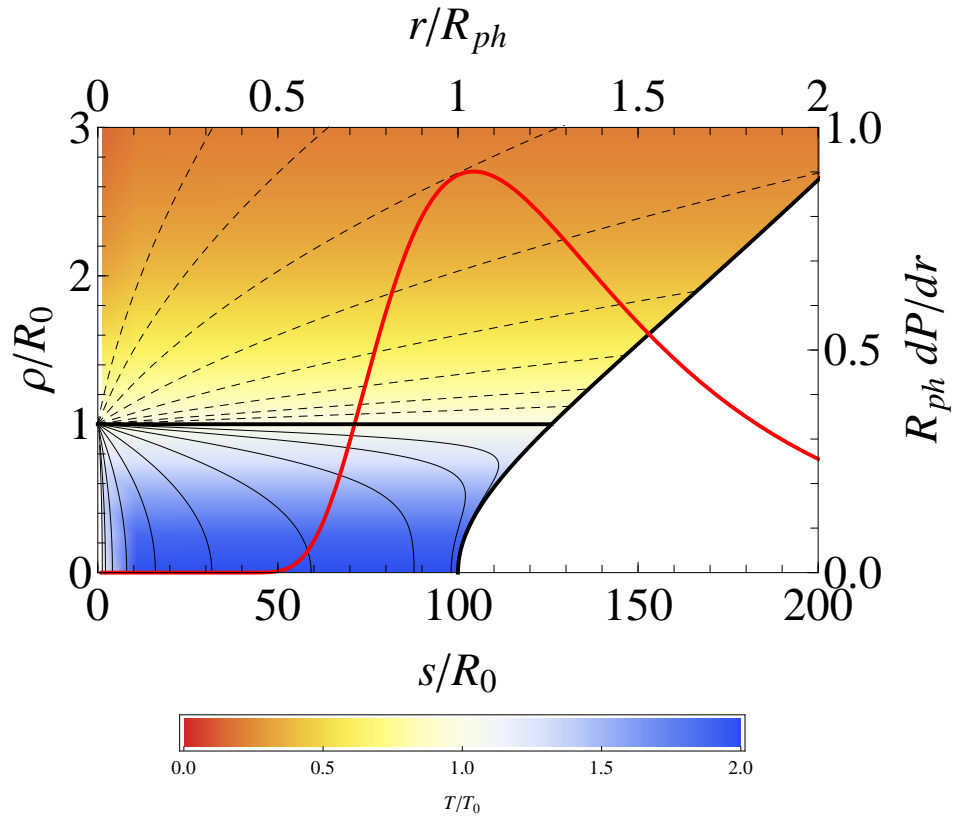


**Figure E.7.:** PhE of the photon thick accelerating outflow at different arrival times, and the probability density function of photon last scattering integrated over angles  $P(r)$  (red thick curve). Thick black curve represents the photosphere of infinitely long accelerating wind. PhEs are illustrated for several arrival times with logarithmic spacing by thin black curves. The surface  $\cos \theta = \beta$  is given by  $\rho = R_0$  and it is shown by thick black line. Dashed curves illustrate the maximal visible size  $\rho$  for several arrival times with logarithmic spacing. The PhE at that arrival times is a part of the wind photosphere limited by the corresponding curves. Range of observed temperature of emission under the asymptotic photosphere is illustrated by color, see legend. Here  $R_{ph} = 100R_0$ .

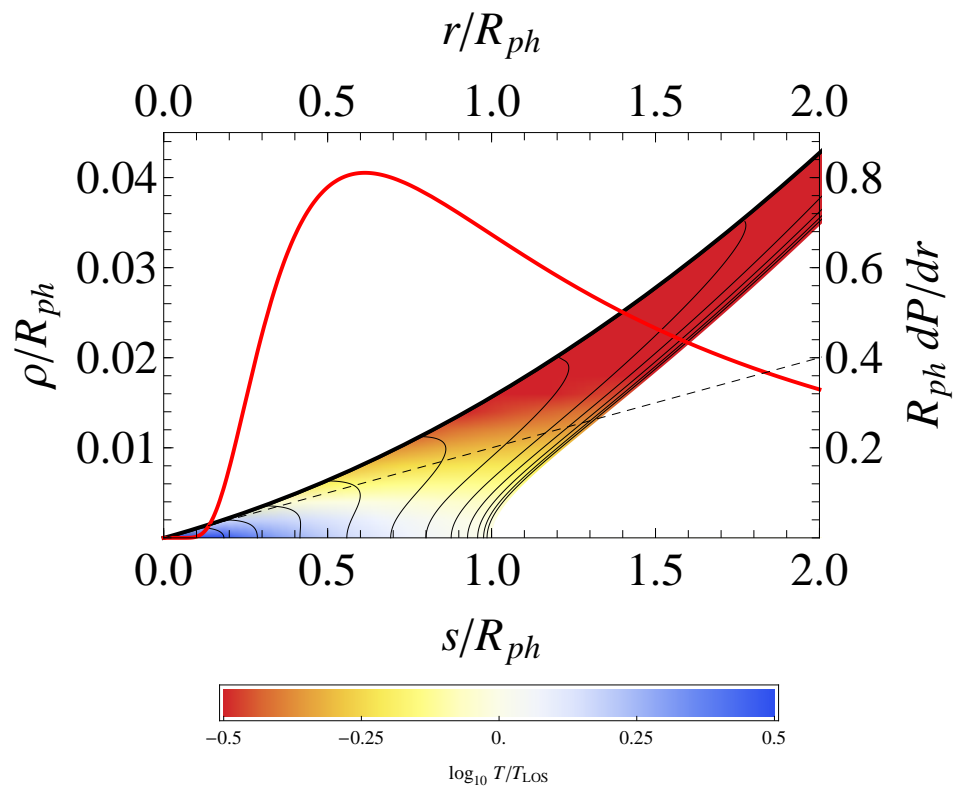


**Figure E.8.:** The same as in Fig. E.7 for a photon thick coasting outflow. PhEs are illustrated by thin curves for several arrival times with linear spacing. Thick black curve bounding PhEs correspond to the position of maximal visible angles at given  $t_a$ . Notice that these angles exceed the relativistic beaming angle, shown by dashed black line. Right edge of the colored area is the photosphere of infinitely long coasting wind (E.5.2). Here  $\Gamma = 100$ .

comoving frame of the outflow. The laboratory source function is then

$$J_\nu(\nu, r, \theta, t) = \frac{2h}{c^2} \frac{\nu^3}{\exp\left(\frac{h\nu\Gamma(1-\beta\cos\theta)}{kT_c(r,t)}\right) - 1}. \quad (\text{E.5.7})$$

This approximation is justified when the radiation field is tightly coupled to the matter. The photospheric emission comes from entire volume of the outflow, and the computational method sketched above is closely related to that used in (Beloborodov, 2011) where the concept of “fuzzy photosphere” was introduced. This method will be referred to as *fuzzy photosphere* approximation.

Most of energy reaching observer is emitted from the region near the PhE, where the probability density function along the ray

$$P(r, \theta, t) = P_0 \frac{d}{ds} \exp[-\tau(r, \theta, t)] \quad (\text{E.5.8})$$

with  $P_0$  being normalization, reaches the maximum. For this reason the dynamics of PhE studied in the previous section determines both light curves and spectra of observed photospheric emission. When the time dependence in this equation is discarded this  $P(r, \theta)$  coincides with the probability density function of the last scattering defined in (Pe’er, 2008). Assuming that all the energy comes from the PhE only, i.e. a surface instead of the volume discussed above, the computation may be reduced to one dimensional integration by substitution of the function  $P$  with a Dirac delta. Such more crude approximation, in contrast to the fuzzy photosphere one, will be referred to as *sharp photosphere* approximation.

For photon thick outflow the optical depth becomes function of  $r$  and  $\theta$  only and the comoving temperature also depends only on radius. In this respect the photon thick case is similar to the infinite wind. Then the integrand in (E.5.6) does not depend on time and only limits of integration provide time dependence due to motion of the outflow boundaries. The probability density function (E.5.8) integrated over angles is shown in Figs. E.7 and E.8 for accelerating and coasting photon thick outflows.

The observed flux of photospheric emission from accelerating outflow is illustrated in Fig. E.9 by thick red curve (fuzzy photosphere) and by dotted blue curve (sharp photosphere). The characteristic raising and decaying time is in both cases

$$\delta t = \frac{R_0^2}{(R_{ph}c)} = \frac{R_0}{\Gamma_{ph}c}. \quad (\text{E.5.9})$$

There is no simple analytic expression describing full light curve, however its decreasing part is close to a power law with index  $-4.7$  and  $-6.5$  within fuzzy and sharp photosphere approximations, respectively. As minimal duration of

the photon thick outflow  $\Delta t$  is of order  $R_0/c$ , then  $\Delta t \gg \delta t$  and the light curve has almost rectangular shape.

Such accelerating outflow appears to a distant observer as a spot with size  $\rho = (R_0^2 - (t_a/c)^2)^{1/2}$ , for  $-R_0/c \leq t_a \leq 0$ . As soon as the PhE reaches the corresponding accelerating infinitely long wind photosphere at  $t_a = 0$  the spot size starts to increase almost linearly with time  $\rho \simeq R_0 + ct_a$ . Finally, as the innermost part of the outflow reaches the photospheric radius the spot transforms to a ring with rapidly decreasing width and brightness.

The observed photospheric emission of the coasting photon thick outflow results in the flux changing as

$$F = F_{max} \left[ 1 - (t_p/t_a)^2 \right], \quad (\text{E.5.10})$$

with

$$t_p = \frac{R_{ph}}{2\eta^2 c'}, \quad (\text{E.5.11})$$

i.e. increase up to the saturation value  $F_{max} \propto L$ , see the raising part of the light curve in Fig. E.10, both in sharp and fuzzy photosphere approximations. Radius of the visible spot then reaches its maximal size (E.5.3). As arrival time exceeds  $t_p + \Delta t$  the innermost part of the outflow approaches the wind photosphere (E.5.2) along the line of sight and the spot transforms to a ring, the flux decreases rapidly in both approximations

$$F \propto t_p^2 \left[ \frac{1}{(t_a - \Delta t)^2} - \frac{1}{t_a^2} \right]. \quad (\text{E.5.12})$$

For  $t_a \gg \Delta t$  it behaves as  $F \propto t_a^{-3}$ , see the decreasing part of the light curve in Fig. E.10. Similarly to the accelerating photon thick outflow the light curve for  $\Delta t \gg t_p$  has almost rectangular shape due to the fact that its increase and decay times are much shorter than  $\Delta t$ .

Accelerating photon thick outflows exhibit photospheric spectra close to thermal ones, see Fig. E.11. In ultrarelativistic case spectra computed using both sharp and fuzzy photosphere approximations are very close to each other. Both have small deviations from thermal spectrum in the low energy part with the corresponding Band low energy indices  $\alpha = 0.82$  and  $\alpha = 0.71$ , respectively.

In contrast, the spectrum of photospheric emission of the coasting photon thick outflow is significantly wider than the thermal spectrum, see Fig. E.12. Low energy part is described by a power law with Band indices respectively  $\alpha = 0.34$  and  $\alpha = 0$ , for sharp and fuzzy photosphere approximations.

After initial phase of evolution, namely rising of the low-energy part, spectra do not evolve until observer detects emission from the innermost part of the outflow. At that moment there is a transition to another phase charac-

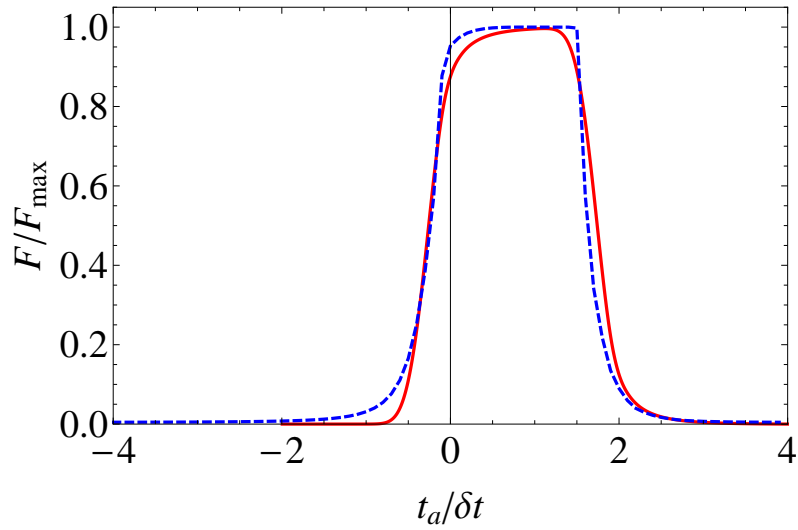


**Figure E.9.:** The light curve of photospheric emission from the photon thick accelerating outflow in fuzzy (red curve) and sharp photosphere approximations (dashed blue curve). Here  $R_{ph} = 100R_0$ , and  $\Delta t = 2\delta t$ , see (E.5.9) below.

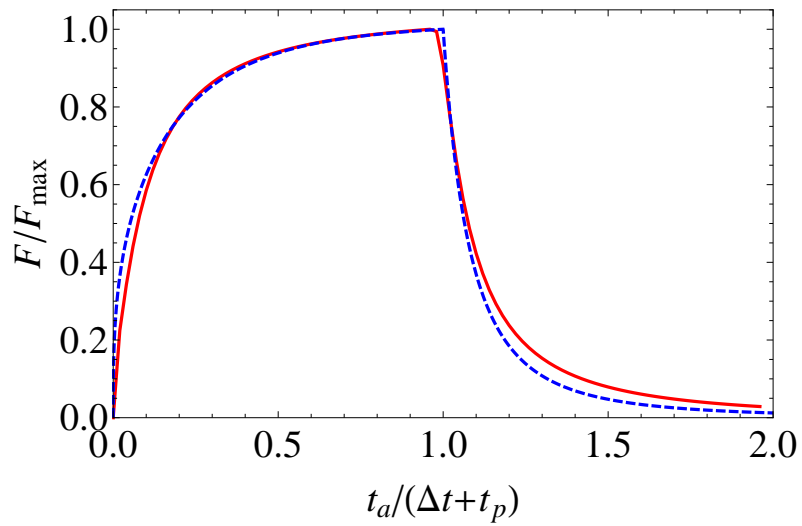


**Figure E.10.:** The same as in Fig. E.9 for a photon thick coasting outflow. Here  $\Gamma = 100$  and  $\Delta t = 5t_p$ , see (E.5.11) below.

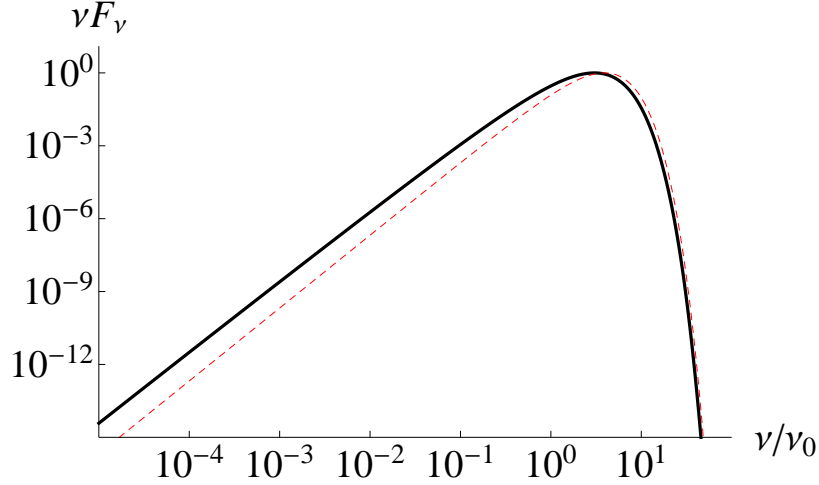


**Figure E.11.:** Instantaneous spectrum of photospheric emission of accelerating photon thick outflow in continuous (blue thick curve) and sharp photosphere approximation (black thick curve). Dashed red curve represents the thermal spectrum with the temperature at the line of sight  $T_{LOS}$ . Lorentz factor at photospheric radius is  $\Gamma_{ph} = 100$ .

terized by the fast decrease of both temperature and flux. Considering time-integrated spectrum we find that as characteristic times of the first and third phases are much less than that of the second one, the spectrum is close to the instantaneous one described above.

### E.5.3. Comparison with previous works

Now we compare the results with obtained by other methods. Beloborodov (2011) considered the photospheric emission from infinitely long wind both at acceleration and coasting phases and solved the corresponding *steady* radiative transfer equation. His main conclusion is that in addition to usual relativistic beaming leading to anisotropy of radiation in laboratory frame, in the coasting wind another anisotropy in the comoving frame of the outflow is developing. This comoving anisotropy results from the fraction of photons which already underwent their last scattering in the bulk photon field of the outflow. The anisotropy of such photons grows with increasing radius for geometrical reasons. Since the amount of such photons increase with radius the entire photon field becomes increasingly anisotropic.

For the finite photon thick outflow the radiative transfer problem becomes explicitly time dependent. The expanding outflow at a given laboratory time spans only a finite part of the probability density distribution shown in Figs.E.7 and E.8, that results in difference in observed spectra for finite and infinite cases. Interesting consequence of ultrarelativistic motion of the outflow is that even geometrically thin outflow  $l \ll R$  at a given arrival time

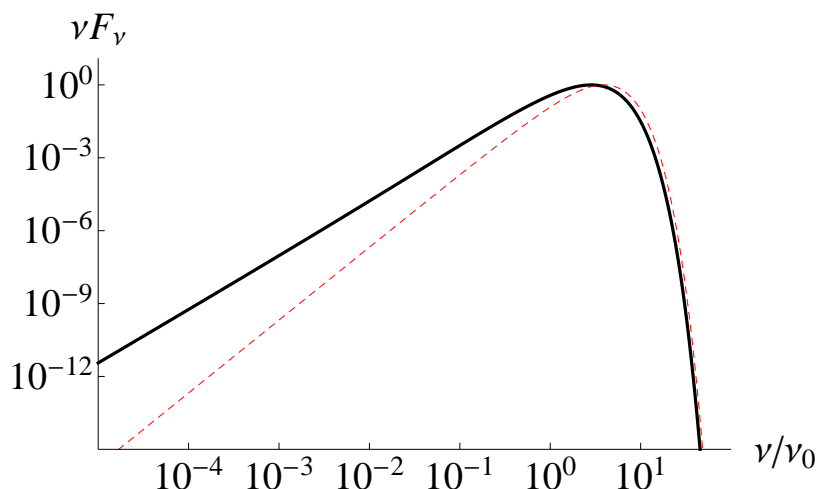


**Figure E.12.:** The same as in Fig. E.9 for a photon thick coasting outflow with Lorentz factor  $\Gamma = 100$ .

spans large interval of laboratory radius  $\Delta r = 2\Gamma^2 l$ .

The effect of additional comoving anisotropy on the source function found by Beloborodov (2011) is actually small. The difference between the probability of last scattering (E.5.8) and the distribution of last scattering in a steady wind does not exceed several percent.

Our method is also similar to the one used by Pe'er (2008) and by Pe'er and Ryde (2011) who described the late-time photospheric emission of switching off relativistic wind considering the probability density function (E.5.8) for the last scattering of photons. An additional approximation adopted by these authors is the possibility to split radial and angular dependencies. Actually Pe'er (2008) computes not the traditional energy flux understood as energy crossing unit area in unit time, but photon flux as number of photons crossing unit area in unit time. For this reason his decay law for photon flux at late times is  $F^{ob}(t_a) \propto t_a^{-2}$ . Lorentz transformation of the photon energy from the comoving frame to the laboratory one results in additional multiplier  $(1 - \beta\mu)^{-1}$  in the energy flux that leads to the observed flux  $F \propto t_a^{-3}$ , which agrees with our result in Eq. (E.5.12), see also Pe'er and Ryde (2011).

We conclude that the fuzzy photosphere approximation in fact follows closely methods of Pe'er and Ryde (2011) and Beloborodov (2011). In fact we obtained similar results for the probability of last scattering as more sophisticated treatment of radiation transfer (Beloborodov, 2011). The sharp photosphere approximation provides good description of light curves including their raising and decaying parts. The observed spectrum from accelerating outflow is also well described in this approximation, while there is some difference for the coasting case. The advantage of sharp photosphere approximation for computing observed light curves and spectra is evident for

intrinsically variable and dynamic outflows.

## **E.6. Photospheric emission from photon thin outflows**

Now we turn to photon thin outflows. In Section E.4 we pointed out that most of the radiation leaves the outflow not at its photospheric radius, but earlier, before the diffusion radius. Given that opacity of the outflow is still large, the emission escapes only from a very narrow region near the outer boundary of the outflow. The probability density function (E.5.8) is strongly peaked there and the photospheric emission for a given arrival time originates from this narrow region. Sharp photosphere approximation is thus completely justified in this case.

Since all the radiation is emitted from the PhE we briefly discuss its geometry and dynamics. The PhE of the photon thin outflow is similar to EQTS of infinitesimally thin constantly emitting relativistic shell considered firstly by Couderc (1939) and then by Rees (1966, 1967). The EQTS of this shell appears to a distant observer as an ellipsoid with axes ratio equal to  $\Gamma$ . However the PhE of photon thin outflow is not the entire ellipsoid: it is only a part of that surface, see Fig. E.13. The external boundary of the PhE for a given  $t_a$  is defined by the condition that photons emitted from the outermost layer of the outflow toward observer leaves the outflow. In the photon thin asymptotics this surface coincides with the relativistic beaming cone.

We again start with the radiative transfer equation (E.5.4). In contrast with the photon thick case, here the source function  $\mathcal{J}$  in (E.5.5) strongly depends on both  $r$  and  $t$ . The main process by which photons are coupled to the matter is Compton scattering which conserves the number of photons. Since opacity is large other processes which do not conserve the photon number lead to local thermodynamic equilibrium with thermal comoving radiation intensity  $I_c$ , number density and spectrum of photons in the outflow. Hence we use the Rosseland radiative diffusion approximation (see e.g. Rybicki and Lightman (1979), pp. 39–42), that we derive from the radiative transfer equations (E.5.4) for expanding outflows.

### **E.6.1. Radiative diffusion in relativistic outflow**

For large opacities the distribution function of photons in comoving reference frame is close to isotropic one and the radiative diffusion approximation is accurate. Following Beloborodov (2011) we use spectral intensity in comoving frame  $J_\nu(t, \xi, \mu)$ . Starting from the radiative transfer equation (E.5.4) along the ray  $s$  in laboratory frame, we transform all variables except time  $t$ , depth

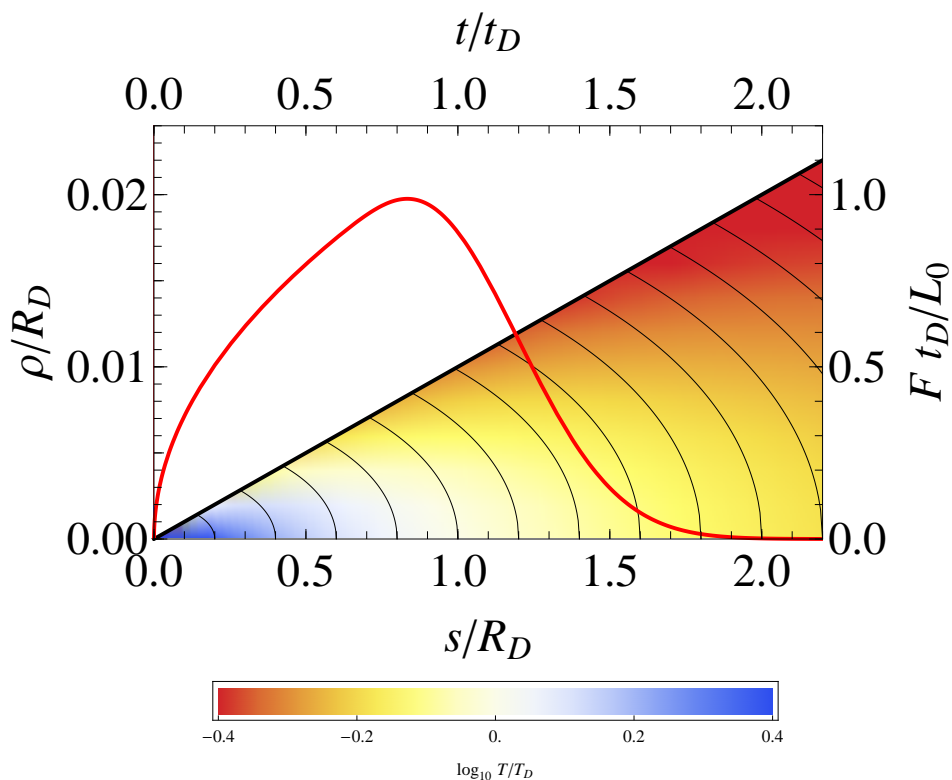


**Figure E.13.:** Evolution of PhE for the photon thin coasting outflow and dimensionless radiative diffusion flux, corrected for adiabatic cooling (red thick curve). PhEs shown by thin curves correspond from left to right to arrival times  $t_a = (t_a^D/5, 2t_a^D/5, \dots)$ , see (E.6.11). Thick black curve bounding PhEs correspond to the surface  $\cos \theta = \beta$ . Relevant range of observed temperature of photospheric emission is illustrated by color, see legend. Here  $\Gamma = 100$ .

$\xi$ , and distance  $s$  into comoving reference frame

$$\nu^3 \frac{d}{ds} \left( \frac{J_\nu}{\nu^3} \right) = \frac{\kappa_\nu}{\mathcal{D}} (S_\nu - J_\nu), \quad (\text{E.6.1})$$

and integrating over comoving frequency  $\nu$  we have

$$\frac{1}{c} \frac{\partial J}{\partial t} - \frac{\mu}{\Gamma \mathcal{D}} \frac{\partial J}{\partial \xi} + \frac{1 - \mu^2}{vt - \xi} \frac{\partial J}{\partial \mu} + 4 \frac{\Gamma \beta}{\mathcal{D}} \frac{1 - \mu^2}{vt - \xi} J = \frac{\kappa}{\mathcal{D}} (S - J), \quad (\text{E.6.2})$$

where  $\mu = \cos \theta_c$ ,  $\theta_c$  is the photon angle with respect to the radial direction in comoving frame,  $\mathcal{D} = \Gamma(1 + \beta\mu)$  is Doppler factor,  $J = \int J_\nu d\nu$  is total photon intensity,  $S = \int S_\nu d\nu$  is total source function,  $\kappa = J^{-1} \int \kappa_\nu J_\nu d\nu$  is effective opacity,  $\kappa_\nu = \sigma n_c$  is opacity in comoving frame.

In the case of small deviations from isotropy decomposition

$$J = J_0(t, \xi) + \mu J_1(t, \xi) \quad (\text{E.6.3})$$

could be applied. Introducing it into (E.6.2) and integrating it over  $\mathcal{D}d\mu$  and over  $\mathcal{D}\mu d\mu$  after some algebra for coherent scattering with  $S = S_0 = J_0$  we have

$$\frac{\partial J_0}{\partial ct} + \frac{\beta}{3} \frac{\partial J_1}{\partial t} - \frac{1}{3\Gamma^2} \frac{\partial J_1}{\partial \xi} + \frac{2J_1}{3(vt - \xi)} + \frac{4J_0\beta}{3(vt - \xi)} = 0, \quad (\text{E.6.4})$$

$$\frac{\partial J_1}{\partial ct} + \beta \frac{\partial J_0}{\partial t} - \frac{1}{\Gamma^2} \frac{\partial J_0}{\partial \xi} + \frac{8J_1\beta}{5(vt - \xi)} = -\frac{\kappa J_1}{\Gamma}. \quad (\text{E.6.5})$$

Diffusion approximation is based on slow variation of total flux through the entire sphere  $L_1 = J_1(t/t_0)^2$  over mean free path, so that  $\frac{\partial L_1}{\partial ct} = 0$ , and it provide  $J_1$  from the equation (E.6.5). Inserting this into (E.6.4) after simple but tedious calculations in ultrarelativistic  $\beta \simeq 1$  photon thin case  $\Gamma^2 \xi \ll vt$  for function  $L = J_0(t/t_0)^{8/3}$  we obtain the diffusion equation

$$\frac{\partial L}{\partial ct} - \frac{c^2 t^2 \Delta}{3R_0} \frac{\partial^2 L}{\partial \xi^2} = 0, \quad \Delta = \frac{1}{\Gamma^2 \sigma n_0 R_0} = \frac{1}{\Gamma^2 \tau_0} = (\Gamma^2 \tau_0)^{-1}. \quad (\text{E.6.6})$$

This equation should be supplemented with boundary conditions. There are two types of boundary conditions used frequently: free-streaming, for example in two-stream approximation (Rybicki and Lightman (1979), pp. 42–45), and zero boundary conditions, that can be used as replacement for free-streaming for "extrapolated boundary" (Haskell et al., 1994). We find that the position of "extrapolated boundary"  $\xi = -k \frac{c^2 t^2 \Delta}{R_0}$  ( $k$  is a constant of order unity, dependent on the approximation used for free-streaming description) for the main part of emission is very close to the real boundary, and in the case of zero boundary conditions  $L|_{\xi=0} = L|_{\xi=l} = 0$  there is a series expansion of

solution, that for initial conditions  $L(\xi, t_0) = 1$  gives

$$L(\xi, t) = \sum_{n=0}^{\infty} \frac{4}{(2n+1)\pi} \exp \left[ -\frac{\Delta(2n+1)^2 \pi^2 c^3 (t^3 - t_0^3)}{9R_0 l^2} \right] \sin \left[ \frac{(2n+1)\pi \xi}{l} \right]. \quad (\text{E.6.7})$$

This solution in comparison with numerical one with free-streaming boundary conditions is accurate to a few percents.

The flux of  $L$  is characterized by an initial burst and then tends to the asymptotic solution, that corresponds to  $t_0 = 0$ , with flux

$$F(t) = \frac{4\Delta c^3 t^2}{3R_0 l^2} \vartheta_2 \left[ 0, \exp \left( -\frac{4\Delta \pi^2 c^3 t^3}{9R_0 l^2} \right) \right], \quad (\text{E.6.8})$$

where  $\vartheta_2$  is the Jacobi elliptic theta function, see Fig. E.13. The peak of the flux of  $L$  is near the diffusion time

$$t_D = \frac{l}{c} \left( \frac{R_0}{l\Delta} \right)^{1/3}, \quad (\text{E.6.9})$$

and "extrapolated boundary"  $\xi = -kl(l\Delta/R_0)^{1/3} \ll l$  is very close to real one as  $\Delta \ll 1$ , that ensures the accuracy of (E.6.7).

## E.6.2. Flux and spectrum of photospheric emission

Notice that the diffusion coefficient is explicitly time dependent due to the expansion of the outflow. An approximate analytic solution for the radiation field inside the photon thin outflow discussed in the previous subsection is represented in Fig. E.13. The raising part of the corresponding flux of  $L_c$  through the external boundary of the outflow scales as  $t^{1/2}$ , while its decaying part is quasi-exponential one. Consequently, while the diffusion in a static object gives the flux decreases as  $t^{-1/2}$ , in our case the observed flux (E.5.6) is a more slowly decreasing function

$$F \propto t_a^{-1/6}, \quad (\text{E.6.10})$$

up to arrival time of diffusion

$$t_a^D = \frac{R_D}{2\eta^2 c} \simeq 0.12 E_{54}^{1/3} \eta_2^{-5/3} l_8^{1/3} \text{ s}, \quad (\text{E.6.11})$$

where large part of energy has left the outflow already. At this moment the energy decrease due to diffusion becomes substantial even in the deepest parts of the outflow and later the observed flux decreases quasi-exponentially with arrival time.

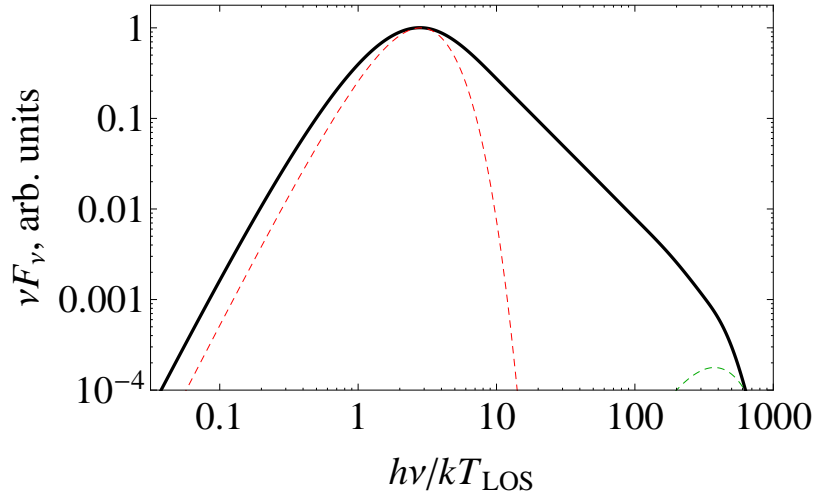


**Figure E.14.:** Time-integrated spectrum of photospheric emission of photon thin outflow (thick curve,  $\eta = 100$ ,  $R_D = 10^5 R_0$ ), superimposed with two instantaneous spectra of that emission, corresponding to arrival time of photons emitted at the moment of transition from acceleration to coasting (dashed green curve on the right) and to arrival time of diffusion (dashed red curve on the left).

The comoving temperature of radiation on the photosphere is determined by the balance between the energy diffusion from the interior of the outflow and radiative losses and it is much smaller than the temperature in the interior. The variation of observed temperature across the PhE is small, see Fig. E.13 and hence the observed instantaneous spectrum is very close to the thermal one and peaks near the observed temperature on the line of sight. We find that the latter decreases as  $t_a^{-13/24}$ , in contrast with adiabatic law  $t_a^{-2/3}$ . However, at diffusion radius both temperatures coincide giving for the line of sight temperature

$$T_{LOS} \simeq 162\eta_2^{4/9} \text{ keV}. \quad (\text{E.6.12})$$

The time integrated spectrum has a Band shape with a cut-off near the temperature of transition from acceleration to coasting, see Fig. E.14. Low energy part of the spectrum has the slope  $\alpha = 1$ , while high-energy part has  $\beta \simeq -3.5$ .

## E.7. Discussion

The expression (E.6.11) gives an estimate for duration of photospheric emission of photon thin outflows. When available observed spectra are integrated on time intervals comparable to (E.6.11) the observed spectrum of photo-

spheric emission is expected to have Band shape. Thus, starting from comoving thermal spectrum for the photospheric emission we obtain for the first time an observed spectrum which may be well described by the Band function with high energy power law index  $\beta$  being determined by the density profile of the outflow. We find this result quite remarkable.

Notice that non thermal spectra as a result of convolution of thermal ones over time has been introduced for afterglows of GRBs by Blinnikov et al. (1999). Double convolution over EQTS and arrival time is also one of the key ideas in the fireshell model (Ruffini et al., 2003a).

Band spectra in photospheric models of GRBs have been obtained by now only assuming additional dissipation mechanisms such as magnetic reconnection (Giannios, 2006), collisional heating (Beloborodov, 2010) and internal shocks (Toma et al., 2011; Ryde et al., 2011). In our model such additional assumption is not required.

It is even more remarkable that GRBs appear to be the only known objects in nature able to reach the photon thin asymptotics in their ultrarelativistic expansion. For thermally accelerated relativistic plasmas which are discussed in connection with their possible synthesis in ground based laboratories (e.g. Ruffini et al. (2010)) it is unreachable. The photon thin asymptotics is reached if the optical depth (E.3.5)

$$\tau_0 \gg 4\Gamma^4 \frac{l}{R_0} = 4 \times 10^8 \eta_2^4 \frac{l_8}{R_8}. \quad (\text{E.7.1})$$

GRBs clearly can satisfy this constraint as the contribution of baryons  $\tau_0 \simeq 3.5 \times 10^{13} E_{54} \eta_2^{-1} R_8^{-1} l_8^{-1}$ .

We obtained both time integrated and instantaneous observed spectra of accelerating photon thick outflow which are close to thermal one with small deviations in the Rayleigh-Jeans part, in agreement with Grimsrud and Wasserman (1998).

Time integrated observed spectrum of coasting photon thick outflow is broader than thermal one, and deviates from it both in low- and high-energy parts. This broadening is also found by Beloborodov (2010) using Monte Carlo simulations, but our spectral index of the low energy part is  $\alpha = 0$  instead of his  $\alpha \simeq 0.4$ . This difference may be attributed to the fact that Monte Carlo simulations do not account for stimulated emission. Interestingly, we found  $\alpha \simeq 0.34$  in the sharp photosphere approximation.

As discussed earlier in Section E.3 each photon thick outflow always contains a photon thin layer with depth  $\xi_{thin} = (R + l)/(2\eta^2)$  located near its outer boundary. Radiation diffused out from this part of the outflow arrives to observer first and modifies the initial part of the light curve and the corresponding spectrum of the outflow. The diffusion length  $\xi_D = [(R + l)^3 / (\eta^2 \tau_0 R_0)]^{1/2}$  remains always within this photon thin layer  $\xi_{thin}$  and our solution for photon thin outflow is applicable for description of this

early emission. The photospheric emission from well developed photon thick outflow and its late time behavior occurring when the outflow crossed the photospheric radius may be described either by fuzzy or by sharp photosphere approximations.

When the outflow becomes transparent in the transition from photon thick to photon thin conditions, the observed time integrated spectrum will contain both Band component produced by the early emission from the photon thin layer and thermal-like component coming from the photon thick part superimposed. This may be the reason why in most GRBs analyzed by Ryde and Pe'er (2009) there are both power law and black body components.

We presented analytic expressions for the photon flux in the simple model of the portion of wind. With more complex density profile composed of presumably many shells the light curve is expected to be variable and arbitrarily complex. The minimal time scale of variability is given Eq. (E.6.11) and it may be very small for small baryon loading. It is necessary to emphasize that the decaying part of the light curve follows  $t_a^{-3}$  for photon thick outflows. Steeper decay of the light curve of photospheric emission it is a clear signature of the photon thin outflow.

The photospheric emission should be additionally identified by the spectral analysis. In particular, power law spectra extending to high energies above 10 MeV cannot be produced by the photospheric emission unless additional mechanisms are involved. What we have shown here, though, is that the observed spectrum may not necessarily be close to the thermal one.

## **E.8. Conclusions**

In summary, in this paper we proposed a unified treatment of ultrarelativistic outflows, which originate both from instantaneous and from continuous energy release, with respect to photospheric emission. We have to stress that these two cases are discussed in the literature and are respectively referred to as shells and winds. Instead of this traditional division we propose a new physically motivated classification, which in our opinion helps to understand in particular why geometrically thin shell may appear as thick wind with respect to the photospheric emission. For this reason we re-examined the existing scattered literature and pointed out the advantage of the proposed classification.

We studied geometry of photospheres in generic relativistic outflows. As we are interested in appearance of the photosphere to a distant observer, we introduced the notion of photospheric equitemporal surface and described its dynamics.

We computed both energy flux and observed spectra of photon thick outflows in two approximations, derived from the radiative transfer equation. In our fuzzy photosphere approximation the effect of simultaneous emission

from entire volume of the outflow is taken into account. We also used another computationally more simple sharp photosphere approximation which is shown to reproduce well both light curves and spectra. These results generalize the corresponding results in the literature for steady relativistic winds.

In photon thin outflows most of radiation is shown to originate not at its photospheric radius, but at smaller radii due to radiation diffusion. Starting from the radiative transfer equation for time dependent outflows we derived the diffusion equation and obtained approximate analytic solution for the energy flux. We present both instantaneous and time integrated observed spectra. The latter are well described by the Band function. For our simple density profile we find values for the low energy power law index  $\alpha = 1$  and the high-energy power law index  $\beta \simeq -3.5$ .



# F. Monte Carlo simulations of the photospheric emission in GRBs

## F.1. Introduction

Photospheric emission is considered among the leading mechanisms generating gamma rays from relativistically expanding plasma in cosmic Gamma Ray Bursts (GRBs) (Goodman, 1986). In both fireball (Piran, 1999) and fireshell (Ruffini et al., 2009b) models photospheric emission is naturally produced when expanding initially optically thick plasma becomes transparent for photons.

While within the fireball model the basic approximation involved is that of (infinitely long) steady *wind*, in the fireshell model the geometry of the outflow is a thin *shell*. It is shown by Ruffini et al. (2011) that in both wind and shell models when outflows with *finite* duration are considered some important aspects of the optical depth behaviour are overlooked. There a new physically motivated classification was introduced: photon thick and photon thin outflows with respectively  $R_{ph} < R_t$  and  $R_{ph} > R_t$  with  $R_{ph}$  being the photospheric radius,  $R_t = 2\Gamma^2 l$  the radius of transition,  $\Gamma$  is the Lorentz factor and  $l$  the laboratory width of the outflow. Light curves and spectra from finite outflows were obtained using two different approximations: sharp and fuzzy photosphere. These approximations were derived there from the transport equation for radiation.

In this work we examine the validity of these approximations using MC simulations of photon scattering. We compute the probability of last scattering in finite relativistic outflows. Then we obtain light curves and spectra from both photon thick and photon thin outflows, and compare them with the results obtained before.

## F.2. The model

Following Ruffini et al. (2011) we consider a spherical wind of finite width  $l$  with laboratory number density of electrons being zero everywhere except

the region  $R(t) < r < R(t) + l$  where it is

$$n_l = n_0 \left( \frac{R_0}{r} \right)^2, \quad (\text{F.2.1})$$

with  $R_0$  and  $n_0$  being respectively the radius and the density at the base of the outflow. This outflow expands with constant Lorentz factor  $\Gamma$ , so that  $R(t) = R_0 + \beta ct$ , where  $\beta = \sqrt{1 - \Gamma^{-2}}$ . Accelerating outflows are not considered here. However, our results are valid also for arbitrary  $l$ . Then the optical depth is given by:

$$\tau(r, \theta, t_e) = \tau_0 R_0 \left[ \frac{\theta - \tan^{-1} \left( \frac{r \sin \theta}{ct + r \cos \theta} \right)}{r \sin(\theta)} - \beta \left( \frac{1}{r} - \frac{1}{\sqrt{(ct + r \cos \theta)^2 + (r \sin \theta)^2}} \right) \right], \quad (\text{F.2.2})$$

where

$$\tau_0 = \sigma n_0 R_0 = \frac{\sigma E_0}{4\pi m_p c^2 R_0 \Gamma'}, \quad (\text{F.2.3})$$

and  $r$  is the position of photon emission,  $\theta$  is the angle between momentum of photon and the radius vector,  $\sigma$  is the Thomson cross section,  $t$  is the time the photon remains within the outflow,  $E_0$  is total energy release in the GRB,  $m_p$  is the proton mass, and  $c$  the speed of light. Time  $t$  is found via the equations of motion of the outflow and that of the photon.

The optical depth in finite relativistic outflows has two different asymptotics, depending on initial conditions: in photon thick case  $\tau$  is almost constant within the outflow; instead in the photon thin case it is linearly increasing with depth from the outer boundary at  $R(t) + R_0$ .

In Ruffini et al. (2011) diffusion of photons within the outflow is found to play a crucial role in photon thin case: the radius at which photons effectively diffuse out of the outflow is smaller than the photospheric radius  $R_{ph}$ . The latter is defined by equating expression (F.2.2) to unity for emission with  $\theta = 0$  and  $t_e$  corresponding to the inner boundary. Hence, when the photon thin outflow reaches the photospheric radius there are few photons left in it.

### F.3. Monte Carlo simulation

We have used a spherically symmetric MC simulations of photon scattering inside the outflow described by Eq. (F.2.1). For more detail on interactions in relativistic expanding plasma (see Bégue, Siutsou and Vereshchagin, in

preparation). In this simulation each photon is followed as it interacts with electrons until it decouples from the outflow. Photons are injected in the outflow when it has the optical depth  $10^2$ . It is also assumed that their initial distribution is isotropic and thermal. The radial position of each photon inside the outflow is chosen randomly.

The code consists mainly of a loop computing each scattering. We proceed in two steps. First an infinite and steady wind (already treated by Beloborodov (2010) with  $l \rightarrow \infty$  and  $R \rightarrow 0$ ) is considered. For a given position characterized by  $r$  and  $\theta$  of photon in the outflow, we compute a maximal value for the optical depth  $\tau_{max}$  using (F.2.2) with  $t \rightarrow \infty$ . The probability for the photon to decouple the outflow is  $\exp(-\tau_{max})$ . Then a random number  $X \in [0, 1]$  is chosen. On the one hand, if  $X < \exp(-\tau_{max})$  the photon is considered decoupled. Afterwards photon remains in the outflow but does not scatter. This case corresponds to decoupling in photon thick case, for which the presence of boundaries is not essential. On the other hand, if  $X \geq \exp(-\tau_{max})$  the position  $r_s$  of next scattering is computed from the optical depth

$$\tau(r, r_s, \theta) = \tau_0 R_0 \left[ \frac{\theta - \theta_s}{r \sin(\theta)} - \beta \left( \frac{1}{r} - \frac{1}{r_s} \right) \right] \quad (\text{F.3.1})$$

where  $\theta_s$  is the angle between photon momentum and the radius vector at the position of scattering. The new radial position  $r_s$  such that  $\exp[-\tau(r, r_s, \theta)] \equiv X$  is found by iterations.

The second step is to take into account the finite width of the outflow. To do so  $r_s$  is compared with the radii of the inner and outer boundaries of the outflow. If  $r_s < R(t_s)$  or  $r_s > R(t_s) + R_0$  the scattering does not take place and photon is considered decoupled. Such decoupling occurring at the boundaries corresponds to the photon thin case. In the opposite case  $R(t_s) \leq r_s \leq R(t_s) + R_0$  the scattering is assumed to occur and the loop is repeated until the photon decouples.

We consider two models of scattering: coherent isotropic scattering and Compton scattering. The former is treated for comparison with results in the literature such as e.g. Beloborodov (2011). Such model is also interesting *per se* since it preserves Planck spectrum and it traces only geometrical effects. Instead when Compton scattering is considered, the equilibrium spectrum is the Wien one because stimulated emission is not taken into account by MC simulation. For initially large optical depth the spectrum indeed firstly acquires the Wien shape, and only at the photosphere it changes the shape again.

The coherent scattering is computed by Lorentz transformation to the reference frame comoving with the outflow. In addition, when Compton scattering is considered, another Lorentz transformation to the rest frame of the electron is performed. The electron is chosen randomly from the Boltzmann

distribution at a given comoving temperature defined as

$$T = T_0 \Gamma^{-1/3} \left( \frac{R_0}{r} \right)^{2/3}, \quad T_0 \simeq \left( \frac{E_0}{4\pi a R_0^2 l} \right)^{1/4}, \quad (\text{F.3.2})$$

where  $a = 4\sigma_{SB}/c$ ,  $\sigma_{SB}$  is the Stefan-Boltzmann constant, see e.g. Ruffini and Vereshchagin (2012).

Various tests of the code are performed. Before dealing with finite outflows we also reproduced the results of Beloborodov (2011). We present below the results for two specific cases. The set of parameters for these simulations are given in Tab. F.1. The left (right) column corresponds to photon thick (thin) case.

**Table F.1.:** Parameters for the simulations.

|               | Photon thick    | Photon thin     |
|---------------|-----------------|-----------------|
| $R_0$ (cm)    | $10^8$          | $10^8$          |
| $l$ (cm)      | $4.5 * 10^8$    | $10^8$          |
| $\tau_0$      | $2.3 * 10^{10}$ | $1.2 * 10^{13}$ |
| $E_0$ (erg)   | $1.5 * 10^{52}$ | $10^{54}$       |
| $\Gamma$      | 500             | 300             |
| $R_{ph}$ (cm) | $4.7 * 10^{12}$ | $3.3 * 10^{14}$ |
| $R_D$ (cm)    | $4.9 * 10^{13}$ | $1.0 * 10^{14}$ |

## F.4. Results

### F.4.1. Probability density function of position of last scattering

Consider first the probability density of photon last scattering position as a function of depth (top panel of Fig.F.1). Photon decoupling from photon thick outflows is expected to be local and the presence of boundaries should not change this probability substantially, indeed the probability distribution function of last scattering is found to be almost independent on the depth. On the contrary in photon thin outflow there is enough time for photons to be transported at the boundaries by diffusion as discussed in Ruffini et al. (2011). As a result the probability density is peaked at the boundaries.

Difference between photon thin and photon thick outflows is also reflected in the probability density of last scattering as a function of the radius, shown at the bottom of Fig.F.1. In the photon thin outflow most photons escape from the outflow well before the photospheric radius, namely near diffusion

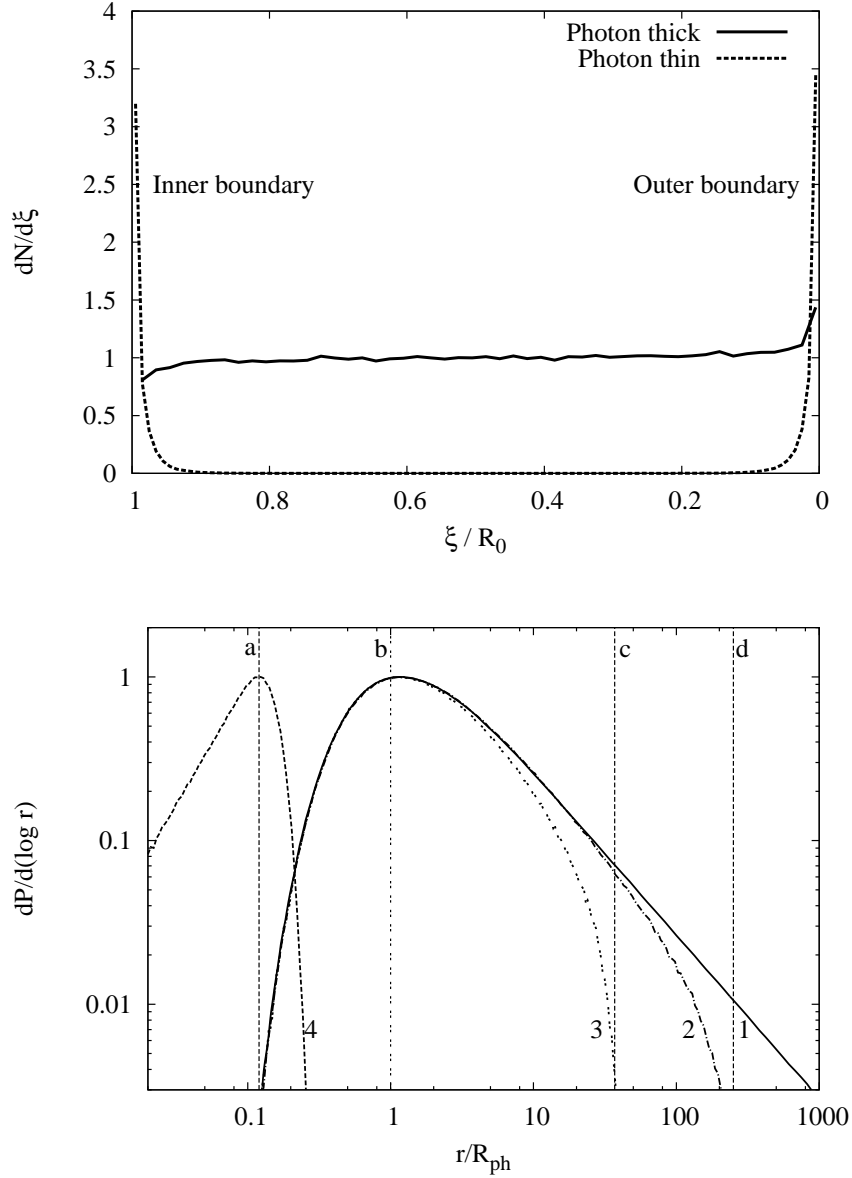


**Figure F.1.:** Upper panel: Probability density of last scattering as a function of normalized depth for photon thick and photon thin outflows (in the latter case decreased by a factor of 10 for a better presentation).

Lower panel: probability density function for the position of last scattering in the following cases: infinite and steady wind (1), photon thick case of Tab F.1 (2), photon thick case of Tab F.1 with a different Lorentz factor  $\Gamma = 300$  (3), and photon thin outflow (4). The vertical line (a) represents the diffusion radius in photon thin case, line (b) represents the photospheric radius while lines (c) and (d) show the transition radius  $R_t$  for curves (2) and (3), respectively. Both coherent and Compton scattering models give the same results.

radius

$$R_D = \left( \tau_0 \Gamma^2 R_0 l^2 \right)^{1/3}. \quad (\text{F.4.1})$$

Instead for photon thick outflows the probability density function of last scattering is found to be close to the one of infinite and steady wind, found by Beloborodov (2011). The finite extension of the outflow results in the exponential cut-off for the probability density function at radii larger than  $R_t$ .

Let us stress how different the probability densities for photon thick and photon thin cases are. Not only the positions of the maximum, but also the shapes are different. In photon thin case at small radii the number of photons that diffuse out is determined by the change in the diffusion coefficient, i.e. the electron density which follows a power law. In expanding plasma while the density decreases, the mean free path for photons increases which makes the diffusion faster. At large radii almost all photons have already diffused out, and the probability has an exponential cut off. As for the photon thick case, the probability density dependence on the radius is opposite. For small radii the probability for last scattering is exponentially suppressed because of large optical depth, while at large radii it follows a power law, as discussed in Pe'er (2008). At larger radii we find an exponential decrease due to the finiteness of the outflow, see Fig. F.1.

#### F.4.2. Spectra and light-curves from photon thick outflow

The average comoving energy of photons for steady wind was considered by Pe'er (2008) and Beloborodov (2010). For finite outflow we show this quantity in Fig. F.2 and compare it with the  $r^{-2/3}$  dependence characteristic of adiabatic cooling. The difference between Compton and coherent scattering comes from the fact that the average energy in the optically thick regim is  $3kT$  for Wien spectrum and  $2.82kT$  for Planck spectrum. In agreement with previous studies we find that the average energy of photons at the photosphere is higher than adiabatic cooling predicts. It is 1.58 in the case of Compton scattering and 1.4 in the case of coherent one.

In Fig. F.3 we compare time integrated spectra of photon thick outflow obtained with different models. Each of them involves  $10^7$  photons. In order to compare the results of Ruffini et al. (2011) with our MC simulations we shifted the spectra for sharp, fuzzy approximations and Plank spectrum by the factor 1.58, which takes into account the effect discussed above. The results obtained in fuzzy approximation are in good agreement with MC simulations. The later give the low energy spectra index  $\alpha = 0.24$  for Compton scattering and  $\alpha = 0.19$  for coherent one to be compared with  $\alpha = 0$  found in Ruffini et al. (2011).

We also show in Fig. F.4 time resolved spectra at selected arrival times which are clearly far from being Planckian. The effect of spectral flattening at late time discovered by Pe'er and Ryde (2011) is visible.

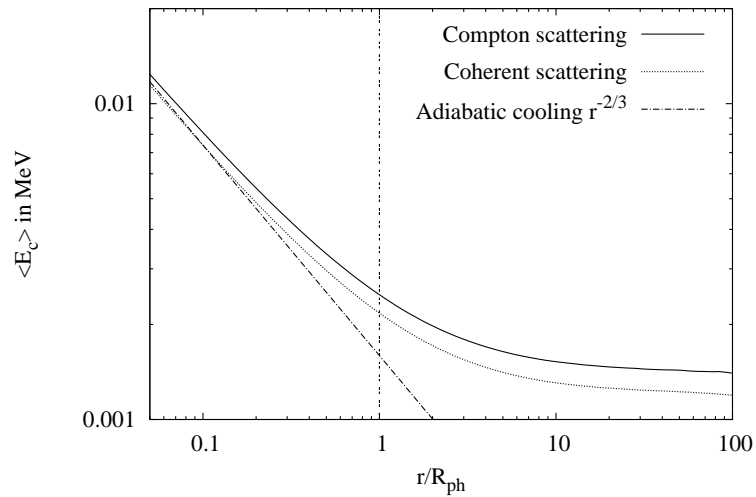


**Figure F.2.:** Average comoving energy of photons in photon thick outflow as function of the radius. The averaging is performed for photons still coupled with the outflow.

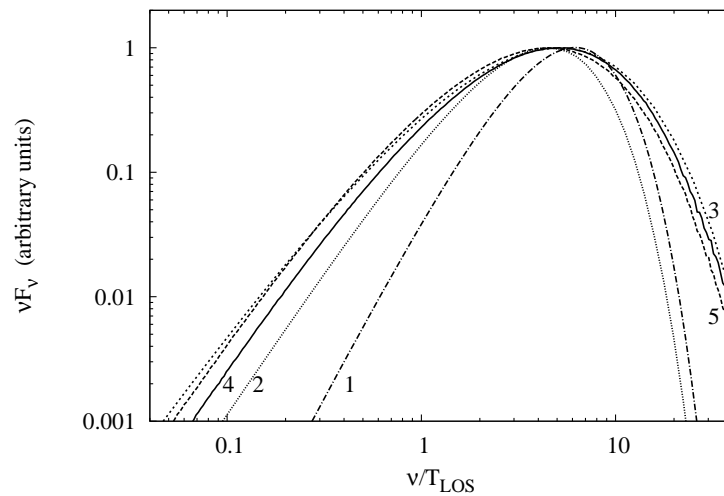


**Figure F.3.:** Time integrated spectrum of photospheric emission from photon thick outflow computed within different approximations: Planck spectrum (1), sharp photosphere approximation (2), fuzzy photosphere approximation (3), Monte Carlo simulation for Compton scattering (4), Monte Carlo simulation for coherent scattering (5). Spectra (1), (2) and (3) are shifted in energy by a factor 1.58 (see text for details).  $T_{LOS}$  is the laboratory temperature of the outflow at the photospheric radius.

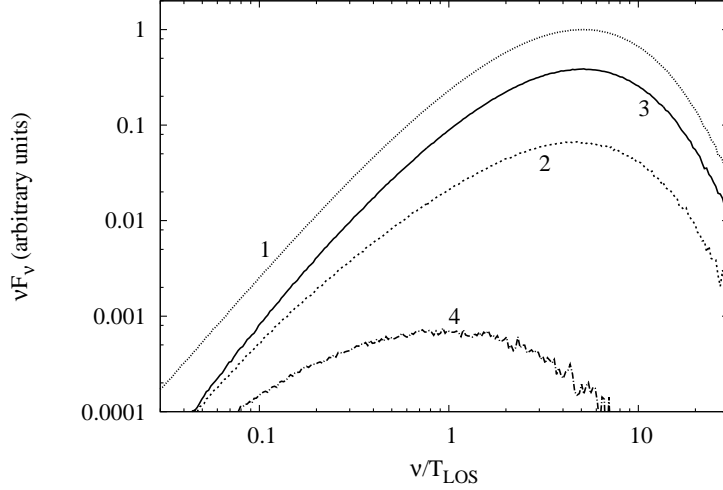


**Figure F.4.:** Time integrated spectrum from photon thick outflow (1) together with time resolved spectra corresponding to the beginning of the plateau in the light curve (2), middle of the plateau (3) and the tail (4).

Finally, light curves are presented in Fig. F.5, where we defined  $t_{ph} = R_0/c$  and  $t_a = t_e - \mu R_e/c$ , with  $r_e$  and  $t_e$  laboratory radius and time of emission. We chose  $t_a = 0$  for a photon emitted at  $R_e = R_0$ . If the rising part is in good agreement with both approximations, the decaying part is better described by the fuzzy photosphere approximation.

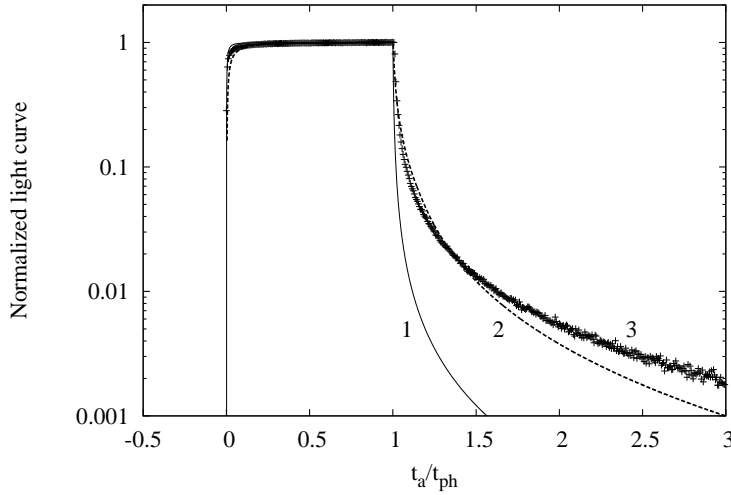


**Figure F.5.:** Light curves from photon thick outflow within different approximations: sharp photosphere (1), fuzzy photosphere (2) and MC simulation (3) for Compton scattering model. Coherent scattering model gives similar results.

### F.4.3. Spectra and light curves from photon thin outflow

In photon thin case diffusion has been shown to be important. Both light curve and spectrum are characterized by the radius of diffusion  $R_D$  and the associated arrival time  $t_D = R_D/(2\Gamma^2 c)$ . Since photons are still strongly coupled to the outflow, local thermodynamic equilibrium is maintained everywhere but at the very boundary. Indeed, this part of the outflow loses photons by random walks. For MC simulations of the photon thin outflows we used the coherent scattering model. The results are compared with Ruffini et al. (2011) where light curve and spectrum are obtained using the sharp photosphere approximation, after solving radiative diffusion equation. It has been demonstrated there that the temperature at the boundary of the outflow follows a different law from the one of adiabatic cooling:  $T(r) \propto r^{-13/24}$  with both temperatures nearly coinciding at the radius of diffusion. So we expect the time integrated spectrum obtained by MC simulations has more power at energies above the peak. However, the spectral evolution until the diffusion radius is hardly accessible through the MC simulations since it requires long CPU time: the number of collisions in optically thick medium is proportional to  $\tau^2$ .

Given these limitations, our simulation starts at  $\tau = 150$ , which results in the cut off at high energy in the time integrated spectrum and the absence of initial part of the light curve, see Figs. F.6 and F.7. For this reason we compare MC simulations with results from Ruffini et al. (2011) computed a) from the beginning of expansion and b) from the starting radius of MC simulations.

Finally, in both MC simulations and the work of Ruffini et al. (2011) the photons emitted outside the relativistic beaming cone from the photon thin outflows are neglected. This is good approximation, since such photons have much lower energy due to the Doppler effect. Besides, their arrival time is  $2\Gamma^2$  longer than the arrival time of diffusion.

Spectra and light curves are shown respectively in Figs. F.6 and F.7. The simulation involves  $10^6$  photons. We see a good agreement between both methods of computation.

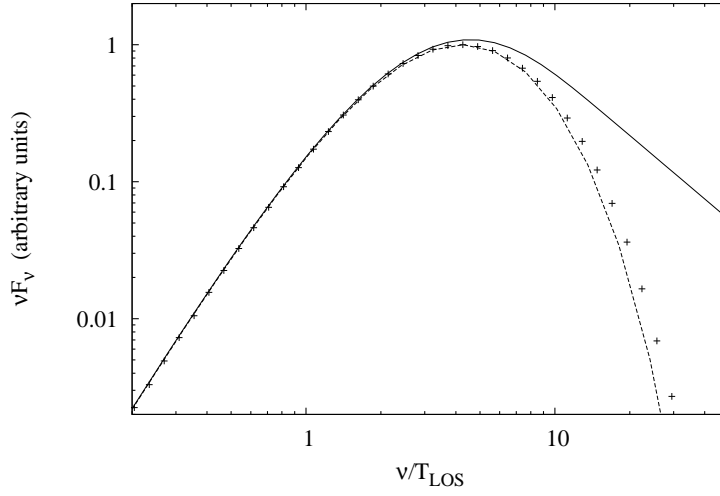


**Figure F.6.:** Time integrated spectrum from photon thin outflow obtained by MC simulation (crosses), sharp photosphere approximation starting at the same radius of MC simulations (dashed) and sharp photosphere approximation starting at the beginning of expansion (thick curve).  $T_{LOS}$  is here the laboratory temperature at  $R_D$ .

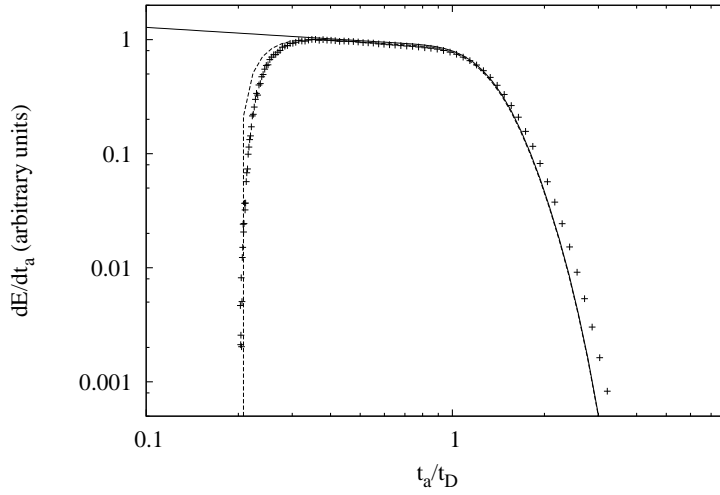


**Figure F.7.:** Light curves from photon thin outflow obtained by MC simulation (crosses), sharp photosphere approximation starting at the same radius of MC simulations (dashed) and sharp photosphere approximation starting at the beginning of expansion (thick curve).

## **F.5. Conclusions**

To summarize, in this work we considered the photospheric emission from finite relativistic outflow by MC simulations of photon scattering. The validity of the assumptions made in Ruffini et al. (2011) is verified and it is found that the fuzzy photosphere approximation used in that paper is adequate in describing both the light curves and the shape of the spectra of photospheric emission from photon thick outflows. The sharp photosphere approximation produces qualitatively acceptable results for photon thick outflows, but underestimates high energy part of the spectrum and the decaying part of the light curve.

As expected, diffusion is found to dominate the photospheric emission of photon thin outflows. The probability density of last scattering is obtained in this case both as function of outflow depth and its radial position. Both these functions differ from their photon thick counterparts, once more pointing out the essential difference between these two cases. Good agreement is obtained between MC simulation and sharp photosphere approximation for both light curve and spectrum from photon thin outflow.



# G. Comptonization of photons near the photosphere of relativistic outflows

## G.1. Introduction

GRB emission originates from plasma which expands relativistically from initial optically thick phase. It necessarily contains the photospheric component which appears when plasma becomes transparent to radiation initially trapped in it (Goodman, 1986; Paczynski, 1986, 1990; Shemi and Piran, 1990).

The fireshell model (Ruffini et al., 1999, 2000) pays special attention to this photospheric component. It is identified as P-GRB (proper GRB). Both its energetics and time separation from the peak of the afterglow are predicted, and comparison with observations allowed identification of this component in many GRBs (970228, 991216, 031203, 050315, 050509B, 060218, 060607A, 060614, 071227, 090618, 090902B, 090423).

Impossibility of explaining observed hard low energy spectra with traditional synchrotron shock models revived the interest to the photospheric emission in the recent literature (Mészáros and Rees, 2000; Mészáros et al., 2002; Daigne and Mochkovitch, 2002; Pe'er et al., 2007; Beloborodov, 2010, 2011; Ryde et al., 2011; Pe'er and Ryde, 2011). Reprocessing of thermal emission assumed to originate from the photosphere by nonthermal distribution of electrons is in the basis of more complicated models with dissipation near the photosphere (Rees and Mészáros, 2005; Giannios, 2006; Toma et al., 2011; Ryde et al., 2011; Vurm et al., 2012; Levinson, 2012). Such models successfully reproduce both high energy and low energy parts of observed spectra in some bursts: e.g. GRB090902B, see Ryde et al. (2011). However, the physics of dissipation is poorly understood. Fine tuning is involved, since such dissipation is required to occur very near the photosphere, see e.g. Vurm et al. (2012).

Several papers claim deviations of theoretically computed spectrum, coming from nondissipative photospheres, from the Planck shape at low energies. Beloborodov (2010) found the low energy photon index  $\alpha = 0.4$  (in contrast with  $\alpha = 1$  for Planck spectrum) solving the radiative transfer equations by Monte Carlo method in the steady relativistic wind with  $\Gamma = 300$ , and  $\Gamma = 600$ . Pe'er (2008) and Pe'er and Ryde (2011) found both analytically

and numerically flattening of the spectrum, considering late time emission from the relativistic wind when it switches off. This result is obtained considering the probability density function of the last scattering. Ruffini et al. (2011) found that the increased power at low energies with respect to the Planck spectrum (the slopes are  $\alpha = 0.82$  and  $0.34$  for accelerating and coasting photon thick instantaneous spectra) is the result of temperature distribution across the Photospheric EQuiTemporal Surface (Bianco et al., 2001; Ruffini et al., 2001).

In this paper we adopt a different approach. We use the radiative transfer equation for the steady wind model of Beloborodov (2011) with collision integrals obtained as the Fokker-Planck approximation to exact collision integrals of Compton scattering. This equation reduces to the classic Kompaneets equation for the medium at rest. However, here we consider relativistically expanding outflow, implying anisotropy in the collision integral. We solve numerically this equation and find the observed spectrum of photospheric emission from steady relativistic wind.

## G.2. The radiative transfer equation

We start with the radiative transfer equation in spherical symmetric steady (time independent) medium written in comoving frame, with the only exceptions for radius  $r$  and Lorentz factor  $\Gamma$  being the quantities measured in the laboratory frame (c.f. Beloborodov (2011)):

$$\frac{\partial n(r, \epsilon, \mu)}{\partial r} + \frac{1 - \mu^2}{r} \frac{\partial n}{\partial \mu} - \frac{1 - \mu}{r} \epsilon \frac{\partial n}{\partial \epsilon} = \frac{1}{\Gamma} \frac{\eta - \chi n}{1 + \mu}, \quad (\text{G.2.1})$$

where  $n$  is occupation number,  $\mu = \cos \vartheta$  parametrizes the angle between the momentum of the photon and the radius vector,  $\eta$  and  $\chi$  are emission and absorption coefficients,  $\epsilon$  is photon energy.

The collision integral takes into account that photons are scattered by the moving medium (see Fukue et al. (1985); Psaltis and Lamb (1997)) and con-

sequently their distribution is anisotropic in the comoving frame:

$$\begin{aligned}
 \eta - \chi n = & \frac{3n_e \sigma_T \epsilon}{16\pi} \left\{ \left( 1 - \frac{2\epsilon}{m_e c^2} \right) \right. & (G.2.2) \\
 & \times \int d\phi' [1 + x^2] n' - n \\
 & + \frac{2\epsilon}{m_e c^2} \int d\phi' [x^3 + x] n' \\
 & + \frac{2kT}{m_e c^2} \int d\phi' [(2x^3 - 3x^2 - 2x + 1)] n' \\
 & + \frac{1}{m_e c^2} \int d\phi' [1 + x^2] [1 - x] \\
 & \left. \times \left[ \frac{kT}{\epsilon^2} \frac{\partial}{\partial \epsilon} \epsilon^4 \frac{\partial}{\partial \epsilon} + \frac{1}{\epsilon^2} \frac{\partial}{\partial \epsilon} \epsilon^4 + 2n \frac{\partial}{\partial \epsilon} \epsilon^2 \right] n' \right\},
 \end{aligned}$$

where  $T$  is electron temperature,  $n = n(\epsilon, \mu)$ ,  $n' = n(\epsilon, \mu')$ ,  $d\phi' = d\mu' d\phi'$ , and  $x = \sqrt{1 - \mu^2} \sqrt{1 - \mu'^2} \cos(\phi - \phi') + \mu\mu'$ .

We integrate (G.2.2) over  $d\phi$ . Then we introduce the Legendre polynomials

$$n(\epsilon, \mu) = \sum_l n_l(\epsilon) P_l(\mu), \quad (G.2.3)$$

$$P_0 = 1, \quad P_1 = \mu, \quad P_2 = \frac{3\mu^2 - 1}{2}, \quad P_3 = \frac{5\mu^3 - 3\mu}{2},$$

and introduce a new variable  $\rho \equiv n\epsilon^2$ . Hence we arrive to the final equation

$$\begin{aligned}
 \frac{\partial \rho}{\partial r} + \frac{2\rho}{r} + \frac{1}{r(1 + \mu)} \frac{\partial}{\partial \mu} [(1 - \mu^2)(1 + \mu)\rho] & & (G.2.4) \\
 - \frac{1 - \mu}{r(1 + \mu)} \frac{\partial(\epsilon\rho)}{\partial \epsilon} = \frac{\epsilon^2(\eta - \chi n)}{\Gamma(1 + \mu)}
 \end{aligned}$$

with

$$\begin{aligned}
 \epsilon^2(\eta - \chi n) = n_e \sigma_T \epsilon & \left\{ \left( \frac{2\epsilon}{m_e c^2} - 1 \right) \right. \\
 & \times \left[ \rho_1 P_1 + \frac{9}{10} \rho_2 P_2 + \rho_3 P_3 \right] \\
 & + \frac{2\epsilon}{m_e c^2} \left( \frac{2}{5} \rho_1 P_1 + \frac{3}{70} \rho_3 P_3 \right) \\
 & - \frac{2kT}{m_e c^2} \left( \frac{1}{5} \rho_1 P_1 - \frac{3}{10} \rho_2 P_2 + -\frac{3}{35} \rho_3 P_3 \right) \\
 & + \frac{1}{m_e c^2} \left[ \frac{\partial}{\partial \epsilon} \left( kT \epsilon^2 \frac{\partial}{\partial \epsilon} + \epsilon(\epsilon - kT) \right) + 2\rho \frac{\partial}{\partial \epsilon} \right] \times \\
 & \left. \times \left( \rho_0 - \frac{2}{5} \rho_1 P_1 + \frac{1}{10} \rho_2 P_2 - \frac{3}{70} \rho_3 P_3 \right) \right\}. \tag{G.2.5}
 \end{aligned}$$

Integrating equation (G.2.4) over angles we have the Kompaneets equation for the variable  $\rho$  as

$$\begin{aligned}
 \frac{\partial \rho}{\partial r} + \frac{2\rho}{r} - \frac{1}{r} \frac{\partial(\epsilon \rho)}{\partial \epsilon} = \frac{\epsilon^2 n_e \sigma_T}{\Gamma m_e c^2} & \left( 1 - \frac{2\epsilon}{m_e c^2} \right) \\
 \times \left[ \frac{\partial}{\partial \epsilon} \left( kT \epsilon^2 \frac{\partial}{\partial \epsilon} + \epsilon(\epsilon - kT) \right) + 2\rho \frac{\partial}{\partial \epsilon} \right] \rho. \tag{G.2.6}
 \end{aligned}$$

As expected, the photon number conservation holds, that is  $\int d\epsilon r^2 \rho = \text{const.}$  When angle dependence is taken into account photon conservation gives

$$\int d\mu d\epsilon (1 + \mu) r^2 \rho = \text{const.} \tag{G.2.7}$$

In what follows we integrate numerically equation (G.2.4) with collision integral (G.2.5). In doing so we have to assume the temperature and number density of electrons dependence on radius. Following Ruffini et al. (2011) we adopt the scaling laws:

$$n_e \propto R^{-2}, T_e \propto R^{-2/3}. \tag{G.2.8}$$

This model describes coasting steady relativistic wind in the optically thick regime. Both these scaling laws are justified by the solution of relativistic hydrodynamic equations. The electron density decreases with radius so does the optical depth. Near the photosphere, where the optical depth reaches unity, the coupling between photons and electrons weakens. We assuming that electrons keep cooling adiabatically even when the outflow becomes optically thin.

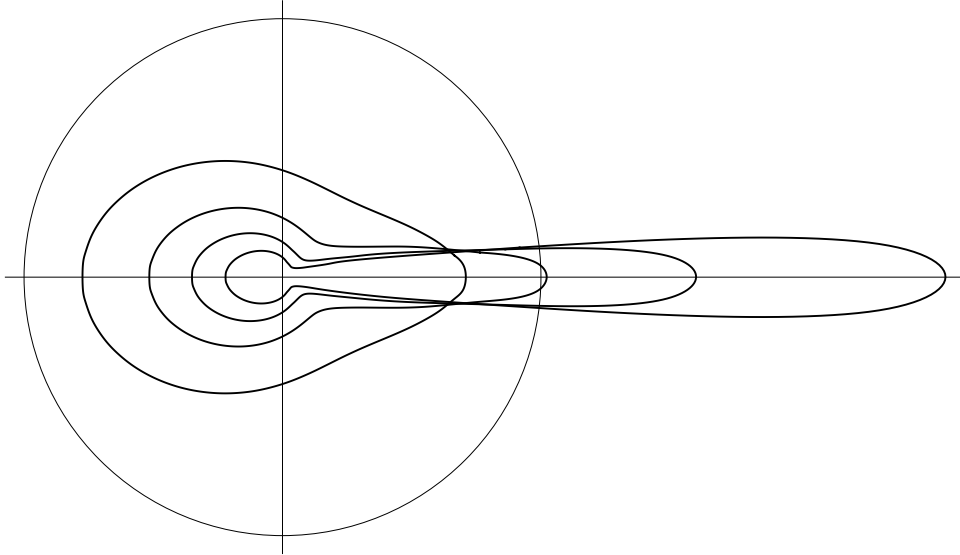


**Figure G.1.:** Anisotropy (in photon number) of photon distribution developing near the photosphere. When the outflow has high optical depth the distribution is isotropic, but near the photosphere it becomes increasingly anisotropic.

Since initially the outflow is highly opaque, photons have thermal spectrum and isotropic distribution in the comoving reference frame. Near the photosphere the coupling of photons to the medium is due to Compton scattering on electrons.

### G.3. Results

The anisotropy of photon distribution near the photosphere in comoving reference frame found by Beloborodov (2011) is an interesting effect which we have also found in our approach. This result is illustrated in Fig. G.1.

This effect can be explained from the geometric point of view. Since collisions tend to isotropize photons, only those photons which are undergoing scatterings have nearly isotropic distribution. In contrast photons that already experienced their last scattering have increasingly anisotropic distribution in the comoving frame due to relativistic aberration. Hence the local photon field at the photosphere which contains all photons, those which continue to scatter and those which already propagate freely, becomes more and more anisotropic.

Our computation is performed in the comoving reference frame. In order to find the photon spectrum which distant observer will detect we have to transform the spectrum into the laboratory reference frame. One has to use the following transformations

$$N(\epsilon_L) = 2\pi \int_0^1 d\mu_L r^2 \mu_L n(\epsilon, \mu) \epsilon_L^2, \quad (\text{G.3.1})$$

$$\epsilon = \Gamma(1 - \beta\mu_L)\epsilon_L, \quad \mu = \frac{\mu_L - \beta}{1 - \beta\mu_L}, \quad (\text{G.3.2})$$

where the subscript "L" denotes quantities in the laboratory frame.

Two asymptotic cases were found in Ruffini et al. (2011) to have very different spectra from the photosphere: photon thick and photon thin ones. Since the photon thin case is characterized by nearly Planck instantaneous observed spectrum, here we concentrate on the photon thick case.

Consider steady relativistic wind with the following parameters: luminosity at the base  $L$ , Lorentz factor at the coasting phase  $\Gamma$  and initial radius  $R_0$ :

$$L = 10^{54} \text{ erg/s}, \Gamma = 500, R_0 = 10^8 \text{ cm}. \quad (\text{G.3.3})$$

Given these values we find for initial optical depth

$$\tau_0 = \frac{\sigma_T L}{4\pi m_p c^3 R_0 \Gamma} = 2.3 \times 10^{10}, \quad (\text{G.3.4})$$

where  $\sigma_T$  is the Thomson cross section, and initial temperature

$$T_0 = \left( \frac{L_0}{16\pi\sigma_{\text{SB}}R_0^2} \right) = 1.2 \text{ MeV}, \quad (\text{G.3.5})$$

where  $\sigma_{\text{SB}}$  is the Stefan-Boltzmann constant. The photospheric radius is

$$R_{ph} = \frac{\tau_0}{2\Gamma^2} R_0 = 4.7 \times 10^{12} \text{ cm}. \quad (\text{G.3.6})$$

We start the computation at the beginning of the coasting phase with  $R_i = 5 \times 10^{10} \text{ cm}$  where the optical depth is  $\tau_i = 10^2$  and compute the spectrum until it settles to a static solution in the laboratory reference frame well above the photospheric radius  $R \gg R_{ph}$ .

In Fig. G.2 we show the evolution of photon spectrum in comoving reference frame for selected values of radii starting at large optical depth through the photosphere ending up at small optical depth  $\tau \sim 10^{-2}$ .

While the spectrum in comoving frame is maintaining the Planck shape at large optical depths, it becomes distorted with the energy transferred to the low energy part of the spectrum. It is the consequence of interaction with electrons which on average have smaller energy than photons do. In fact, near the photosphere the average energy of photons saturates Beloborodov (2011), but the one of electrons continues to decrease. When this spectrum is

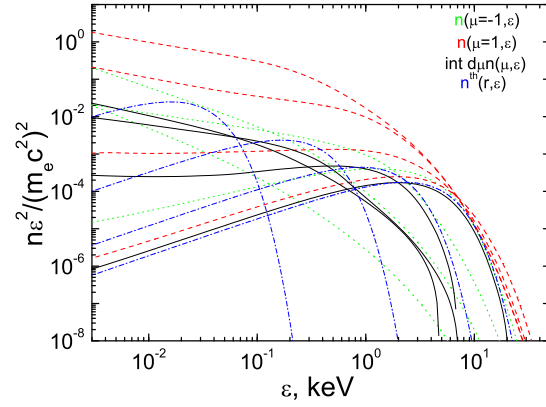


**Figure G.2.:** The spectrum of photons ( $F_V$ ) in the comoving reference frame is shown for selected values of radii:  $10^{11}$ ,  $10^{12}$ ,  $10^{13}$  and  $5 \times 10^{14}$  cm. Solid curve shows integrated spectrum over angles, dashed curve shows the spectrum of photons propagating towards the observer in the comoving frame, dotted curve shows the spectrum of photons propagating from the observer in the comoving frame, dashed-dotted curve shows the Planck spectrum with the temperature following the relation (G.2.8) for comparison.

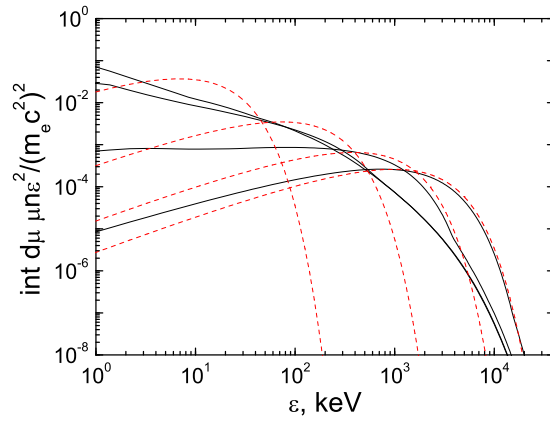


**Figure G.3.:** The spectrum of photons ( $F_V$ ) transformed to the laboratory reference frame is shown for selected values of radii, corresponding to Fig. G.2. Solid curve shows the observed spectrum of photons integrated over angles, dashed curve shows the spectrum of photons arriving to a given radius with thermal spectrum in the comoving reference frame, transformed to the laboratory reference frame.

transformed to the laboratory frame using (G.3.2) we find that in addition to deviations from Planck spectrum due to contribution from large angles, we also have the effect of comptonization. Clearly this effect becomes less and less prominent with decreasing optical depth, and decreasing electron temperature. The final shape of the spectrum is reached for  $\tau > 10^{-2}$ . As the result, we find that observed spectrum is broader than the Planck one, with low energy part of observed spectrum from the steady relativistic wind has the index  $\alpha = -0.7$ , to be compared with  $\alpha = 1$  for Planck spectrum. The difference with respect to results obtained by Monte Carlo simulations Beloborodov (2010) where the low energy index is  $\alpha = 0$ , see also Ruffini et al. (2011); Begue et al. (2012) for isotropic scattering model and  $\alpha = 0.4$  for Compton scattering model arise essentially because the Kompaneets-type collision integral (G.2.2) takes into account stimulated emission of photons. In fact, equilibrium distribution for large optical depths without stimulated emission is the Wien spectrum Begue et al. (2012).

## **G.4. Conclusions**

We considered relativistic steady wind and computed the observed spectrum of its photospheric emission. In doing this we solved the equation of radiative transfer in comoving frame with exact Compton collision term in Fokker-Planck approximation, including the effect of anisotropy. We obtained the photon spectra in the laboratory frame, as seen by a distant observer.

We confirm the result of Beloborodov (2011) indicating the presence of strong anisotropy developed in the comoving frame at the photosphere. Some qualitative differences in our results are due to the fact that he used approximate collision term, instead of our exact one.

The observed spectrum from the photosphere is much broader than the Planck function. The low energy photon index is found to be  $\alpha = -0.7$  in good agreement with typical low energy index  $\alpha \sim -1$  observed in GRBs.

# H. Semidegenerate self-gravitating system of fermions as a model for dark matter halos and universality laws

## H.1. Introduction

The problem of dark matter distribution in galactic halos has traditionally been treated in the realm of newtonian physics in view of the low velocities of the stars in the galaxies, like the simulations from Navarro et al. (1997). In the meantime, phenomenological profiles of dark matter have been advanced by Einasto (1965); Burkert (1995), and universal properties of the dark matter distribution have been inferred from dwarf galaxies and probably globular clusters all the way to very massive galaxies (Gentile et al., 2009; Donato et al., 2009; Walker et al., 2010; Boyarsky et al., 2009). However, a problem arises: while simulations like those from NFW point to a cusped halo, observations from various types of galaxies seem to show cored halos Salucci et al. (2011). This discrepancy between theory and observations is not yet fully understood, but could show a problem with the simulations done so far.

In a completely unrelated field (as of yet), the physics of Active Galactic Nuclei (AGN) has been recognized for more than 50 years as dominated by relativistic gravitational effects of a black hole. The formation of these black holes is not yet fully understood, although black holes formed all the way to  $z \approx 8$  have been observed in AGNs with mass ranging all the way to  $10^8 M_{\odot}$  Peterson (2010). Due to the lack of understanding on the energetics of AGNs and on the formation of the black holes, the possibility of an extended object in the core of galaxies has been advanced by Viollier et al. (1993).

The aim of this paper is to present a unified approach to the dark matter distribution in the galactic halos and also in the galactic center. In order to do that, some assumptions have been made:

1. The treatment must be a fully relativistic one from the beginning, in order to explain both the galactic nuclei and galactic haloes.
2. The matter particles are semi-degenerated fermions and so obey the Fermi-Dirac statistics, together with the relativistic thermodynamic

equilibrium conditions.

## H.2. Model

The equilibrium configurations of a self-gravitating semi-degenerate system of fermions were already studied by Gao et al. (1990). It is shown that in any such system the density at large radii scales as  $r^{-2}$  quite independently of the values of the central density, making the system unbounded and with infinite mass. This problem can be solved by introducing an energy cutoff in the distribution function (Ingrosso et al., 1992).

Since we are considering spherical symmetry, the line element is written in standard Schwarzschild coordinates as

$$ds^2 = -e^{\nu(r)} dt^2 + e^{\lambda(r)} dr^2 + r^2(d\theta^2 + \sin^2 \theta d\phi^2). \quad (\text{H.2.1})$$

The equilibrium equations are given by

$$\frac{dP}{dr} = -\frac{G}{c^2} \frac{(P + \rho c^2)(M(r) + 4\pi\rho r^3)}{r(rc^2 - 2GM(r))} \quad (\text{H.2.2})$$

$$\frac{dM}{dr} = 4\pi\rho r^2, \quad (\text{H.2.3})$$

with  $M$  the mass within a radius  $r$ ,  $\rho$  and  $P$  the energy density and the pressure respectively, given by

$$\rho = m \frac{g}{h^3} \int_0^{\epsilon_c} \left(1 + \frac{\epsilon}{mc^2}\right) \frac{1 - e^{(\epsilon - \epsilon_c)/kT}}{e^{(\epsilon - \mu)/kT} + 1} d^3p \quad (\text{H.2.4})$$

$$P = \frac{2g}{3h^3} \int_0^{\epsilon_c} \left(1 + \frac{\epsilon}{2mc^2}\right) \left(1 + \frac{\epsilon}{mc^2}\right)^{-1} \frac{(1 - e^{(\epsilon - \epsilon_c)/kT})\epsilon}{e^{(\epsilon - \mu)/kT} + 1} d^3p, \quad (\text{H.2.5})$$

with  $\epsilon_c$  being the cutoff energy,  $g = 2s + 1$  being the multiplicity factor,  $m$  being the mass of the particle, and  $T$  being the temperature and  $\mu$  the chemical potential. The volume element in momentum space can be expressed in terms of the kinetic energy  $\epsilon$  of the particles as

$$d^3p = 4\pi p^2 dp = 4\sqrt{2}m^3 c^3 \sqrt{1 + \epsilon/2mc^2} (1 + \epsilon/mc^2) \sqrt{\epsilon/mc^2} d(\epsilon/mc^2). \quad (\text{H.2.6})$$

The particle energy is a constant of motion, so

$$(\epsilon + mc^2)e^{\nu/2} = \text{const}, \quad (\text{H.2.7})$$

while thermodynamical equilibrium implies

$$(\mu + mc^2)e^{\nu/2} = (\mu_R + mc^2)e^{\nu_R/2} \quad (\text{H.2.8})$$

$$Te^{\nu/2} = T_R e^{\nu_R/2}, \quad (\text{H.2.9})$$

where the quantities with subscript ‘‘R’’ refer to the boundary of the configuration. For the cutoff energy we have

$$(\epsilon_c + mc^2)e^{\nu/2} = mc^2 e^{\nu_R/2}, \quad (\text{H.2.10})$$

since  $\epsilon_c(R) = 0$ .

Introducing the function  $W = \epsilon_c/kT$  and the temperature parameter at the boundary  $\beta_R = kT_R/mc^2$ , and using eqs. (H.2.9) and (H.2.10) we can find that

$$\frac{mc^2}{kT} = \frac{1 - \beta_R W}{\beta_R}. \quad (\text{H.2.11})$$

Note that the condition  $0 \leq \beta_R W < 1$  has to be fulfilled. Using eq. (H.2.9) to substitute the temperature in eq. (H.2.8) we get the relation between the metric function  $\nu$  and  $W$ :

$$e^\nu = e^{\nu_R} (1 - \beta_R W)^2 \quad (\text{H.2.12})$$

so now the spacetime metric is completely determined:

$$e^\nu = e^{\nu_R} [1 - \beta_R W]^2, \quad e^\lambda = \left(1 - \frac{2GM}{rc^2}\right)^{-1} \quad (\text{H.2.13})$$

with  $\nu_R + \lambda_R = 0$ .

Differentiating eq. (H.2.12) and using the conservation of the energy momentum tensor

$$\frac{dP}{dr} = -\frac{1}{2}(P + \rho c^2) \frac{d\nu}{dr} \quad (\text{H.2.14})$$

gives

$$\frac{dP}{dr} = \frac{\beta_R(P + \rho c^2)}{1 - \beta_R W} \frac{dW}{dr} \quad (\text{H.2.15})$$

and we can write eq. (H.2.2) as

$$\frac{dW}{dr} = -\frac{G}{c^2} \left[ \frac{1 - \beta_R W}{\beta_R} \right] \frac{Mc^2 + 4\pi Pr^3}{r(rc^2 - 2GM)} \quad (\text{H.2.16})$$

In order to numerically integrate the final set of equations (H.2.3) and (H.2.16) with initial conditions  $W(0) = W_0$  and  $M(0) = 0$ , it is useful to

transform all of our physical variables into dimensionless ones:

$$\rho = \frac{c^2}{G\chi^2}\hat{\rho} \quad (\text{H.2.17})$$

$$P = \frac{c^4}{G\chi^2}\hat{P} \quad (\text{H.2.18})$$

$$M = \frac{c^2\chi}{G}\hat{M} \quad (\text{H.2.19})$$

$$r = \chi\hat{r}, \quad (\text{H.2.20})$$

where

$$\chi = \frac{\hbar}{mc} \left( \frac{m_p}{m} \right) \left( \frac{8\pi^3}{g} \right)^{1/2} \quad (\text{H.2.21})$$

has dimension of length and  $m_p = (\hbar c/G)^{1/2}$  is the Planck mass.

It is instructive to write down characteristic length  $\chi$ , that is inversely proportional to square of the mass of the particle, in conventional units

and the unit of mass is

$$\log_{10} \frac{c^2\chi}{GM_\odot} = 13.26 - 2 \log_{10} \frac{m}{\text{keV}/c^2}, \quad (\text{H.2.22})$$

where  $M_\odot = 1.989 \cdot 10^{33}$  g is mass of the Sun.

We then obtain the dimensionless equations

$$\begin{aligned} \frac{dW}{d\hat{r}} &= - \left[ \frac{1 - \beta_R W}{\beta_R} \right] \frac{\hat{M}(r) + 4\pi\hat{P}\hat{r}^3}{\hat{r}(\hat{r} - 2\hat{M}(r))} \\ \frac{d\hat{M}(r)}{d\hat{r}} &= 4\pi\hat{\rho}\hat{r}^2, \end{aligned} \quad (\text{H.2.23})$$

where

$$\begin{aligned} \hat{\rho} &= 4\sqrt{2}\pi \left[ \frac{\beta_R}{1 - \beta_R W} \right]^{3/2} \int_0^W \left[ 1 + \frac{\beta_R x/2}{1 - \beta_R W} \right]^{1/2} \left[ 1 + \frac{\beta_R x}{1 - \beta_R W} \right]^2 \frac{1 - e^{x-W}}{e^{x-\theta} + 1} x^{1/2} dx \\ \hat{P} &= \frac{8\sqrt{2}}{3}\pi \left[ \frac{\beta_R}{1 - \beta_R W} \right]^{5/2} \int_0^W \left[ 1 + \frac{\beta_R x/2}{1 - \beta_R W} \right]^{3/2} \frac{1 - e^{w-W}}{e^{x-\theta} + 1} x^{3/2} dx, \end{aligned} \quad (\text{H.2.24})$$

where  $\theta = \mu/kT$  is the degeneracy parameter and we introduced the variable  $x = \epsilon/kT$ . We have for this variable

$$\frac{\epsilon}{mc^2} = \frac{\beta_R x}{1 - \beta_R W}. \quad (\text{H.2.25})$$

The relation between the degeneracy parameter  $\theta$  and  $W$  is

$$W = \theta - \theta_R, \quad (\text{H.2.26})$$

so that  $W(R) = 0$ , where  $\theta_R$  is the value of the degeneracy parameter at the boundary. We can relate the parameters in the boundary with those in the center

$$\theta_R = \theta_0 - W_0 \quad \beta_R = \frac{\beta_0}{1 + \beta_0 W_0} \quad (\text{H.2.27})$$

so that  $\beta_R \approx \beta_0$  for  $\beta_0 \ll 1$ . Besides that we have

$$\frac{1 - \beta_R W}{\beta_r} = \frac{1 - \beta_0 (W - W_0)}{\beta_0}. \quad (\text{H.2.28})$$

Now the system can be completely solved (numerically) by solving the equations eq. (H.2.23) together with

$$\theta = \theta_0 + W - W_0 \quad (\text{H.2.29})$$

and using eq. (H.2.24) with three independent parameters:  $W_0$ ,  $\theta_0$  and  $\beta_0$ . The only remaining free parameter is the mass of the particle, which occurs only in the definition of  $\beta$  and the characteristic length  $\chi$ .

### H.2.1. Properties of the equilibrium configurations

We have solved numerically the system of integral-differential equations given by (H.2.16), the two equations corresponding to  $\beta$  and  $\theta$  and (H.2.24), with a set of initial conditions  $M_0$ ,  $W_0$ ,  $\beta_0$  and  $\theta_0$ . Galactic dark matter halos have asymptotic rotation velocities of the order of ten to thousands km/s, i.e., they are not relativistic. As that velocities are of the same order as thermal velocities of fermionic particles forming the halo, this means that  $\beta_R \ll 1$  and consequently  $\beta_0 \ll 1$ . For semidegenerate configurations  $\theta_0 \gtrsim 20$ , and in this case we have three regions of halo (fig. H.1): a degenerate core of almost constant density, an inner halo also with almost constant density and a tail where density scales as  $r^{-2}$  until the cutoff.

On the velocity curve, we can see 4 characteristic regions (fig. H.2):

- Part I: The core with constant density, where  $v \propto r$ ;
- Part II: The first part of the inner halo, where the mass of the core prevails over the mass of the halo and  $v \propto r^{-1/2}$ ;
- Part III: Second part of the inner halo, where now the mass of the halo prevails and again  $v \propto r$ ;

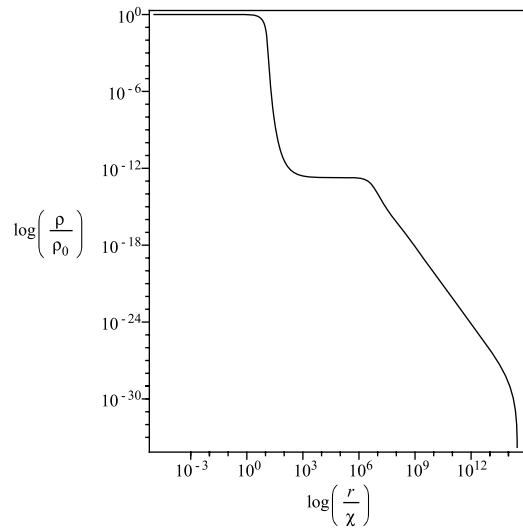


**Figure H.1.:** Density profile of the model for  $\beta_0 = 10^{-8}$ ,  $\theta_0 = 32$  and  $W_0 = 92$ .

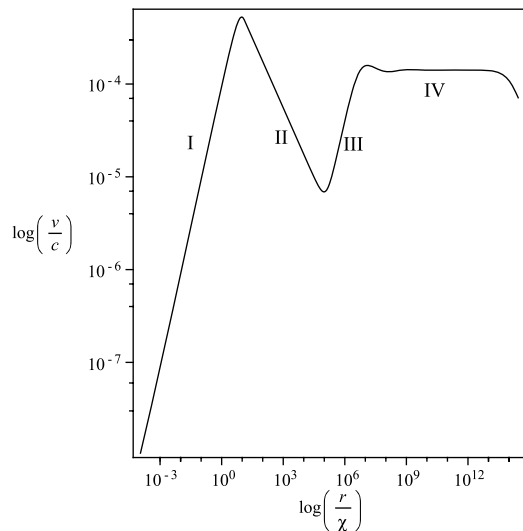


**Figure H.2.:** Velocity curve for the same parameter values as before

- Part IV: The outer halo, where the velocity tends to a constant value  $v_0$  after some oscillations of diminishing magnitude.

### H.3. Comparison with other DM profiles

To compare results obtained with known Dark Matter properties we need to find out the correspondence between fits of circular velocity, much like it was suggested in Boyarsky et al. (2009). There is some controversy in current literature about the undisturbed profile of dark matter in Galaxies and

clusters. Cold dark matter simulations suggest the so-called Navarro-Frenk-White profile (Navarro et al., 1997)

$$\rho = \frac{\rho_{NFW}}{r/r_{NFW}(1 + r/r_{NFW})^2} \quad (\text{H.3.1})$$

and Einasto profile (Navarro et al., 2010) introduced by J. Einasto for modeling of matter distribution in Milky Way (Einasto, 1965)

$$\rho = \rho_E \exp\left(-\frac{2}{\alpha} [(r/r_E)^\alpha - 1]\right) \quad (\text{H.3.2})$$

while phenomenological pseudoisothermal sphere

$$\rho = \frac{\rho_{iso}}{1 + (r/r_{iso})^2} \quad (\text{H.3.3})$$

and Burkert profile (Burkert, 1995)

$$\rho = \frac{\rho_B}{(1 + r/r_B)(1 + (r/r_B)^2)}. \quad (\text{H.3.4})$$

are commonly used for fitting. Comparing profiles of circular velocity for all these profiles with the one of the semidegenerate solution, we came to conclusion that NFW and Burkert profiles, having wrong asymptotics as  $r \rightarrow \infty$ , better reproduce the characteristic "bump" in the circular velocity near the edge of inner halo (fig. H.3). The best reproduction is obtained for Burkert profile.

As we move outside from the border of inner/outer halo, the fits by pseudoisothermal sphere became better than that of other profiles (fig. H.4). The fits by other profiles suffer due to their different outer slope, so constant circular velocity can be only approximated in a finite range of radii by a decreasing function. As a result we have systematic deviations from the real flat curve in the beginning and the end of fitting range.

The result obtained means that all fits of rotational curves by Burkert, NFW and pseudoisothermal sphere profiles could be fitted as well by semidegenerate fermion halo.

## H.4. Scaling Laws

The solutions obtained show remarkable self-similarity properties. The characteristics of solutions obey five scaling laws against the free parameters of the model  $\beta_0$ ,  $\theta_0$ ,  $W_0$  and  $m_f$ . These are laws for the asymptotic velocity of the rotation curves, for the core mass, for the core radius, for the halo mass and for the halo radius.

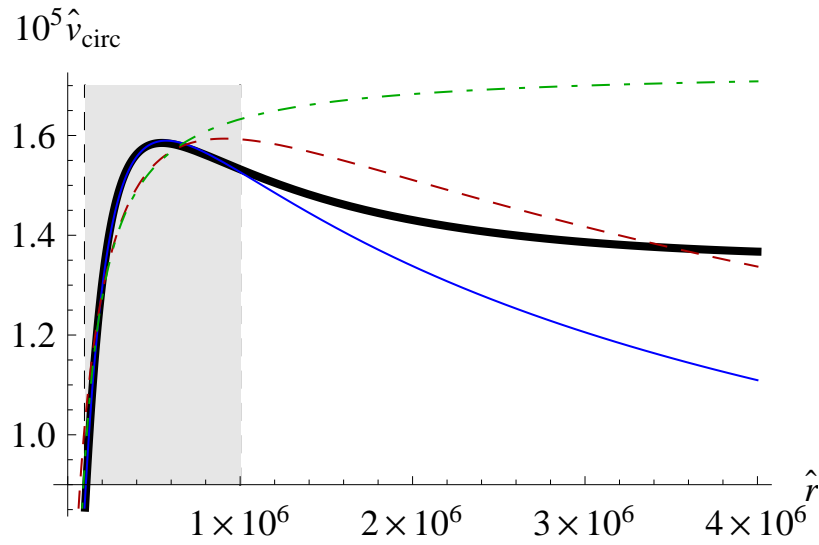


**Figure H.3.:** Dependence of  $\hat{v}_{\text{circ}} = v_{\text{circ}}/c$  on dimensionless radius  $\hat{r}$  (black thick line) for  $\beta = 10^{-10}$ ,  $\theta_0 = 20$  near the edge of the inner halo and its fits by NFW (red dashed line), Burkert (blue thin line) and pseudothermal sphere (green dot-dashed line) profiles. The range of  $\hat{r}$  used for fitting is shown by grey shading ( $\hat{r} = 10^5$  to  $\hat{r} = 10^6$ ).

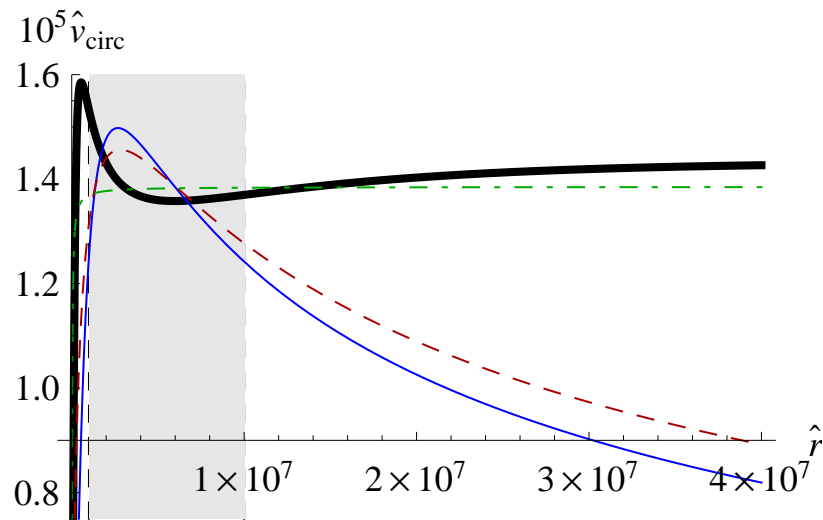


**Figure H.4.:** Dependence of  $\hat{v}_{\text{circ}} = v_{\text{circ}}/c$  on dimensionless radius  $\hat{r}$  (black thick line) for  $\beta = 10^{-10}$ ,  $\theta_0 = 20$  in the outer halo and its fits by NFW (red dashed line), Burkert (blue thin line) and pseudothermal sphere (green dot-dashed line) profiles. The range of  $\hat{r}$  used for fitting is shown by grey shading ( $\hat{r} = 10^6$  to  $\hat{r} = 10^7$ ).

Asymptotic rotation velocity scaling law

$$\log_{10} \frac{v_0}{\text{km/s}} = 5.65 + 0.500 \log_{10} \beta_0 \quad (\text{H.4.1})$$

show dependence on the temperature of the configuration only. This is essentially the same scaling law that appears in the case of isothermal sphere (Binney and Tremaine, 1987).

Core is defined as region from the center of the system till the first maximum of the rotation velocity curve (region I in fig. H.2). Near that point the density of fermions decreases fast. Scalings of mass and radius of the core are

$$\log_{10} \frac{M_c}{M_\odot} = 12.292 + 0.75 \log_{10} \beta_0 + 0.75 \log_{10} \theta_0 - 2 \log_{10} \frac{m_f}{\text{KeV}/c^2}, \quad (\text{H.4.2})$$

$$\log_{10} \frac{r_c}{\text{pc}} = -0.744 - 0.25 \log_{10} \beta_0 - 0.25 \log_{10} \theta_0 - 2 \log_{10} \frac{m_f}{\text{KeV}/c^2}. \quad (\text{H.4.3})$$

Characteristics of core is dependent not on  $\beta_0$  and  $\theta_0$  separately, but only on their product  $\beta_0 \theta_0$ , i.e. on the chemical potential  $\mu$  at the semidegenerate center of configuration, in accordance with results of Narain et al. (2006). From the laws an important relation could be obtained, involving only  $M_c$ ,  $r_c$  and  $m$

$$\log_{10} \left( \frac{M_c \text{ pc}^3}{r_c^3 M_\odot} \right) = 10.06 + 4 \log_{10} \frac{m_f}{\text{KeV}/c^2}. \quad (\text{H.4.4})$$

Halo is defined as region up  $r_0$ , where density drops to 1/4 of that in minimum rotational velocity point  $\rho = \rho(r_h) = \frac{\rho_0}{4}$  (regions II and III in fig. H.2). Scaling laws of halo properties are

$$\log_{10} \frac{M_h}{M_\odot} = 13.172 + 0.77 \log_{10} \beta_0 + 0.16 \theta_0 - 2 \log_{10} \frac{m_f}{\text{KeV}/c^2}, \quad (\text{H.4.5})$$

$$\log_{10} \frac{r_h}{\text{pc}} = -0.49 - 0.25 \log_{10} \beta_0 + 0.16 \theta_0 - 2 \log_{10} \frac{m_f}{\text{KeV}/c^2}. \quad (\text{H.4.6})$$

The equations above are exact in  $m_f$  and hold in the following physical range of the other parameters:  $\log_{10} \beta_0 \in [-10, -5]$ ,  $\theta_0 \in [20, 200]$ ,  $W_0 \in [110, 200]$ . Note that  $W_0$  does not appear in the scaling laws, so that its value does not change inner structure of configuration.

#### **H.4.1. Solving the scaling laws system of equations**

In order to find out the order of semidegenerate halo parameters corresponding to observed ones, we adopted the four most reliable observed characteristics of the Milky Way, i.e. its asymptotic rotational velocity  $v_0 \approx 220$  km/s, mass of the central object in the Galactic center  $M_c \approx 4 \times 10^6 M_\odot$ , radius of Galactic halo  $r_h \equiv r_0 \approx 14 \times 10^3$  pc, ( $r_0$ : one dark halo scale length) and its mass  $M_h \approx 2 \times 10^{11} M_\odot$ .

We take three equations corresponding to the number of three unknown parameters, (H.4.1), (H.4.5) with (H.4.2) and (H.4.6)

$$\log_{10} \frac{v_0}{\text{km/s}} = 5.65 + 0.5 \log_{10} \beta_0, \quad (\text{H.4.7})$$

$$\log_{10} \frac{M_c}{M_\odot} = 12.292 + 0.75 \log_{10} \beta_0 + 0.75 \log_{10} \theta_0 - 2 \log_{10} \frac{m_f}{\text{KeV}/c^2} \quad (\text{H.4.8})$$

$$\log_{10} \frac{r_h}{\text{pc}} = -0.49 - 0.25 \log_{10} \beta_0 + 0.16 \theta_0 - 2 \log_{10} \frac{m_f}{\text{KeV}/c^2}. \quad (\text{H.4.9})$$

Then solving (H.4.7–H.4.9) using the data presented above we arrive to

$$\beta_0 = 10^{-6.6}, \quad (\text{H.4.10})$$

$$\theta_0 = 32.25 \quad (W_0 = 130), \quad (\text{H.4.11})$$

$$m_f = 12.3 \text{ KeV}. \quad (\text{H.4.12})$$

Finally we can take the law (H.4.3) to obtain  $r_c = 8.7 \times 10^{-3}$  pc. Although this value is quite far from the size of very compact region known as SgrA\*, it is still in the very inner region of the bulge, in accordance with the observations of Ghez et al. 2008 and Gillessen et al. 2009b made for orbits of S2(blue) stars, where can be seen that at a radius of around  $1 \times 10^{-2}$  pc the enclosed mass for the orbit must be around  $4 \times 10^6 M_\odot$ .

#### **H.4.2. Application to spiral, elliptical and group of galaxies**

The application of the model to galaxies has been inspired by the recent observations showing that the mean dark matter surface density within one dark halo scale/length  $r_0$  (within this radius the volume density profile of dark matter remains approximately flat) is constant across a wide range of galaxies (Gentile et al., 2009; Donato et al., 2009), or equivalently, an almost constant DM acceleration at  $r_0$ :  $a_{DM} \approx 1 \frac{\text{km}^2}{\text{s}^2 \cdot \text{pc}}$  is observed (Walker et al., 2010). This Universality laws have also been extended by Boyarsky et al. (2009) for matter distributions at all observed scales.

### Spiral galaxies

We based our analysis within the phenomenological work made by Walker et al. (2010) from the MO7 data, consisting in HI rotation curves, and then isolating the DM contribution to an observed rotation curve subtracting contributions from stellar and HI regions. This data is based on 686 independent resolved rotation velocities measurements for 60 galaxies, spanning radii between  $1 \text{ kpc} \leq r_h \leq 75 \text{ kpc}$ . The important feature is that this sample covers virtually the entire range of spiral properties; ie. circular velocities  $50 \text{ km/s} \leq v_0 \leq 300 \text{ km/s}$  within others. With this data they could find a constant acceleration due to DM  $a_{DM} = 0.9^{+0.9}_{-0.5} \frac{\text{km}^2}{\text{s}^2 \cdot \text{pc}} = 3^{+3}_{-2} \times 10^{-9} \frac{\text{cm}}{\text{s}^2}$ , in complete accordance with the Universality law found by Gentile et al. (2009).

In the context of our model, and in order to reproduce the  $a_{DM}$  with the corresponding scatter in a plot  $a_{DM}$  vs  $r_h$ , we proceeded as follows:

- i) From (H.4.1) we obtained the corresponding  $b_0$  for the lowest observed value of the circular velocity  $v_0 = 50 \frac{\text{km}}{\text{s}}$ ;  $\log_{10} \beta_0 = -7.9$ ;
- ii) From (H.4.6) and using the lowest limit for  $\beta_0$ ,  $\log_{10} \beta_0 = -7.9$ ,  $m_f = 13.5 \text{ KeV}$  and the two observed border values for  $r_h$  (1 kpc till 75 kpc) we obtained the entire range of validity for  $\theta_0$ , namely  $23.6 \leq \theta_0 \leq 35.3$ ;
- iii) The same as in i), but now for the highest value of the circular velocity  $v_0 = 300 \text{ km/s}$ , and then finding the corresponding  $\log_{10} \beta_0 = -6.34$ ;
- iv) The same as in ii), but now with the highest limit of  $\beta_0$ , obtaining now a new range of validity for  $\theta_0$ ,  $26 \leq \theta_0 \leq 38$ ;
- v) Considering that  $a_{DM} = \frac{GM_h}{r_h^2}$  and making use of the equations (H.4.5) and (H.4.6), we obtained the corresponding scaling law for the acceleration due to DM as

$$\log_{10} \frac{a_{DM}}{\text{km}^2/(\text{s}^2 \cdot \text{pc})} = 11.786 + 1.27 \log_{10} \beta_0 - 0.16 \theta_0 + 2 \log_{10} \frac{m}{\text{keV}/c^2} \quad (\text{H.4.13})$$

vi) Finally, with (H.4.6) and (H.4.13) and the physical ranges for  $\beta_0$  and  $\theta_0$  obtained above, we made a plot  $a_{DM}$  vs  $r_h$ , that shows that all the data points of the Universality law for  $a_{DM}$  made by Walker et al. (2010) are included by the physical range of parameters of our model. The two sloped lines indicates the  $\beta_0$  range (ie. the velocity range), and the length of these lines indicates the  $\theta_0$  range; while the two horizontal lines are the limits related to the scatter from the observations.

The comparison between the two graphics is shown in Fig. H.5.

### Spiral, elliptical and group of galaxies

The application of the model in this section was inspired in the phenomenological work made by Boyarsky et al. (2009) based on analogous observations as in the former case mentioned in the work. The objects covered in this case

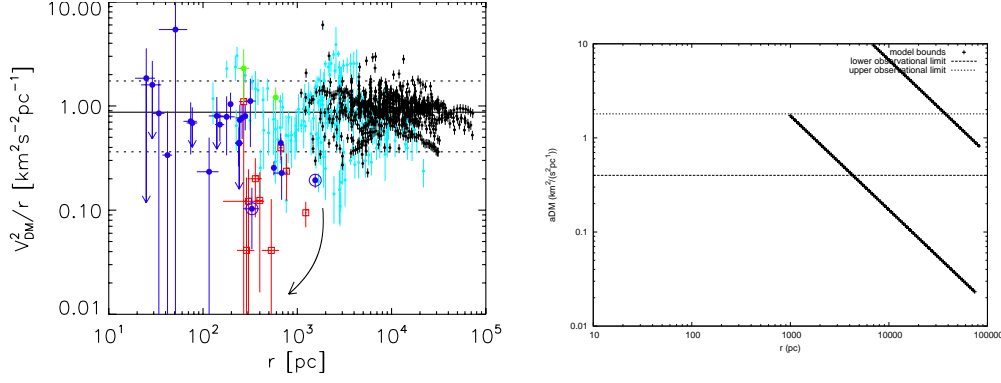


**Figure H.5.:** The acceleration due to dark matter vs the halo scale-length  $r_h$ . The left bound corresponds to  $v_0 = 50$  km/s ( $\log \beta_0 = -7.9$ ), while the right bound corresponds to  $v_0 = 300$  km/s ( $\log \beta_0 = -6.34$ ). Left panel figure is reproduced from Walker et al. (2010).

are: 124 spiral galaxies, 10 elliptical ones and 25 groups of galaxies (within specific selection criteria explained in that paper).

Authors present the Universality law in terms of the DM column density

$$S = \frac{2}{r_0^2} \int_0^{r_0} r dr \int dz \rho_{DM} \sqrt{r^2 + z^2} \approx \frac{M_{cyl}}{\pi r_0^2}, \quad (\text{H.4.14})$$

so that the column density can be approximated as the mass within a cylinder of radius  $r_0$  (meaning this as always for our purpose, the one halo scale-length). This quantity is also proportional to  $\rho_0 r_0$ , so it should be constant for a wide span of magnitudes.

Interpreting  $M_{cyl}$  as the mass of the halo, and using the formula mentioned in (Boyersky et al., 2009),  $S \approx \frac{M_{cyl}}{\pi r_0^2}$  and noting that  $S G \pi = a_{DM}$  we find from (H.4.5) and (H.4.6) the corresponding scaling law in this case as

$$\log_{10} \frac{S}{M_{\odot}/\text{pc}^2} = 16.115 + 1.27 \log_{10} \beta_0 - 0.16 \theta_0 + 2 \log_{10} \frac{m_f}{\text{keV}/c^2}. \quad (\text{H.4.15})$$

Then, in order to reproduce the  $\log_{10} S$  with the corresponding scatter in a plot  $\log_{10} S$  vs  $M_h$ , we proceeded in a complete analogous way as in the points i)-iv) for the former case.

The comparison between the two graphics is shown in Fig. H.6.

Two important remarks concerning the richness of the model are: *i*) we don't take into account the data of Dwarf Galaxies due to the very high error bars in the observations, and *ii*) as it can be seen from making a direct comparison between the two graphics for the second case, although the groups of galaxies are covered by the range of parameters mentioned above, the model

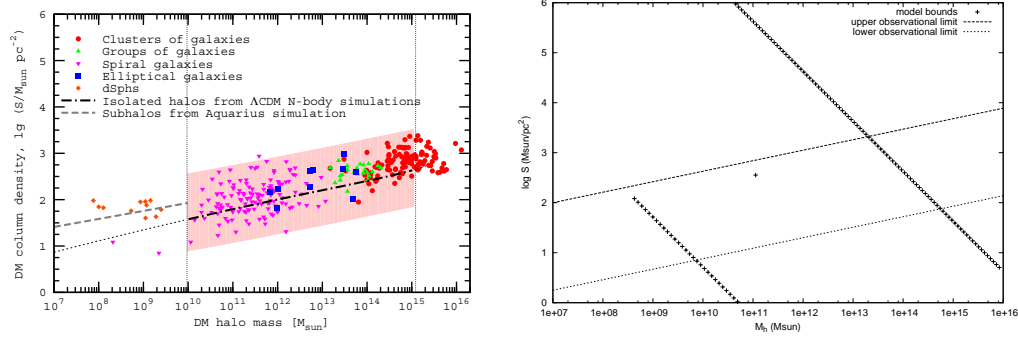


**Figure H.6.:** The dark matter column density  $\mathcal{S}$  vs the halo mass  $M_h$ . The left bound from the model corresponds to  $v_0 = 50$  km/s ( $\log \beta_0 = -7.9$ ) and the right one to  $v_0 = 1400$  km/s ( $\log \beta_0 = -5$ ). The dot is the Milky Way. Left panel figure is reproduced from Boyarsky et al. (2009).

exclude the clusters of galaxies as a part of a Universality law.

So we have showed within the model that always exists a physical range of parameters  $\beta_0$ ,  $\theta_0$  and  $W_0$  that reproduces the graphics showing the Universality laws in the different scopes.



# I. Featuring the primordial power spectrum: new constraints on interrupted slow-roll from CMB and LRG data

## I.1. Introduction

The inflationary paradigm is an integral part of the currently accepted concordance cosmological model, explaining the flatness and homogeneity of the observed Universe, as well as providing a mechanism to produce the primordial curvature perturbations that eventually led to the formation of structures. The shape of the power spectrum of primordial perturbations can be constrained, at least at the largest scales, using cosmic microwave background (CMB) data. The 7-year WMAP data are in excellent agreement with the assumption of a nearly scale-invariant power spectrum of scalar perturbations (Komatsu et al., 2011; Larson et al., 2011). Such a spectrum, described by a simple power law with spectral index  $n_s$  very close to (albeit different from) unity, is the one that would be produced in the simplest inflationary scenario, that of a single, minimally-coupled scalar field slowly rolling down a smooth potential. The expectation of a power-law spectrum continues to hold up against scrutiny also when tested against observations at scales smaller than those probed by WMAP, like the small-scale CMB measurements of the Atacama Cosmology Telescope (ACT) (Das et al., 2011; Dunkley et al., 2011; Hlozek et al., 2011) and South Pole Telescope (SPT) (Keisler et al., 2011), and the spectrum of luminous red galaxies (Reid et al., 2010). Nevertheless, a scale invariant power spectrum with  $n_s = 1$  could be easily put in agreement with data in some non-minimal models, e.g. considering an extended reionization process (Mortonson and Hu, 2008; Pandolfi et al., 2010b,a), non standard processes during recombination like dark matter annihilation (Galli et al., 2009, 2011; Giesen et al., 2012), extra relativistic particles (see e.g. (Hamann et al., 2010; Archidiacono et al., 2011)) and so on.

In spite of this, however, models with localized “features” in the primordial power spectrum provide a better fit to the data (Peiris et al., 2003; Covi et al., 2006; Hamann et al., 2007; Mortonson et al., 2009; Hazra et al.,

2010; Benetti et al., 2011; Meerburg et al., 2011) with respect to a smooth power-law spectrum. This is mainly due to the presence, in the WMAP temperature anisotropy spectrum, of two outliers in correspondence of  $\ell = 22$  and  $\ell = 40$ . In particular, these “glitches” are well fitted by a primordial power spectrum featuring oscillations localized in a suitable range of wave numbers. On the other hand, it is worth noticing that the “glitches” could have a more conventional explanation, steaming from some still unknown systematics in the WMAP data.

Features in the primordial power spectrum can be generated following departures from slow roll, that can happen in more general inflationary models. In particular, in multifield supergravity- or M-theory-inspired models (Adams et al., 1997b,a), a field coupled to the inflaton can undergo a symmetry-breaking phase transition and acquire a vacuum expectation value. Such a phase transition corresponds to a sudden change in the inflaton effective mass and can be modeled as a step in the inflationary potential. The presence of the step produces, in turn, a burst of oscillations in the power spectrum of curvature perturbations (Adams et al., 2001; Hunt and Sarkar, 2004), localized around the scale that is crossing the horizon at the time the phase transition occurred. Departures from the standard power-law behaviour can also be present in trans-planckian models (Brandenberger and Martin, 2001; Easther et al., 2002; Burgess et al., 2003; Martin and Brandenberger, 2003), in models with a phase of fast roll (Contaldi et al., 2003), or with a sudden change in the speed of sound (Bean et al., 2008; Nakashima et al., 2011; Park and Sorbo, 2012). Similarly, in the so-called Starobinsky model (Starobinsky, 1992), a change in the slope of the potential causes a step in the perturbation spectrum. In addition to their effect on the power spectrum, these non-standard inflationary scenarios can also be constrained through their predicted bispectrum (Adshead et al., 2012; Martin and Sriramkumar, 2012; Park and Sorbo, 2012).

The purpose of the present work is to use current data to update previous constraints that have been put on the presence of such a step-like feature in the inflaton potential. We improve over previous works by using a more complete dataset that includes the WMAP temperature and polarization data, the small-scale CMB data from ACT and SPT, and the matter power spectrum obtained from the Luminous Red Galaxies (LRG) sample of the Sloan Digital Sky Survey (SDSS) 7th data release (Abazajian et al., 2009)). The inclusion of different datasets allows us to explore a wider range of scales with respect to previous analyses, going from the Hubble radius down to the smallest linear scales,  $k \simeq 0.1 \text{ Mpc}^{-1}$ . In particular, this leads to the clear identification of a “forbidden” range where oscillations are not allowed.

The appendix is organized as follows: in Section I.2 we briefly recall the theory concerning the evolution of inflationary perturbations in interrupted slow roll models; in Section I.3 we describe the phenomenological model used to describe a step in the inflationary potential, and the analysis method

adopted in the present work; in Section I.4 we present the results of the analysis, and in Section I.5 we derive our conclusion.

## I.2. Inflationary perturbations in models with interrupted slow roll

### I.2.1. Inflationary perturbations

Let us start by briefly recalling how to compute the spectrum of primordial perturbations for a given inflationary potential  $V(\phi)$  (Adams et al., 2001). In the following we shall work in reduced Planck units ( $c = \hbar = 8\pi G = 1$ ). The first step is to solve the Friedmann and Klein-Gordon equations (dots denote derivatives with respect to the cosmological time  $t$ ):

$$3H^2 = \frac{\dot{\phi}^2}{2} + V(\phi), \quad (\text{I.2.1})$$

$$\ddot{\phi} + 3H\dot{\phi} + \frac{dV}{d\phi} = 0. \quad (\text{I.2.2})$$

to determine the background dynamics of the Hubble parameter  $H$  and of the (unperturbed) inflaton field  $\phi$ .

In order to study the evolution of the curvature perturbation  $\mathcal{R}$ , one introduces the gauge-invariant quantity (Sasaki, 1986; Mukhanov, 1988; Stewart and Lyth, 1993)  $u \equiv -z\mathcal{R}$ , where  $z = a\dot{\phi}/H$  and  $a$  is the scale factor. The Fourier modes  $u_k$  of  $u$  evolve according to (primes denote derivatives with respect to conformal time  $\eta$ ):

$$u_k'' + \left(k^2 - \frac{z''}{z}\right) u_k = 0. \quad (\text{I.2.3})$$

In the limit  $k^2 \gg z''/z$ , the solution to the above equation should match the free-field solution  $u_k = e^{-ik\eta}/\sqrt{2k}$ . The evolution of  $z$  is determined directly by the solution of Eqs. (I.2.1) and (I.2.2), although during slow roll one can approximate  $z''/z \simeq 2a^2H^2$ . At this point, it is possible to integrate Eq. (I.2.3) to get  $u_k(\eta)$  for free-field initial conditions.

Finally, the power spectrum of the curvature perturbation  $P_{\mathcal{R}}$  is related to  $u$  and  $z$  through

$$P_{\mathcal{R}} = \frac{k^3}{2\pi} \left| \frac{u_k}{z} \right|^2, \quad (\text{I.2.4})$$

evaluated when the mode crosses the horizon.

### **I.2.2. Models with interrupted slow roll**

In the following we shall consider models where slow roll is briefly violated. Phenomenologically, these can be described by adding a step feature to a  $V(\phi) = m^2\phi^2/2$  chaotic potential, i.e., by considering a potential of the form

$$V(\phi) = \frac{1}{2}m^2\phi^2 \left[ 1 + c \tanh \left( \frac{\phi - b}{d} \right) \right], \quad (\text{I.2.5})$$

where  $b$  is the value of the field where the step is located,  $c$  is the height of the step and  $d$  its slope. Although the underlying potential is taken to be the one of chaotic inflation, we shall see below that this form can also be used to describe different kinds of potential.

A sharp step in the inflaton potential, like that described by Eq. (I.2.5), can appear for example in multi-field inflation models, following a symmetry-breaking phase transition undergone by another field coupled to the inflaton. This induces a rapid variation in the inflaton effective mass  $m_{\text{eff}}$  that is reflected in the potential (indeed, the potential (I.2.5) is of the form  $V(\phi) = \frac{1}{2}m_{\text{eff}}^2\phi^2$ , with a step in  $m_{\text{eff}}$ ). In this regard, one can think of  $b$  as being related to the time when the phase transition occurs,  $c$  to the change in the inflaton mass, and  $d$  to the width of the transition.

The spectrum of primordial perturbations resulting from the potential (I.2.5) can be calculated as outlined in the previous section, and is found to be essentially a power-law with superimposed oscillations. The oscillations are localized only in a limited range of wavenumbers (centered on a value that depends on  $b$ ) so that asymptotically the spectrum recovers the familiar  $k^{n_s-1}$  form typical of slow-roll inflationary models. In particular, for a chaotic potential, the underlying power law has a spectral index  $n_s \simeq 0.96$ .

One issue that we have left aside so far is how to relate the horizon size at the time the step occurs to a physical scale. This depends on the number  $N_*$  of e-folds taking place between the time a given mode has left the horizon and the end of inflation. We choose  $N_* = 50$  for the pivot wavenumber  $k_* = k_0 = 0.05 \text{ Mpc}^{-1}$ . This choice is somewhat arbitrary; however, a different choice would correspond to a translation in the position of the step in  $\phi$  and would thus be highly degenerate with  $b$ . For this reason we do not treat  $N_*$  as a free parameter, consistent with what has been done in previous studies (Covi et al., 2006; Hamann et al., 2007).

## **I.3. Analysis Method**

In order to compare the theoretical predictions for the constraints on the parameters characterizing inflationary models with a step in the inflaton potential with observational data, we performed a Monte Carlo Markov Chain analysis via the publicly available package CosmoMC (Lewis and Bridle, 2002).

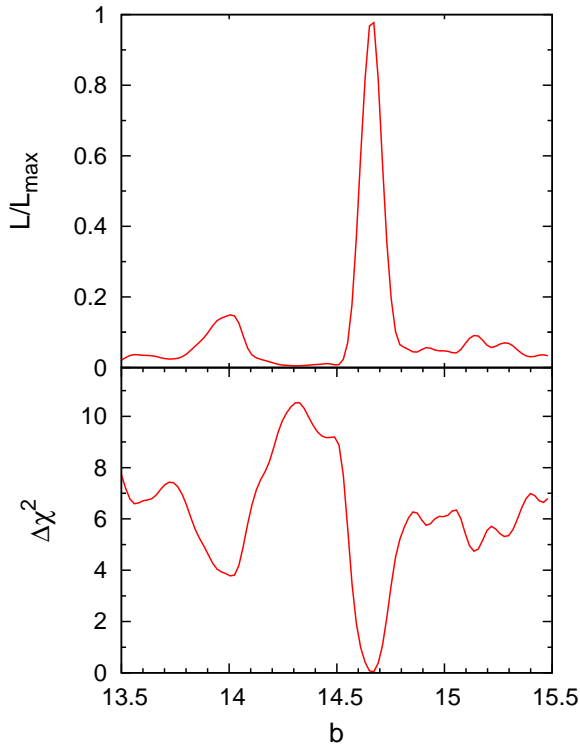


**Figure I.1.:** Model likelihood (upper panel) and  $\Delta\chi^2$  (lower panel) as functions of  $b$  for the CMB dataset, obtained by maximization.

We used a modified version of the CAMB ((Lewis et al., 2000)) code in which we numerically solve Eqs. (I.2.1)–(I.2.3) using a Bulirsch-Stoer algorithm in order to theoretically calculate the initial perturbation spectrum (I.2.4), needed to compute the CMB anisotropies spectrum for any given values of the parameters describing this type of inflationary model. Then we compare these theoretical models with two different combination of data sets. We will briefly come back on describing the principal characteristics of each of the dataset considered in this work.

We consider chaotic inflation potentials of the type of Eq. I.2.5. Following the prescription described in Sec. I.2.1, this potential leads to a well-defined primordial perturbation spectrum  $\mathcal{P}_{\mathcal{R}}$ . The free parameters in Eq. I.2.5 are then the inflaton mass  $m$  and the step parameters  $b$ ,  $c$  and  $d$ . In our analysis we map the mass  $m$  onto  $A_s$ , i.e. the amplitude of the primordial spectrum at the pivot wavenumber  $k_0 = 0.05 \text{ Mpc}^{-1}$ , as indeed the inflaton mass sets the overall scale for the potential and consequently for the amplitude of the perturbations. We note also that the choice of the pivot wavenumber changes the relationship between the value of  $b$  and the position of oscillations in  $k$ -space; this should be taken into account when comparing the results of different studies. In particular, changing  $k_0$  from 0.05 to  $0.002 \text{ Mpc}^{-1}$  shifts  $b$  by  $\sim 0.5$  towards lower values.

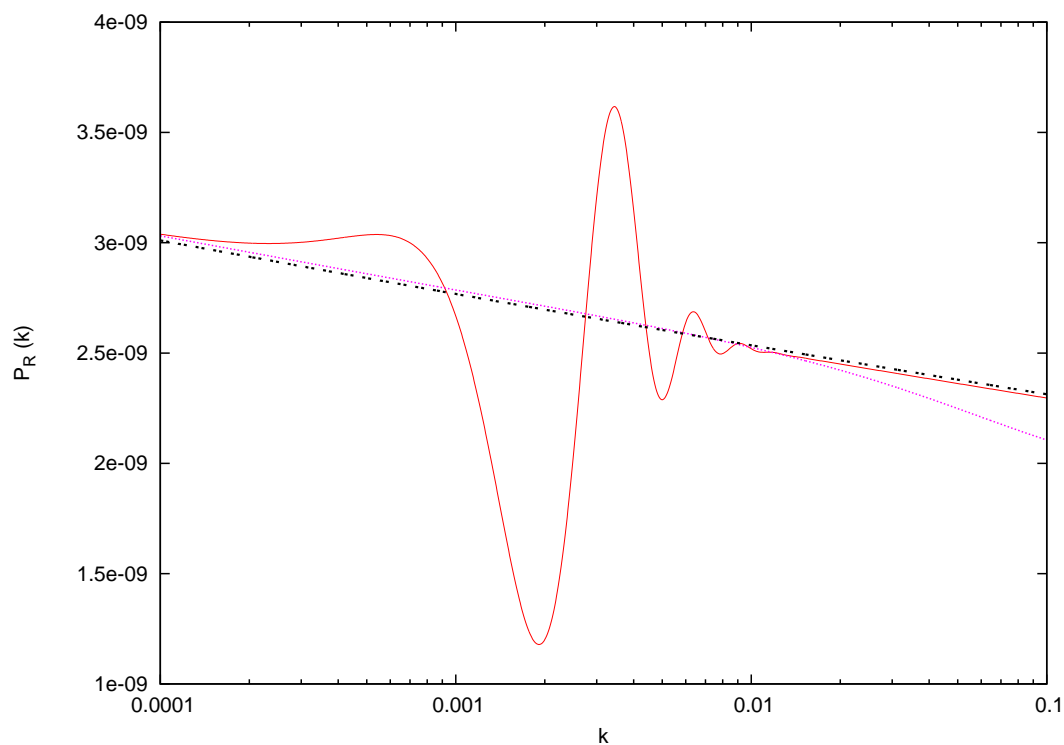


**Figure I.2.:** Primordial power spectrum for an inflationary potential of the form (I.2.5) with  $m = 7.5 \times 10^{-6}$ . The values of the step parameters are :  $b = 14.66$ ,  $\log c = -2.75$ ,  $\log d = -1.42$  (red),  $b = 14.00$ ,  $\log c = -2.66$ ,  $\log d = -0.54$  (magenta dotted), corresponding to the two peaks in the likelihood. For comparison, we also show the best-fit  $\Lambda$ CDM power spectrum (black dot-dashed). We note that the model with  $b = 14$  resembles, in the  $k$ -range considered, a model with a negative running index.

As previously noted in Sec. I.2.2, for the chaotic potential of Eq. I.2.5 the smooth power law has a fixed spectral index, that is  $n_s \simeq 0.96$ . However, as noted in Ref. (Hamann et al., 2007), more general forms of the potential can be phenomenologically taken into account by promoting  $n_s$  back to a free parameter and defining a “generalized” primordial spectrum as

$$\mathcal{P}_{\mathcal{R}}^{\text{gen}}(k) = \mathcal{P}_{\mathcal{R}}^{\text{ch}}(k) \times \left(\frac{k}{k_0}\right)^{n_s - 0.96}, \quad (\text{I.3.1})$$

where  $\mathcal{P}_{\mathcal{R}}^{\text{ch}}(k)$  is the spectrum induced by the chaotic potential (I.2.5).

Therefore the theoretical model we are considering is described by the following set of parameters:

$$\{\omega_b, \omega_c, \theta, \tau, b, c, d, \mathcal{A}_s, n_s\} \quad (\text{I.3.2})$$

where  $\omega_b = \Omega_b h^2$  and  $\omega_c = \Omega_c h^2$  are the physical baryon and cold dark matter densities,  $\theta$  is the ratio between the sound horizon and the angular diameter distance at decoupling,  $\tau$  is the optical depth to reionization,  $b$ ,  $c$  and  $d$  are the parameters of the step-inflation model,  $\mathcal{A}_s$  is the overall normalization of the primordial power spectrum (equivalent to specifying  $m^2$  as discussed above), and  $n_s$  is the effective tilt. We consider purely adiabatic initial conditions, impose flatness and neglect neutrino masses, and limit our analysis to scalar perturbations.

We consider as our basic dataset a combination of three different CMB datasets: WMAP7, ACT and SPT (in what follows we will refer to this case simply as “CMB”), and then we also consider an enlarged dataset, dubbed “CMB+LRG”, where we also add the LRG SDSS catalog (Reid et al., 2010), the Supernovae Ia Union Compilation 2 data (Amanullah et al., 2010), and impose a prior on the Hubble constant from the Hubble Space Telescope (HST) (Riess et al., 2009).

To compute the likelihood of the data we have properly modified the CosmoMC package in order to make use of the routines supplied by the WMAP and ACT teams for their datasets, both publicly available from the LAMBDA website<sup>1</sup>, and of the likelihood code provided by the SPT team (Keisler et al., 2011) for the SPT dataset.

The ACT and SPT experiments allow to extend the dynamic range of CMB observations to larger multipoles with the respect of WMAP7, thus measuring the damping tail of the CMB angular power spectrum. While SPT probes the small scales in the range of multipoles  $650 < \ell < 3000$ , the ACT telescope spans a range of multipoles that goes up to  $\ell = 10000$ , although the signal at  $\ell \gtrsim 3000$  is dominated by the power coming from extragalactic point sources. For this reason, for ACT we only consider the less contaminated 148 GHz spectrum up to  $\ell_{\text{max}} = 3300$  to perform cosmological parameters

<sup>1</sup><http://lambda.gsfc.nasa.gov/>

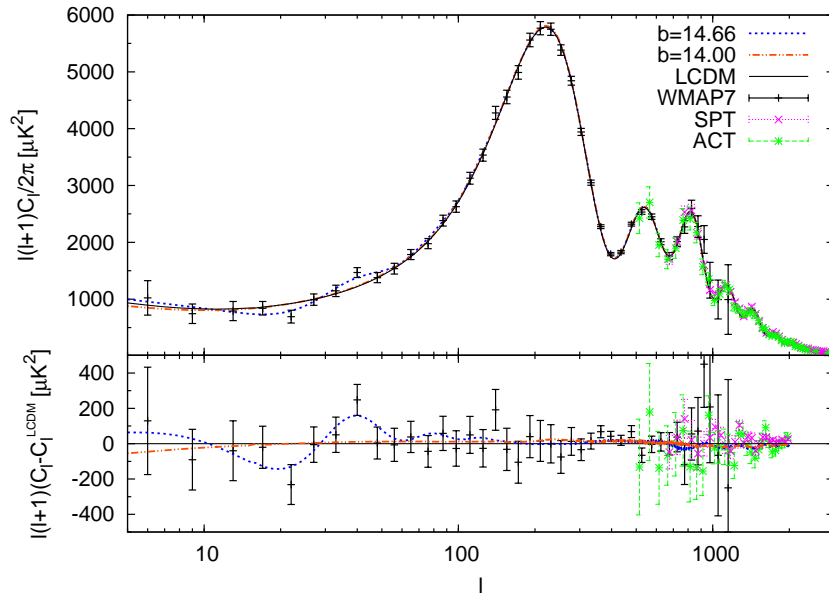


**Figure I.3.:** Upper panel: Power spectrum of CMB Anisotropies Power Spectrum for the best-fit  $\Lambda$ CDM model (black line) and two step models with  $b = 14$  (red dashed) and  $b = 14.66$  (blue dot-dashed), corresponding to the two minima in  $\chi^2$ , compared with WMAP7, ACT and SPT data. Lower panel: The same as above, but plotted in terms of residuals with respect to the  $\Lambda$ CDM best fit.

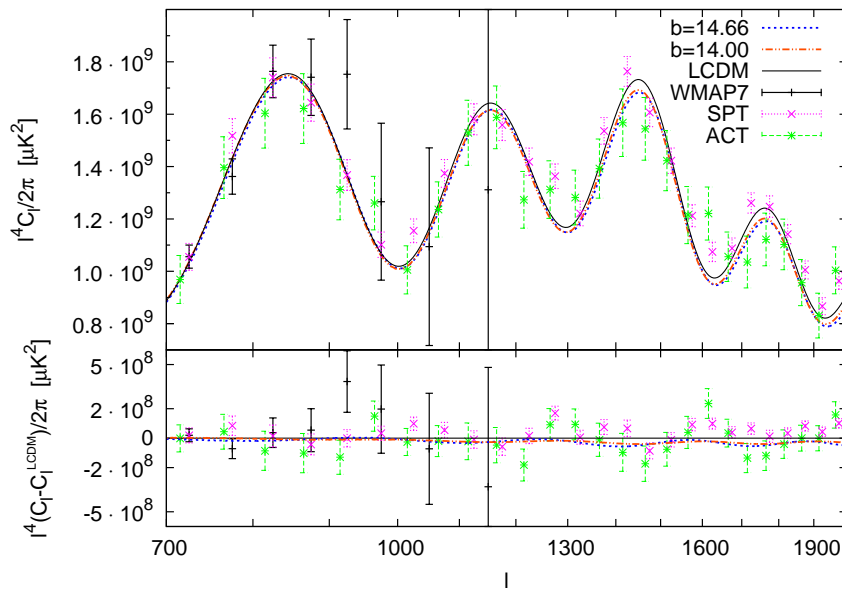


**Figure I.4.:** The same as Fig. I.3, but zoomed in the region  $700 \leq \ell \leq 2000$ . Note that in order to improve clarity, the vertical axis shows  $\ell^4 C_\ell$  instead than  $\ell(\ell + 1)C_\ell$ .

**Table I.1.:** Posterior mean for the vanilla cosmological parameters. The errors refer to 68% credible intervals.

| Parameter                         | $\Lambda$ CDM (WMAP7+CMB) | Features (CMB)      | Features (CMB+LRG)  |
|-----------------------------------|---------------------------|---------------------|---------------------|
| $100 \Omega_b h^2$                | $2.253 \pm 0.054$         | $2.204 \pm 0.044$   | $2.215 \pm 0.037$   |
| $\Omega_c h^2$                    | $0.1103 \pm 0.0052$       | $0.1125 \pm 0.0050$ | $0.1122 \pm 0.0029$ |
| $100 \theta$                      | $1.0396 \pm 0.0025$       | $1.0409 \pm 0.0016$ | $1.0414 \pm 0.0015$ |
| $\tau$                            | $0.088^{+0.015}_{-0.014}$ | $0.086 \pm 0.014$   | $0.087 \pm 0.015$   |
| $n_s$                             | $0.962^{+0.014}_{-0.013}$ | $0.959 \pm 0.014$   | $0.959 \pm 0.011$   |
| $10^9 A_s$                        | $2.15 \pm 0.11$           | $2.18 \pm 0.08$     | $2.19 \pm 0.07$     |
| Age [Gyr]                         | $13.72 \pm 0.12$          | $13.81 \pm 0.09$    | $13.78 \pm 0.07$    |
| $z_{re}$                          | $10.5 \pm 1.2$            | $10.5 \pm 1.2$      | $10.5 \pm 1.2$      |
| $H_0$ [km s $^{-1}$ Mpc $^{-1}$ ] | $71.4 \pm 2.4$            | $69.9 \pm 2.3$      | $70.3 \pm 1.3$      |

**Table I.2.:** Best fit values.

| Parameter            | CMB    | CMB+LRG |
|----------------------|--------|---------|
| $b$                  | 14.66  | 14.66   |
| $\log c$             | -2.65  | -2.85   |
| $\log d$             | -1.42  | -1.57   |
| $n_s$                | 0.946  | 0.958   |
| $\ln[10^{10} A_s]$   | 3.08   | 3.06    |
| $-\log(\mathcal{L})$ | 3765.8 | 4043.7  |

extraction. In order to account for the foreground contributions at  $\ell \lesssim 3000$ , we add three extra amplitude parameters: the Sunyaev-Zel'dovich (SZ) amplitude  $A_{SZ}$ , the clustered point sources amplitude  $A_C$  and the amplitude of Poisson distributed point sources  $A_P$ . We consider for both ACT and SPT experiments a joint amplitude parameter for each component and the templates provided by (Keisler et al., 2011). No SZ contribution is considered for WMAP7, as explained in the analysis performed by (Keisler et al., 2011). We have however verified that different choices for the foreground templates has negligible effect on the constraints of cosmological parameters and produces minimal effects on foreground parameters.

For what concerns the SDSS LRG7 catalog, we chose to consider data only in the linear scales regime, i.e., up to  $k = 0.1 \text{ h Mpc}^{-1}$ . Indeed, HALOFIT, the CAMB routine that should correct for non-linearity effects at the smallest scales, is tested only for a smooth primordial power spectrum and therefore is not appropriate for dealing with power spectra with features, like those considered in the present analysis.

Regarding the prior on the model parameters, we impose flat priors on  $\omega_b$ ,  $\omega_c$ ,  $\theta$ ,  $\tau$  and  $n_s$  and a logarithmic prior on  $A_s$ . We check a posteriori that these

priors result to be much wider than the corresponding posteriors and thus their upper and lower limits do not affect our final results. The priors on the step parameters need however to be discussed in more detail. The parameter  $b$  controls the position of the oscillations in  $k$ -space. Larger values of  $b$  correspond to “later” phase transitions and thus move the oscillations towards larger scales (smaller values of  $k$  and  $\ell$ ). Viceversa, smaller values of  $b$  shift the oscillations in the direction of large wave numbers. As a rule of thumb, we note that the peak in the oscillations is located at  $k \simeq 0.015 \text{ Mpc}^{-1}$  ( $\ell \simeq 200$ ) for  $b = 14.5$ , and that it is shifted down (up) by roughly a factor 2 in  $k$  for each 0.1 increment (decrement) in  $b$ . Thus, outside of a given range in  $b$ , oscillations are moved to wave numbers that are not probed by observations of the CMB nor of large scale structures. Based on the considerations above, we initially choose a flat prior for  $b$  in the range  $13.5 \leq b \leq 15.5$ , that conservatively encompasses the whole range probed by the WMAP, ACT, SPT and LRG datasets. We use this prior for the CMB only dataset. Then, in view of the results of the first Monte Carlo run, we also consider a restricted prior  $14.2 \leq b \leq 15$ , that we use for the analysis of the enlarged dataset. We have also explicitly checked that adding, in  $b = 13.5$  or  $b = 15.5$ , a step-like feature with  $c = 10^{-2}$  (a value already large enough to produce, on average, oscillations that are at variance with observations (Benetti et al., 2011)) and  $d = 3 \times 10^{-2}$  (the median point of our prior) to the WMAP7 best-fit model produces no appreciable effect (at least within CAMB’s numerical precision) in the CMB spectrum up to  $\ell = 3000$  nor in the matter power spectrum between  $k = 0.02$  and  $k = 0.1 \text{ Mpc}^{-1}$ . For what concerns  $c$  and  $d$ , parameterizing the height and width of the step respectively, we choose a logarithmic prior for both of them, i.e., a uniform prior on  $\log c$  and  $\log d$ . The reason for this choice is that we want for these parameters to, potentially, assume values spanning several orders of magnitude with equal *a priori* probability. Indeed this is accomplished using a logarithmic prior that naturally assigns equal probability to each decade. In particular, we take  $-4 \leq \log c \leq -1$  and  $-2.5 \leq \log d \leq -0.5$ .

We derive our constraints from parallel chains generated using the Metropolis-Hastings algorithm. We use the Gelman and Rubin  $R$  parameter to evaluate the convergence of the chains, demanding that  $R - 1 < 0.04$ . We note that there are some issues related to the fact that some of the posteriors do not vanish at infinity; we address them in section I.4 .

## I.4. Results and Discussion

First of all, we check how the constraints on the six “vanilla” parameters are changed when the possibility of having features in the primordial power spectrum is considered. To this purpose, we show in Tab. I.1 the mean of

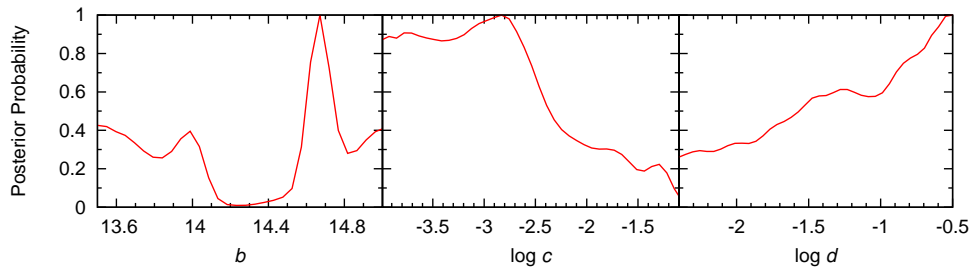


**Figure I.5.:** One-dimensional posterior probability density for the step parameters from the CMB dataset.

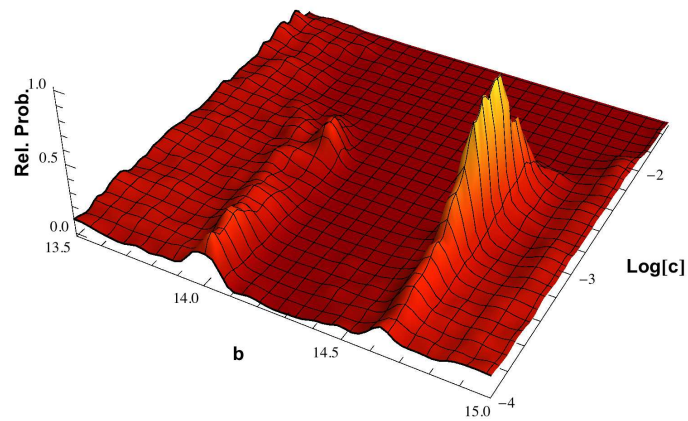


**Figure I.6.:** Joint two-dimensional posterior for  $(b, \log c)$  using the CMB dataset.

the posterior distribution, and the corresponding 68% credible intervals, for each vanilla parameter, as well as for some derived parameters (most notably the reionization redshift  $z_{\text{re}}$ , the age of the Universe, the Hubble constant  $H_0$ ), and compare them with the corresponding values found by the WMAP7 team in their analysis of the  $\Lambda$ CDM model; however, in order to have the maximum homogeneity between datasets, we consider the dataset dubbed “WMAP7+CMB” in the LAMBDA website that includes, in addition to WMAP, also the data from small scale CMB experiments. We note that the uncertainty on the determination of the vanilla parameters is not degraded when features are included (and it is actually better for the CMB+LRG dataset, although this should probably be ascribed to the inclusion of additional data). The mean values found for the features model are all within one sigma of the corresponding  $\Lambda$ CDM values, with the partial exception of the baryon density  $\omega_b h^2$ , whose mean lies at the edge of the WMAP 68% credible interval. We argue that this is due at least in part to the fact that some of the primordial spectra considered here mimic the presence of a negative running in the spectral index (see below); the lower value of  $\omega_b h^2$  is thus due to the correlation with the running.

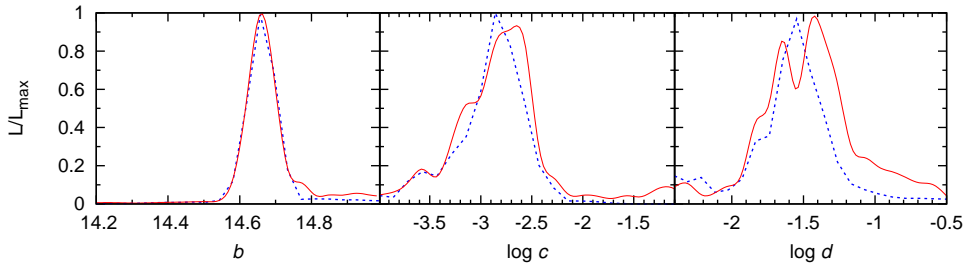


**Figure I.7.:** Comparison of the model likelihood as a function of the step parameters, obtained from the the CMB (red solid line) and CMB+LRG (blue dashed) datasets.

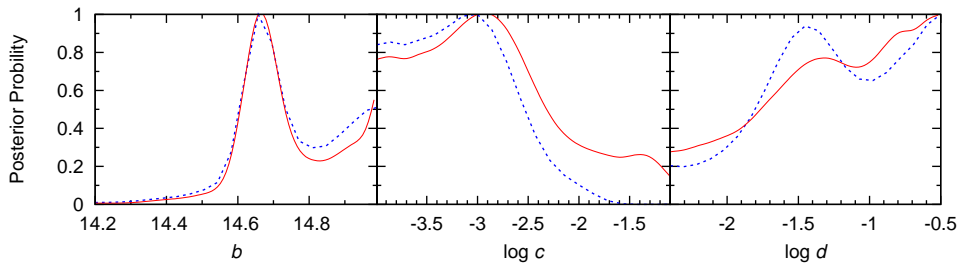


**Figure I.8.:** Comparison of the one-dimensional posterior probability density for the step parameters from the CMB (red solid line) and CMB+LRG (blue dashed line) datasets.

Now let us analyze the results on the primordial spectrum parameters from

one dataset at a time, starting from the CMB-only dataset. We recall that this analysis assumes the prior  $13.5 \leq b \leq 15.5$ . We first focus the best-fit parameters, i.e., the parameter values that maximize the likelihood. In the second column of Tab. I.2 we show the best-fit values, for this dataset, of the primordial spectrum parameters. In the best-fit model, the step in the primordial spectrum is located in  $b = 14.66$ , consistently with previous studies (Mortonson et al., 2009; Benetti et al., 2011). We explicitly show the projected likelihood, as well as  $\Delta\chi^2 = \chi^2 - \chi^2_{\min}$ , as a function of  $b$  in the two panels of Fig. I.1. It is interesting however that a distinct although low peak is present in the likelihood in  $b \simeq 14$ . We also note that the  $\chi^2$  does not become arbitrarily large (i.e., the likelihood does not asymptotically vanish) far from the minimum, but instead tends to a constant value. This is related to the fact that, as explained to the previous section, towards the extremes of the  $b$  range the oscillations are moved outside the range of scales probed by the dataset, and thus the model becomes completely equivalent, as long as data fitting is concerned, to  $\Lambda$ CDM. Thus from the plot we can roughly estimate that the best-fit at  $b = 14.66$  represents a  $\Delta\chi^2 \simeq 7$  improvement with respect to the  $\Lambda$ CDM best-fit, while for the model with  $b = 14$ ,  $\Delta\chi^2 \simeq 3.5$ . The primordial power spectra corresponding to the two minima in the  $\chi^2$  are shown in Fig. I.2. On the other hand, models with  $14.1 \lesssim b \lesssim 14.5$  perform worse with respect to  $\Lambda$ CDM.

For a better understanding, we also show in Figs. I.3 and I.4 the comparison between the WMAP7 best-fit, the two models with features corresponding to the two peaks in the likelihood seen in Fig. I.1, and the data present in the CMB dataset. It is clear from these plots (especially from the plot of residuals shown in the lower panel) that the model with  $b = 14.66$  improves over  $\Lambda$ CDM by being able to fit the two outliers in  $\ell = 22$  and  $\ell = 40$ , thus confirming our previous findings (Benetti et al., 2011). The interpretation of the peak in  $b = 14$  is more puzzling; by looking at the lower panel of Fig. I.3, however, it can be seen that the CMB spectrum for this model resembles what it would be obtained by adding a negative running  $dn_s/d \ln k$  to the scalar spectral index. Thus this result could be reminiscent of the WMAP7 preference for a negative running, that is indeed even more pronounced when high- $\ell$  data are added to the analysis (Komatsu et al., 2011):  $dn_s/d \ln k = -0.034 \pm 0.026$  (WMAP7 only) and  $dn_s/d \ln k = -0.041^{+0.022}_{-0.023}$  (WMAP7+ACBAR+QUaD).

We now turn to the posterior distributions. In Fig. I.5, we show the one-dimensional posteriors for  $b$ ,  $\log c$  and  $\log d$ . The posterior for  $b$  still shows the two peaks in  $b \simeq 14.7$  and  $b \simeq 14$  that were present in the likelihood. The largest value at the edges of the prior range is due to a volume effect, since the one-dimensional posterior is obtained by marginalization (as opposed to the one-dimensional likelihood that was obtained by maximization). On the other hand, the probability density for  $14.1 \lesssim b \lesssim 14.4$  is practically equal to zero. For what concerns  $\log c$ , as it could be expected, “large” values are disfavored by the data (as they produce large - in amplitude - oscillations that

cannot, on average, be reconciled with observations) while for smaller values the posterior tends to a constant value as the oscillations become so weak as to be practically undetectable for the current experimental precision and thus the value of  $c$  becomes unimportant. As already noted, a posterior with this characteristic that extends, in principle, down to  $\log c = -\infty$ , cannot be properly normalized (since the corresponding probability mass is infinite) and, as a consequence, credible intervals are ill-defined. One could be tempted to impose a lower cut-off but then the credible intervals will end up depending on the choice of the cut-off itself, so this should be avoided, at least in the absence of a clear physical reason for doing so.

We can still, however, compare probability densities, as well as probabilities integrated over finite intervals, since probability ratios *do not* depend on the overall normalization. We can use, as a benchmark value to compare the constraining power of different datasets, for example, the value of  $\log c$  where  $P(\log c)$  is half of its asymptotic value for  $\log c \rightarrow \infty$ . This should not be taken as an “upper limit” in the common sense of the word, but as said is a useful tool for comparison. In the case under consideration, we estimate that this happens for  $\log c = -2.32$ , or  $c = 4.8 \times 10^{-3}$ .

For comparison, the corresponding value that we had previously found using WMAP7 and ACT data only was  $\log c = -2$  (Benetti et al., 2011). We also show, in Fig. I.6 the two-dimensional posterior  $P(b, \log c)$  where it is clear that probability is concentrated in two distinct, disconnected regions. One corresponds to models with  $b \simeq 14.7$  and  $\log c \simeq -3$ , while the other to models with  $b \simeq 14$  and  $\log c$  located more towards the edge of the prior range,  $\log c \lesssim -3.5$ . Finally, we examine the posterior for  $\log d$ . This is in part similar to the posterior for  $\log c$ , once one recalls that small values of  $\log d$  produce a steep step in the potential and consequently large oscillations, so one should expect the probability to go to zero for small values of  $\log d$ , as it is. However, in this case, the posterior range is not wide enough to see the asymptotic part, for  $\log d \rightarrow \infty$  (where  $\Lambda$ CDM should be recovered), of the distribution.

The fact that the posterior is bimodal in  $b$  creates some difficulty for the Monte Carlo, as the chains cannot easily jump from one peak to the other, and thus take a longer time to sample satisfactorily the actual distribution. For this reason, in our second Monte Carlo run, using the CMB+LRG dataset, we have decided to concentrate on the region of the peak at  $b = 14.66$  and impose the prior  $14.2 \leq b \leq 15$ . We find that the best-fit for this dataset, shown in the third column of Tab. I.2 has still  $b = 14.66$ . In Figs. I.7 and I.8 we compare the one-dimensional likelihoods and posteriors, respectively, for the step parameters in the CMB+LRG dataset with those obtained previously with the CMB dataset. In order to allow for comparison, the distributions for the latter have been obtained by imposing a posteriori the condition  $b \geq 14.2$  (which, in practical terms, that we have discarded all samples with  $b < 14.2$ , and reanalyzed these new chains from scratch). We find that there is

practically no difference with respect to the position of the oscillations (which makes sense, since this is driven by the requirement of fitting the outliers in the WMAP7 data at relatively low  $\ell$ 's). The amplitude of the oscillations is slightly more constrained, with the posterior going down at half of its plateau value at  $\log c = -2.48$  ( $c \simeq 3 \times 10^{-3}$ ). The posterior for  $\log d$  is also slightly different, as it shows a more distinct peak in correspondence of the best-fit value  $\log d \simeq -1.5$ .

## I.5. Concluding Remarks

We have studied cosmological models with a step-like feature in the inflationary potential. Such a feature would produce oscillations in the primordial spectrum of scalar perturbations, whose presence can be tested through the analysis of CMB and large-scale structures data. We have found, consistently with previous studies, that in these models the agreement with the CMB data is improved, with respect to the  $\Lambda$ CDM model, when the oscillations are placed in such a way as to match the two outliers in the WMAP7 spectrum at  $\ell = 22$  and  $\ell = 40$  (in particular, the  $\chi^2$  changes by  $\Delta\chi^2 \simeq 7$ ). The posterior probability also has a maximum close to this point, corresponding to  $b = 14.66$ , while it clearly shows that oscillations in the range  $14.1 \leq b \leq 14.5$  are currently forbidden by the data. The possibility of no oscillation at all is still, however, perfectly consistent with the data. In conclusion, although multifield inflationary models can definitely reproduce the two glitches in the WMAP7 temperature spectrum, current data are not yet constraining enough to allow to discriminate between these models and the standard inflationary scenario.



# J. The Fine Structure Constant and the CMB Damping Scale

## J.1. Introduction

An interesting discrepancy with the expectations of the standard model has recently been uncovered in the small CMB scale measurements of the ACT (Dunkley et al., 2011) and SPT (Keisler et al., 2011) experiments. Namely, the effective number of relativistic degrees of freedom  $N_{\text{eff}}$  (see e.g. Kolb and Turner (1990) for a definition) has been reported as higher (at more than two standard deviations) than the expected standard value of  $N_{\text{eff}} = 3.046$ <sup>1</sup>. This result has been confirmed by several recent analyses of the ACT and SPT datasets (see e.g. (Archidiacono et al., 2011; Hou et al., 2011; Smith et al., 2012b; Hamann, 2012; Giusarma et al., 2011)).

However it is important to stress that the current bounds on  $N_{\text{eff}}$  rely on the assumption of a theoretical model. More recently the dependence of the constraints on  $N_{\text{eff}}$  on the assumption of a flat universe or a different dark energy component have been investigated by several authors ((Smith et al., 2012a; Giusarma et al., 2012; Joudaki, 2012)). Here we revisit the issue, by obtaining analogous constraints in the framework of a non-standard recombination process.

As expected (see e.g. (Hou et al., 2011)) a variation of  $N_{\text{eff}}$  affects the value of the Hubble parameter  $H$  at recombination. This changes two very important scales in CMB anisotropy physics: the size of the sound horizon and the damping scale at recombination. An approximate expression for the damping scale is given by

$$r_d^2 = (2\pi)^2 \int_0^{a_*} \frac{da}{a^3 \sigma_T n_e H} \left[ \frac{R^2 + \frac{16}{15} (1 + R)}{6(1 + R^2)} \right] \quad (\text{J.1.1})$$

where  $n_e$  is the number density of free electrons,  $\sigma_T$  is the Thompson cross-section,  $a_*$  is the scale factor at recombination and  $R = 3\rho_b / (4\rho_\gamma)$  is proportional to the ratio between the baryon and photon densities. It is clear that a change in  $H$  could be compensated by a change in  $n_e$  and  $a_*$  in order to keep

---

<sup>1</sup>This is the value expected in the case of 3 relativistic neutrinos species. The little deviation from  $N_{\text{eff}} = 3$  takes into account effects from the non-instantaneous neutrino decoupling from the primordial photon-baryon plasma (see e.g. (Mangano et al., 2005))

the same damping scale. Consequently, a change in the recombination process, motivated by some non-standard and unaccounted mechanism, could alter the current conclusions on  $N_{\text{eff}}$ .

Possible changes in the recombination process have been investigated by several authors. Dark matter annihilation, for example, could significantly alter the evolution of the free electron density  $n_e$  by the injection of extra-ionizing photons around recombination (see e.g. Galli et al. (2011) and references therein). Another possible mechanism, which we consider in this paper, is based on the hypothesis of a change in the fundamental constants of nature, specifically the fine structure constant,  $\alpha$ .

Changing  $\alpha$  modifies the strength of the electromagnetic interaction and therefore the only effect on the formation of CMB anisotropies is via the modifications to the differential optical depth of photons due to Thomson scattering between electrons and photons

$$\dot{\tau} = x_e n_e c \sigma_T, \quad (\text{J.1.2})$$

where  $x_e$  is the free electron fraction, dependent on the temperature of the electrons and therefore on the scale factor of the universe  $a(t)$ . The optical depth  $\tau$  is then defined as the integral of the scattering rate over time.

These two combined processes change  $T^*$ , the temperature at which last scattering takes place, and  $x_e(t_0)$ , the free electron fraction that remains after recombination, both of which influence the CMB anisotropies (see (Battye et al., 2001)). The main imprint on CMB power spectrum is a shift in the modulation of the peak heights by baryon drag. The modulation of the peaks heights is determined by the relative density of baryons to photons at  $\eta^*$ ,  $R = 3\rho_b/(4\rho_\gamma) \sim T^{*-1}$ . A variation in  $\alpha$  changes the photon diffusion damping length as well and the two effects combined lead to subtle degeneracies between  $\Delta\alpha/\alpha$  and  $N_{\text{eff}}$ .

CMB anisotropies are therefore one of the canonical ways of constraining variations in the fine structure constant in the early universe. They provide a measurement of  $\alpha$  at the epoch of recombination (see e.g. (Avelino et al., 2001; Martins et al., 2002, 2004; Rocha et al., 2004; Ichikawa et al., 2006; Nakashima et al., 2008; Stefanescu, 2007; Calabrese et al., 2011; Menegoni et al., 2009; Landau and Scoccola, 2010)), with a current sensitivity the level of  $\sim 1\%$ . In the most recent analysis, parameterizing a variation in the fine structure constant as  $\alpha/\alpha_0$ , where  $\alpha_0 = 1/137.03599907$  is the standard (local) value and  $\alpha$  is the value during the recombination process, the authors of (Calabrese et al., 2011; Menegoni et al., 2009) used the five year WMAP data, finding the constraint  $0.987 \pm 0.012$  at 68% c.l.. Meanwhile, a recent analysis of a large dataset of spectroscopic data from the VLT and Keck telescopes (Webb et al., 2011) is consistent with earlier claims of variations in the value of  $\alpha$  at parts-per-million level at redshifts  $z \sim 3$ .

## J.2. Analysis Method

We perform a COSMOMC (Lewis and Bridle, 2002) analysis combining the following CMB datasets: WMAP7 (Komatsu et al., 2011), ACBAR (Reichardt et al., 2009), ACT (Dunkley et al., 2011), and SPT (Keisler et al., 2011), and we analyze datasets out to  $l_{\max} = 3000$ . We also include information on dark matter clustering from the galaxy power spectrum extracted from the SDSS-DR7 luminous red galaxy sample (Reid et al., 2010). Finally, we impose a prior on the Hubble parameter based on the last Hubble Space Telescope observations (Riess et al., 2011).

The analysis method we adopt is based on the publicly available Monte Carlo Markov Chain package *cosmomc* (Lewis and Bridle, 2002) with a convergence diagnostic done through the Gelman and Rubin statistic.

We sample the following six-dimensional standard set of cosmological parameters, adopting flat priors on them: the baryon and cold dark matter densities  $\Omega_b$  and  $\Omega_c$ , the Hubble constant  $H_0$ , the optical depth to reionization  $\tau$ , the scalar spectral index  $n_s$ , and the overall normalization of the spectrum  $A_S$  at  $k = 0.002 \text{ Mpc}^{-1}$ . We consider purely adiabatic initial conditions and we impose spatial flatness. As discussed in the introduction we allow for variations in the fine structure constant  $\alpha/\alpha_0$  where  $\alpha_0$  is the current, local, value by modifying the RECFAST recombination subroutine following the procedure described in (Calabrese et al., 2011; Menegoni et al., 2009).

We also allow for variations in the effective number of relativistic degrees of freedom  $N_{\text{eff}}$  and the primordial Helium abundance  $Y_p$ , otherwise fixed at the values  $N_{\text{eff}} = 3.046$  and  $Y_p = 0.24$ , respectively. Since we are varying also the Helium abundance, we considered variations in the fine structure constant also in the process of Helium recombination. A  $\sim 5\%$  change of  $\alpha$  for Helium recombination changes the CMB angular spectra by less than 0.5% up to  $\ell = 1500$ . During reionization the fine structure constant is fixed to the local standard value  $\alpha = \alpha_0$ .

We account for foregrounds contributions including three extra amplitudes: the SZ amplitude  $A_{SZ}$ , the amplitude of clustered point sources  $A_C$ , and the amplitude of Poisson distributed point sources  $A_P$ . We marginalize the contribution from point sources only for the ACT and SPT data, based on the templates provided by (Keisler et al., 2011). We quote only one joint amplitude parameter for each component (clustered and Poisson distributed). The SZ amplitude is obtained fitting the WMAP data with the WMAP own template, while for SPT and ACT it is calculated using the (Trac et al., 2011) SZ template at 148 GHz; this differs from the analysis performed in (Keisler et al., 2011) where no SZ contribution was considered for the WMAP data.

### J.3. Results

As stated in the previous section, we perform three different analyses always considering the same set of data but different number of parameters. To the 6 standard  $\Lambda$ -CDM parameters we cumulatively add as additional free parameters the fine structure constant (first case), the number of relativistic degrees of freedom  $N_{\text{eff}}$  (second case) and the primordial Helium abundance  $Y_p$  (third case). In Table J.1 we report the constraints on the cosmological parameters for these three scenarios.

| <i>Parameter</i>    | $\alpha/\alpha_0$   | $\alpha/\alpha_0+N_{\text{eff}}$ | $\alpha/\alpha_0+N_{\text{eff}}+Y_p$ |
|---------------------|---------------------|----------------------------------|--------------------------------------|
| $\Omega_b h^2$      | $0.0218 \pm 0.0004$ | $0.0224 \pm 0.0005$              | $0.0223 \pm 0.0007$                  |
| $\Omega_c h^2$      | $0.1144 \pm 0.0034$ | $0.1302 \pm 0.0095$              | $0.1303 \pm 0.0094$                  |
| $\tau$              | $0.086 \pm 0.014$   | $0.088 \pm 0.015$                | $0.088 \pm 0.016$                    |
| $H_0$               | $68.9 \pm 1.4$      | $71.52 \pm 2.0$                  | $71.8 \pm 2.1$                       |
| $\alpha/\alpha_0$   | $0.984 \pm 0.005$   | $0.990 \pm 0.006$                | $0.987 \pm 0.014$                    |
| $n_s$               | $0.976 \pm 0.013$   | $0.991 \pm 0.015$                | $0.992 \pm 0.016$                    |
| $\log[10^{10} A_s]$ | $3.193 \pm 0.037$   | $3.169 \pm 0.040$                | $3.167 \pm 0.042$                    |
| $A_{SZ}$            | $< 2.00$            | $< 2.00$                         | $< 2.00$                             |
| $A_C$               | $< 16.0$            | $< 15.8$                         | $< 14.8$                             |
| $A_P$               | $< 24.7$            | $< 24.9$                         | $< 22.4$                             |
| $\Omega_\Lambda$    | $0.7137 \pm 0.0070$ | $0.7020 \pm 0.0094$              | $0.704 \pm 0.013$                    |
| <i>Age/Gyr</i>      | $13.76 \pm 0.24$    | $13.18 \pm 0.38$                 | $13.15 \pm 0.37$                     |
| $\Omega_m$          | $0.2863 \pm 0.0070$ | $0.2980 \pm 0.0094$              | $0.296 \pm 0.013$                    |
| $\sigma_8$          | $0.836 \pm 0.023$   | $0.862 \pm 0.028$                | $0.859 \pm 0.034$                    |
| $z_{re}$            | $10.7 \pm 1.2$      | $11.0 \pm 1.3$                   | $11.0 \pm 1.3$                       |
| $N_{\text{eff}}$    | —                   | $4.10^{+0.24}_{-0.29}$           | $4.19^{+0.31}_{-0.35}$               |
| $Y_p$               | —                   | —                                | $0.215 \pm 0.096$                    |
| $\chi^2_{min}$      | 7600.2              | 7596.8                           | 7596.5                               |

**Table J.1.:** MCMC estimation of the cosmological parameters from the dataset described in the text. Results for the three analyses described in the text are reported. Upper bounds at 95% c.l. are reported for foregrounds parameters.

As we can see the dataset considered prefers a value of  $\alpha/\alpha_0$  smaller than unity at more than two standard deviations when both the  $N_{\text{eff}}$  and  $Y_p$  are kept fixed at their standard values. This result, while interesting, is to be expected since is clearly driven by data preference for larger values of  $N_{\text{eff}}$ . Allowing for variations in  $N_{\text{eff}}$  significantly shifts the best fit value for  $\alpha/\alpha_0$ , which is now consistent with the standard value. However, even in this case the best fit value for  $N_{\text{eff}}$  is still  $\sim 4$ , i.e. allowing for variation in the fine structure constant enlarges the error bars on  $N_{\text{eff}}$  of about  $\sim 30\%$  but does not shift the best fit value towards the standard result. The largest effect on

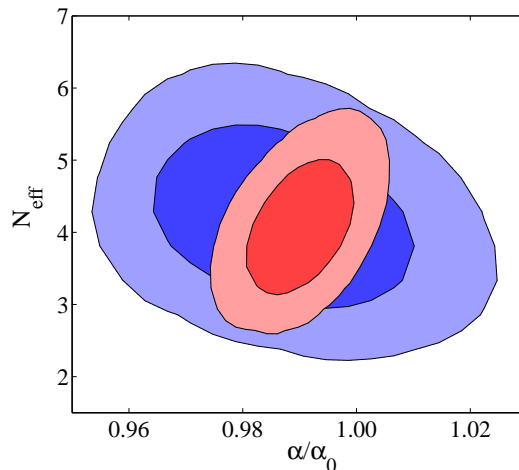


**Figure J.1.:** Likelihood contour plot for  $\alpha/\alpha_0$  vs  $N_{\text{eff}}$  at 68% c.l. and 95% c.l. in the case of  $Y_p = 0.24$  (red smaller contours) and  $Y_p$  allowed to vary (blue larger contours).

$\alpha$  comes however when also the helium abundance  $Y_p$  is let to vary. In this case, indeed, the errors on  $\alpha$  are almost doubled.

We can better understand the impact of  $Y_p$  on the determination of  $\alpha/\alpha_0$  by looking at Figure 1, where we plot the 2-D likelihood contours in the  $\alpha/\alpha_0$ - $N_{\text{eff}}$  plane in the cases of  $Y_p = 0.24$  and free  $Y_p$ . As we can see when the helium abundance is fixed there is a clear but moderate degeneracy between  $\alpha/\alpha_0$  and  $N_{\text{eff}}$ . When  $N_{\text{eff}}$  is increased the Hubble parameter at recombination increases. In order to keep the damping scale at the same value fixed by observations (see Eq.J.1.1) we need to decrease the free electron density at recombination. This can be achieved by simply accelerating the recombination process. This effect is clearly obtained by an increase in the fine structure constant. This explains the direction of the degeneracy in contour plot.

When also a variation in the Helium abundance is considered, the degeneracy changes direction. A larger value for  $Y_p$  produces a large free electron fraction at recombination and a smaller value for  $N_{\text{eff}}$  is needed to keep the damping scale small. On the other hand a large value for  $Y_p$  needs large values for  $\alpha$ . So now small values of  $N_{\text{eff}}$  are more compatible with observations when  $\alpha$  is larger.



## K. Future constraints on the fine structure constant from combined CMB and weak lensing measurements

CMB anisotropies have provided in the past years a powerful method to constrain variations in the fine structure constant. Since the CMB anisotropies were generated at the epoch of recombination, approximately  $\sim 340.000$  years after the Big Bang, they probe the value of the fine structure constant at that time, when the universe was nearly isotropic and homogeneous and on scales of the order of  $\sim 10Mpc$ .

Several constraints have been obtained analyzing the CMB data in the past (see e.g. (Avelino et al., 2001; Martins et al., 2002, 2004; Rocha et al., 2004; Ichikawa et al., 2006; Nakashima et al., 2008; Stefanescu, 2007; Calabrese et al., 2011; Menegoni et al., 2009; Landau and Scoccola, 2010; Menegoni et al., 2010)) with an accuracy at the level of  $\sim 10 - 1\%$ . In the most recent analysis, parameterizing a variation in the fine structure constant as  $\alpha/\alpha_0$ , where  $\alpha_0 = 1/137.03599907$  is the standard (local) value and  $\alpha$  is the value during the recombination process, Menegoni et al. (2012) used the latest CMB data, finding the constraint  $\alpha/\alpha_0 = 0.984 \pm 0.005$ , i.e. hinting also to a more than two standard deviation from the current value.

While the current CMB bound is considerably weaker than the observed variation from quasar spectra, the CMB recombination occurred at a time period corresponding to  $z \sim 1300$ . It is quite possible that  $\alpha$  varied more at higher redshifts, i.e. there is no reason for the variation to be constant in time. The CMB bound provides therefore important constraints on the running of the fine structure constant.

In the next few years, we expect a further significant improvement in the quantity and quality of cosmological data. The Planck satellite mission (see (Planck Collaboration, 2006)), for example, will provide accurate temperature CMB maps by the end of this year. On the other hand new and larger galaxy surveys are either already operating either under study. Some of these surveys will provide new galaxy weak lensing measurements that, when combined with Planck, will drastically improve the constraints on cosmological parameters. The Euclid satellite mission (Laureijs et al., 2011), part

of ESAs Cosmic Visions programme and due for launch in 2019, probably represents the most advanced weak lensing survey that could be achieved in the current decade.

Future weak lensing surveys will measure photometric redshifts of billions of galaxies allowing the possibility of 3D weak lensing analysis (e.g. (Castro et al., 2005; Heavens et al., 2006; Kitching et al., 2007)) or a tomographic reconstruction of growth of structure as a function of time through a binning of the redshift distribution of galaxies, with a considerable gain of cosmological information (e.g. on neutrinos (Hannestad et al., 2006; Kitching et al., 2008); dark energy (Kitching et al., 2007); the growth of structure (Bacon et al., 2005; Massey et al., 2007) and the dark matter distribution as a function of redshift (Taylor et al., 2004)). As far as we know, there is however still no paper in the literature that studied the improvement in constraining variation in fundamental constant from these surveys.

It is therefore timely to forecast the constraints on variation of the fine structure constant achievable from a combined analysis of CMB data from Planck and weak lensing data from the future Euclid satellite mission. In this paper we indeed perform this kind of analysis. As expected, weak lensing probes are shown to be highly complementary to CMB measurements and to significantly improve the constraints on variation in the fine structure constant.

The structure of the paper is as follows. In Section K.1 contains the description of the future data used in our analyses. The results from our Markov Chain Monte Carlo (MCMC) analyses are presented in Sec. K.2.

## **K.1. Future data**

In this section we describe the simulated data for future CMB and weak lensing surveys used in our analysis to forecast the future constraints achievable on cosmological parameters.

The fiducial cosmological model assumed in the simulated data is the best-fit from the WMAP seven year data analysis of Ref. (Komatsu et al., 2011) with baryon density  $\Omega_b h^2 = 0.02258$ , cold dark matter density  $\Omega_c h^2 = 0.1109$ , spectral index  $n_s = 0.963$ , optical depth  $\tau = 0.088$ , scalar amplitude  $A_s = 2.43 \times 10^{-9}$  and Hubble constant  $H_0 = 71$ . For the fine structure constant we assume a standard value  $\alpha/\alpha_0 = 1$ . As stated in the introduction we consider CMB data from Planck and galaxy weak lensing from Euclid. For CMB data the main observables are the  $C_\ell$  angular power spectra for temperature, polarization and cross temperature-polarization. For weak lensing data we consider the convergence power spectra  $P(\ell)$  following the procedure described in (De Bernardis et al., 2011; Martinelli et al., 2011). All spectra are generated using a modified version of the CAMB code (Lewis et al., 2000) taking into account the possible variation in the fine structure constant as discussed in (Calabrese et al., 2011; Menegoni et al., 2009).

### K.1.1. CMB data

We create a full mock CMB dataset with noise properties consistent with the Planck (Planck Collaboration, 2006) experiment (see Tab. K.1 for specifications).

| Experiment       | Channel | FWHM | $\Delta T/T$ |
|------------------|---------|------|--------------|
| Planck           | 70      | 14'  | 4.7          |
|                  | 100     | 10'  | 2.5          |
|                  | 143     | 7.1' | 2.2          |
| $f_{sky} = 0.85$ |         |      |              |

**Table K.1.:** Planck experimental specifications. Channel frequency is given in GHz, FWHM (Full-Width at Half-Maximum) in arc-minutes, and the temperature sensitivity per pixel in  $\mu K/K$ . The polarization sensitivity is  $\Delta E/E = \Delta B/B = \sqrt{2}\Delta T/T$ .

We consider for each channel a detector noise of  $w^{-1} = (\theta\sigma)^2$ , where  $\theta$  is the FWHM (Full-Width at Half-Maximum) of the beam assuming a Gaussian profile and  $\sigma$  is the temperature sensitivity  $\Delta T$  (see Tab. K.1 for the polarization sensitivity). We therefore add to each  $C_\ell$  fiducial spectra a noise spectrum given by:

$$N_\ell = w^{-1} \exp(\ell(\ell + 1)/\ell_b^2), \quad (\text{K.1.1})$$

where  $\ell_b$  is given by  $\ell_b \equiv \sqrt{8 \ln 2}/\theta$ .

Alongside temperature and polarization power spectra ( $C_\ell^{TT}$ ,  $C_\ell^{EE}$  and  $C_\ell^{TE}$ ) we include also the the deflection power spectra  $C_\ell^{dd}$  and  $C_\ell^{Td}$  obtained through the quadratic estimator of the lensing deflection field  $d$  presented in (Okamoto and Hu, 2003)

$$d(a, b)_L^M = n_L^{ab} \sum_{\ell\ell' mm'} W(a, b)_{\ell\ell'L}^{mm'} M a_\ell^m b_{\ell'}^{m'} \quad (\text{K.1.2})$$

where  $n_L^{ab}$  is a normalization factor,  $W$  is a function of the power spectra  $C_\ell^{ab}$ , which include both CMB lensing and primary anisotropy contributions, and  $ab = TT, TE, EE, EB, TB$ ; the  $BB$  case is excluded because the method of Ref. (Okamoto and Hu, 2003) is only valid when the lensing contribution is negligible compared to the primary anisotropy, assumption that fails for the B modes in the case of Planck.

The five quadratic estimators can be combined into a minimum variance estimator which provides the noise on the deflection field power spectrum  $C_\ell^{dd}$ :

$$N_\ell^{dd} = \frac{1}{\sum_{aa'bb'} (N_\ell^{aa'bb'})^{-1}}. \quad (\text{K.1.3})$$

We compute the minimum variance lensing noise for the Planck experiment by means of a routine publicly available at <http://lesgourg.web.cern.ch/lesgourg/codes.html>. The datasets (which include the lensing deflection power spectrum) are analyzed with a full-sky exact likelihood routine available at the same URL.

### K.1.2. Galaxy weak lensing data

Here we use the typical specifications for future weak lensing surveys like those of the Euclid experiment. Euclid will observe about 35 galaxies per square arcminute in the redshift range  $0.5 < z < 2$  with an uncertainty of about  $\sigma_z = 0.05(1+z)$  (see (Laureijs et al., 2011)). We build mock datasets of convergence power spectra for this survey. Table K.2 shows the number of galaxies per arcminute<sup>-2</sup> ( $n_{gal}$ ), redshift range,  $f_{sky}$  and intrinsic ellipticity for these surveys.

| $n_{gal}(\text{arcmin}^{-2})$ | redshift      | $f_{sky}$ | $\gamma_{rms}$ |
|-------------------------------|---------------|-----------|----------------|
| 30                            | $0.5 < z < 2$ | 0.38      | 0.22           |

**Table K.2.:** Specifications for the Euclid like survey considered in this paper. The table shows the number of galaxies per square arcminute ( $n_{gal}$ ), redshift range,  $f_{sky}$  and intrinsic ellipticity ( $\gamma_{rms}^2$ ) per component.

The expected  $1\sigma$  uncertainty on the convergence power spectra  $P(\ell)$  is given by (Cooray, 1999):

$$\sigma_\ell = \sqrt{\frac{2}{(2\ell+1)f_{sky}\Delta_\ell} \left( P(\ell) + \frac{\gamma_{rms}^2}{n_{gal}} \right)}, \quad (\text{K.1.4})$$

where  $\Delta_\ell$  is the  $\ell$ -bin width used to generate data. Here we choose  $\Delta_\ell = 1$  for the range  $2 < \ell < 100$  and  $\Delta_\ell = 40$  for  $100 < \ell < 1500$ . For the convergence power spectra we use  $\ell_{max} = 1500$  in order to exclude the scales where the non-linear growth of structure is more relevant and the shape of the non-linear matter power spectra is, as a consequence, more uncertain (see (Smith et al., 2003)). We describe the galaxy distribution of Euclid survey as in (Laureijs et al., 2011),  $n(z) \propto z^2 \exp(-(z/z_0)^{1.5})$  where  $z_0$  is set by the median redshift of the sources,  $z_0 = z_m/1.41$ . Here we calculate the power spectra assuming a median redshift  $z_m = 0.9$ . Although this assumption is reasonable for the Euclid survey, it is known that the parameters that control the shape of the distribution function may have strong degeneracies with some cosmological parameters as the matter density,  $\sigma_8$  and the spectral

index (Fu et al., 2008).

### K.1.3. Analysis method

Here we compute the expected constraints on the fine structure constant  $\alpha/\alpha_0$  from Planck and Euclid data.

We also investigate the effects of a wrong assumption about the value of the fine structure constant on the values of the cosmological parameters: we generate a dataset with a non-standard  $\alpha/\alpha_0$  fiducial value, but analyze the data assuming that  $\alpha/\alpha_0 = 1$ .

We perform a MCMC analysis based on the publicly available package `cosmomc` (Lewis and Bridle, 2002) with a convergence diagnostic using the Gelman and Rubin statistics. In principle, since we are dealing only with statistical uncertainties on the observables and neglecting any systematic effects, we could perform a simple Fisher matrix analysis. The Fisher matrix method offers the advantage of being less time-consuming and to reduce the forecast process to a series of matrices operations. Nevertheless, we prefer to conduct a MCMC exploration of the parameter space to avoid possible numerical instabilities that may arise in the computation of the derivatives. Moreover the gaussian approximation implied by the Fisher matrix is reliable for the standard cosmological parameters but may become risky for non-standard parameters.

We sample the following set of cosmological parameters, adopting flat priors on them: the baryon and cold dark matter densities  $\Omega_b h^2$  and  $\Omega_c h^2$ , the Hubble constant  $H_0$ , the scalar spectral index  $n_s$ , the overall normalization of the spectrum  $A_s$  at  $k = 0.002 \text{ Mpc}^{-1}$ , the optical depth to reionization  $\tau$ , and, finally, the variation of the fine structure constant parameter  $\alpha/\alpha_0$ .

Finally, we analyse a dataset with a fiducial value  $\alpha/\alpha_0 = 0.996$  assuming (wrongly) a standard  $\Lambda$ CDM scenario with  $\alpha/\alpha_0 = 1$ , with Planck and Euclid forecasted data. This exercise will allow us to investigate the bias introduced on cosmological parameter inference from a wrong assumption about the coupling model.

## K.2. Results

In Table K.3 we show the MCMC constraints on cosmological parameters at 68% c.l. from our simulated dataset. We consider two cases: a standard analysis where  $\alpha/\alpha_0 = 1$  and an analysis where also  $\alpha/\alpha_0 = 1$  is varied. This is important in order to show the impact of the cosmic degeneracies introduced by a variation in  $\alpha$  in the estimate of the remaining cosmological parameters.

*K. Future constraints on the fine structure constant from combined CMB and weak lensing measurements*

---

Moreover, in order to better quantify the improvement from the Euclid data we report the constraints obtained using the Planck data alone and Planck plus Euclid.

| Model Parameter             | Planck                    |                       | Planck+Euclid             |                       |
|-----------------------------|---------------------------|-----------------------|---------------------------|-----------------------|
|                             | Varying $\alpha/\alpha_0$ | $\alpha/\alpha_0 = 1$ | Varying $\alpha/\alpha_0$ | $\alpha/\alpha_0 = 1$ |
| $\Delta(\Omega_b h^2)$      | 0.00013                   | 0.00013               | 0.00011                   | 0.00010               |
| $\Delta(\Omega_c h^2)$      | 0.0012                    | 0.0010                | 0.00076                   | 0.00061               |
| $\Delta(\tau)$              | 0.0043                    | 0.0042                | 0.0041                    | 0.0029                |
| $\Delta(n_s)$               | 0.0062                    | 0.0031                | 0.0038                    | 0.0027                |
| $\Delta(\log[10^{10} A_s])$ | 0.019                     | 0.013                 | 0.0095                    | 0.0092                |
| $\Delta(H_0)$               | 0.76                      | 0.43                  | 0.34                      | 0.31                  |
| $\Delta(\Omega_\Lambda)$    | 0.0063                    | 0.0050                | 0.0034                    | 0.0033                |
| $\Delta(\alpha/\alpha_0)$   | 0.0018                    | —                     | 0.0008                    | —                     |

**Table K.3.:** 68% c.l. errors on cosmological parameters.

As we can see from the Table, the Euclid data will improve the Planck constraint on  $\alpha/\alpha_0$  by a factor  $\sim 2.6$ . This is a significant improvement since for example, a  $\sim 2\sigma$  detection by Planck for a variation of  $\alpha$  could be confirmed by the inclusion of Euclid data at more than 5 standard deviation. Moreover the precision achieved by a Planck+Euclid analysis is at the level of  $\sim 10^{-4}$ , that could be in principle further increased by the inclusion of other datasets. This is just one order of magnitude larger than the current evidence for variation in  $\alpha$  from QSO spectral lines, but at much lower redshift.

It is interesting to see what is the impact of a variation in the fine structure constant in the estimate of the remaining cosmological parameters. There is a high level of correlation among  $\alpha/\alpha_0$  and the parameters  $H_0$  and  $n_s$  when only the Planck data is considered. This is also clearly shown in Figs. K.1 and K.2 where we plot the 2-D likelihood contours at 68% and 95% c.l. between  $\alpha/\alpha_0$ ,  $n_s$  and  $H_0$ . Namely, a larger/lower value for  $\alpha$  is more consistent with observations with a larger/lower value for  $H_0$  and a lower/larger value for  $n_s$ .

When Planck and Euclid data are combined, the degeneracy with  $H_0$  is removed, yielding a better determination of  $\alpha$ . However the degeneracy with  $n_s$  (see Fig.K.2) is only partially removed. This is mainly due to the fact that the  $n_s$  parameter is degenerate with the reionization optical depth  $\tau$ .

In fact, as can be seen in Fig.K.3, using Euclid with Planck highlights a previously hidden degeneracy between  $\alpha/\alpha_0$  and  $\tau$ ; both these parameters do not affect the convergence power spectrum, thus they are not measured by Euclid, but they are both correlated with other parameters, such as  $n_s$  (Fig.K.2 and Fig.K.4), whose constraints are improved through the analysis of weak lensing. This improvement on  $n_s$  allows to clarify the degeneracy between  $\alpha/\alpha_0$  and  $\tau$ . Clearly, when a variation of the fine structure constant is consid-

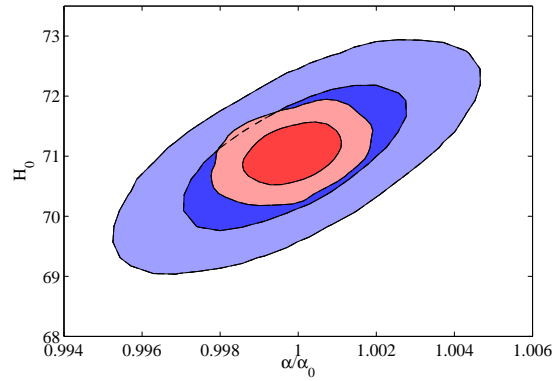


**Figure K.1.:** 2-D constraints on  $\alpha$  and  $H_0$  using Planck data (blue contours) and Planck+Euclid data (red contours).

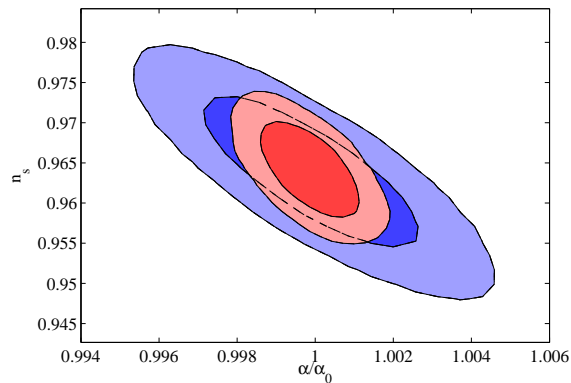


**Figure K.2.:** 2-D constraints on  $\alpha$  and  $n_s$  using Planck data (blue contours) and Planck+Euclid data (red contours).

ered in the analysis, the improvement of including Euclid in Planck data in the constraints of  $n_s$  and  $\tau$  is significantly reduced. As we can see also from Table I, the errors on  $n_s$  and  $\tau$  are increased by  $\sim 40\%$  and  $\sim 57\%$  respectively when  $\alpha$  is varying respect to the case when  $\alpha$  is fixed to the standard value.

From this discussion is clear that a better determination of the optical depth  $\tau$ , through, for example, measurements of the CMB polarization from experiments as SPIDER, would further improve the constraints on  $\alpha$  and other parameters.

Future surveys like Euclid will be able to tomographically reconstruct the matter distribution with a consequent gain of a three-dimensional information. Exploiting this possibility would improve the constraints. The non tomographic analysis we performed here can be thought as a conservative

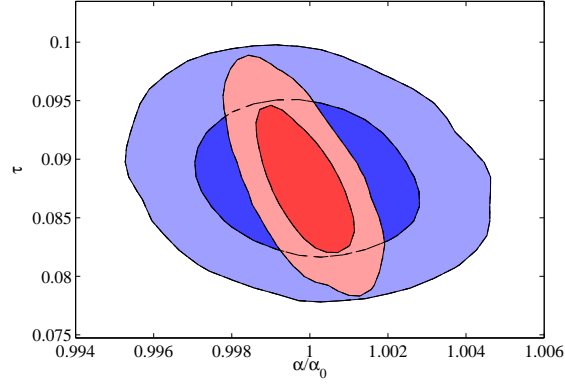


**Figure K.3.:** 2-D constraints on  $\alpha$  and  $\tau$  using Planck data (blue contours) and Planck+Euclid data (red contours).

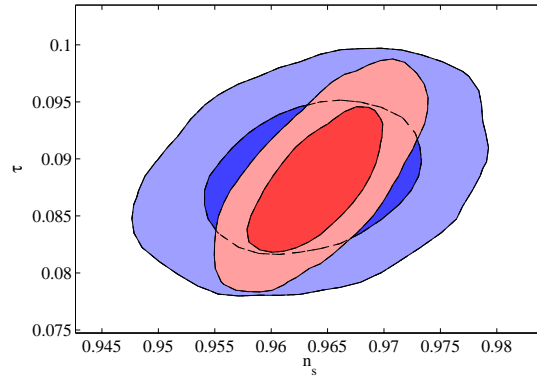


**Figure K.4.:** 2-D constraints on  $n_s$  and  $\tau$  using Planck data (blue contours) and Planck+Euclid data (red contours).

estimation of the constraints as we are not including the systematic effects that may affect a galaxy weak lensing survey.

### K.3. Conclusions

In this work we have presented new constraints on variation of the fine structure constant from the latest CMB anisotropy measurements of the ACT and SPT experiments, combined with other cosmological datasets. We have found that assuming the standard value for  $N_{\text{eff}}$  and a primordial Helium abundance of  $Y_p = 0.24$  the current data favours a lower value for the fine structure constant at more than two standard deviations with  $\alpha/\alpha_0 =$

$0.984 \pm 0.005$ .

We have shown that this result relies on the assumption of the number of relativistic degrees of freedom. When we let this parameter vary freely, the standard value is again consistent with the data considered. Varying also the primordial Helium content further enlarges the error bars. Despite the existing degeneracies, the current data offers the tantalizing suggestion of the presence of new physics at the epoch of recombination.

Clearly, further experimental confirmation of the result is needed. Fortunately, the results from the Planck satellite mission, expected to be released early next year, will most probably clarify the issue. The Planck experiment is indeed expected to have a sensitivity of  $\Delta N_{\text{eff}} \sim 0.2$  and  $\delta(\alpha/\alpha_0) \sim 0.002$  at 68% c.l. (see e.g. (Galli et al., 2010)).

We have evaluated the ability of a combination of CMB and weak lensing measurements as those expected from the Planck and Euclid satellite experiments in constraining variations in the fine structure constant  $\alpha$ . We have found that combining the data from those two experiments would provide a constraint on  $\alpha$  of the order of  $\Delta\alpha/\alpha \sim 10^{-4}$ , significantly improving current constraints. This constraint can be reasonably improved by considering additional datasets. In particular, further measurements of large angle CMB polarization and a better determination of the reionization optical depth will certainly make the constraints more stringent.

On the other hand we found that allowing in the analysis for variations in  $\alpha$  has important impact in the determination of parameters as  $n_s$  and  $\tau$  from a Planck+Euclid analysis. This should be considered when, for example, similar Planck+Euclid forecasts are produced focusing on selection between inflationary models as in (Huang et al., 2012). Considering unknown physical processes that could change the physics at recombination will clearly affect the constraints on inflationary parameters from combined Planck+Euclid future analyses.



# Bibliography

ABAZAJIAN, K.N. ET AL.

*The Seventh Data Release of the Sloan Digital Sky Survey.*  
*Astrophys.J.Suppl.*, **182**, pp. 543–558 (2009).  
doi:10.1088/0067-0049/182/2/543.

ABRAMOWICZ, M.A., NOVIKOV, I.D. AND PACZYNSKI, B.

*The appearance of highly relativistic, spherically symmetric stellar winds.*  
*ApJ*, **369**, pp. 175–178 (1991).  
doi:10.1086/169748.

ADAMS, J.A., CRESSWELL, B. AND EASTHER, R.

*Inflationary perturbations from a potential with a step.*  
*Phys. Rev.*, **D64**, p. 123514 (2001).  
doi:10.1103/PhysRevD.64.123514.

ADAMS, J.A., ROSS, G.G. AND SARKAR, S.

*Multiple inflation.*  
*Nucl.Phys.*, **B503**, pp. 405–425 (1997a).  
doi:10.1016/S0550-3213(97)00431-8.

ADAMS, J.A., ROSS, G.G. AND SARKAR, S.

*Natural supergravity inflation.*  
*Phys.Lett.*, **B391**, pp. 271–280 (1997b).  
doi:10.1016/S0370-2693(96)01484-0.

ADSHEAD, P., DVORKIN, C., HU, W. AND LIM, E.A.

*Non-Gaussianity from Step Features in the Inflationary Potential.*  
*Phys.Rev.*, **D85**, p. 023531 (2012).  
doi:10.1103/PhysRevD.85.023531.

AKSENOV, A.G., MILGROM, M. AND USOV, V.V.

*Structure of Pair Winds from Compact Objects with Application to Emission from Hot Bare Strange Stars.*  
*ApJ*, **609**, pp. 363–377 (2004).  
doi:10.1086/421006.

AKSENOV, A.G., RUFFINI, R. AND VERESHCHAGIN, G.V.

*Thermalization of Nonequilibrium Electron-Positron-Photon Plasmas.*  
*Phys. Rev. Lett.*, **99(12)**, pp. 125003–+ (2007).  
doi:10.1103/PhysRevLett.99.125003.

- AKSENOV, A.G., RUFFINI, R. AND VERESHCHAGIN, G.V.  
*Thermalization of the mildly relativistic plasma.*  
Phys. Rev. D, **79(4)**, p. 043008 (2009).  
doi:10.1103/PhysRevD.79.043008.
- AKSENOV, A.G., RUFFINI, R. AND VERESHCHAGIN, G.V.  
*Pair plasma relaxation time scales.*  
Phys. Rev. E, **81**, p. 046401 (2010).
- AKSENOV, A.G., RUFFINI, R. AND VERESHCHAGIN, G.V.  
*Radiative transfer near the photosphere of ultrarelativistic outflows.*  
*in preparation* (2012).
- ALCOCK, C., FARHI, E. AND OLINTO, A.  
*Strange stars.*  
ApJ, **310**, pp. 261–272 (1986).  
doi:10.1086/164679.
- AMANULLAH, R., LIDMAN, C., RUBIN, D., ALDERING, G., ASTIER, P. ET AL.  
*Spectra and Light Curves of Six Type Ia Supernovae at 0.511 <math>z</math> <math>1.12</math> and the Union2 Compilation.*  
Astrophys.J., **716**, pp. 712–738 (2010).  
doi:10.1088/0004-637X/716/1/712.
- ARBOLINO, M.V. AND RUFFINI, R.  
*The ratio between the mass of the halo and visible matter in spiral galaxies and limits on the neutrino mass.*  
A&A, **192**, pp. 107–116 (1988).
- ARCHIDIACONO, M., CALABRESE, E. AND MELCHIORRI, A.  
*The Case for Dark Radiation.*  
Phys.Rev., **D84**, p. 123008 (2011).  
doi:10.1103/PhysRevD.84.123008.
- AVELINO, P., ESPOSITO, S., MANGANO, G., MARTINS, C., MELCHIORRI, A.  
ET AL.  
*Early universe constraints on a time varying fine structure constant.*  
Phys.Rev., **D64**, p. 103505 (2001).  
doi:10.1103/PhysRevD.64.103505.
- BACON, D.J., TAYLOR, A.N., BROWN, M.L., GRAY, M.E., WOLF, C.,  
MEISENHEIMER, K., DYE, S., WISOTZKI, L., BORCH, A. AND KLEINHEIN-  
RICH, M.  
*Evolution of the dark matter distribution with three-dimensional weak lensing.*  
MNRAS, **363**, pp. 723–733 (2005).  
doi:10.1111/j.1365-2966.2005.09420.x.

- BAND, D., MATTESON, J., FORD, L., SCHAEFER, B., PALMER, D., TEEGARDEN, B., CLINE, T., BRIGGS, M., PACIASAS, W., PENDLETON, G. ET AL.  
*BATSE observations of gamma-ray burst spectra. I - Spectral diversity.*  
*ApJ*, **413**, pp. 281–292 (1993).  
doi:10.1086/172995.
- BATTYE, R.A., CRITTENDEN, R. AND WELLER, J.  
*Cosmic concordance and the fine structure constant.*  
*Phys.Rev.*, **D63**, p. 043505 (2001).  
doi:10.1103/PhysRevD.63.043505.
- BEAN, R., CHEN, X., HAILU, G., TYE, S.H.H. AND XU, J.  
*Duality Cascade in Brane Inflation.*  
*JCAP*, **0803**, p. 026 (2008).  
doi:10.1088/1475-7516/2008/03/026.
- BEGUE, D., SIUTSOU, I.A. AND VERESHCHAGIN, G.V.  
*Monte carlo simulations of the photospheric emission in grbs.*  
*ApJ*, submitted (2012).
- BELL, A.R. AND KIRK, J.G.  
*Possibility of Prolific Pair Production with High-Power Lasers.*  
*Physical Review Letters*, **101(20)**, 200403 (2008).  
doi:10.1103/PhysRevLett.101.200403.
- BELOBORODOV, A.M.  
*Collisional mechanism for gamma-ray burst emission.*  
*MNRAS*, **407**, pp. 1033–1047 (2010).  
doi:10.1111/j.1365-2966.2010.16770.x.
- BELOBORODOV, A.M.  
*Radiative Transfer in Ultrarelativistic Outflows.*  
*ApJ*, **737**, p. 68 (2011).  
doi:10.1088/0004-637X/737/2/68.
- BELVEDERE, R., PUGLIESE, D., RUEDA, J.A., RUFFINI, R. AND XUE, S.S.  
*Neutron star equilibrium configurations within a fully relativistic theory with strong, weak, electromagnetic, and gravitational interactions.*  
*Nuclear Physics A*, **883**, pp. 1–24 (2012).  
doi:10.1016/j.nuclphysa.2012.02.018.
- BENEDETTI, A., HAN, W.B., RUFFINI, R. AND VERESHCHAGIN, G.V.  
*On the frequency of oscillations in the pair plasma generated by a strong electric field.*  
*Physics Letters B*, **698**, pp. 75–79 (2011).  
doi:10.1016/j.physletb.2011.02.050.

- BENEDETTI, A. AND VERESHCHAGIN, G.V.  
*Kinetic approach to the photospheric emission from relativistic outflows. in preparation* (2012).
- BENETTI, M., LATTANZI, M., CALABRESE, E. AND MELCHIORRI, A.  
*Features in the primordial spectrum: new constraints from WMAP7+ACT data and prospects for Planck.*  
*Phys.Rev.*, **D84**, p. 063509 (2011).  
doi:10.1103/PhysRevD.84.063509.
- BENETTI, M., PANDOLFI, S., LATTANZI, M., MARTINELLI, M. AND MELCHIORRI, A.  
*Featuring the primordial power spectrum: new constraints on interrupted slow-roll from CMB and LRG data.*  
*arXiv* (2012).
- BERESTETSKII, V.B., LIFSHITZ, E.M. AND PITAEVSKII, V.B.  
*Quantum Electrodynamics* (Elsevier, 1982).
- BIANCO, C.L., RUFFINI, R. AND XUE, S.  
*The elementary spike produced by a pure  $e^+e^-$  pair-electromagnetic pulse from a Black Hole: The PEM Pulse.*  
*A&A*, **368**, pp. 377–390 (2001).  
doi:10.1051/0004-6361:20000556.
- BINNEY, J. AND TREMAINE, S.  
*Galactic dynamics* (Princeton, NJ, Princeton University Press, 1987).
- BISNOVATYI-KOGAN, G.S., ZEL'DOVICH, Y.B. AND SYUNYAEV, R.A.  
*Physical Processes in a Low-Density Relativistic Plasma.*  
*Soviet Ast.*, **15**, pp. 17–+ (1971).
- BLASCHKE, D.B., DMITRIEV, V.V., RÖPKE, G. AND SMOLYANSKY, S.A.  
*BBGKY kinetic approach for an  $e^-e^+\gamma$  plasma created from the vacuum in a strong laser-generated electric field: The one-photon annihilation channel.*  
*Phys. Rev. D*, **84(8)**, 085028 (2011).  
doi:10.1103/PhysRevD.84.085028.
- BLASCHKE, D.B., PROZORKEVICH, A.V., ROBERTS, C.D., SCHMIDT, S.M. AND SMOLYANSKY, S.A.  
*Pair Production and Optical Lasers.*  
*Phys. Rev. Lett.*, **96(14)**, pp. 140402–+ (2006).  
doi:10.1103/PhysRevLett.96.140402.
- BLINNIKOV, S.I., KOZYREVA, A.V. AND PANCHENKO, I.E.  
*Gamma-ray bursts: When does a blackbody spectrum look non-thermal?*  
*Astronomy Reports*, **43**, pp. 739–747 (1999).

- BLOCH, J.C.R., MIZERNY, V.A., PROZORKEVICH, A.V., ROBERTS, C.D., SCHMIDT, S.M., SMOLYANSKY, S.A. AND VINNIK, D.V.  
*Pair creation: Back reactions and damping.*  
Phys. Rev. D, **60(11)**, 116011 (1999).  
doi:10.1103/PhysRevD.60.116011.
- BOYARSKY, A., RUCHAYSKIY, O., IAKUBOVSKIY, D., MACCIO', A.V. AND MALYSHEV, D.  
*New evidence for dark matter.*  
ArXiv e-prints (2009).
- BRANDENBERGER, R.H. AND MARTIN, J.  
*The robustness of inflation to changes in super-Planck- scale physics.*  
Mod. Phys. Lett., **A16**, pp. 999–1006 (2001).  
doi:10.1142/S0217732301004170.
- BRENIG, W. AND HAAG, R.  
*Allgemeine quantentheorie der stoßprozesse.*  
Fortschr. Phys., **7(4-5)**, p. 183242 (1959).  
doi:10.1002/prop.19590070402.
- BRIGGS, M.S., CONNAUGHTON, V., WILSON-HODGE, C., PREECE, R.D., FISHMAN, G.J., KIPPEN, R.M., BHAT, P.N., PACIESAS, W.S., CHAPLIN, V.L., MEEGAN, C.A. ET AL.  
*Electron-positron beams from terrestrial lightning observed with Fermi GBM.*  
Geophys. Res. Lett., **380**, L02808 (2011).  
doi:10.1029/2010GL046259.
- BULA, C., McDONALD, K.T., PREBYS, E.J., BAMBER, C., BOEGE, S., KOTSEROGLOU, T., MELISSINOS, A.C., MEYERHOFER, D.D., RAGG, W., BURKE, D.L. ET AL.  
*Observation of Nonlinear Effects in Compton Scattering.*  
Physical Review Letters, **76**, pp. 3116–3119 (1996).  
doi:10.1103/PhysRevLett.76.3116.
- BULANOV, S.S., ESIRKEPOV, T.Z., THOMAS, A.G.R., KOGA, J.K. AND BULANOV, S.V.  
*Schwinger Limit Attainability with Extreme Power Lasers.*  
Physical Review Letters, **105(22)**, 220407 (2010).  
doi:10.1103/PhysRevLett.105.220407.
- BURGESS, C.P., CLINE, J.M., LEMIEUX, F. AND HOLMAN, R.  
*Are inflationary predictions sensitive to very high energy physics?*  
JHEP, **02**, p. 048 (2003).

BURKE, D.L., FIELD, R.C., HORTON-SMITH, G., SPENCER, J.E., WALZ, D., BERRIDGE, S.C., BUGG, W.M., SHMAKOV, K., WEIDEMANN, A.W., BULA, C. ET AL.

*Positron Production in Multiphoton Light-by-Light Scattering.*

*Physical Review Letters*, **79**, pp. 1626–1629 (1997).

doi:10.1103/PhysRevLett.79.1626.

BURKERT, A.

*The Structure of Dark Matter Halos in Dwarf Galaxies.*

*ApJ*, **447**, p. L25 (1995).

doi:10.1086/309560.

CALABRESE, E., MENEGONI, E., MARTINS, C., MELCHIORRI, A. AND ROCHA, G.

*Constraining Variations in the Fine Structure Constant in the presence of Early Dark Energy.*

*Phys.Rev.*, **D84**, p. 023518 (2011).

doi:10.1103/PhysRevD.84.023518.

CALZETTI, D., GIAVALISCO, M. AND RUFFINI, R.

*The normalization of the correlation functions for extragalactic structures.*

*A&A*, **198**, pp. 1–2 (1988).

CALZETTI, D., GIAVALISCO, M., RUFFINI, R., EINASTO, J. AND SAAR, E.

*The correlation function of galaxies in the direction of the Coma cluster.*

*Ap&SS*, **137**, pp. 101–106 (1987).

CASTRO, P.G., HEAVENS, A. AND KITCHING, T.

*Weak lensing analysis in three dimensions.*

*Phys.Rev.*, **D72**, p. 023516 (2005).

doi:10.1103/PhysRevD.72.023516.

CHEN, H., WILKS, S.C., BONLIE, J.D., LIANG, E.P., MYATT, J., PRICE, D.F., MEYERHOFER, D.D. AND BEIERSDORFER, P.

*Relativistic Positron Creation Using Ultraindense Short Pulse Lasers.*

*Phys. Rev. Lett.*, **102(10)**, pp. 105001–+ (2009).

doi:10.1103/PhysRevLett.102.105001.

CHERNIKOV, N.A.

*Equilibrium distribution of the relativistic gas ii.*

*Acta Phys. Polonica.*, **26(5)**, pp. 1069–1092 (1964).

CHLUBA, J.

*Spectral Distortions of the Cosmic Microwave Background.*

Ph.D. thesis, Ludwig-Maximilians-Universität München (2005).

- CHURAZOV, E., SUNYAEV, R., SAZONOV, S., REVNIVTSEV, M. AND VARSHALOVICH, D.  
*Positron annihilation spectrum from the Galactic Centre region observed by SPI/INTEGRAL.*  
MNRAS, **357**, pp. 1377–1386 (2005).  
doi:10.1111/j.1365-2966.2005.08757.x.
- CONTALDI, C.R., PELOSO, M., KOFMAN, L. AND LINDE, A.D.  
*Suppressing the lower Multipoles in the CMB Anisotropies.*  
JCAP, **0307**, p. 002 (2003).  
doi:10.1088/1475-7516/2003/07/002.
- COORAY, A.R.  
*Weighing neutrinos: Weak lensing approach.*  
*Astron.Astrophys.*, **348**, p. 31 (1999).
- COUDERC, P.  
*Les aureoles lumineuses des Novaelig.*  
*Annales d’Astrophysique*, **2**, pp. 271–+ (1939).
- COVI, L., HAMANN, J., MELCHIORRI, A., SLOSAR, A. AND SORBERA, I.  
*Inflation and WMAP three year data: Features have a future!*  
*Phys. Rev.*, **D74**, p. 083509 (2006).  
doi:10.1103/PhysRevD.74.083509.
- DAIGNE, F. AND MOCHKOVITCH, R.  
*The expected thermal precursors of gamma-ray bursts in the internal shock model.*  
MNRAS, **336**, pp. 1271–1280 (2002).  
doi:10.1046/j.1365-8711.2002.05875.x.
- DAMOUR, T. AND RUFFINI, R.  
*Quantum electrodynamical effects in Kerr-Newman geometries.*  
*Phys. Rev. Lett.*, **35**, pp. 463–466 (1975).
- DAS, S., MARRIAGE, T.A., ADE, P.A., AGUIRRE, P., AMIR, M. ET AL.  
*The Atacama Cosmology Telescope: A Measurement of the Cosmic Microwave Background Power Spectrum at 148 and 218 GHz from the 2008 Southern Survey.*  
*Astrophys.J.*, **729**, p. 62 (2011).  
doi:10.1088/0004-637X/729/1/62.  
\* Temporary entry \*.
- DE BERNARDIS, F., MARTINELLI, M., MELCHIORRI, A., MENA, O. AND COORAY, A.  
*Future weak lensing constraints in a dark coupled universe.*  
*Phys.Rev.*, **D84**, p. 023504 (2011).  
doi:10.1103/PhysRevD.84.023504.

- DE BERNARDIS, P. ET AL.  
*A Flat universe from high resolution maps of the cosmic microwave background radiation.*  
*Nature*, **404**, pp. 955–959 (2000).  
doi:10.1038/35010035.
- DERISHEV, E.V., KOCHAROVSKY, V.V. AND KOCHAROVSKY, V.V.  
*Effects of neutrons in fireball dynamics.*  
*Nuclear Physics B Proceedings Supplements*, **80**, pp. C612+ (2000).
- DI PIAZZA, A., MÜLLER, C., HATSAGORTSYAN, K.Z. AND KEITEL, C.H.  
*Extremely high-intensity laser interactions with fundamental quantum systems.*  
*Reviews of Modern Physics*, **84**, pp. 1177–1228 (2012).  
doi:10.1103/RevModPhys.84.1177.
- DOLGOV, A.D.  
*Neutrinos in cosmology.*  
*Phys. Rep.*, **370**, pp. 333–535 (2002).
- DONATO, F., GENTILE, G., SALUCCI, P., FRIGERIO MARTINS, C., WILKINSON, M.I., GILMORE, G., GREBEL, E.K., KOCH, A. AND WYSE, R.  
*A constant dark matter halo surface density in galaxies.*  
*MNRAS*, **397**, pp. 1169–1176 (2009).  
doi:10.1111/j.1365-2966.2009.15004.x.
- DUNKLEY, J., HLOZEK, R., SIEVERS, J., ACQUAVIVA, V., ADE, P. ET AL.  
*The Atacama Cosmology Telescope: Cosmological Parameters from the 2008 Power Spectra.*  
*Astrophys.J.*, **739**, p. 52 (2011).  
doi:10.1088/0004-637X/739/1/52.
- EASTHER, R., GREENE, B.R., KINNEY, W.H. AND SHIU, G.  
*A generic estimate of trans-Planckian modifications to the primordial power spectrum in inflation.*  
*Phys. Rev.*, **D66**, p. 023518 (2002).  
doi:10.1103/PhysRevD.66.023518.
- EHLERS, J.  
*Survey of general relativity theory.*  
In *Relativity, Astrophysics and Cosmology*, pp. 1–125 (1973).
- EINASTO, J.  
*Kinematics and dynamics of stellar systems.*  
In *Trudy Inst. Astrofiz.*, volume 5, p. 87 (Alma-Ata, 1965).
- FEDOTOV, A.M., NAROZHNY, N.B., MOUROU, G. AND KORN, G.  
*Limitations on the Attainable Intensity of High Power Lasers.*

- Physical Review Letters*, **105(8)**, 080402 (2010).  
doi:10.1103/PhysRevLett.105.080402.
- FRIEMAN, J., TURNER, M. AND HUTERER, D.  
*Dark Energy and the Accelerating Universe.*  
*Ann. Rev. Astron. Astrophys.*, **46**, pp. 385–432 (2008).  
doi:10.1146/annurev.astro.46.060407.145243.
- FU, L., SEMBOLONI, E., HOEKSTRA, H., KILBINGER, M., VAN WAERBEKE, L. ET AL.  
*Very weak lensing in the CFHTLS Wide: Cosmology from cosmic shear in the linear regime.*  
*Astron. Astrophys.*, **479**, pp. 9–25 (2008).  
doi:10.1051/0004-6361:20078522.
- FUKUE, J., KATO, S. AND MATSUMOTO, R.  
*Radiation hydrodynamics in a moving plasma with Compton scattering.*  
*PASJ*, **37**, pp. 383–397 (1985).
- GALLI, S., IOCCO, F., BERTONE, G. AND MELCHIORRI, A.  
*CMB constraints on Dark Matter models with large annihilation cross-section.*  
*Phys. Rev.*, **D80**, p. 023505 (2009).  
doi:10.1103/PhysRevD.80.023505.
- GALLI, S., IOCCO, F., BERTONE, G. AND MELCHIORRI, A.  
*Updated CMB constraints on Dark Matter annihilation cross-sections.*  
*Phys. Rev.*, **D84**, p. 027302 (2011).  
doi:10.1103/PhysRevD.84.027302.
- GALLI, S., MARTINELLI, M., MELCHIORRI, A., PAGANO, L., SHERWIN, B.D. ET AL.  
*Constraining Fundamental Physics with Future CMB Experiments.*  
*Phys. Rev.*, **D82**, p. 123504 (2010).  
doi:10.1103/PhysRevD.82.123504.
- GAO, J.G., MERAFINA, M. AND RUFFINI, R.  
*The semidegenerate configurations of a selfgravitating system of fermions.*  
*A&A*, **235**, pp. 1–7 (1990).
- GAO, J.G. AND RUFFINI, R.  
*Relativistic limits on the masses of self-gravitating systems of degenerate neutrons.*  
*Physics Letters B*, **97**, pp. 388–390 (1980).
- GATOFF, G., KERMAN, A.K. AND MATSUI, T.  
*Flux-tube model for ultrarelativistic heavy-ion collisions: Electrohydrodynamics of a quark-gluon plasma.*

- Phys. Rev. D, **36**, pp. 114–129 (1987).  
doi:10.1103/PhysRevD.36.114.
- GENTILE, G., FAMAHEY, B., ZHAO, H. AND SALUCCI, P.  
*Universality of galactic surface densities within one dark halo scale-length.*  
Nature, **461**, pp. 627–628 (2009).  
doi:10.1038/nature08437.
- GERSTNER, E.  
*Laser physics: Lasing at the limit.*  
Nature Physics, **6**, pp. 638–+ (2010).  
doi:10.1038/nphys1785.
- GIANNIOS, D.  
*Prompt emission spectra from the photosphere of a GRB.*  
A&A, **457**, pp. 763–770 (2006).  
doi:10.1051/0004-6361:20065000.
- GIAVALISCO, M.  
*The gravitational formation of cosmological structures.*  
Ph.D. thesis, University of Rome “La Sapienza” (1992).
- GIESEN, G., LESGOURGUES, J., AUDREN, B. AND ALI-HAIMOUD, Y.  
*CMB photons shedding light on dark matter.*  
arXiv (2012).
- GIUSARMA, E., ARCHIDIACONO, M., DE PUTTER, R., MELCHIORRI, A. AND MENA, O.  
*Sterile neutrino models and nonminimal cosmologies.*  
Phys.Rev., **D85**, p. 083522 (2012).  
doi:10.1103/PhysRevD.85.083522.
- GIUSARMA, E., CORSI, M., ARCHIDIACONO, M., DE PUTTER, R., MELCHIORRI, A. ET AL.  
*Constraints on massive sterile neutrino species from current and future cosmological data.*  
Phys.Rev., **D83**, p. 115023 (2011).  
doi:10.1103/PhysRevD.83.115023.
- GOODMAN, J.  
*Are gamma-ray bursts optically thick?*  
ApJ, **308**, pp. L47–L50 (1986).  
doi:10.1086/184741.
- GOULD, R.J.  
*Kinetic theory of relativistic plasmas.*  
Physics of Fluids, **24**, pp. 102–107 (1981).

- GREENBERGER, D., HENTSCHEL, K. AND WEINERT, F.  
*Compendium of Quantum Physics* (Springer Berlin Heidelberg, 2009).  
doi:10.1007/978-3-540-70626-7.
- GREINER, W. AND REINHARDT, J.  
*Quantum Electrodynamics* (Berlin, Springer, 2003).
- GRIMSRUD, O.M. AND WASSERMAN, I.  
*Non-equilibrium effects in steady relativistic  $e^+ + e^-$ -gamma winds.*  
MNRAS, **300**, pp. 1158–1180 (1998).
- GROOT, S., LEEUWEN, W. AND WEERT, C.  
*Relativistic kinetic theory: principles and applications* (North-Holland Pub. Co., 1980).  
ISBN 9780444854537.
- GUILBERT, P.W. AND STEPNEY, S.  
*Pair production, Comptonization and dynamics in astrophysical plasmas.*  
MNRAS, **212**, pp. 523–544 (1985).
- HALL, G. AND WATT, J.M.  
*Modern Numerical Methods for Ordinary Differential Equations* (New York, Oxford University Press, 1976).
- HAMANN, J.  
*Evidence for extra radiation? Profile likelihood versus Bayesian posterior.*  
JCAP, **1203**, p. 021 (2012).  
doi:10.1088/1475-7516/2012/03/021.
- HAMANN, J., COVI, L., MELCHIORRI, A. AND SLOSAR, A.  
*New Constraints on Oscillations in the Primordial Spectrum of Inflationary Perturbations.*  
*Phys.Rev.*, **D76**, p. 023503 (2007).  
doi:10.1103/PhysRevD.76.023503.
- HAMANN, J., HANNESTAD, S., LESGOURGUES, J., RAMPF, C. AND WONG, Y.Y.  
*Cosmological parameters from large scale structure - geometric versus shape information.*  
JCAP, **1007**, p. 022 (2010).  
doi:10.1088/1475-7516/2010/07/022.
- HANNESTAD, S., TU, H. AND WONG, Y.Y.Y.  
*Measuring neutrino masses and dark energy with weak lensing tomography.*  
JCAP, **0606**, p. 025 (2006).

- HASKELL, R.C., SVAASAND, L.O., TSAY, T.T., FENG, T.C., MCADAMS, M.S. AND TROMBERG, B.J.  
*Boundary conditions for the diffusion equation in radiative transfer.*  
*Journal of the Optical Society of America A*, **11**, pp. 2727–2741 (1994).  
doi:10.1364/JOSAA.11.002727.
- HAUG, E. AND NAKEL, W.  
*The Elementary Process of Bremsstrahlung* (World Scientific Publishing Co., Singapore, 2004).
- HAZRA, D.K., AICH, M., JAIN, R.K., SRIRAMKUMAR, L. AND SOURADEEP, T.  
*Primordial features due to a step in the inflaton potential.*  
*JCAP*, **1010**, p. 008 (2010).  
doi:10.1088/1475-7516/2010/10/008.
- HEAVENS, A., KITCHING, T.D. AND TAYLOR, A.  
*Measuring dark energy properties with 3D cosmic shear.*  
*Mon.Not.Roy.Astron.Soc.*, **373**, pp. 105–120 (2006).  
doi:10.1111/j.1365-2966.2006.11006.x.
- HEISENBERG, W. AND EULER, H.  
*Folgerungen aus der diracschen theorie des positrons.*  
*Zeits. Phys.*, **98**, pp. 714–732 (1935).
- HLOZEK, R., DUNKLEY, J., ADDISON, G., APPEL, J.W., BOND, J. ET AL.  
*The Atacama Cosmology Telescope: a measurement of the primordial power spectrum.*  
*arXiv* (2011).  
\* Temporary entry \*.
- HOU, Z., KEISLER, R., KNOX, L., MILLEA, M. AND REICHARDT, C.  
*How Massless Neutrinos Affect the Cosmic Microwave Background Damping Tail.*  
*arXiv* (2011).
- HUANG, Z., VERDE, L. AND VERNIZZI, F.  
*Constraining inflation with future galaxy redshift surveys.*  
*JCAP*, **1204**, p. 005 (2012).  
doi:10.1088/1475-7516/2012/04/005.
- HUNT, P. AND SARKAR, S.  
*Multiple inflation and the WMAP 'glitches'.*  
*Phys.Rev.*, **D70**, p. 103518 (2004).  
doi:10.1103/PhysRevD.70.103518.

- ICHIKAWA, K., KANZAKI, T. AND KAWASAKI, M.  
*CMB constraints on the simultaneous variation of the fine structure constant and electron mass.*  
*Phys.Rev.*, **D74**, p. 023515 (2006).  
doi:10.1103/PhysRevD.74.023515.
- INGROSSO, G., MERAFINA, M., RUFFINI, R. AND STRAFELLA, F.  
*System of self-gravitating semidegenerate fermions with a cutoff of energy and angular momentum in their distribution function.*  
*A&A*, **258**, pp. 223–233 (1992).
- JOUDAKI, S.  
*Constraints on Neutrino Mass and Light Degrees of Freedom in Extended Cosmological Parameter Spaces.*  
*arXiv* (2012).
- KAFEXHIU, E.  
*Excitation and destruction of nuclei in hot astrophysical plasmas around black holes.*  
In *25th Texas Symposium on Relativistic Astrophysics* (2010).
- KAJANTIE, K. AND MATSUI, T.  
*Decay of strong color electric field and thermalization in ultra-relativistic nucleus-nucleus collisions.*  
*Physics Letters B*, **164**, pp. 373–378 (1985).  
doi:10.1016/0370-2693(85)90343-0.
- KATZ, J.I.  
*A Cubic Micron of Equilibrium Pair Plasma?*  
*ApJS*, **127**, pp. 371–373 (2000).  
doi:10.1086/313350.
- KEISLER, R., REICHARDT, C., AIRD, K., BENSON, B., BLEEM, L. ET AL.  
*A Measurement of the Damping Tail of the Cosmic Microwave Background Power Spectrum with the South Pole Telescope.*  
*Astrophys.J.*, **743**, p. 28 (2011).  
doi:10.1088/0004-637X/743/1/28.  
\* Temporary entry \*.
- KHATRI, R., SUNYAEV, R.A. AND CHLUBA, J.  
*Does Bose-Einstein condensation of CMB photons cancel  $\mu$  distortions created by dissipation of sound waves in the early Universe?*  
*A&A*, **540**, A124 (2012).  
doi:10.1051/0004-6361/201118194.
- KITCHING, T.D., HEAVENS, A.F., VERDE, L., SERRA, P. AND MELCHIORRI, A.

- Finding Evidence for Massive Neutrinos using 3D Weak Lensing.*  
*Phys. Rev.*, **D77**, p. 103008 (2008).  
doi:10.1103/PhysRevD.77.103008.
- KITCHING, T.D., HEAVENS, A., TAYLOR, A., BROWN, M., MEISENHEIMER, K. ET AL.  
*Cosmological constraints from COMBO-17 using 3D weak lensing.*  
*Mon.Not.Roy.Astron.Soc.*, **376**, pp. 771–778 (2007).  
doi:10.1111/j.1365-2966.2007.11473.x.
- KLUGER, Y., EISENBERG, J.M., SVETITSKY, B., COOPER, F. AND MOTTOLA, E.  
*Pair production in a strong electric field.*  
*Phys. Rev. Lett.*, **67**, pp. 2427–2430 (1991).  
doi:10.1103/PhysRevLett.67.2427.
- KLUGER, Y., EISENBERG, J.M., SVETITSKY, B., COOPER, F. AND MOTTOLA, E.  
*Fermion pair production in a strong electric field.*  
*Phys. Rev. D*, **45**, pp. 4659–4671 (1992).  
doi:10.1103/PhysRevD.45.4659.
- KLUGER, Y., MOTTOLA, E. AND EISENBERG, J.M.  
*Quantum Vlasov equation and its Markov limit.*  
*Phys. Rev. D*, **58(12)**, 125015 (1998).  
doi:10.1103/PhysRevD.58.125015.
- KOLB, E.W. AND TURNER, M.S.  
*The Early Universe* (Frontiers in Physics, Reading, MA: Addison-Wesley, 1990).
- KOMATSU, E. ET AL.  
*Seven-Year Wilkinson Microwave Anisotropy Probe (WMAP) Observations: Cosmological Interpretation.*  
*Astrophys.J.Suppl.*, **192**, p. 18 (2011).  
doi:10.1088/0067-0049/192/2/18.
- LANDAU, L.D. AND LIFSHITZ, E.M.  
*Statistical physics. Pt.1, Pt.2* (Oxford: PergamonPress, 1980).
- LANDAU, L.D. AND LIFSHITZ, E.M.  
*Physical Kinetics* (Elsevier, 1981).
- LANDAU, S. AND SCOCCOLA, C.G.  
*Constraints on variation in  $\alpha$  and  $m_e$  from WMAP 7-year data.*  
*Astron.Astrophys.*, **517**, p. A62 (2010).

- LARSON, D., DUNKLEY, J., HINSHAW, G., KOMATSU, E., NOLTA, M. ET AL.  
*Seven-Year Wilkinson Microwave Anisotropy Probe (WMAP) Observations: Power Spectra and WMAP-Derived Parameters.*  
*Astrophys.J.Suppl.*, **192**, p. 16 (2011).  
doi:10.1088/0067-0049/192/2/16.
- LATTANZI, M., RUFFINI, R. AND VERESHCHAGIN, G.  
*On the possible role of massive neutrinos in cosmological structure formation.*  
In M. Novello and S.E. Perez Bergliaffa (eds.), *Cosmology and Gravitation*, volume 668 of *American Institute of Physics Conference Series*, pp. 263–287 (2003).
- LATTANZI, M., RUFFINI, R. AND VERESHCHAGIN, G.V.  
*Joint constraints on the lepton asymmetry of the Universe and neutrino mass from the Wilkinson Microwave Anisotropy Probe.*  
*Phys. Rev. D*, **72(6)**, pp. 063003–+ (2005).  
doi:10.1103/PhysRevD.72.063003.
- LATTANZI, M., RUFFINI, R. AND VERESHCHAGIN, G.V.  
*Do WMAP data constraint the lepton asymmetry of the Universe to be zero?*  
In *Albert Einstein Century International Conference*, volume 861 of *American Institute of Physics Conference Series*, pp. 912–919 (2006).  
doi:10.1063/1.2399677.
- LAUREIJS, R., AMIAUX, J., ARDUINI, S., AUGUERES, J.L., BRINCHMANN, J. ET AL.  
*Euclid Definition Study Report.*  
*arXiv* (2011).
- LEE, B.W. AND WEINBERG, S.  
*Cosmological lower bound on heavy-neutrino masses.*  
*Phys. Rev. Lett.*, **39**, pp. 165–168 (1977).
- LEVINSON, A.  
*Observational Signatures of Sub-photospheric Radiation-mediated Shocks in the Prompt Phase of Gamma-Ray Bursts.*  
*ApJ*, **756**, 174 (2012).  
doi:10.1088/0004-637X/756/2/174.
- LEWIS, A. AND BRIDLE, S.  
*Cosmological parameters from CMB and other data: A Monte Carlo approach.*  
*Phys.Rev.*, **D66**, p. 103511 (2002).  
doi:10.1103/PhysRevD.66.103511.
- LEWIS, A., CHALLINOR, A. AND LASENBY, A.  
*Efficient Computation of CMB anisotropies in closed FRW models.*

- Astrophys. J.*, **538**, pp. 473–476 (2000).  
doi:10.1086/309179.
- LI, C. AND SARI, R.  
*Analytical Solutions for Expanding Fireballs.*  
*ApJ*, **677**, pp. 425–431 (2008).  
doi:10.1086/527551.
- LIGHTMAN, A.P.  
*Double Compton emission in radiation dominated thermal plasmas.*  
*ApJ*, **244**, pp. 392–405 (1981).  
doi:10.1086/158716.
- LIGHTMAN, A.P.  
*Relativistic thermal plasmas - Pair processes and equilibria.*  
*ApJ*, **253**, pp. 842–858 (1982).  
doi:10.1086/159686.
- LYUTIKOV, M.  
*The electromagnetic model of gamma-ray bursts.*  
*New Journal of Physics*, **8**, pp. 119–+ (2006).  
doi:10.1088/1367-2630/8/7/119.
- MANDL, F. AND SKYRME, T.H.R.  
*The Theory of the Double Compton Effect.*  
*Royal Society of London Proceedings Series A*, **215**, pp. 497–507 (1952).  
doi:10.1098/rspa.1952.0227.
- MANGANNO, G. ET AL.  
*Relic neutrino decoupling including flavour oscillations.*  
*Nucl. Phys.*, **B729**, pp. 221–234 (2005).  
doi:10.1016/j.nuclphysb.2005.09.041.
- MARASCHI, L.  
*Jets at different scales.*  
In S. Collin, F. Combes and I. Shlosman (eds.), *Active Galactic Nuclei: From Central Engine to Host Galaxy*, volume 290 of *Astronomical Society of the Pacific Conference Series*, pp. 275–+ (2003).
- MARTIN, J. AND BRANDENBERGER, R.  
*On the dependence of the spectra of fluctuations in inflationary cosmology on trans-Planckian physics.*  
*Phys. Rev.*, **D68**, p. 063513 (2003).  
doi:10.1103/PhysRevD.68.063513.
- MARTIN, J. AND SRIRAMKUMAR, L.  
*The scalar bi-spectrum in the Starobinsky model: The equilateral case.*

- JCAP, **1201**, p. 008 (2012).  
doi:10.1088/1475-7516/2012/01/008.
- MARTINELLI, M., CALABRESE, E., DE BERNARDIS, F., MELCHIORRI, A., PAGANO, L. ET AL.  
*Constraining Modified Gravity with Euclid.*  
*Phys.Rev.*, **D83**, p. 023012 (2011).  
doi:10.1103/PhysRevD.83.023012.
- MARTINELLI, M., MENEGONI, E. AND MELCHIORRI, A.  
*Future constraints on variations of the fine structure constant from combined CMB and weak lensing measurements.*  
*Phys.Rev.*, **D85**, p. 123526 (2012).  
doi:10.1103/PhysRevD.85.123526.
- MARTINS, C., MELCHIORRI, A., ROCHA, G., TROTTA, R., AVELINO, P. ET AL.  
*Wmap constraints on varying alpha and the promise of reionization.*  
*Phys.Lett.*, **B585**, pp. 29–34 (2004).  
doi:10.1016/j.physletb.2003.11.080.
- MARTINS, C., MELCHIORRI, A., TROTTA, R., BEAN, R., ROCHA, G. ET AL.  
*Measuring alpha in the early universe. 1. CMB temperature, large scale structure and fisher matrix analysis.*  
*Phys.Rev.*, **D66**, p. 023505 (2002).  
doi:10.1103/PhysRevD.66.023505.
- MASSEY, R., RHODES, J., LEAUTHAUD, A., CAPAK, P., ELLIS, R., KOEKE-MOER, A., RÉFRÉGIER, A., SCOVILLE, N., TAYLOR, J.E., ALBERT, J. ET AL.  
*COSMOS: Three-dimensional Weak Lensing and the Growth of Structure.*  
*ApJS*, **172**, pp. 239–253 (2007).  
doi:10.1086/516599.
- MEERBURG, P.D., WIJERS, R. AND VAN DER SCHAAR, J.P.  
*WMAP 7 Constraints on Oscillations in the Primordial Power Spectrum.*  
*arXiv* (2011).
- MENEGONI, E., PANDOLFI, S., GALLI, S., LATTANZI, M. AND MELCHIORRI, A.  
*Constraints on the Dark Energy Equation of State in Presence of a Varying Fine Structure Constant.*  
*International Journal of Modern Physics D*, **19**, pp. 507–512 (2010).  
doi:10.1142/S0218271810016506.
- MENEGONI, E., ARCHIDIACONO, M., CALABRESE, E., GALLI, S., MARTINS, C. ET AL.

- The Fine Structure Constant and the CMB Damping Scale.*  
*Phys.Rev.*, **D85**, p. 107301 (2012).  
doi:10.1103/PhysRevD.85.107301.
- MENEGONI, E., GALLI, S., BARTLETT, J.G., MARTINS, C.J.A.P. AND MEL-  
CHIORRI, A.  
*New Constraints on variations of the fine structure constant from CMB*  
*anisotropies.*  
*Phys. Rev.*, **D80**, p. 087302 (2009).  
doi:10.1103/PhysRevD.80.087302.
- MÉSZÁROS, P., LAGUNA, P. AND REES, M.J.  
*Gasdynamics of relativistically expanding gamma-ray burst sources - Kinematics,*  
*energetics, magnetic fields, and efficiency.*  
*ApJ*, **415**, pp. 181–190 (1993).
- MÉSZÁROS, P., RAMIREZ-RUIZ, E., REES, M.J. AND ZHANG, B.  
*X-Ray-rich Gamma-Ray Bursts, Photospheres, and Variability.*  
*ApJ*, **578**, pp. 812–817 (2002).  
doi:10.1086/342611.
- MÉSZÁROS, P. AND REES, M.J.  
*Steep Slopes and Preferred Breaks in Gamma-Ray Burst Spectra: The Role of Pho-*  
*tospheres and Comptonization.*  
*ApJ*, **530**, pp. 292–298 (2000).  
doi:10.1086/308371.
- MIHALAS, D. AND MIHALAS, B.W.  
*Foundations of Radiation Hydrodynamics* (New York, Oxford University  
Press, 1984).
- MORTONSON, M.J., DVORKIN, C., PEIRIS, H.V. AND HU, W.  
*CMB polarization features from inflation versus reionization.*  
*Phys.Rev.*, **D79**, p. 103519 (2009).  
doi:10.1103/PhysRevD.79.103519.
- MORTONSON, M.J. AND HU, W.  
*Reionization constraints from five-year WMAP data.*  
*Astrophys.J.*, **686**, pp. L53–L56 (2008).  
doi:10.1086/593031.
- MUKHANOV, V.F.  
*Quantum Theory of Gauge Invariant Cosmological Perturbations.*  
*Sov.Phys.JETP*, **67**, pp. 1297–1302 (1988).
- MUSTAFA, M.G. AND KÄMPFER, B.  
*Gamma flashes from relativistic electron-positron plasma droplets.*

- Phys. Rev. A, **79(2)**, pp. 020103–+ (2009).  
doi:10.1103/PhysRevA.79.020103.
- MYATT, J., DELETTREZ, J.A., MAXIMOV, A.V., MEYERHOFER, D.D., SHORT, R.W., STOECKL, C. AND STORM, M.  
*Optimizing electron-positron pair production on kilojoule-class high-intensity lasers for the purpose of pair-plasma creation.*  
Phys. Rev. E, **79(6)**, pp. 066409–+ (2009).  
doi:10.1103/PhysRevE.79.066409.
- NAKAR, E., PIRAN, T. AND SARI, R.  
*Pure and Loaded Fireballs in Soft Gamma-Ray Repeater Giant Flares.*  
ApJ, **635**, pp. 516–521 (2005).  
doi:10.1086/497296.
- NAKASHIMA, M., NAGATA, R. AND YOKOYAMA, J.  
*Constraints on the time variation of the fine structure constant by the 5-year WMAP data.*  
Prog.Theor.Phys., **120**, pp. 1207–1215 (2008).  
doi:10.1143/PTP.120.1207.
- NAKASHIMA, M., SAITO, R., TAKAMIZU, Y.I. AND YOKOYAMA, J.  
*The effect of varying sound velocity on primordial curvature perturbations.*  
Prog.Theor.Phys., **125**, pp. 1035–1052 (2011).  
doi:10.1143/PTP.125.1035.
- NARAIN, G., SCHAFFNER-BIELICH, J. AND MISHUSTIN, I.N.  
*Compact stars made of fermionic dark matter.*  
Phys. Rev. D, **74(6)**, 063003 (2006).  
doi:10.1103/PhysRevD.74.063003.
- NASELSKY, P.D., NOVIKOV, D.I. AND NOVIKOV, I.D.  
*The Physics of the Cosmic Microwave Background.*  
Cambridge Astrophysics (Cambridge Univ. Press, 2011).
- NAVARRO, J.F., FRENK, C.S. AND WHITE, S.D.M.  
*A Universal Density Profile from Hierarchical Clustering.*  
ApJ, **490**, p. 493 (1997).  
doi:10.1086/304888.
- NAVARRO, J.F., LUDLOW, A., SPRINGEL, V., WANG, J., VOGELSBERGER, M., WHITE, S.D.M., JENKINS, A., FRENK, C.S. AND HELMI, A.  
*The diversity and similarity of simulated cold dark matter haloes.*  
MNRAS, **402**, pp. 21–34 (2010).  
doi:10.1111/j.1365-2966.2009.15878.x.

- OKAMOTO, T. AND HU, W.  
*CMB lensing reconstruction on the full sky.*  
*Phys.Rev.*, **D67**, p. 083002 (2003).  
doi:10.1103/PhysRevD.67.083002.
- PACZYNSKI, B.  
*Gamma-ray bursters at cosmological distances.*  
*ApJ*, **308**, pp. L43–L46 (1986).  
doi:10.1086/184740.
- PACZYNSKI, B.  
*Super-Eddington winds from neutron stars.*  
*ApJ*, **363**, pp. 218–226 (1990).  
doi:10.1086/169332.
- PANDOLFI, S., GIUSARMA, E., KOLB, E.W., LATTANZI, M., MELCHIORRI, A.  
ET AL.  
*Impact of general reionization scenarios on extraction of inflationary parameters.*  
*Phys.Rev.*, **D82**, p. 123527 (2010a).  
doi:10.1103/PhysRevD.82.123527.
- PANDOLFI, S. ET AL.  
*Harrison-Z'eldovich primordial spectrum is consistent with observations.*  
*Phys. Rev.*, **D81**, p. 123509 (2010b).  
doi:10.1103/PhysRevD.81.123509.
- PARK, M. AND SORBO, L.  
*Sudden variations in the speed of sound during inflation: features in the power spectrum and bispectrum.*  
*Phys.Rev.*, **D85**, p. 083520 (2012).  
doi:10.1103/PhysRevD.85.083520.
- PATRICELLI, B., BERNARDINI, M.G., BIANCO, C.L., CAITO, L., IZZO, L.,  
RUFFINI, R. AND VERESHCHAGIN, G.  
*a New Spectral Energy Distribution of Photons in the Fireshell Model of GRBS.*  
*International Journal of Modern Physics D*, **20**, pp. 1983–1987 (2011).  
doi:10.1142/S0218271811020056.
- PEEBLES, P.J.E.  
*Recombination of the Primeval Plasma.*  
*ApJ*, **153**, pp. 1–+ (1968).  
doi:10.1086/149628.
- PE'ER, A.  
*Temporal Evolution of Thermal Emission from Relativistically Expanding Plasma.*  
*ApJ*, **682**, pp. 463–473 (2008).  
doi:10.1086/588136.

- PE'ER, A. AND RYDE, F.  
*A Theory of Multicolor Blackbody Emission from Relativistically Expanding Plasmas.*  
ApJ, **732**, pp. 49–+ (2011).  
doi:10.1088/0004-637X/732/1/49.
- PE'ER, A., RYDE, F., WIJERS, R.A.M.J., MÉSZÁROS, P. AND REES, M.J.  
*A New Method of Determining the Initial Size and Lorentz Factor of Gamma-Ray Burst Fireballs Using a Thermal Emission Component.*  
ApJ, **664**, pp. L1–L4 (2007).  
doi:10.1086/520534.
- PEIRIS, H.V. ET AL.  
*First year Wilkinson Microwave Anisotropy Probe (WMAP) observations: Implications for inflation.*  
*Astrophys. J. Suppl.*, **148**, p. 213 (2003).  
doi:10.1086/377228.
- PETERSON, B.M.  
*Toward Precision Measurement of Central Black Hole Masses.*  
In *IAU Symposium*, volume 267 of *IAU Symposium*, pp. 151–160 (2010).  
doi:10.1017/S1743921310006095.
- PILLA, R.P. AND SHAHAM, J.  
*Kinetics of Electron-Positron Pair Plasmas Using an Adaptive Monte Carlo Method.*  
ApJ, **486**, pp. 903–+ (1997).  
doi:10.1086/304534.
- PIRAN, T.  
*Gamma-ray bursts and the fireball model.*  
*Phys. Rep.*, **314**, pp. 575–667 (1999).
- PIRAN, T.  
*The physics of gamma-ray bursts.*  
*Reviews of Modern Physics*, **76**, pp. 1143–1210 (2004).  
doi:10.1103/RevModPhys.76.1143.
- PIRAN, T., SHEMI, A. AND NARAYAN, R.  
*Hydrodynamics of Relativistic Fireballs.*  
*MNRAS*, **263**, pp. 861–867 (1993).
- PLANCK COLLABORATION.  
*The Scientific programme of planck.*  
*arXiv* (2006).

PSALTIS, D. AND LAMB, F.K.

*Compton Scattering by Static and Moving Media. I. The Transfer Equation and Its Moments.*

ApJ, **488**, p. 881 (1997).

doi:10.1086/304711.

REES, M.J.

*Appearance of Relativistically Expanding Radio Sources.*

Nature, **211**, pp. 468–470 (1966).

doi:10.1038/211468a0.

REES, M.J.

*Studies in radio source structure-I. A relativistically expanding model for variable quasi-stellar radio sources.*

MNRAS, **135**, pp. 345–+ (1967).

REES, M.J. AND MÉSZÁROS, P.

*Dissipative Photosphere Models of Gamma-Ray Bursts and X-Ray Flashes.*

ApJ, **628**, pp. 847–852 (2005).

doi:10.1086/430818.

REICHARDT, C., ADE, P., BOCK, J., BOND, J.R., BREVIK, J. ET AL.

*High resolution CMB power spectrum from the complete ACBAR data set.*

Astrophys.J., **694**, pp. 1200–1219 (2009).

doi:10.1088/0004-637X/694/2/1200.

REID, B.A., PERCIVAL, W.J., EISENSTEIN, D.J., VERDE, L., SPERGEL, D.N.  
ET AL.

*Cosmological Constraints from the Clustering of the Sloan Digital Sky Survey DR7 Luminous Red Galaxies.*

Mon.Not.Roy.Astron.Soc., **404**, pp. 60–85 (2010).

doi:10.1111/j.1365-2966.2010.16276.x.

RIESS, A.G., MACRI, L., CASERTANO, S., LAMPEITL, H., FERGUSON, H.C.  
ET AL.

*A 3Hubble Space Telescope and Wide Field Camera 3.*

Astrophys.J., **730**, p. 119 (2011).

doi:10.1088/0004-637X/732/2/129,10.1088/0004-637X/730/2/119.

RIESS, A.G. ET AL.

*A Redetermination of the Hubble Constant with the Hubble Space Telescope from a Differential Distance Ladder.*

Astrophys. J., **699**, pp. 539–563 (2009).

doi:10.1088/0004-637X/699/1/539.

ROCHA, G., TROTTA, R., MARTINS, C., MELCHIORRI, A., AVELINO, P.  
ET AL.

*Measuring alpha in the early universe: cmb polarization, reionization and the fisher matrix analysis.*

*Mon.Not.Roy.Astron.Soc.*, **352**, p. 20 (2004).

doi:10.1111/j.1365-2966.2004.07832.x.

ROTONDO, M., RUEDA, J.A., RUFFINI, R. AND XUE, S.S.

*Relativistic Thomas-Fermi treatment of compressed atoms and compressed nuclear matter cores of stellar dimensions.*

*Phys. Rev. C*, **83(4)**, 045805 (2011).

doi:10.1103/PhysRevC.83.045805.

RUFFINI, R.

*On the de Vaucouleurs density-radius relation and the cellular intermediate large-scale structure of the universe.*

In H.G. Corwin Jr. and L. Bottinelli (eds.), *World of Galaxies (Le Monde des Galaxies)*, pp. 461–472 (1989).

RUFFINI, R., AKSENOV, A., BERNARDINI, M.G., BIANCO, C.L., CAITO, L., DAINOTTI, M.G., DE BARROS, G., GUIDA, R., VERESHCHAGIN, G. AND XUE, S.

*The canonical Gamma-Ray Bursts: long, “fake”-“disguised” and “genuine” short bursts.*

In G. Giobbi, A. Tornambe, G. Raimondo, M. Limongi, L. A. Antonelli, N. Menci, & E. Brocato (ed.), *American Institute of Physics Conference Series*, volume 1111 of *American Institute of Physics Conference Series*, pp. 325–332 (2009a).

doi:10.1063/1.3141569.

RUFFINI, R., AKSENOV, A.G., BERNARDINI, M.G., BIANCO, C.L., CAITO, L., CHARDONNET, P., DAINOTTI, M.G., DE BARROS, G., GUIDA, R., IZZO, L. ET AL.

*The Blackholic energy and the canonical Gamma-Ray Burst IV: the “long,” “genuine short” and “fake-disguised short” GRBs.*

In M. Novello and S. Perez (eds.), *American Institute of Physics Conference Series*, volume 1132 of *American Institute of Physics Conference Series*, pp. 199–266 (2009b).

doi:10.1063/1.3151839.

RUFFINI, R., BIANCO, C.L., CHARDONNET, P., FRASCHETTI, F., VITAGLIANO, L. AND XUE, S.

*New perspectives in physics and astrophysics from the theoretical understanding of Gamma-Ray Bursts.*

In *AIP Conf. Proc. 668: Cosmology and Gravitation*, pp. 16–107 (2003a).

RUFFINI, R., BIANCO, C.L., FRASCHETTI, F., XUE, S. AND CHARDONNET, P.  
*On the Interpretation of the Burst Structure of Gamma-Ray Bursts.*

- ApJ, **555**, pp. L113–L116 (2001).  
doi:10.1086/323176.
- RUFFINI, R., SALMONSON, J.D., WILSON, J.R. AND XUE, S.S.  
*On the pair electromagnetic pulse of a black hole with electromagnetic structure.*  
A&A, **350**, pp. 334–343 (1999).
- RUFFINI, R., SALMONSON, J.D., WILSON, J.R. AND XUE, S.S.  
*On the pair-electromagnetic pulse from an electromagnetic black hole surrounded by a baryonic remnant.*  
A&A, **359**, pp. 855–864 (2000).
- RUFFINI, R., SIUTSOU, I.A. AND VERESHCHAGIN, G.V.  
*Theory of photospheric emission from relativistic outflows.*  
ArXiv e-prints (2011).
- RUFFINI, R., SONG, D.J. AND TARAGLIO, S.  
*The 'ino' mass and the cellular large-scale structure of the universe.*  
A&A, **190**, pp. 1–9 (1988).
- RUFFINI, R. AND VERESHCHAGIN, G.  
*Electron-positron plasma in GRBs and in cosmology.*  
ArXiv e-prints (2012).
- RUFFINI, R., VERESHCHAGIN, G.V. AND XUE, S.S.  
*Vacuum polarization and plasma oscillations.*  
Phys. Lett. A, **371**, pp. 399–405 (2007).
- RUFFINI, R., VERESHCHAGIN, G. AND XUE, S.S.  
*Electron-positron pairs in physics and astrophysics.*  
Physics Reports, **487**, pp. 1–140 (2010).
- RUFFINI, R., VITAGLIANO, L. AND XUE, S.S.  
*On plasma oscillations in strong electric fields.*  
Phys. Lett. B, **559**, pp. 12–19 (2003b).
- RYBICKI, G.B. AND LIGHTMAN, A.P.  
*Radiative processes in astrophysics* (New York, Wiley-Interscience, 1979).
- RYDE, F. AND PE'ER, A.  
*Quasi-blackbody Component and Radiative Efficiency of the Prompt Emission of Gamma-ray Bursts.*  
ApJ, **702**, pp. 1211–1229 (2009).  
doi:10.1088/0004-637X/702/2/1211.
- RYDE, F., PE'ER, A., NYMARK, T., AXELSSON, M., MORETTI, E., LUNDMAN, C., BATTELINO, M., BISSALDI, E., CHIANG, J., JACKSON, M.S. ET AL.

- Observational evidence of dissipative photospheres in gamma-ray bursts.*  
MNRAS, **415**, pp. 3693–3705 (2011).  
doi:10.1111/j.1365-2966.2011.18985.x.
- SALUCCI, P., FRIGERIO MARTINS, C. AND LAPI, A.  
*DMAW 2010 LEGACY the Presentation Review: Dark Matter in Galaxies with its Explanatory Notes.*  
*ArXiv e-prints* (2011).
- SASAKI, M.  
*Large Scale Quantum Fluctuations in the Inflationary Universe.*  
*Prog.Theor.Phys.*, **76**, p. 1036 (1986).  
doi:10.1143/PTP.76.1036.
- SAUTER, F.  
*Über das Verhalten eines Elektrons im homogenen elektrischen Feld nach der relativistischen Theorie Diracs.*  
*Zeits. Phys.*, **69**, pp. 742–+ (1931).
- SCHMIDT, S., BLASCHKE, D., RÖPKE, G., SMOLYANSKY, S.A., PROZORKEVICH, A.V. AND TONEEV, V.D.  
*A Quantum Kinetic Equation for Particle Production in the Schwinger Mechanism.*  
*International Journal of Modern Physics E*, **7**, pp. 709–722 (1998).  
doi:10.1142/S0218301398000403.
- SCHWINGER, J.  
*On Gauge Invariance and Vacuum Polarization.*  
*Phys. Rev.*, **82**, pp. 664–679 (1951).
- SHEMI, A. AND PIRAN, T.  
*The appearance of cosmic fireballs.*  
*ApJ*, **365**, pp. L55–L58 (1990).
- SMITH, A., ARCHIDIACONO, M., COORAY, A., DE BERNARDIS, F., MELCHIORRI, A. ET AL.  
*The Impact of Assuming Flatness in the Determination of Neutrino Properties from Cosmological Data.*  
*Phys.Rev.*, **D85**, p. 123521 (2012a).  
doi:10.1103/PhysRevD.85.123521.
- SMITH, R. ET AL.  
*Stable clustering, the halo model and nonlinear cosmological power spectra.*  
*Mon.Not.Roy.Astron.Soc.*, **341**, p. 1311 (2003).  
doi:10.1046/j.1365-8711.2003.06503.x.

- SMITH, T.L., DAS, S. AND ZAHN, O.  
*Constraints on neutrino and dark radiation interactions using cosmological observations.*  
*Phys.Rev.*, **D85**, p. 023001 (2012b).  
doi:10.1103/PhysRevD.85.023001.
- SMOLYANSKY, S.A., ROEPKE, G., SCHMIDT, S., BLASCHKE, D., TONEEV, V.D. AND PROZORKEVICH, A.V.  
*Dynamical derivation of a quantum kinetic equation for particle production in the Schwinger mechanism.*  
*ArXiv High Energy Physics - Phenomenology e-prints* (1997).
- STAROBINSKY, A.A.  
*Spectrum of adiabatic perturbations in the universe when there are singularities in the inflation potential.*  
*JETP Lett.*, **55**, pp. 489–494 (1992).
- STEFANESCU, P.  
*Constraints on time variation of fine structure constant from WMAP-3yr data.*  
*New Astron.*, **12**, pp. 635–640 (2007).  
doi:10.1016/j.newast.2007.06.004.
- STEPNEY, S.  
*Two-body relaxation in relativistic thermal plasmas.*  
*MNRAS*, **202**, pp. 467–481 (1983).
- STEWART, E.D. AND LYTH, D.H.  
*A more accurate analytic calculation of the spectrum of cosmological perturbations produced during inflation.*  
*Phys. Lett.*, **B302**, pp. 171–175 (1993).  
doi:10.1016/0370-2693(93)90379-V.
- SVENSSON, R.  
*Electron-Positron Pair Equilibria in Relativistic Plasmas.*  
*ApJ*, **258**, pp. 335–+ (1982).  
doi:10.1086/160082.
- SVENSSON, R.  
*Steady mildly relativistic thermal plasmas - Processes and properties.*  
*MNRAS*, **209**, pp. 175–208 (1984).
- TAYLOR, A.N., BACON, D.J., GRAY, M.E., WOLF, C., MEISENHEIMER, K., DYE, S., BORCH, A., KLEINHEINRICH, M., KOVACS, Z. AND WISOTZKI, L.  
*Mapping the 3D dark matter with weak lensing in COMBO-17.*  
*MNRAS*, **353**, pp. 1176–1196 (2004).  
doi:10.1111/j.1365-2966.2004.08138.x.

- TEGMARK, M. ET AL.  
*Cosmological Constraints from the SDSS Luminous Red Galaxies.*  
*Phys. Rev.*, **D74**, p. 123507 (2006).  
doi:10.1103/PhysRevD.74.123507.
- THOMA, M.H.  
*Colloquium: Field theoretic description of ultrarelativistic electron-positron plasmas.*  
*Reviews of Modern Physics*, **81**, pp. 959–968 (2009).  
doi:10.1103/RevModPhys.81.959.
- THORNE, K.S.  
*Relativistic radiative transfer - Moment formalisms.*  
*MNRAS*, **194**, pp. 439–473 (1981).
- TOMA, K., WU, X.F. AND MÉSZÁROS, P.  
*Photosphere-internal shock model of gamma-ray bursts: case studies of Fermi/LAT bursts.*  
*MNRAS*, **415**, pp. 1663–1680 (2011).  
doi:10.1111/j.1365-2966.2011.18807.x.
- TRAC, H., BODE, P. AND OSTRIKER, J.P.  
*Templates for the Sunyaev-Zel'dovich Angular Power Spectrum.*  
*Astrophys.J.*, **727**, p. 94 (2011).  
doi:10.1088/0004-637X/727/2/94.
- TREMAINE, S. AND GUNN, J.E.  
*Dynamical role of light neutral leptons in cosmology.*  
*Phys. Rev. Lett.*, **42**, pp. 407–410 (1979).
- UEHLING, E.A.  
*Transport Phenomena in Einstein-Bose and Fermi-Dirac Gases. II.*  
*Physical Review*, **46**, pp. 917–929 (1934).  
doi:10.1103/PhysRev.46.917.
- UEHLING, E.A. AND UHLENBECK, G.E.  
*Transport Phenomena in Einstein-Bose and Fermi-Dirac Gases. I.*  
*Physical Review*, **43**, pp. 552–561 (1933).  
doi:10.1103/PhysRev.43.552.
- USOV, V.V.  
*Bare Quark Matter Surfaces of Strange Stars and  $e^+e^-$  Emission.*  
*Phys. Rev. Lett.*, **80**, pp. 230–233 (1998).
- USOV, V.V.  
*Thermal Emission from Bare Quark Matter Surfaces of Hot Strange Stars.*  
*ApJ*, **550**, pp. L179–L182 (2001).

doi:10.1086/319639.

VAN VLIET, C.

*Equilibrium and Non-Equilibrium Statistical Mechanics* (World Scientific Pub., 2008).

ISBN 9789812704771.

VINNIK, D.V., PROZORKEVICH, A.V., SMOLYANSKY, S.A., TONEEV, V.D., HECHT, M.B., ROBERTS, C.D. AND SCHMIDT, S.M.

*Plasma production and thermalisation in a strong field.*

*European Physical Journal C*, **22**, pp. 341–349 (2001).

doi:10.1007/s100520100787.

VIOLLIER, R.D., TRAUTMANN, D. AND TUPPER, G.B.

*Supermassive neutrino stars and galactic nuclei.*

*Physics Letters B*, **306**, pp. 79–85 (1993).

doi:10.1016/0370-2693(93)91141-9.

VURM, I., LYUBARSKY, Y. AND PIRAN, T.

*On thermalization in gamma-ray burst jets and the peak energies of photospheric spectra.*

*ArXiv e-prints* (2012).

WALKER, M.G., MCGAUGH, S.S., MATEO, M., OLSZEWSKI, E.W. AND KUZIO DE NARAY, R.

*Comparing the Dark Matter Halos of Spiral, Low Surface Brightness, and Dwarf Spheroidal Galaxies.*

*ApJ*, **717**, pp. L87–L91 (2010).

doi:10.1088/2041-8205/717/2/L87.

WEBB, J., KING, J., MURPHY, M., FLAMBAUM, V., CARSWELL, R. ET AL.

*Indications of a spatial variation of the fine structure constant.*

*Phys.Rev.Lett.*, **107**, p. 191101 (2011).

doi:10.1103/PhysRevLett.107.191101.

WEINBERG, S.

*Cosmology* (Oxford University Press, April 2008., 2008).

WILKS, S.C., KRUEER, W.L., TABAK, M. AND LANGDON, A.B.

*Absorption of ultra-intense laser pulses.*

*Physical Review Letters*, **69**, pp. 1383–1386 (1992).

doi:10.1103/PhysRevLett.69.1383.

YARESKO, R., MUSTAFA, M.G. AND KÄMPFER, B.

*Relativistic expansion of electron-positron-photon plasma droplets and photon emission.*

*Physics of Plasmas*, **17(10)**, p. 103302 (2010).

doi:10.1063/1.3499410.

ZELDOVICH, Y.B., KURT, V.G. AND SYUNYAEV, R.A.

*Recombination of Hydrogen in the Hot Model of the Universe.*

*Zhurnal Eksperimental noi i Teoreticheskoi Fiziki*, **55**, pp. 278–286 (1968).

